Doctoral Dissertation
Doctoral Program in Mechanical Engineering (34th Cycle)

Experimental investigation of nonlinear structural dynamics of shrouded turbine blade

By

Rizwan Ahmed

******

Supervisor(s):

Prof. Stefano Zucca

Prof. Christian Maria Firrone

Doctoral Examination Committee:

Prof. Dario di Maio, Referee, University of Twente, Netherlands

Prof. Marcelo Braga Dos Santos, Referee, Universidade Federal de Uberlandia, Brazil

Politecnico di Torino
2022

Declaration

I hereby declare that, the contents and organization of this dissertation constitute my own original work and does not compromise in any way the rights of third parties, including those relating to the security of personal data.

Rizwan Ahmed

2022

* This dissertation is presented in partial fulfillment of the requirements for **Ph.D. degree** in the Graduate School of Politecnico di Torino (ScuDo).

I would like to dedicate this thesis to my parents, my wife and my children

Acknowledgment

First of all, I am thankful to The Almighty Allah for blessing me with this opportunity, the knowledge and the strength to undertake and complete this journey.

I am extremely grateful to my academic supervisors and kind mentors, Prof. Stefano Zucca and Prof. Christian Maria Firrone, for their invaluable advice, continuous support, and constructive approach during the course of my PhD study. It was an honor and a great pleasure to learn and work under their guidance and supervision.

I thank the technical staff of DIMEAS laboratory for the support provided during the experimental phase of my research work. I also thank my colleague and former PhD student Reddy for the collaboration during the software validation phase of my study.

I would like to thank and acknowledge Higher Education Commission (HEC), Pakistan for providing this wonderful opportunity through HRDI-UESTP Scholarship Project.

Although I cannot thank them enough, but I am indebted to my parents for their unconditional love, prayers and everlasting support throughout my life. I am immensely grateful and appreciative of my wife, Anum for being supportive, understanding and encouraging at all times. My children Anaba and Zahran whose bright future I look forward to, have also been a source of motivation for me.

Many thanks to fellow researchers of AERMEC research group; my seniors Umer, Mehrdad, Zeeshan and my colleagues Peyman and Erhan for the good times and fruitful discussions regarding different aspects of knowledge and life.

Finally, I thank my family, friends and teachers who supported and motivated me during my whole life.

Rizwan Ahmed
Torino, June 2022

Abstract

Low Pressure Turbine (LPT) blades operate as one of the most crucial components of turbomachinery. These blades are subjected to highly stressed forced vibrations during the operation, which can cause high cycle fatigue failure. To avoid such type of a catastrophic failure during operation, the estimation and reduction of these vibration amplitudes is mandatory during the design phase. Generally, the vibration amplitudes are reduced by using friction-damping devices in the blade assembly like shrouds, under-platform dampers and snubbers. Shrouded turbine blades comprise of shrouds as covers at the blade tip that are in contact with the shrouds of the adjacent blades and engage due to the centrifugal forces. During blade vibration, the coupled shrouded turbine blades undergo relative motion where three-dimensional periodic shroud contact forces are activated resulting in energy dissipation because of the friction. To simulate the effect of the complex friction damping process on the dynamics of the shrouded turbine blade, numerical contact models are implemented in non-linear solvers to predict the nonlinear forced response of the shrouded turbine blades and shroud contact forces. Experimental validation of these contact models is necessary for continuous improvement and the need arises to also measure the contact forces acting at shrouds during the experiments. Furthermore, modern industrial requirement of more accurate and detailed simulations and models necessitates a comprehensive experimental validation, which demands the measurement of additional parameters from purposely designed application specific test rigs.

This doctoral thesis deals with the design, development and operation of an experimental test rig that provides for the simultaneous measurement of dynamic response of shrouded blade and three-dimensional shroud contact forces during forced vibration testing. The proposed experimental setup allows the collection of an experimental database that will be used for the experimental validation of the contact models implemented in nonlinear solvers to predict the nonlinear forced response and shroud contact forces. The description of the design phase starts with the outline of the design requirements of the test rig considering the research objectives. The design requirements and finite element analysis in ANSYS assisted

in finalizing the design of the test rig components and their mechanisms. The major components designed for the test rig i.e. the mockup shrouded blade, tri-directional contact force measurement system and the torque screw mechanism are explained. The design, calibration and validation of the novel contact force measurement system is presented that was designed to engage both the shroud contacts simultaneously in order to measure three-dimensional static and periodic shroud contact forces.

The study highlights different aspects of the test rig commissioning that involve the experimental modal testing of the test rig to determine the actual natural frequencies of the system. Details of the experimental setup describe the role of the other involved components and instrumentation i.e. the force sensors, accelerometers, shaker and data acquisition systems. Experimental procedure and the defined test matrix demonstrate how the test campaign was performed for different normal preloads and excitation force levels. In the results section, the effects of the variation in the normal preload and excitation force levels on the measured response and shroud contact forces are discussed. The variation of the static contact forces during the experimental campaign was analyzed and the behavior of the periodic shroud contact forces during the stepped sine testing was also explained. Finally, the study demonstrates how the experimental results established the efficacy of the proposed test rig to provide a complete representation of the dynamic response of the shrouded blade and three-dimensional shroud contact forces that will lead to a more detailed and accurate experimental validation of the simulation tools.

Contents

List of Figures

List of Tables

Chapter 1

Introduction

1.1 Motivation

Turbomachinery forms an important part of modern-day power plant technology with wide ranging applications in sectors related to power generation, marine, automotive and aerospace. The evolution of turbomachine technologies leading to the development of sophisticated gas turbine engines was not only centered on thrust generation in modern aircraft propulsion systems but also focused on reducing costs, increasing reliability, and improving the efficiency without compromising on the environmental impacts. On the other hand, with the advent of improved combined cycle power plants (CCPP), advanced power generation schemes were able to achieve high performance.

Aerospace gas turbine engines provided the advantages of compactness, greater power to weight ratio and lengthy operation times as compared to the previously used reciprocating engines. Moreover, higher speeds were achieved along with the possibility of using different fuel types. Nevertheless, to develop a reliable gas turbine engine that could withstand extreme operating environments, the designing intricacies and manufacturing complexities meant the use of exclusive engineering materials and advanced manufacturing processes. Although, these factors made the development process very expensive, implementation of new and improved coatings, cooling schemes and high-performance alloys resulted in increasing the operation envelope of gas turbine engines especially with respect to

high pressure ratios and high temperatures thereby increasing the overall efficiency of modern gas turbine engines over the last two decades [1].

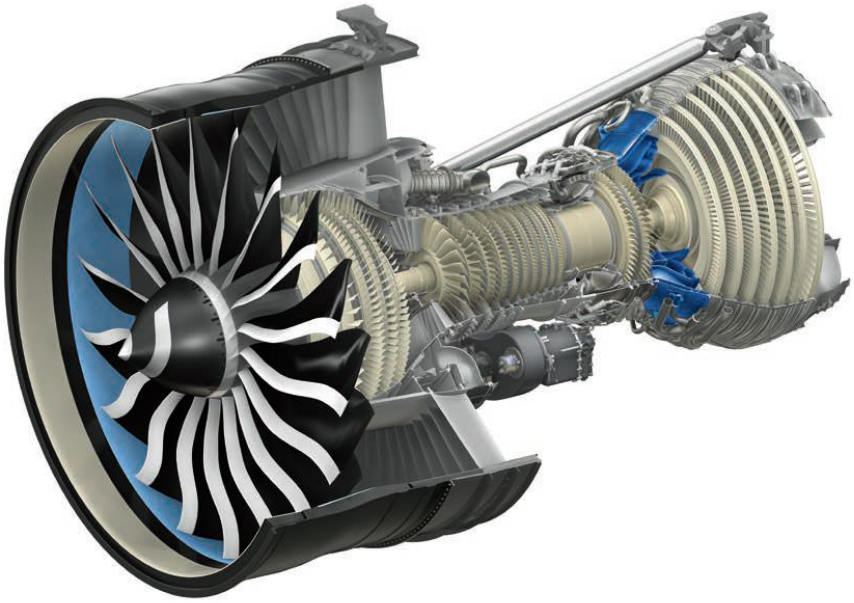

Figure 1: GE GEnx Engine (https://www.geaviation.com/propulsion/commercial/genx)

A typical aircraft gas turbine engine (Figure 1) mainly consists of three components i.e., a compressor, combustion chamber and turbine. The compressor takes air into the engine, where it is highly pressurized before being fed to the combustion chamber at high speeds. In the combustion chamber, continuous stream of fuel is injected and mixed with the high-pressure air at very high temperatures exceeding 1800°C. The resulting high temperature and high-pressure gas stream moves through the turbine section, which has a sophisticated sequence of alternating stationery blades (stators) and rotating blades (rotors) having airfoil cross section profile. The hot gas stream expanding through the turbine turns the rotating blades thereby also driving the compressor which takes in more pressurized air into the combustion chamber. The compressor, combustion chamber and turbine are connected by one or more shafts. Both, the compressor, and turbine sections consist of low pressure - high pressure stages of compressor blades and turbine blades respectively to attain the necessary pressure ratios.

The design criteria of any gas turbine engine comprise of high efficiency, high reliability, ease of installation and ease of service. Other important design considerations involve compliance with environmental standards, integration of reliable auxiliary as well as control systems and flexibility to fulfill different fuel

and maintenance requirements [1]. In order to achieve high reliability of gas turbine engine and its critical components while trying to accomplish higher efficiency, one of the most important factors considered by the designers are the stresses at blades, bladed disks and shafts during the operation when these are subjected to different type of mechanical loads and extremely high temperatures.

1.1.1 Turbine blade vibrations and High Cycle Fatigue (HCF)

The thermal loads and mechanical stresses encountered by the turbine blades during operation are meticulously evaluated as the structural integrity of the engine and its rotating parts is highly dependent on its capability to resist these stresses. The nature of these mechanical stresses can be either static or dynamic. The static stresses occur, firstly, because of the centrifugal forces acting on the blade during rotation and secondly due to the static part of the fluid dynamic forces. Whereas the dynamic stresses are caused by the oscillatory aerodynamic loads that result in highly stressed forced vibrations [2], [3]. Mostly, the issues related to these vibrations arise due to the resonant vibrations taking place at integral multiple of rotation speed and aeroelastic instabilities (flutter) taking place as non-integral order vibration [2]. High vibration responses due to periodic excitation forces near the resonance frequencies result in continuous amplification of vibration amplitudes until the components fail. Although the related stress field may be well below the yield point, the increasing vibration amplitudes can lead to crack initiation for high number of cycles. Therefore, if not properly addressed, these repeated instances of increased vibration amplitudes near blade resonance frequencies, can lead to high cycle fatigue (HCF) failure which can be catastrophic. Almost 50% of the jet engine failures occur due to damaged turbine blades and discs. Moreover, fatigue failures are the cause of around 50% of damaged components in jet engines in which HCF is responsible for about half of these fatigue failures [4].

In consideration of the risk mentioned above, one of the primary objectives of the design is to reduce these vibration amplitudes. This can be accomplished, firstly, by avoidance of resonance i.e., avoidance of excitation forces near natural frequencies and secondly by improvement of system damping. Averting excitation at resonance frequencies is generally achieved with modification of the mechanical design configuration. This involves changing the quantity of blades or by adjusting the mass and stiffness distributions that effect the dynamic behavior of the system. However, since the turbine bladed disks have high modal density and the frequency range of the aerodynamic excitation forces is widespread, absolute avoidance of resonance is impracticable. The alternate approach relies on the exploitation of the

system damping. The damping of the system usually includes aerodynamic damping, material damping and friction damping. Aerodynamic damping comes from the blade motion due to the aerodynamic forces exerted by the gas stream flowing out of the combustor and forms a major part of the overall damping of the bladed disk. Material damping due to material hysteresis is physically represented by the conversion of kinetic energy of the vibrating turbine blade into thermal energy. However, it can be considered negligible due to the advanced materials as monocrystalline metals being used nowadays for the fabrication of turbine blades. Friction damping takes place due to the mechanical joints and contact interfaces and is further discussed in the next section.

1.1.2 Friction Damping and Shrouded Turbine Blades

As stated, one of the methods to reduce the vibration amplitude of turbine blades is friction damping. Friction damping is the type of damping that initiates when two mechanical or structural components come into contact and slide against each other to produce a resistive frictional force that results in energy dissipation. Energy is dissipated due to the uneven microscopic motion of the asperities and particles present at the contact interface. The frictional force or the tangential contact force produced at the sliding contact interface depends on the tribosystem conditions (surface topography, material properties, temperature) as well as the normal load applied on the contact interface.

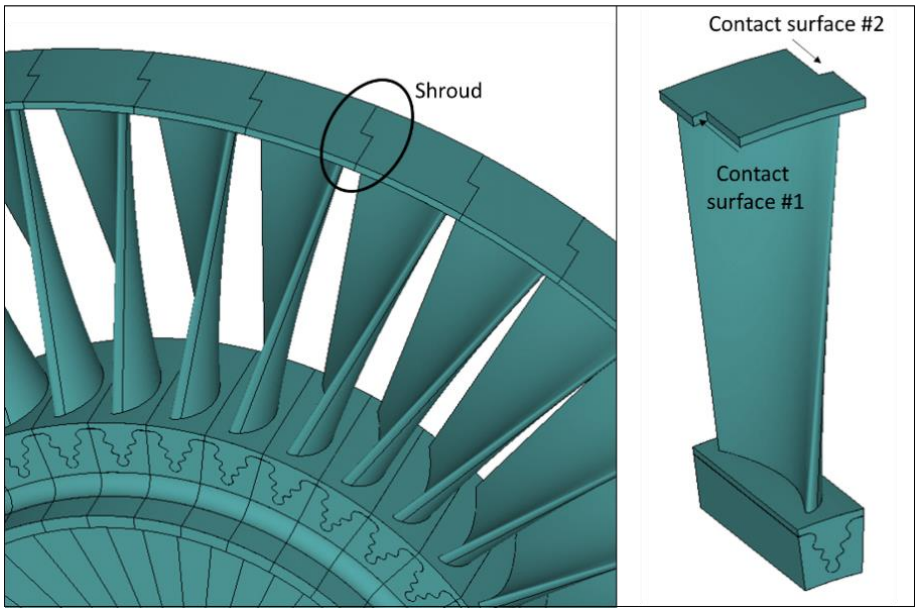

Figure 2: Shrouded turbine blade assembly

In turbomachinery, friction damping is usually implemented in the form of blade-root joints, under-platform dampers, shrouds, or snubbers [5], [6]. This damping method has been found to be efficient, simple, cost-effective and reliable. In case of shrouded blades, which will be the focus of this study, shrouds (Figure 2) form as covers placed at the tip of each blade, designed to enforce blade-to-blade coupling by means of contact surfaces, where energy is dissipated by friction. As a result of the assembly process, two contact surfaces exist at each blade shroud. In static condition, a constant normal contact force N is acting on the shroud contact surfaces of adjacent shrouded blades. When the blade begins to vibrate, due to the relative displacement between the shroud contacts, a tangential contact force T develops in addition to the varying normal contact force N, where $|T| \leq \mu N$ with μ being the coefficient of friction. The relative displacements and the corresponding contact forces determine the status of the contact during the oscillations. A full stick condition occurs at higher normal contact force N and is governed by linear relation between the tangential contact force T and the relative displacement. In this scenario, $|T| < \mu N$ and involves elastic deformation of asperities at the contact interface. On the contrary, a gross slip or macro slip condition occurs at higher excitation force F_E or weaker normal contact force N, where $|T| = \mu N$ and the contact interface undergoes complete sliding motion. The transition between the full stick condition and gross slip condition involves partial slip at the contact interface which is known as microslip. Another extreme condition is lift off or separation which happens when the normal contact force N is zero and there is no contact. As expected, in this case, the tangential contact force is zero. However, impacts can still result in energy dissipation. The stick/slip phenomena is usually explained by the hysteresis cycles that demonstrate how the tangential contact forces vary with respect to the tangential displacements.

1.1.3 Contact models and their implementation

Friction is a complex process which involves transmission of forces, conversion of mechanical energy, alteration of surface topographies, removal, or formation of interface materials and different physical as well as chemical changes. For a dynamic system with a sliding interface where friction is a variable, the boundary condition is not static and deterministic because of the interfacial variations in geometrical, material, mechanical, physical, and chemical characteristics. The friction coefficients are not inherent material properties, but they are dependent on type of contact surfaces, their interactions, time history, operational and environmental conditions [7]. For these reasons, a universal friction model or

contact model is unfeasible and accurate contact modeling for any specific application like prediction of dynamic response and contact forces due to friction damping in turbine blades is an intricate process especially considering the different contact conditions and nonlinearity involved.

In case of turbine blades, friction damping methods were addressed by several studies introducing various modeling approaches. These studies broadly presented lumped parameter models [6], [8], analytical models [9] and finite element models [10]–[12]. Some of the studies also extended the scope of the models to describe the contact interface in terms of macroslip [5], [10], [12], [13] and microslip [14], [15] that helped to improve the way in which non-linear forced response levels were predicted. Several contact models described contact kinematics [10], [13], [16]–[18] which were useful for the computation of non-linear contact forces. With respect to friction modeling, four main types of contact elements can be categorized in literature:

1. 1D tangential relative displacement and constant normal load [5]
2. 1D tangential relative displacement and variable normal load [10], [16]
3. 2D tangential relative displacement and constant normal load [17]
4. 2D tangential relative displacement and variable normal load [18]

In order to compute periodic contact forces using these contact models, it is necessary to provide the static normal pre-load value after carrying out an initial static analysis of the system. However, studies [19] showed that the preliminary static analysis is not required because of the possibility to calculate static and dynamic contact forces simultaneously.

For the computation of non-linear forced response for shrouded turbine bladed disks, commercially available finite element codes are not feasible as they make use of time integration method for non-linear differential equations which is computationally time consuming and therefore unsuitable for a detailed parametric analysis during the design process. Hence, customized numerical codes are developed for the computation of forced response in frequency domain. These codes implement Harmonic Balance Method (HBM) converting the non-linear differential equations to a set of non-linear algebraic equations [20].

1.1.4 Experimental validation

Considering the complexities in the development of the contact models, it is vital to address and resolve the uncertainties involved in the prediction of dynamic response and contact forces with respect to turbine blades with friction contacts. The considerable effect of the friction dampers on the shift in natural frequencies and vibration amplitudes must be carefully evaluated. For accurate validation of numerical models, it is necessary to obtain the measured forced response and contact forces from the experiments for a representative comparison of numerical and experimental results under the specified boundary conditions. Moreover, actual values of friction coefficient and contact stiffness obtained from the experiments can be specified as inputs in the simulations. Generally, the aforementioned experimental validation is accomplished by means of purposely designed experimental test rigs. Existing experimental test setups in literature can be divided into three groups which are dealt in detail in the next chapter. These groups can be distinguished on the basis of the parameters that are measured. First group of experiments measured forced response of shrouded blades in the form of displacements and accelerations to study the effect of friction damping over the blade dynamics. The second group of experiments focused on the measurement of contact parameters like friction coefficient and contact stiffness to understand the relative contact kinematics. The third group of experiments measured the forced response and the contact forces simultaneously. The proposed experimental test rig in this doctoral study aims to bring novelty to this third group as described in the ensuing research objectives.

1.2 Research Objectives

Modern turbomachinery industry demand more accurate and detailed numerical models related to the critical components of gas turbine engines. Likewise, this entails more detailed and comprehensive experimental results and subsequent validation, which requires the measurement of additional parameters in simplified experimental test rigs particularly the shroud contact forces in case of shrouded turbine blades. The current experimental test setups available in the literature are not sufficient to obtain the comprehensive three-dimensional characteristics of shroud contact forces. For a thorough explanation of shroud contact dynamics that improves the experimental validation of contact models, it is necessary to measure three-dimensional shroud contact forces i.e. one normal contact force and two

orthogonal tangential contact forces during the forced response testing of the shrouded turbine blade.

The primary goal of this study is to design and develop an experimental test setup to investigate the nonlinear structural dynamics of a shrouded turbine blade. The novelty of this test rig is the measurement of forced response and three-dimensional shroud contact forces simultaneously. In order to achieve the objectives, the following goals are outlined:

1. Design and calibration of a tri-directional contact force measurement system

2. Design, development and commissioning of a novel experimental test rig to simultaneously measure the forced response and three-dimensional shroud contact forces of a shrouded turbine blade.

3. Validation of the experimental results with the results obtained by numerical simulations.

1.3 Thesis Overview

The thesis is divided into eight chapters with the CHAPTER 1 consisting of the introduction, background and research objectives.

CHAPTER 2 deals with the state of the art and literature review explaining the different experimental test rigs already existing in the literature based on the measurement technology and the parameters they measure.

CHAPTER 3 explains the design objectives and components of the proposed experimental test rig. The design of the major components of the test rig i.e. the mockup shrouded blade assembly, the tri-directional contact force measurement system and the torque screw mechanism are discussed. This chapter also includes the details of the finite element analysis performed on the designed test rig.

CHAPTER 4 discusses design, calibration and validation of the novel tri-directional contact force measurement specifically designed for this test rig in order to measure the three-dimensional shroud contact forces.

CHAPTER 5 deals with different phases of test rig commissioning that starts with a preliminary analysis of the system's actual natural frequencies determined by modal testing of the free and engaged shrouded blade. This is followed by a brief

description of the instrumentation and experimental setup. Finally, the procedure and the sequence of the experiments is explained.

CHAPTER 6 discusses the results of the different experiments performed with different excitation forces and different normal preloads. The various trends in the variation of static as well as periodic contact forces are explained.

CHAPTER 7 explains the Harmonic Balance Method and the nonlinear solver implementing the contact models to characterize the friction contacts in shrouded turbine blades. The computed forced response of the shrouded blade and the shroud contact forces are compared with the experimental results under the specified conditions.

CHAPTER 8 presents the conclusions drawn from this study that dealt with the design and development of the novel test rig to measure three-dimensional shroud contact forces and the forced response of the shrouded blade simultaneously. The advantages, the extensions as well as the limitations are briefly discussed. Moreover, the potential of the test rig to perform new and useful measurements in future is described.

Chapter 2

Literature Review

2.1 Introduction

This chapter outlines the existing experimental studies available in the literature and which are related to the research topic of this doctoral thesis. The emphasis will be on the different techniques employed to measure different parameters during the experiments performed to understand friction damping and especially the application of friction damping with respect to shrouded turbine blades.

2.2 Existing Experimental Rigs

As mentioned before, experimental validation of contact models is achieved by means of customized and simplified experimental test rigs. Overall, these experimental studies can be classified into three groups based on the parameters they measured:

1. Measurement of forced response
2. Measurement of contact forces
3. Measurement of forced response and contact forces

2.2.1 Measurement of forced response

Numerous test rigs were developed to measure the dynamic response of the shrouded blades [21]–[28]. Sextro [21] introduced a test rig that used a shrouded blade with two non-Hertzian contacts in order to measure the Frequency Response Function (FRF) for verification of an established contact model. Comparison of measured and computed FRF yielded sound agreement.

Ambrosio et. al [22] presented a test setup that involved shrouded bladed assembly comprising of thirteen beams and twenty-six shrouds with simple

geometry. Considering only single couple of blades engaged at shrouds that were equipped with strain gauges, FRF was measured for different normal loads. The corresponding modes where the blades vibrated in or out of phase were investigated and compared with the numerical results.

Hong Jie et al. [23] described a test rig where the effect of shroud contact angles and shroud positions on the dynamic response of the shrouded blade were studied for different normal preload and excitation force levels. Optimal normal preload to achieve best friction damping for a specific excitation force was determined. For small angle between the contact surface and direction of vibration, relative motion of contact surfaces was found larger and with better damping effect. The position of shroud on the blade was also found to affect the natural frequency and mode shape.

Albanesi [24] used an experimental test rig comprising of two shrouded blades clamped in a disk with a circular Hertz contact for which the preload was set using strain gauges. After a preliminary system identification with the help of a hammer test, a stepped sine forced response testing was performed with a shaker. Consequently, the effect of the static preload and excitation forces on the friction damping effects were investigated.

Pesek et al. [25] developed an experimental setup where frictional effects were studied and dynamic response of two non-rotating blades was measured with a friction element inserted between the tip of the blades. Basic and complex dynamic models were developed for the same configuration and comparison of experimental results with the numerical results was found satisfactory.

Kaptan et al. [26] presented a single blade test rig with a shrouded blade coupled with two adjacent dummy shrouds attached on air bearings. Normal load was applied to the shroud tip using dead weights. The structure was excited by a controlled excitation force using a shaker and response was measured using Laser Doppler Vibrometry (LDV). A good agreement was observed between the experimental and simulation results.

Savchenko et al. [27] experimentally investigated the effect of contact conditions between shrouded flanges on the stress state of shrouded blades. Multi-angle shrouded flanges on a pair of beam like specimens were incorporated to achieve different contact angles from 0° to 90°. Strain gauges were used to measure

the strain during the engagement of shrouds and during the excitation of specimens by the vibrating platform.

Hui Ma et al. [28] performed an experiment with two shrouded blades to investigate the effect of shroud gap, excitation amplitude and excitation frequency on the vibration impact responses of shrouded blade. The experiment was performed to compare the experimental and simulation results. It was found that an increase in shroud gap and excitation frequency resulted in weak vibration impact responses between the shrouded blades whereas an increase in excitation amplitude caused stronger vibration impact responses.

The experimental studies mentioned above emphasized on measuring the response in the form of displacements and accelerations to investigate the effect of shroud contacts on vibration amplitudes and resonance frequencies under different conditions. The applied techniques are useful to assess the benefits achieved by friction damping method involving shrouded blades. However, they do not provide complete experimental data for the validation of contact models implemented in non-linear solvers because these experiments do not measure shroud contact forces directly.

2.2.2 Measurement of contact forces

Alternatively, there are several experimental studies in literature describing test rigs that measured periodic contact forces [29]–[33] for oscillating contacts harmonically excited under one dimensional and two-dimensional relative kinematics. An experimental setup presented by Filippi et al. [29] was used to measure the tangential forces along with relative displacements to determine contact hysteresis cycles in microslip and sliding regimes. Contact parameters like friction coefficient and tangential contact stiffness were consequently determined. Broad range of relative displacements, normal loads and excitation frequencies were considered. Potential measurement errors were analyzed, and possible corrections were described. As desired in measuring contact parameters, strong repeatability was indicated by initial measurements.

A one-dimensional friction test rig presented by Schwingshackl et al. [30] was setup to measure the relative displacement and friction force during relative sliding between two materials while a known normal load was applied on the contact. The resulting hysteresis loops were used to determine the friction

coefficient and tangential contact stiffness which were then applied in a numerical model to validate the procedure.

Likewise, another test rig was presented by Lavella et al. [31] comprising of flat-on-flat contacts, engaged by constant normal load at high temperatures of around 1000°C. Relative displacements along with tangential forces were measured to achieve the hysteresis loop and subsequently determine the contact stiffness and friction coefficient during the wear process.

A two-directional friction test setup developed by Asai et al. [32] allowed the application of alternating normal as well as tangential forces during the measurement of relative displacements and contact forces. Comparison of frictional behavior and energy dissipation under constant normal force and variable normal force equal in amplitude with tangential force with no phase difference was presented. The variation of the tangential contact stiffness with the change in contact pressure and nominal contact area was also investigated.

Another friction test setup by Fantetti et. al [33] used ultrasonic waves to investigate the state of dry friction contact during vibration cycles.

In the above-mentioned test rigs, the focus was the accurate measurement of the contact parameters i.e., friction coefficient and contact stiffness and to achieve that, these test rigs operated far from their resonance frequencies in order to reduce the interference of test rig dynamics.

2.2.3 Measurement of forced response and contact forces

Another group of experimental setups [34], [35] allowed simultaneous measurement of dynamic response of the blade and periodic contact forces. The test rig with a single simplified blade developed by Tamai et al. [34] comprised of a rectangular cantilever beam that was bolted on ground with a pair of contact regions on the tip and FRF was measured for different normal contact forces. These normal contact forces were applied by a hydraulic pressure piston at one end and measured by a load cell at the other end. The response was measured by Laser Doppler Velocimeter (LDV) as the blade was excited by the shaker at half length. The resonance frequency was observed to increase as the contact force was increased. The displacement at the pressure piston side was larger than that of the load cell side due to the unwanted looseness at the pressure piston side.

The test rig designed by Umer et al. [35] was designed for blades with under platform dampers in which blade response was measured along with the normal and tangential contact forces on both damper sides using L-separator configuration of force sensors and assuming a one-dimensional tangential relative motion of the damper with respect to the blade.

In addition to the forced response, the contact forces measured in the above-mentioned studies consisted of either one normal contact force as in [34] or one normal contact force along with one tangential contact force component as in [35]. Nevertheless, none of the studies dealt with measurement of the two orthogonal tangential contact forces along with normal contact force which is a significant measurement with respect to the complete three-dimensional profile of shroud contact forces during forced vibration testing.

2.3 Summary

Literature review of the existing experimental test rigs highlighted different experiments that were grouped based on the parameters they measured. Table 1 summarizes the advantages and disadvantages of the existing experimental setups that have dealt with the measurement of forced response and contact forces.

Table 1: Summary of the literature review

Experiments	Group 1	Group 2	Group 3
Measured parameters	Forced response	Periodic contact forces	Forced response and contact forces
Pros	Influence of shroud and effects of friction damping on the response	Accurate measurement of contact parameters (coefficient of friction and contact stiffness)	Forced response and contact forces measured together simultaneously
Cons	Incomplete validation due to non-availability of contact forces data	Not applied to shrouded blades Operated far from resonance frequencies Only 1D and 2D contact forces measured	Limited to 1D normal contact force in case of shrouded blade and 2D contact forces (normal + 1D tangential) in case of under-platform dampers

The review showed that simultaneous measurement of forced response and three-dimensional shroud contact forces which is necessary for a complete and detailed experimental validation of numerical models has not been presented till now. Therefore, the current doctoral study was undertaken with the objective of the designing and developing an experimental test rig that is capable of measuring forced response as well as 3D shroud contact forces of shrouded turbine blade simultaneously. The 3D shroud contact forces would include two orthogonal tangential contact forces and normal preload. The measurements obtained with the designed experiment should allow for the compilation of an experimental database that would be used for the validation of contact models implemented in the nonlinear solvers. In this way, the proposed study will fill the voids currently left by the existing experimental test rigs to achieve more detailed and accurate experimental validation.

Chapter 3

Novel Experimental Test Rig

3.1 Introduction

As discussed in the previous chapter, the experimental test rigs presently available are insufficient to acquire the complete three-dimensional attributes of shroud contact forces during forced response testing of a shrouded turbine blade. But for a detailed description of shroud contact dynamics that enhances the experimental validation of contact models, it is necessary to measure three-dimensional shroud contact forces along with the forced response of the shrouded turbine blade.

The main objective and novelty of this study is to design and develop an experimental test setup to simultaneously measure forced response and three-dimensional shroud contact forces. The acquired experimental results will allow to compile an experimental database that will be used to validate the contact models implemented in non-linear solvers. The accomplishment of this goal requires a set of design objectives and criteria that are outlined in the proceeding section.

3.2 Design Objectives

The design of the test rig was developed to achieve specific objectives where the design criteria was:

1. To measure three-dimensional shroud contact forces during forced response test by employing a measurement system that accommodates the blade shrouds ensuring proper alignment to measure the contact forces accurately.

2. To contemplate an adjustable mounting of the contact force measurement system suitable for the sensor calibration as well as different blade sizes and shroud contact angles with slight amendments in the test rig.

3. To implement a mechanism for normal pre-load application on both the shroud contact surfaces simultaneously.

4. To design a robust structure for housing the force measurement system to achieve a full dynamic decoupling between the first bending mode of the shrouded blade and the first bending mode of the housing structure.

3.3 Components of the proposed test rig

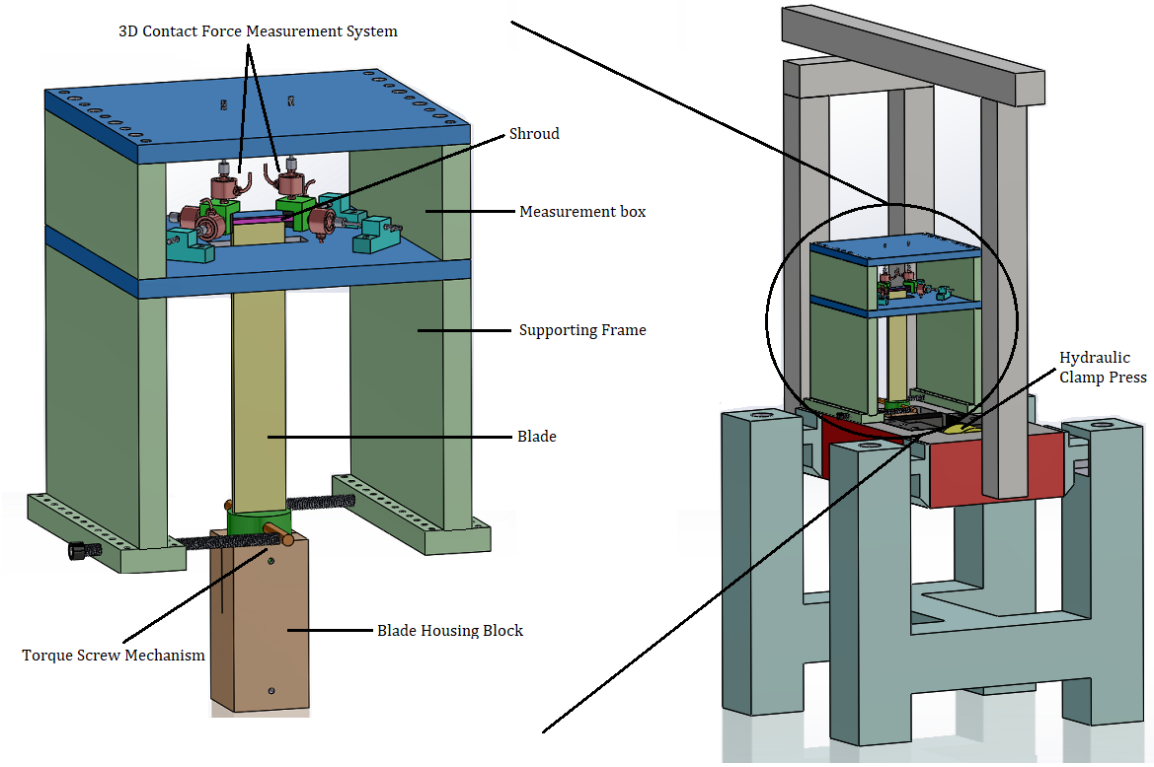

Figure 3: 3D model of the proposed experimental test rig

Considering the design criteria listed above, the test rig was designed to be mounted on an existing test bench with a hydraulic clamp press. The test rig had the following specifications as seen in Figure 3:

- A supporting frame housed the shrouded blade while supporting a measurement box attached on its top.
- The measurement box assembled with thick plates, accommodated a 3D contact force measurement system.
- The 3D contact force measurement system, designed to engage both the shroud ends simultaneously, was installed to measure the 3D periodic shroud contact forces during forced response testing of the blade.

- A torque screw mechanism, incorporated at the base of the supporting frame was used for the application of the normal pre-load on both the shroud contact surfaces simultaneously.
- For this experimental campaign, a mockup shrouded blade was designed as a beam with a rectangular cross-section, with a 45-degree shroud angle and a cylindrical base.

3.3.1 Mockup shrouded blade in blade housing block

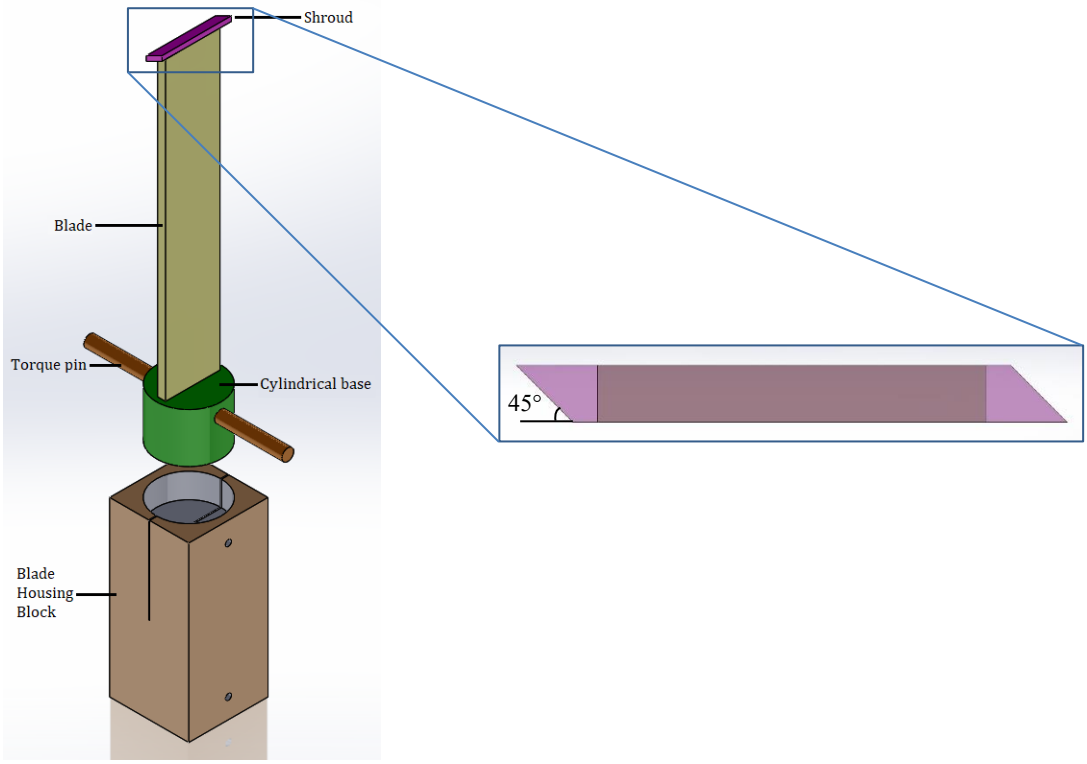

Figure 4: 3D model of mockup-shrouded blade placed in blade housing block

For this experimental campaign, a 300 mm long mockup shrouded blade was designed like a beam with a rectangular cross-section (Figure 4). The shroud cover located at the tip was 5mm thick with a 45-degree shroud angle and at the blade root was a cylindrical base, built as one single body without any joints or attachments. Detailed dimensions of the mockup shrouded blade can be found in Appendix A. The upper half of the cylindrical base had a through hole for the insertion of a torque pin whereas the lower half was placed in the socket of the blade housing block to fix the shrouded blade during the assembly like a cantilever beam. During the experiment, after selection and application of the normal preload, a

hydraulic clamping press was used to clamp the blade housing block to lock the blade. The attachment and clamping replaces the blade root constraints of the actual turbine blade in the bladed disk and the cylindrical base allows to twist the blade for the application of the normal preload as discussed later.

3.3.2 Tri-directional Contact force measurement system

The two shroud contacts of the mockup shrouded blade were engaged with the two tri-directional contact force measurement systems fitted inside a measurement box. Considering the length of the mockup shrouded blade, the measurement box was attached to a supporting frame for the required elevation. This type of bolted attachment also allowed to detach and re-attach the measurement box from the top of supporting frame in case of sensor calibration. The tri-directional contact force measurement system (Figure 5) was designed and developed to investigate for the first time, the complete three-dimensional periodic shroud contact forces that are established at shrouds during blade vibration. The contact force measurement system was composed of three uniaxial force sensors HBM U9C (0.5 kN) that were integrated in a tripod configuration. The strain gauge-based force sensors measured both the static and dynamic components of the periodic contact forces. The tripod arrangement involved three mutually orthogonal branches and each branch incorporated a force sensor attached to a contact reference block on one end and a collar link on the other end.

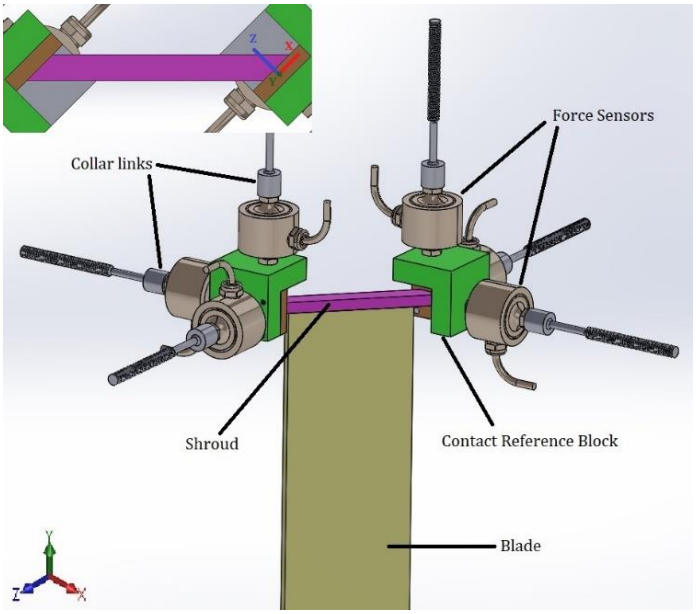

Figure 5: Tri-directional contact force measurement system

The design of the contact reference block was intended to engage the shroud contact through the attached contact pads so that the shroud contact was centrally aligned with the contact pad. In this way, the contact interface was in line with the axial direction of the force sensors in all the three directions. Therefore, when the shroud was in contact with the contact pad surface, one force sensor would measure the normal contact force in Z direction and two force sensors would measure the two orthogonal tangential contact forces in X and Y directions respectively as shown in Figure 6 . The design, calibration and validation of the tri-directional contact force measurement was carried out in a simplified calibration setup whose details are explained in the next chapter.

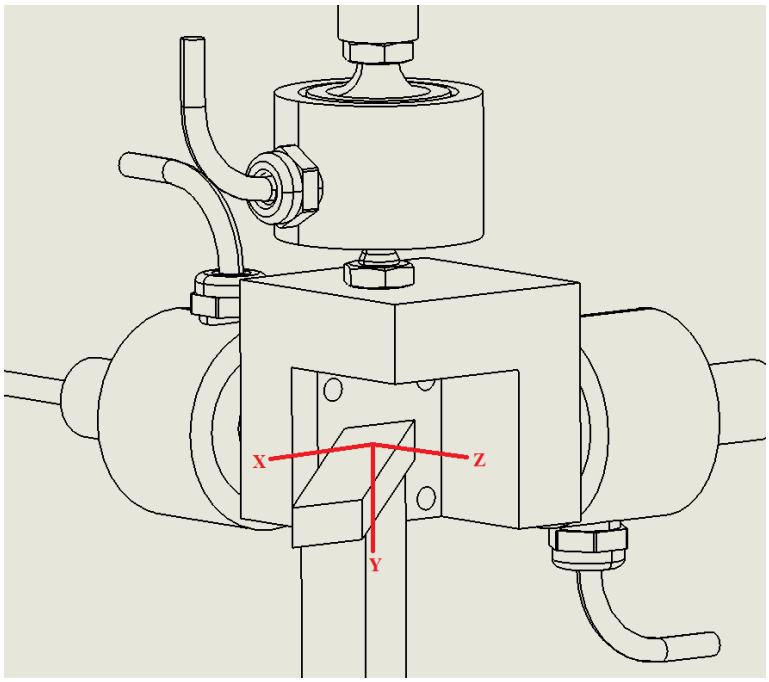

Figure 6: Shroud contact forces measured in three directions

3.3.3 Torque screw mechanism

In turbine blades, the shroud contacts get engaged by the static torque produced by the centrifugal forces acting on the blade. In the proposed test rig, a similar shroud loading mechanism was designed and employed, in which the torque is applied by screw loading mechanism for the application of normal preload on the contact surfaces. As seen in Figure 7, this mechanism comprised of two lengthy screws driven horizontally through threaded holes at the base of supporting frame that, when rotated, pushed against the ends of an extended torque pin inserted through

the cylindrical base of the shrouded blade. This formed a force couple system and rotated the blade such that the two shroud contacts applied normal force on the contact pad surfaces attached to the contact reference blocks. The torque screws and the corresponding holes were threaded with a fine pitch of 1mm to regulate the rotation of the torque screws and control the amount of normal contact force with a better resolution.

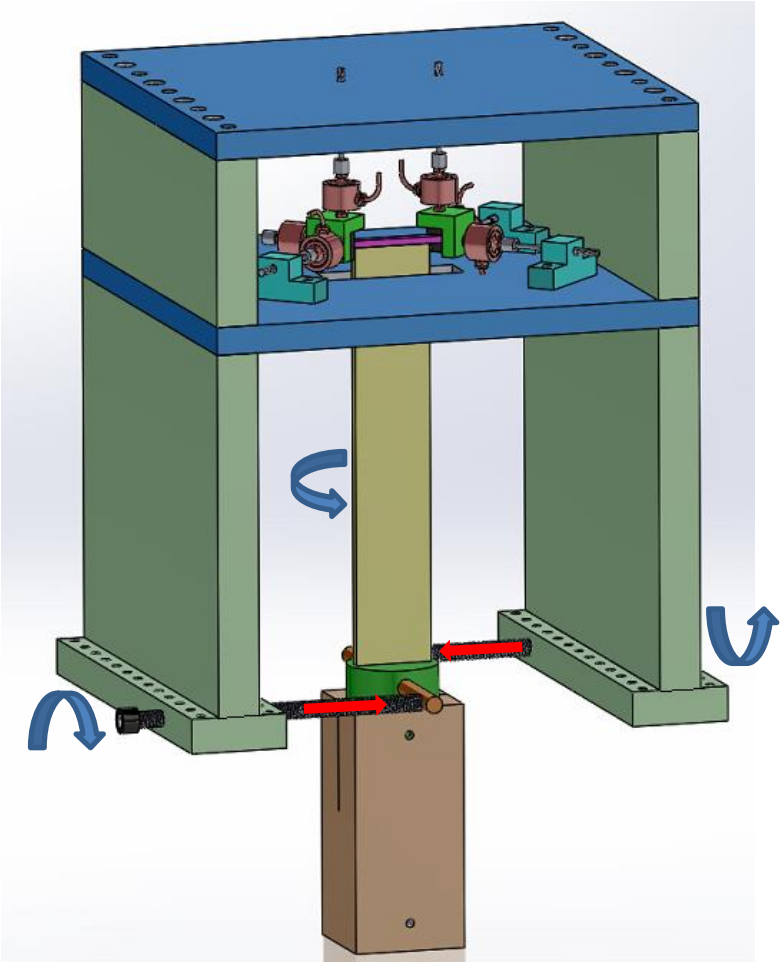

Figure 7: Torque screw mechanism to apply normal preload

Furthermore, a static analysis performed in ANSYS during the design phase helped to investigate the normal preload levels to be applied on the contact pads using the designed torque mechanism (Figure 8). With the base of the supporting frame constrained, a nominal uniaxial force was applied perpendicularly on the opposite ends of the extended pin in opposite directions to simulate the force couple. The resulting normal force levels and distribution on the contact pads by

the shroud contacts were examined. In this way, a parametric analysis was done by adjusting length of the extended pin and distance of the torque screws to maintain the normal force levels within the realistic range of 0 - 60N. The proposed torque screw mechanism can also be adapted to accommodate real blades with their specific blade root attachments after appropriate customization and machining process.

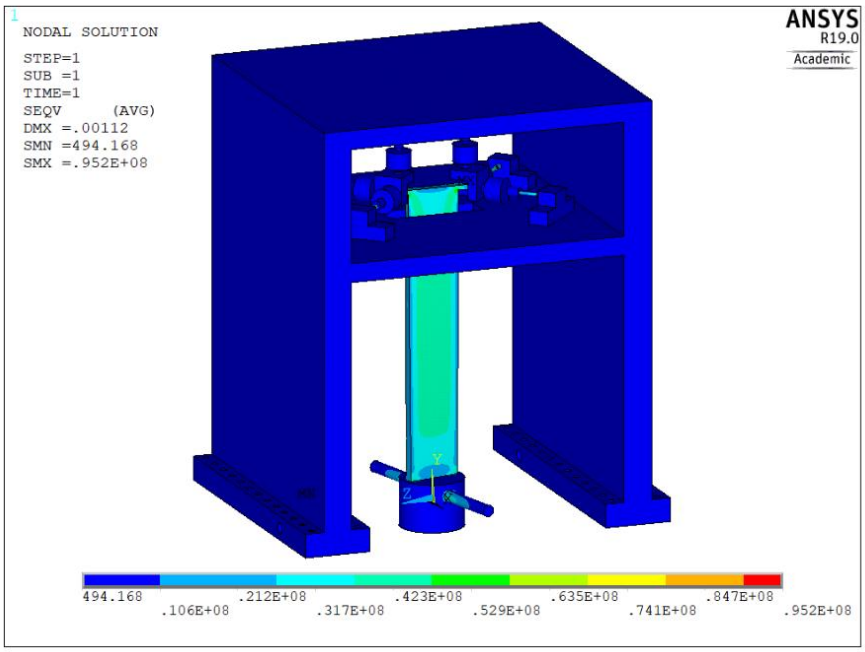

Figure 8: Static analysis of torque screw mechanism

As for the blade root damping, it should be noted that the mockup shrouded blade and its cylindrical base are manufactured as a single body, and not like the blade root in real turbine blades. This prevents the damping at mockup shrouded blade root and the tight clamping of the blade housing block does not influence the amount of damping nor does it introduce any significant non-linearity.

3.4 Finite Element Modal Analysis

Since the experimental test rig would be used to measure the dynamic response of the shrouded blade with engaged shroud contacts, it was necessary to analyze and investigate the natural frequencies of proposed assembly during the preliminary design phase. For this purpose, a finite element (FE) modal analysis of the designed mockup shrouded blade in free condition and subsequently of the complete test rig assembly with engaged shrouded blades (full stick contact) condition was

performed in ANSYS to determine the natural frequencies of the system. This type of parametric analysis was necessary to finalize the dimensions of the test rig and to specify the range of excitation frequencies for the forced response tests so that the accuracy of the contact force measurement system was not affected by resonance frequencies of the supporting frame and the tripod assembly.

3.4.1 FE modal analysis of free mockup shrouded blade

Firstly, an FE modal analysis of the mockup shrouded blade in free condition was performed. In this case, the model of the designed mockup shrouded blade with the cylindrical base was meshed with solid elements with eight nodes as shown in Figure 9. The lower half of the cylindrical base was constrained for all degrees of freedom to simulate the actual boundary conditions of the shrouded blade clamped in the blade housing block. The first bending mode of the shrouded blade that is the mode of interest was investigated and found to be at 70Hz (Figure 10).

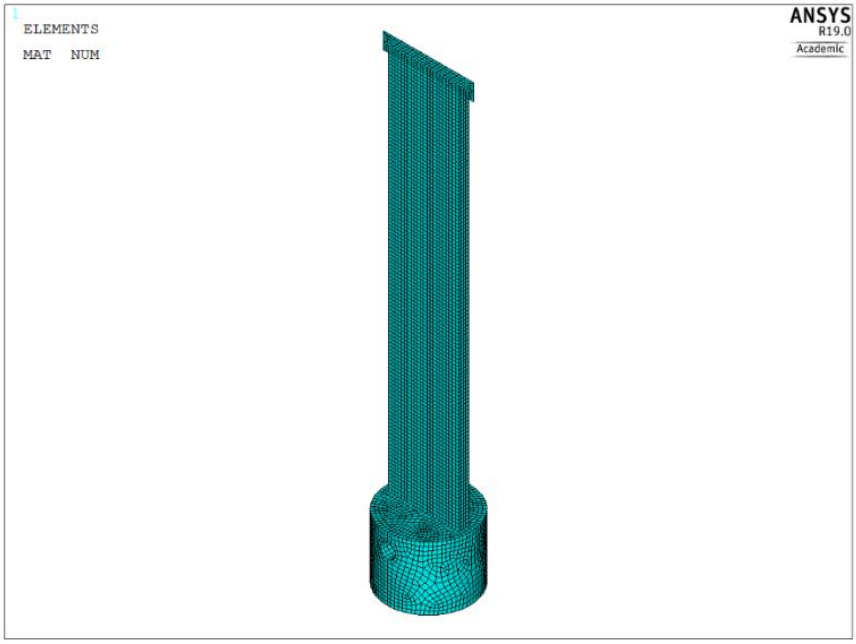

Figure 9: Mockup shrouded blade model meshed with solid elements

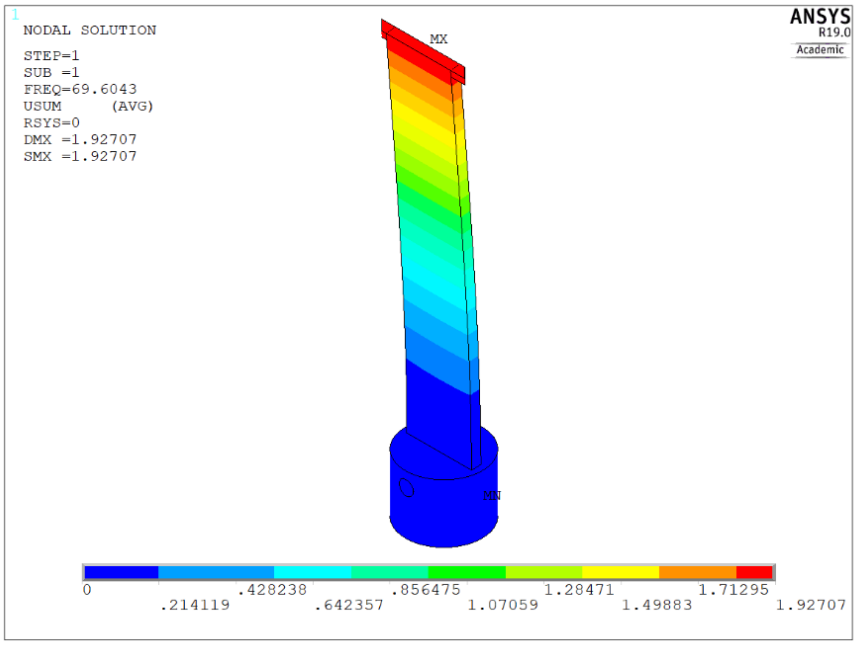

Figure 10: First bending mode of mockup shrouded blade in free condition

3.4.2 FE modal analysis of test rig assembly

Subsequently, the FE modal analysis of the whole test rig assembly was performed with the shrouded blade engaged with the contact force measurement system. During the analysis, the force sensors being a pre-designed and manufactured commercial product had to be assigned an accurate value of stiffness that could be used as an input to ANSYS since this information was not available in the datasheet. It was important that input value of the sensors' stiffness was as close as possible to the actual value for an accurate model of the whole test rig to be used for the FE analysis. Therefore, to achieve an accurate value of sensor's stiffness, a numerical-experimental validation pathway was adopted. For this approach, an experimental modal analysis of a simplified calibration setup comprising of the tripod assembly, was performed, and the results were compared with the FE modal analysis of the same setup. The simplified calibration setup was used for the design, calibration, and validation of the installed tri-directional contact force measurement system and is explained in the next chapter. In short, it consisted of the three force sensors arranged in a tripod configuration with one end of the force sensors attached to the wall supports while the other end was attached to a central cube (Figure 12). The cube allows loading in three axial directions of the force sensors. The natural

frequencies of this setup were determined experimentally by an impact hammer test.

For this test, a hammer (Figure 11) was used to excite the structure, where the applied impulse force characterized the broadband range excitation as the contained energy spans a specific range of frequency. The impacts or the hits from the hammer result in a very quick on and off contact with the structure. It comprises of a piezoelectric force sensor at the head to measure the impulse force or the force of the impact. Since the impacts are made manually, the excitation force applied to the structure differs every time. From the operational point of view, the skill required from the operator involves making hammer impact perpendicular to the surface and the avoidance of double hammer hit. The size of the hammer and the impact velocity determine the impact force. Likewise, the hardness of the hammer's tip can be used to determine the measurement frequency range like soft rubber tip for measuring at low frequencies and hard metal tip for measurements at high frequencies. For the experimental modal testing of the simplified calibration setup, a hard metal tip was used.

Figure 11: Hammer used for impact hammer test

To determine the natural frequencies of the simplified calibration setup, shown in Figure 12, the impacts were made at locations (1, 2, 3) and the response measured by a uniaxial accelerometer attached at one edge of the cube and on the collar links. To compute the FRF displayed in Figure 13, acquisition and processing of the force and response measurements was done by LMS Test.Lab using LMS Scadas III.

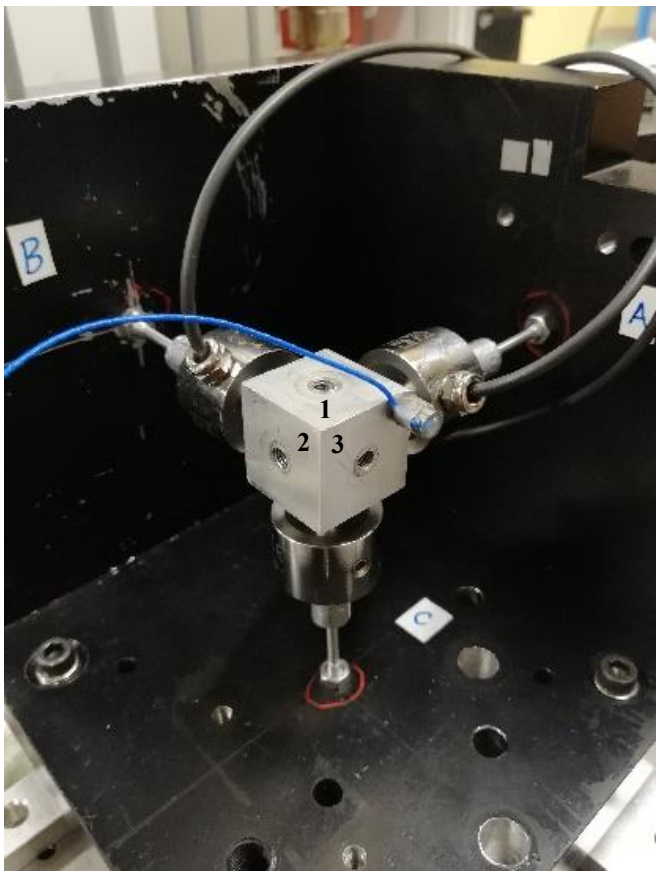

Figure 12: Simplified calibration setup

From Figure 13, the experimental modal analysis reveals two modes between 300-350 Hz indicating the global bending modes of the setup due to the two frame walls and three consecutive modes very near to each other at around 400 Hz that denote the bending modes of the collar links that make up the tripod assembly of the force sensors.

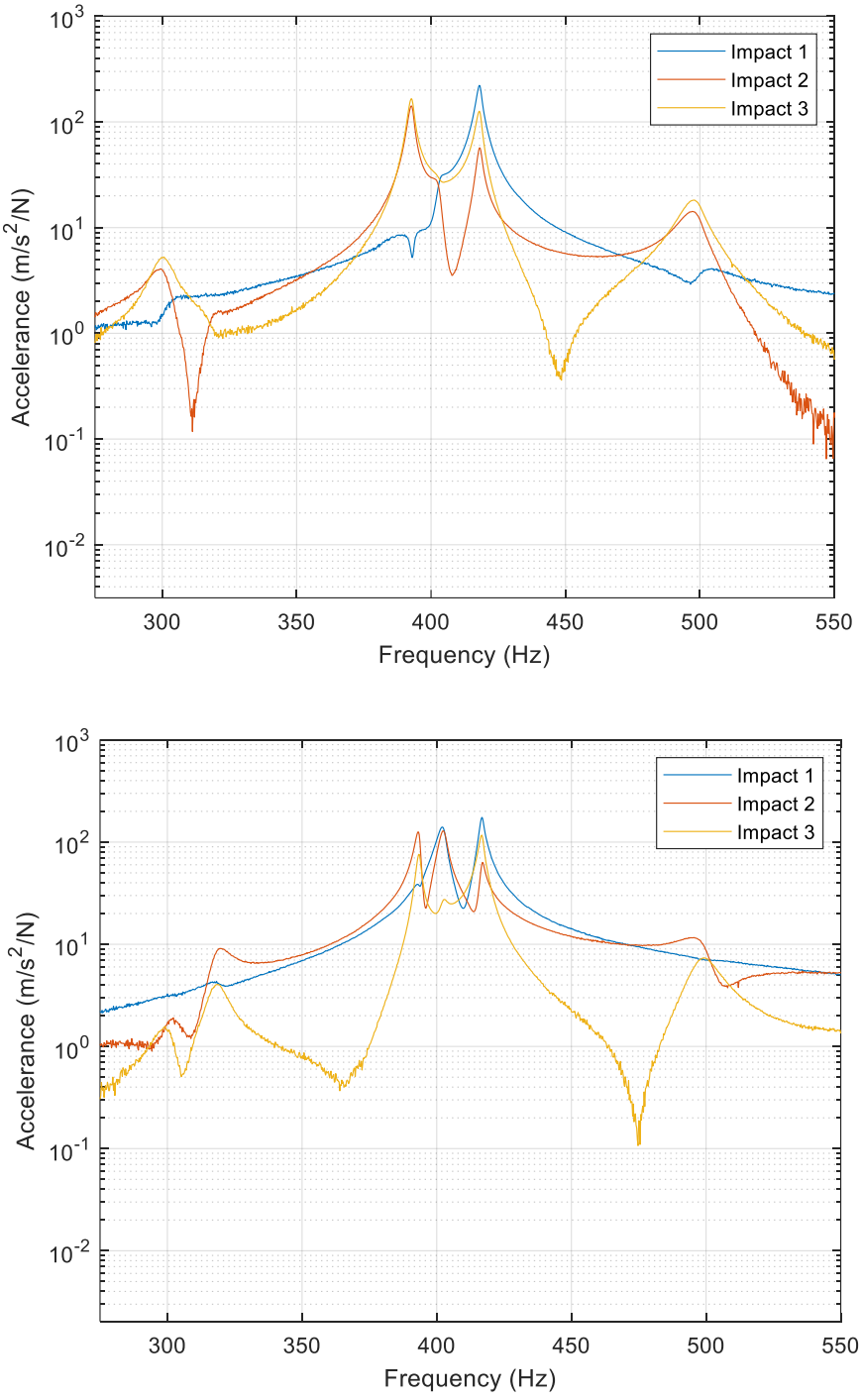

Figure 13: FRF; response measured on cube edge (above) and on collar link C (below)

Followed by this, the FE modal analysis of the simplified calibration setup was performed in ANSYS. Material properties were specified, and the model was meshed with solid elements (Figure 14). Next, the model was tuned and material properties of the sensor model were adjusted. The stiffness of the force sensor model was estimated by matching natural frequencies attained by FE modal analysis as shown in Figure 15, with the natural frequencies obtained by the experimental modal analysis (Figure 13) by inspection of the first five modes of the simplified calibration setup in particular.

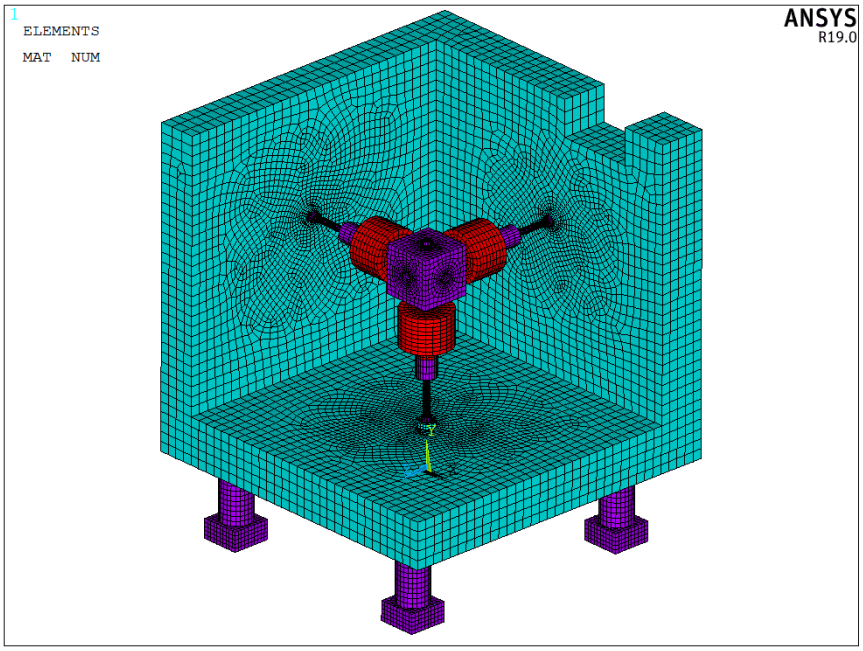

Figure 14: Meshed model of simplified calibration setup for FE modal analysis

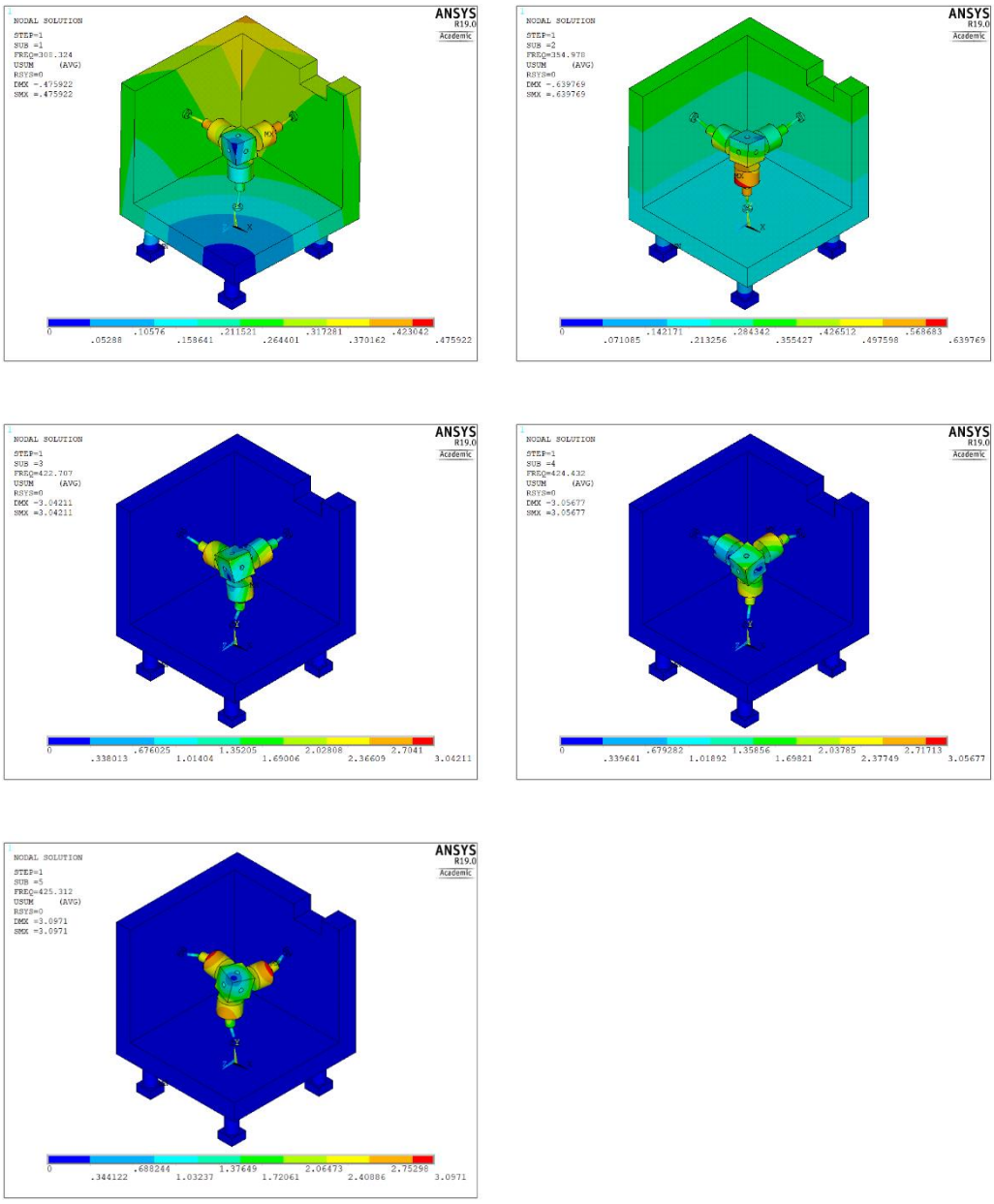

Figure 15: FE modal analysis of the simplified calibration setup

After the determination of the force sensor's stiffness value to be used as an input parameter, the FE modal analysis of the complete test rig assembly with engaged shrouds was done. The mockup shrouded blade and test rig model were meshed with solid elements having eight nodes (Figure 16). For a preliminary nonlinear analysis, the contact pads and shroud contacts making up the contact

interface were modeled with surface-surface contact elements. The supporting frame and the shrouded blade assembly were constrained as planned in the actual experiment. For the specified boundary conditions, the design parameters i.e., the thickness of the plates enclosing the measurement box, the sidewalls of the supporting frame, the diameter of the collar links and the thickness of the shrouded blade were defined and the effects on the natural frequencies and mode shapes of the system were investigated.

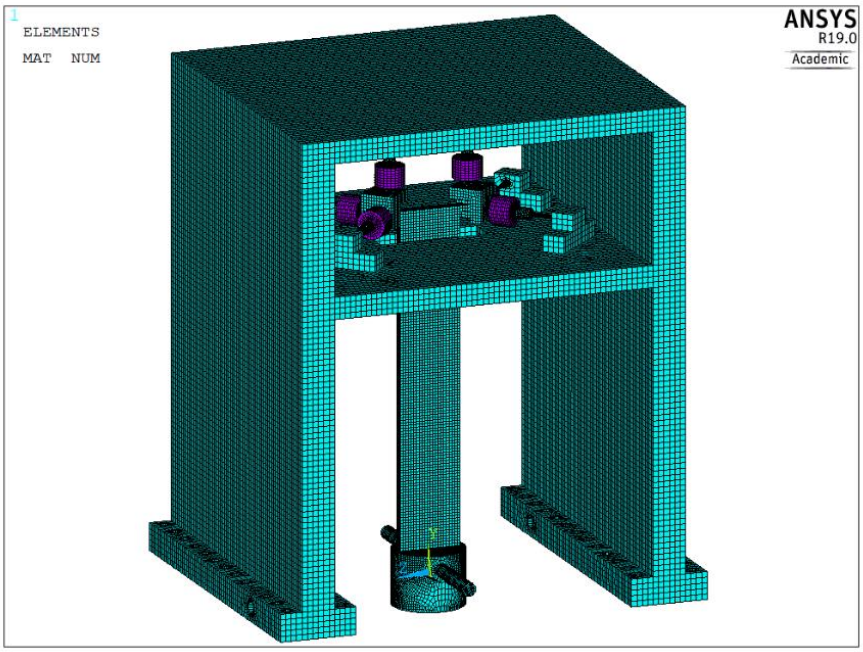

Figure 16: 3D model of test rig meshed with solid elements

These design parameters were adjusted accordingly to achieve a stiff supporting frame and shrouded blade assembly with known resonance frequency intervals as seen in Figure 17, Figure 18, Figure 19, Figure 20. In particular, the first bending mode of the shrouded blade in engaged condition that is our mode of interest, was found to be 323.5 Hz (Figure 18). It should be noted that attaching the force sensors to the supports might increase the useful frequency band but then their distance from the point of force application would increase and there would be an increase in the bending moment applied by the lateral forces acting on the sensors. Moreover, the FE modal analysis results show that first natural frequency of the tripod assemblies was far from the first bending mode of the engaged shrouded blade that was the mode of interest. Secondly, the open box configuration of the measurement box might result in a less rigid structure but most importantly, the

dynamic decoupling of the first bending mode of the frame and the first bending mode of the engaged shrouded blade was achieved and this configuration also provided easy access to the contact force measurement systems.

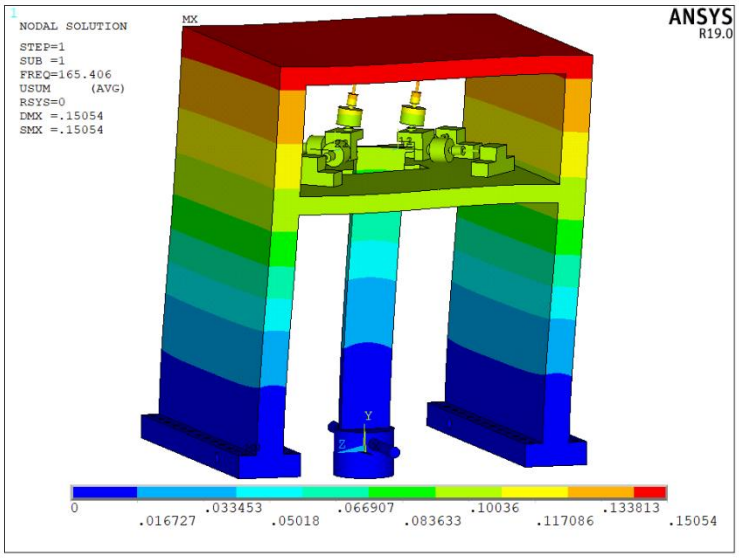

Figure 17: First bending mode of the supporting frame

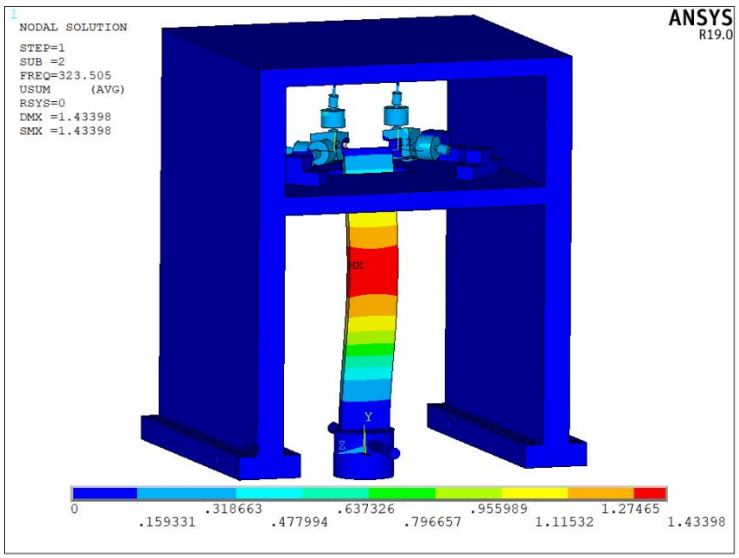

Figure 18: Second mode i.e. the first bending mode of engaged shrouded blade

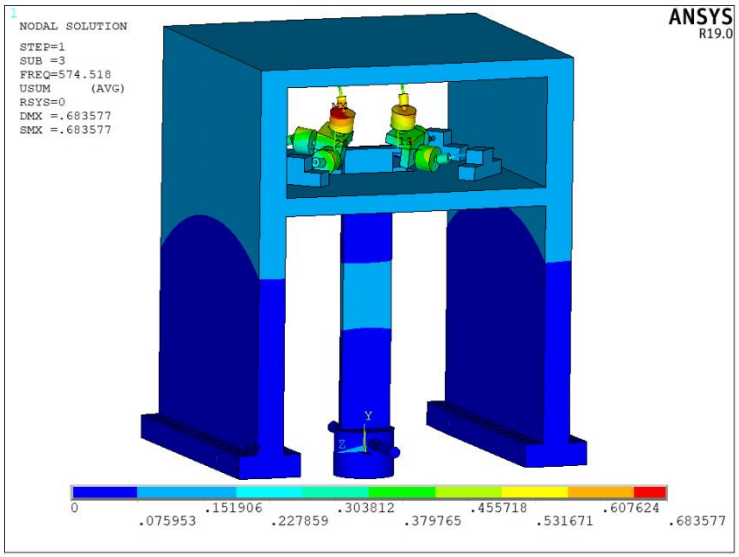

Figure 19: Third mode related to tripod assembly and supporting frame

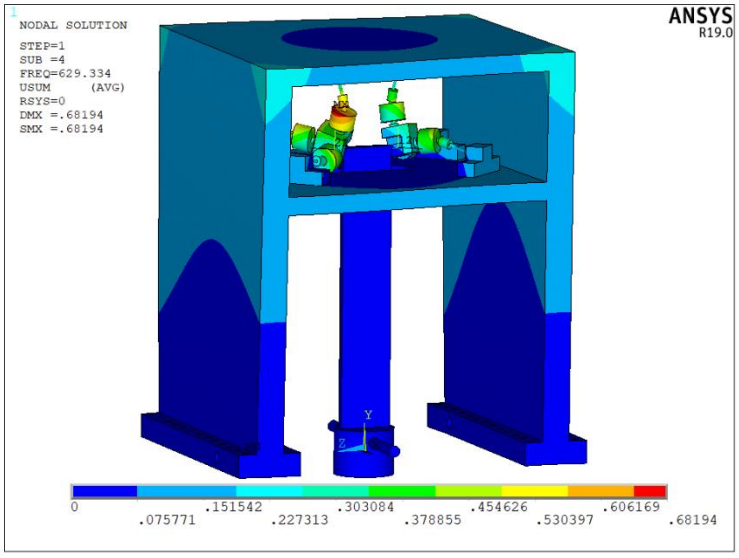

Figure 20: Torsion mode related to the tripod assembly and supporting frame

Chapter 4

Tri-directional Contact Force Measurement System

4.1 Introduction

As described briefly in Section 3.3.2, a novel tri-directional contact force measurement system was designed and implemented in the proposed test rig to measure three-dimensional shroud contact forces. This chapter will highlight the motivation and design considerations that defined the strategy and layout to realize the tri-directional contact force measurement system. The proceeding sections will present and discuss the calibration method and its importance in achieving accurate results, which is determined by the validation process.

4.2 Motivation and state of the art

Design considerations for the tri-directional contact force measurement relied on the nature and orientation of contact forces in vibrating blades that was determined by the mode of vibration being studied. Hence, for the investigation of multiple resonances, two forms of tri-directional force measurement systems can be taken into consideration, i.e., (i) a multi-axis force sensor; (ii) a set of single axis force sensors that are mechanically connected to each other. Nowadays, in aerospace and automation industries, multi-axis force sensors are being widely used. However, the commercially available multi-axis force sensors are very expensive and can be complicated keeping in view their complex mounting and calibration requirements with respect to the shrouded blades. On the other hand, numerous studies were undertaken to develop multi-axial force measurement technologies [36]–[44] that dealt with different arrangements of multiple strain gauges and various designs of the load transferring elements to accomplish valuable results. Likewise, several three directional contact force measurement systems were investigated and employed for diverse applications like tactile sensors [45], [46], clinical examination [47], surgical robots [48] and measurement of ground reaction force

(GRF) [49], [50]. However, most of these multi axial force sensors are not small enough to be fixed or mounted in the tight and confined space where the blade shroud contact forces are to be measured. Other multi-axis load cells do not possess the dynamic characteristics required for the measurement of the periodic contact forces acting on the blade shrouds. Alternatively, in order to achieve the required accuracy, reliability, and robustness from the mechanically connected set of single axis sensors, the elastic structure on which they are mounted on must be carefully designed [36].

The construction or assembly of multiple axis force sensors can make them either *mechanically decoupled* or *mechanically coupled*. In case of *mechanically decoupled* force sensors, the applied loads are measured directly as the output of the sensor, which means that there is minimum, or no crosstalk. Nevertheless, their geometry is complex, which results in complications related to manufacturing and fabrication. On the other hand, when load is applied on *mechanically coupled* force sensors, they measure lateral force components as well, which then requires the determination of a decoupling matrix to find the actual loads. This also implies that they can be designed with simpler geometries [37].

An essential design feature is the accuracy of the multi-axis force measurement system (for both multi-axis sensor and mechanically connected set of uniaxial force sensors) which largely depends on the configuration of force sensing components and minimization of errors occurring due to coupling or noise. Therefore, accuracy must be ensured during the calibration process of a multi-axis force measurement system that requires recording of the measured values corresponding to the known load set. Taking into consideration all the above-mentioned factors and limitations, in order to design an accurate and robust contact force measurement solution, it was decided to adopt the multi-axial force sensing method of integrating three uniaxial force sensors to measure the three orthogonal components of shroud contact forces simultaneously during the forced response tests of shrouded blade.

4.3 Strain gauge-based force sensor – HBM U9C

As stated in the previous chapter, the proposed contact force measurement system comprised of three strain gauge based uniaxial force sensors HBM U9C (0.5kN) assembled in a tripod configuration having three mutually orthogonal branches, where each branch included a force sensor attached to a contact reference block on one end and collar link on the other. In the proposed experimental test rig, the blade

shrouds will be in contact with the contact reference block that is especially designed with a contact pad surface centrally aligned with the shroud contact surface. The three branches will be fixed to the supports inside the measurement box with the help of three collar links. Two of these force measurement systems based on the tripod sensor configuration were installed in the test rig for each blade shroud end as shown in the Figure 5.

With respect to the technology and principle associated with force measurement devices, it was important to understand the various reasons to support the choice of employing either strain gauge based forced sensors or piezoelectric ones depending upon what suited our application [51]. Strain gauge-based force sensors consist of a spring element that undergoes slight deformation when force is applied. Strain gauges connected at suitable points are extended which results in a change in resistance. In a Wheatstone bridge circuit, four strain gauges are connected in a full bridge configuration. However, there are also the half bridge and quarter bridge configurations. When voltage is supplied to the measuring bridge, the output voltage that results will be proportional to the force that is applied. On the other hand, the alternate option is that of piezo electric force sensors that consist of two crystal disks and electrode foil fixed between them. Application of force causes an electric charge flow, which is measured by a charge amplifier.

Strain gauge-based sensors show nearly zero drift and can be used for long term applications that need to be monitored. Moreover, the time dependent creep phenomena is negligible as it can be reduced by carefully selecting the strain gauge arrangement. For this reason, strain gauge-based sensors have a clear advantage over the piezo electric sensors, which have a drift, and the measurement error due to the drift is not favorable for measuring constant and harmonic forces with very low frequency.

Generally, for measuring dynamic forces, piezoelectric sensors provide higher stiffness and higher resonance frequency as compared to strain gauge based force sensors. Nevertheless, the dynamic characteristics depend on the overall measuring chain as the additional mass of their mounting parts can affect the cut-off frequency. The strain gauge-based sensors with greater nominal rated forces will have higher cut off frequencies because force sensors designed to measure smaller forces have softer spring elements that results in lower resonance frequency.

The circuitry used for the connection of strain gauges allows the compensation of several errors. This includes the effects of temperature on zero value, sensitivity, linear behavior of the transducers and the effect of bending moment. Moreover, strain gauge-based sensors facilitate accurate static calibration and the spring elements can be designed to accomplish optimum reproducibility. Therefore, strain gauge-based force sensors can be used in the field of reference force measurement.

Nowadays, strain gauge-based sensors offer an IP68 degree of protection and hermetically sealed casings that ensure the protection of the sensitive strain gauges. These protective features make them rugged and allow them to be used in all types of environments.

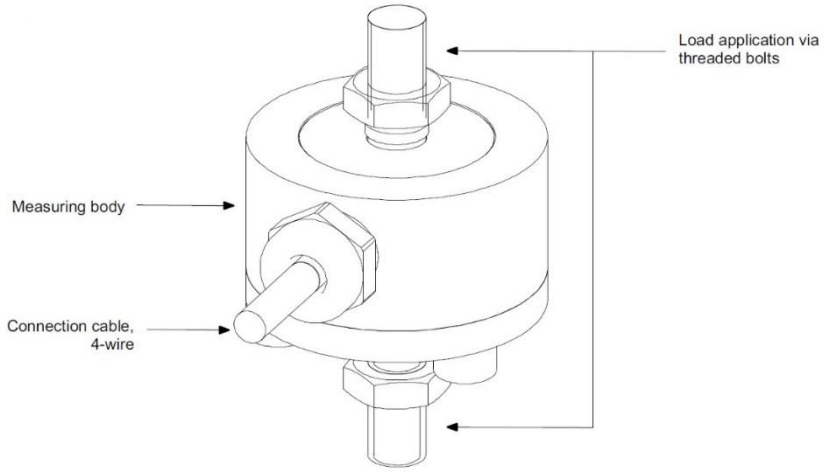

Figure 21: Strain gauge-based force sensor HBM U9C
(https://www.hbm.com/fileadmin/mediapool/hbmdoc/technical/B03812.pdf)

The strain gauge-based force sensor HBM U9C (Figure 21) used in the proposed tri-directional contact force measurement system with nominal (rated) force of 500N, is compact and can measure both tensile and compressive forces. Because of its high stiffness and high natural frequency, it can measure static as well as dynamic forces applied in axial direction with good accuracy and minimum crosstalk.

4.4 Error estimation for the tripod configuration

As discussed in Section 3.3.2, for the tri-directional contact force measurement system, the uniaxial strain gauge-based force sensors were arranged in a tripod configuration where each branch was mutually perpendicular to each other. During

the design phase, it was important to determine the feasibility with respect to the accuracy of such an arrangement. Therefore, an error estimation of the proposed tripod configuration was carried out to analyze the extent to which the lateral forces and the load misalignment affect the force measurement system. For this reason, a static FE analysis was performed on the tripod assembly of force sensors in ANSYS and loads were applied on the contact pad in three directions individually while the reaction forces were evaluated for each of the fixed ends of three collar links. Assuming the sensors attached axially will measure all the force transferred on the collar links in each axial direction, the effect of the mechanical coupling on the force measurement was determined. On the other hand, these reaction forces were also investigated for an offset in the load application from the central point.

For this FE static analysis, the stiffness of the force sensor was specified as the one that was determined and used for FE modal analysis in the previous chapter. In case of centrally aligned load applied in x, y and z direction as shown in Figure 22, the results summarized in Table 2 indicate that 99.5% of the force was transferred axially and only about 0.2% of the reaction forces were observed laterally.

Table 2: Percentage of the reaction forces in x, y and z direction for centrally aligned loading

Percentage - %		**Applied loads**		
		F_x	F_y	F_z
Reaction Forces (%)	F_1	99.54	-0.206	-0.206
	F_2	-0.192	99.48	-0.19
	F_3	-0.19	-0.19	99.56

Alternatively, FE static analysis was performed with a loading offset from the center and the corresponding reaction forces from the fixed end of the collar links were investigated. Load with offset from the center affects the axial force conveyed through collar links and as summarized in Table 3, an offset of more than 2 mm results in an error of up to 2% in the reaction forces evaluated axially and laterally.

Table 3: Percentage of the reaction forces due to load applied with an offset from the center

Percentage - % Offset (From center)		**Applied loads**		
		F_x (2.5mm above)	F_y (2.8mm left)	F_z (2.8mm left)
Reaction Forces (%)	F_1	97.88	-2.07	-2.2016
	F_2	-1.7	101.62	-0.1914
	F_3	-0.19	-0.19	101.77

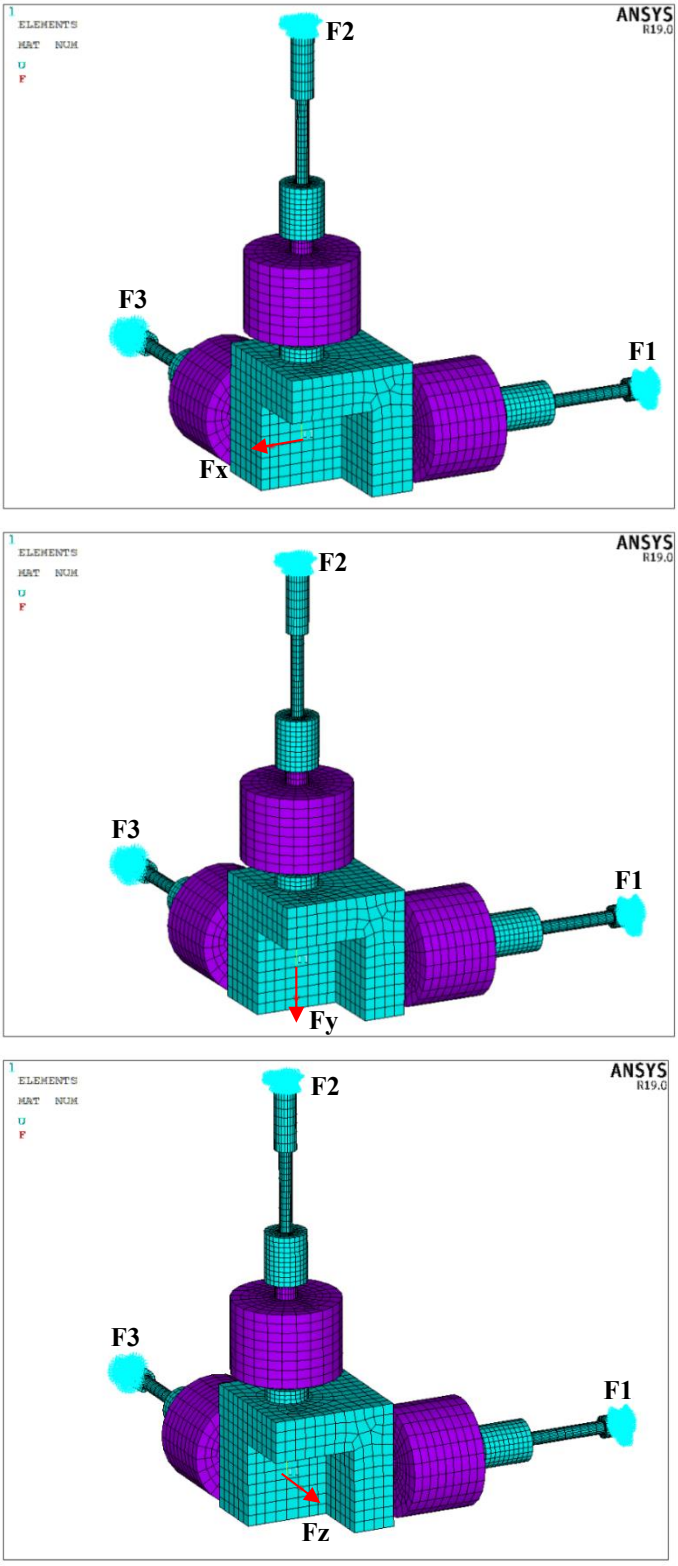

Figure 22: FE static analysis of tripod assembly for loading in x (top), y (middle), z (bottom) directions

Therefore, due to the design of the configuration and considering the nature of the contact forces to be 3D point forces, it is assumed that the bending moment applied by the contact forces on the force sensor will be negligible. However, for accurate assessment of the measurement error due to mechanical coupling in actual conditions, testing was done on a simplified calibration setup.

4.5 Simplified calibration setup

Before the installation of the tri-directional contact force measurement system in the proposed experimental test rig, the configuration design of the integrated force sensors was tested in a simplified calibration setup. In this simplified calibration setup, the tripod assembly of force sensors was fitted on a two walled frame with bolted base, as shown in Figure 23a, with the following configuration: Sensor 1 aligned with the x-axis, Sensor 2 aligned with the y-axis and Sensor 3 aligned with the z-axis. Each force sensor was connected to a cube instead of the contact reference block to be used in the proposed test rig. This was done in order to facilitate the application of forces in the axial direction of the sensors by using deadweights and wire-pulley systems during the calibration. The other end of the force sensor was screwed in collar link which was then connected to a wall. Two different types of collar links were used and tested Figure 23b) i.e., locknut collar and necked collar, in order to assess their effect on the mechanical coupling of the three branches and therefore on the measurement accuracy. The locknut collar link was assembled using a standard M5 bolt screwed in an extended locknut whereas the necked collar consisted of a slender section machined in cylinder attachment to compensate for the lateral component of the force and allow bending.

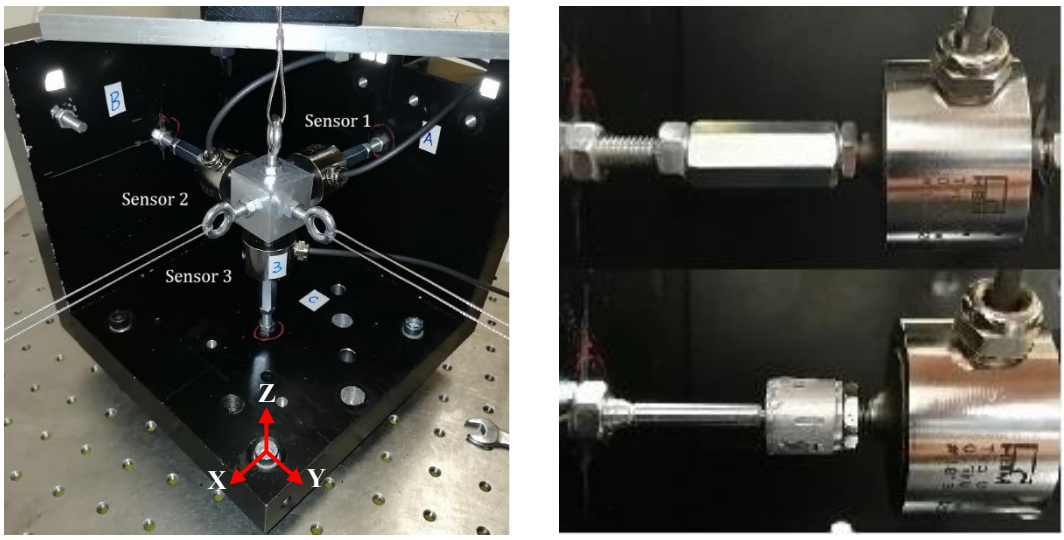

(a) (b)

Figure 23: a) Simplified calibration setup b) Locknut collar link (above),necked collar link(below)

4.6 Calibration

4.6.1 Calibration setup and procedure

To check the feasibility of the proposed measurement system, a classical calibration procedure was performed to assess the level of mechanical coupling between the three branches and to define a decoupling matrix to be used during the experiment to measure actual contact forces. For the calibration, three wire-pulley systems were setup to apply tensile forces in the axial direction of each sensor with the help of dead weights. The dead weights were suspended with wires over pulleys, connected to hooks that were fastened on the face of the cube opposite to the face where the force sensor was attached as seen in Figure 23a. The measurement setup consisted of HBM QuantumX MX410 measurement amplifier that was used with MX Assistant software to acquire and record force sensor output values. HBM QuantumX MX410 was used because it is a highly dynamic 4-channel data acquisition module that offers high precision with accuracy class of up to 0.05%, high resolution of up to 200kS/s. The dynamic force measurements were acquired at the rate of 4800 Hz.

The calibration procedure involved sequential application of pure forces in the form of known loads in one direction at a time using a set of dead weights with no eccentricity. Before the loads were applied, all the force sensors were reset and

zeroed after the mounting and assembly. The weights suspended using the wire-pulley systems, were then gradually increased with a fixed force interval from 0 – 100 N and sensor output values were recorded for each force sensor for each orthogonal direction. Only tensile forces were applied to each force sensor assuming linear behavior in both the axial directions. The calibration procedure was carried out for the measurement system with locknut collar links and necked collar links alternatively. In order to investigate the repeatability of force measurement system, the calibration procedure was also repeated after disassembling and reassembling the calibration setup.

4.6.2 Calibration matrix

It is expected that, due to the mechanical coupling between the three orthogonal branches, a linear relationship between the measured force values $\{F^*\} = (F_1, F_2, F_3)^T$ and the actual applied loads $\{F\} = \left(F_x\ , F_y\ , F_z\right)^T$ can be expressed as

$$\{F^*\} = [C]\{F\} \tag{4.1}$$

where $[C]$ represents the 3x3 calibration matrix in this case and can be defined as follows:

$$[C] = \begin{bmatrix} F_1(F_x) & F_1(F_y) & F_1(F_z) \\ F_2(F_x) & F_2(F_y) & F_2(F_z) \\ F_3(F_x) & F_3(F_y) & F_3(F_z) \end{bmatrix}$$

where F_1 , F_2 and F_3 represent the force measured by Sensor 1, Sensor 2 and Sensor 3 respectively when load i.e. F_x , F_y or F_z was applied along the x-axis, y-axis and z-axis respectively. The columns of the calibration matrix were determined using the sensor output values recorded during the calibration procedure. In other words, when F_x was applied the coefficients of the first column of $[C]$ were determined and so on for the remaining columns. The above-mentioned calibration procedure was performed at multiple force levels obtaining a set of calibration matrices whose coefficients can be interpolated to determine the calibration matrix for a given load.

4.6.3 Calibration results

Results of calibration procedure exhibit a linear relationship between applied and measured loads, as shown in Figure 24 and Figure 25 that refer to locknut and necked collar links respectively. As summarized in Table 4, where the average

normalized calibration matrices are shown with standard deviation stated in parenthesis, the mechanical coupling between the branches of the measurement system is very low (less than 4% in the worst case). In particular, the necked collar link, more flexible in the transverse direction than the locknut, shows better performances with a lower coupling. The standard deviation for measurements with necked collar link were lower as compared with the locknut collar link. In case of a perfect decoupling between the sensors, the matrices shown in Table 4, would be diagonal with 100% values along the main diagonal.

Table 4: Calibration matrices indicating distribution of loads applied in the directions x, y, and z onto sensors 1, 2, and 3. Locknut collar and necked collar cases

Averaged Percentage - % (Standard Deviation) Lock Nut Collar Link		**Applied loads**		
		F_x	F_y	F_z
Measured Force Outputs (%)	F_1	98.12 (0.61)	0.17 (0.17)	2.61 (0.2)
	F_2	3.89 (0.065)	99.89 (0.91)	2.60 (0.15)
	F_3	-3.36 (0.053)	0.12 (0.15)	97.16 (0.55)
Averaged Percentage - % (Standard Deviation) Necked Collar Link		**Applied loads**		
		F_x	F_y	F_z
Measured Force Outputs (%)	F_1	99.51 (0.23)	-0.34 (0.065)	-0.50 (0.28)
	F_2	1.98 (0.26)	98.76 (0.47)	2.08 (0.34)
	F_3	-3.34 (0.10)	0.11 (0.13)	99.00 (0.12)

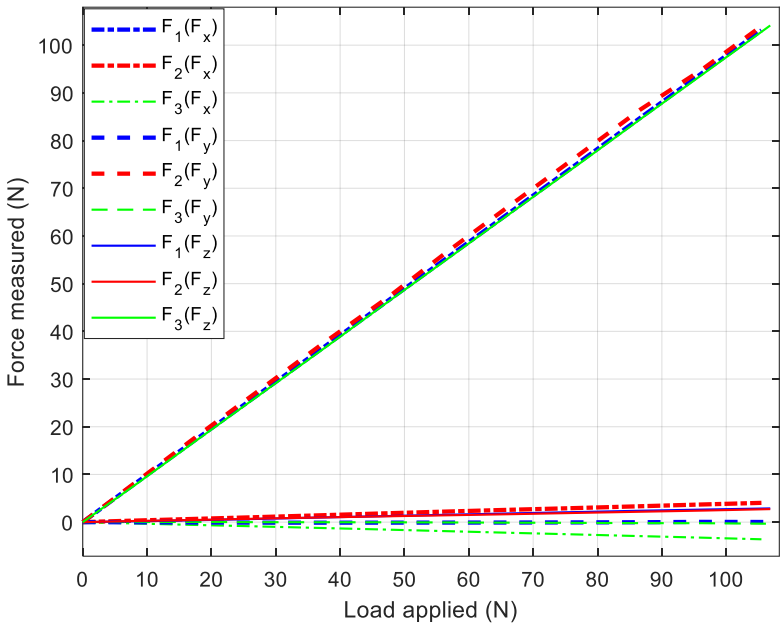

Figure 24: Calibration plot for system with locknut collar link

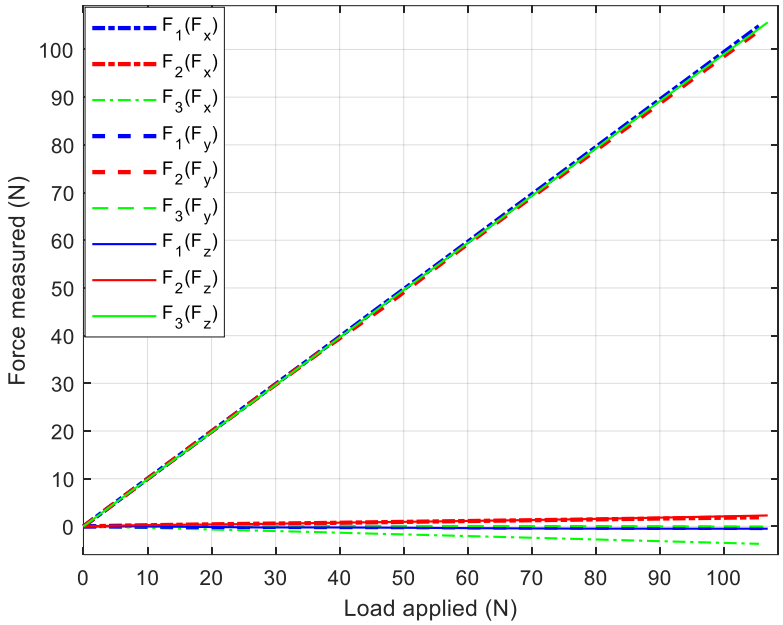

Figure 25: Calibration plot for system with necked collar link

4.7 Validation with static loading experiment

For the validation of the calibration process, the calibrated tri-directional force measurement system was appropriately loaded in three orthogonal directions simultaneously using the wire-pulley setups as seen in Figure 26. Several load cases consisting of different load combinations along x, y and z axis (F_x , F_y and F_z) were applied and the output force values read by sensors (F_1 , F_2 and F_3) were logged for each set of simultaneously applied loads. The calibrated tri directional force measurement system was zeroed before commencing the load cases to eliminate the possibility of any offset errors. Table 5 summarizes some of the load cases comprising of three forces applied in three directions simultaneously.

Table 5: Load cases applied to tri-directional contact force measurement system

Combination Of Loads	Applied loads (N)		
	F_x	F_y	F_z
Load Case 1	45.97	56.67	47.34
Load Case 2	6.47	86.59	86.84
Load Case 3	45.97	17.17	47.34
Load Case 4	6.47	96.17	7.84
Load Case 5	6.47	17.17	86.84

Figure 26: Simultaneous application of static loads in three orthogonal directions

4.7.1 Decoupling matrix

From Equation (4.1), the following expression was derived to compute the decoupled applied forces, $\{\tilde{F}\} = \left(\tilde{F}_x\,, \tilde{F}_y\,, \tilde{F}_z\,\right)^T$

$$\{\tilde{F}\} = [C]^{-1}\{F^*\} = [D]\{F^*\} \tag{4.2}$$

where the inverse of the calibration matrix $[C]$ forms $[D]$ representing the decoupling matrix. The decoupled applied forces $\tilde{F}_x\,, \tilde{F}_y\,, \tilde{F}_z$ for Sensor 1 along x-axis, Sensor 2 along y-axis and Sensor 3 along z-axis respectively, were calculated by multiplying the decoupling matrix with the vector of measured force values for each case. Finally, these decoupled applied forces $(\tilde{F}_x\,, \tilde{F}_y\,, \tilde{F}_z)$ were compared with the actual applied forces $\left(F_x\,, F_y\,, F_z\right)$ for each sensor to validate the effectiveness of the calibration test and the decoupling matrix.

4.7.2 Results

The results shown in Table 6 refer to the decoupling method applied to the load cases. For all the load cases, the measurement error is pertinent with both the locknut and necked collar links if no decoupling is performed, while it decreases significantly (less than 2% in the worst case), after the application of the decoupling matrix, that is defined in Equation (4.2). Moreover, it was observed, as expected, that the maximum relative errors (35% and 17%) occur in the direction of the lowest force component (*x* in load case 2 and load case 5 and *y* in load case 3).

For the sake of comparison, the measured forces and the decoupled forces, obtained after application of Equation (4.2), are shown in Figure 27 (locknut collar link) and Figure 28 (necked collar link) for two load cases i.e. load case 2 and load case 3, where each point coordinates are the applied load (x-axis) and the measured force (y-axis). These load cases were selected since they showed larger coupling errors that need to be recovered. It is clear that filled markers, representing the decoupled forces, lie closer to the bi-sector line of the plot, demonstrating the need for a decoupling process of the measured quantities.

Table 6: Percentage error of the measured forces and decoupled forces for simultaneous loading experiment

Percentage Error	Measured Force Outputs (%)			Decoupled Applied Forces (%)		
	F_1	F_2	F_3	$\widetilde{F}_x$	$\widetilde{F}_y$	$\widetilde{F}_z$
Lock Nut Collar Link						
Load Case 1	0.27	4.04	-5.86	-0.18	-1.40	0.21
Load Case 2	35.52	1.45	-3.07	-0.75	-1.04	-0.04
Load Case 3	0.27	17.33	-5.62	-0.22	-1.65	0.25
Load Case 4	3.71	-1.1	-9.12	0.50	-0.37	1.03
Load Case 5	35.33	14.43	-2.86	-0.03	-1.14	-0.09
Necked Collar Link						
Load Case 1	-1.27	1.50	-4.76	0.19	-0.32	-0.75
Load Case 2	-10.51	0.54	-1.45	1.16	-0.22	-0.32
Load Case 3	-1.29	9.81	-4.39	-0.02	-0.26	-0.37
Load Case 4	-3.99	-1.35	-5.46	0.13	-0.38	-1.62
Load Case 5	-8.76	11.10	-1.16	-0.20	0.29	-0.07

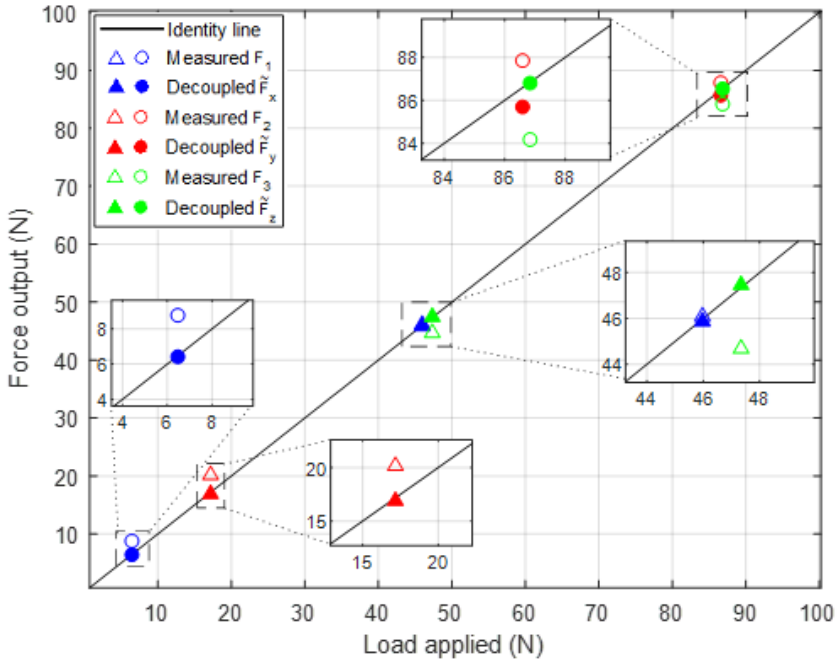

Figure 27: Decoupling method applied to locknut collar link (Load case 2: Circles; Load case 3: Triangles)

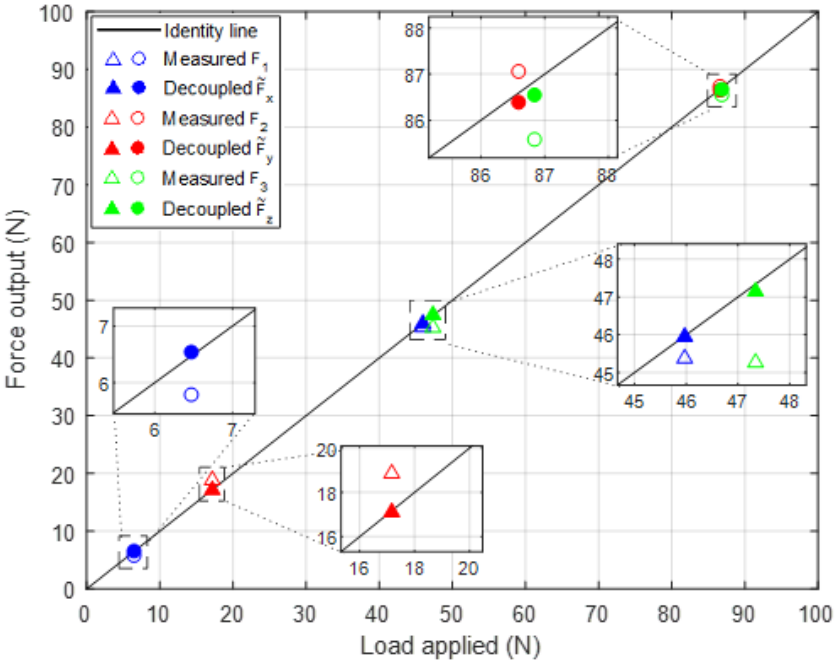

Figure 28: Decoupling method applied to necked collar links (Load case 2: Circles; Load case 3: Triangles)

4.8 Validation with dynamic loading experiment

4.8.1 Dynamic loading experiment setup and procedure

In the previous experiment, the calibrated force measurement system was subjected to static loading with the help of wire-pulley systems and dead weights. Since the system is envisaged to be employed for the measurement of periodic contact forces at blade shrouds, it was necessary to examine the behavior of the system with dynamic forces. In order to investigate the performance of the calibrated tri-directional force measurement system with dynamic loading, an experiment was devised to apply dynamic forces to two force sensors simultaneously while one force sensor was loaded statically.

This configuration (Figure 29) was designed to simulate the three directional contact forces typical of oscillating friction contacts, which includes a static normal preload and two oscillating tangential components. In order to accommodate an LDS V408 permanent magnet shaker driven through an LDS amplifier by LMS Testlab system, necessary to provide harmonic excitation, a new reference block with a 45°- chamfered edge was designed. In order to measure the actual dynamic force provided by the shaker, a fourth force sensor was fitted between the shaker stinger and the chamfered block.

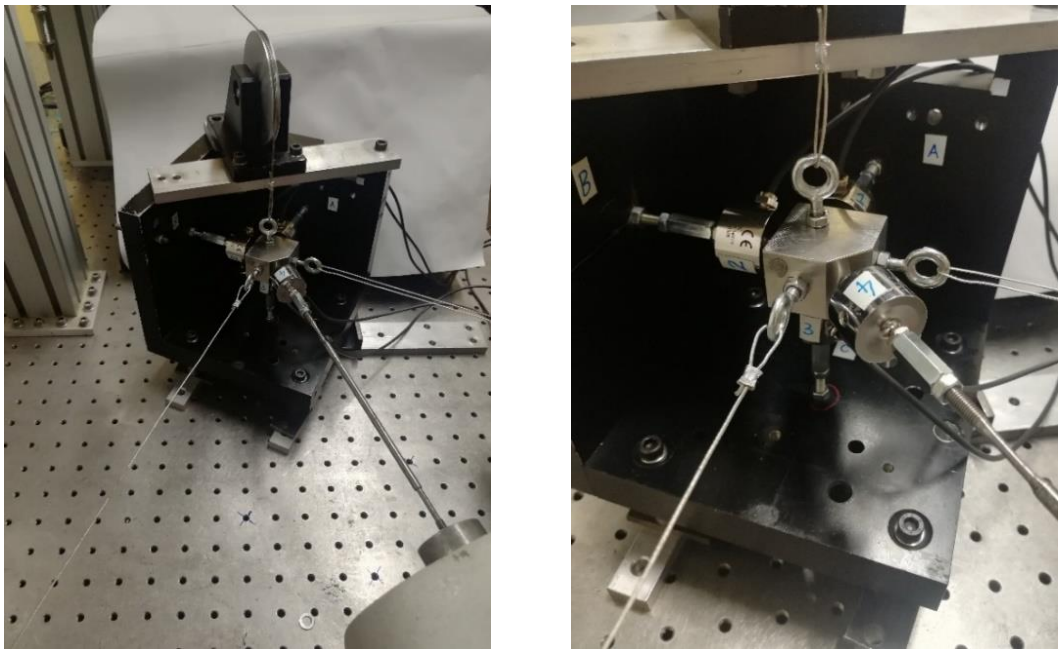

Figure 29: Experimental setup for dynamic loading with chamfered block and shaker

A static calibration of the modified force measurement system was also performed by means of the wire-pulley setups and a set of standard weights, generating a new set of calibration and decoupling matrices, as described in Section 4.6.1.

Before the dynamic tests, a preliminary experimental modal analysis of the assembly was performed with the aim of assessing the natural frequencies and the associated mode shapes of the system. In particular, the lower natural frequency of the system becomes a threshold frequency value, above which the inertia forces of the tripod itself would start affecting the contact force measurements, thus making the measurement system unreliable. Consequently, a lower accuracy of the measurement system is expected when the excitation frequency exceeds that threshold value, which has to be experimentally identified in advance.

During the experimental modal analysis, a stepped sine with controlled excitation force signal was provided by the shaker for the specified range of frequency, while response of the system was measured by three accelerometers placed on the chamfered block oriented along X, Y and Z directions. Acquisition and processing of the force and response measurements was done by LMS Scadas III data acquisition system using LMS Test.Lab software. The acquisition process involved the specification of excitation force level which in this case was as low as 2N, frequency range from 100-500 Hz and frequency resolution with step size of 1Hz. A reference profile was defined, and force control parameters allowed to specify the abort limit, upper and lower tolerance limits. This was followed by an initial check of the settings by LMS Test.Lab software and then finally the measurement.

During the dynamic loading experiment, a controlled excitation force was applied in the (x,y) plane, while a static force was applied in the z direction. In case of a fully uncoupled measurement system, Sensors 1 and 2 would measure the two components of the oscillating force, also measured by Sensor 4, while Sensor 3 would measure the applied static force. Of course, due to the mechanical coupling, coupling errors actually occur and they were analyzed for each data set and consequently decoupled during the post-processing phase.

4.8.2 Results of the dynamic loading experiment

To identify the threshold frequency, FRF curves (Figure 30) were obtained during the preliminary experimental modal testing to determine the natural frequencies of

the measurement system and to determine the maximum allowable excitation frequency.

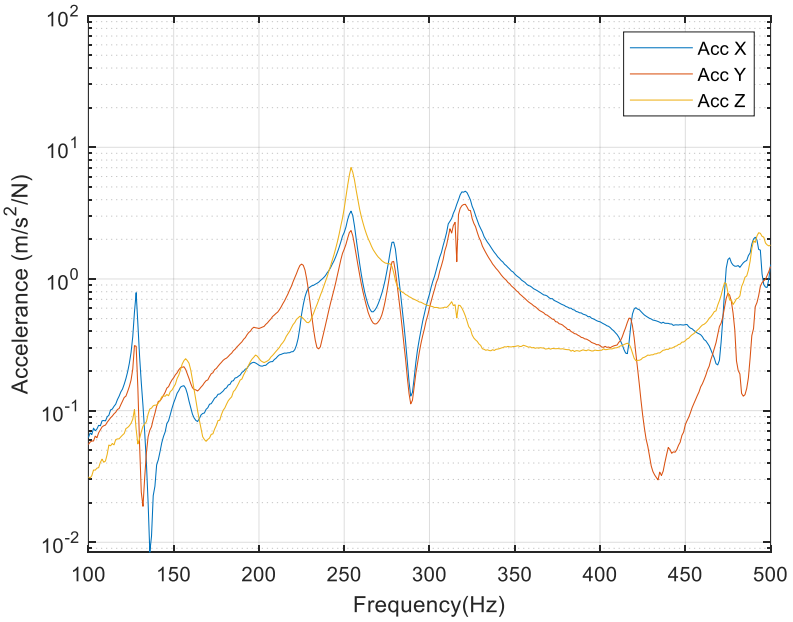

Figure 30: FRF plot of the tri-directional force measurement calibration setup

Based on the results in Figure 30, the first natural frequency of the system is around 130 Hz and as a result, excitation frequencies of 100Hz and 200Hz were defined. At 100 Hz the system dynamics is not expected to affect the measurement accuracy, while at 200 Hz, significant periodic inertia forces of the system are expected.

After determining the natural frequencies of the setup, dynamic loading experiment was performed by simultaneous application of a harmonic force in the x and y direction, while a static force was applied in the z direction. The mean absolute error of both measured and decoupled forces was computed over 100 cycles and results are shown in Table 7, at the two selected excitation frequencies and two different load cases.

Table 7: Dynamic loading test result comparison and effect due to variation in excitation frequency

Applied Forces (N)			**Mean Absolute Error (N)**					
Freq	**Amp**	**Static**	**Measured Force Outputs**			**Decoupled Applied Forces**		
Hz	F_x, F_y	F_z	F_1	F_2	F_3	$\tilde{F}_x$	$\tilde{F}_y$	$\tilde{F}_z$
100	6.5	7.8	0.2218	0.4966	0.3642	0.1630	0.2269	0.1403
200	6.5	7.8	0.3008	1.0378	0.7806	0.3377	0.7563	0.4419
100	12	17.8	0.5290	1.1998	0.7268	0.3244	0.1880	0.1732
200	12	17.8	0.6468	1.6479	1.1920	0.5984	0.8607	0.6917

Furthermore, the application of the decoupling method to the raw measurements generally improves the accuracy of the measurement. In the first load case, at both the excitation frequencies, a relative error reduction of 61% and 43% is observed respectively, except for Sensor 1 at 200Hz where a marginal increase (12%) is observed. A similar behavior is observed for the second load case, with a relative error reduction up to 84% and 47% respectively. As expected, at 200 Hz the mean absolute error is larger than at 100 Hz for both the load cases.

A more detailed investigation about the effect of the excitation frequency on the measurement accuracy is shown in Figure 31 and Figure 32, where the periodic measured and decoupled forces are plotted vs. the applied loads. The plots confirm the higher accuracy of the measurements at 100 Hz. It is worth noting that at 200 Hz, the decoupling method is not able to remove the artificial periodic component measured by Sensor 3.

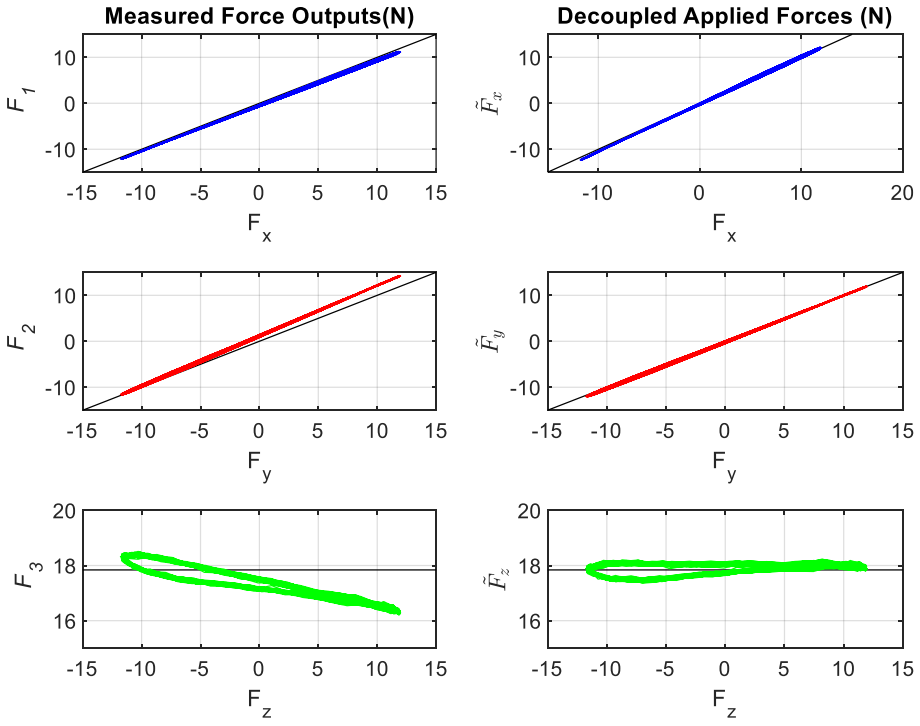

Figure 31:Decoupling method applied in dynamic loading experiment at 100 Hz

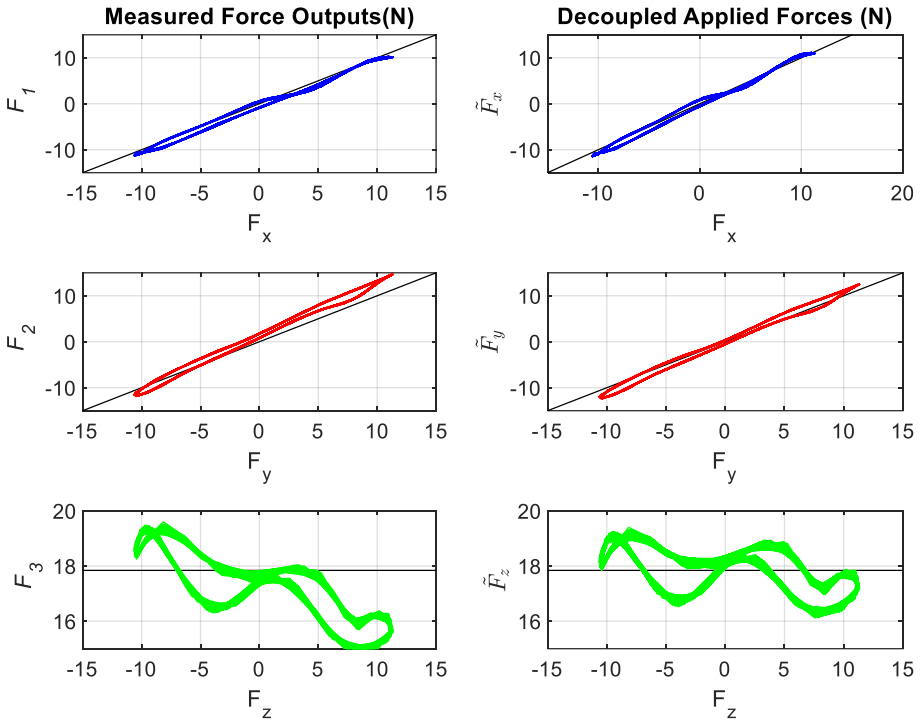

Figure 32:Decoupling method applied in dynamic loading experiment at 200 Hz

Having ruled out the 200 Hz frequency, due to the inaccuracy of the resulting measurements, the effect of the force amplitude on the accuracy of the measurement was performed at 100 Hz only. Results in Table 8 show that the initial measurement error increases as the amplitude of the excitation forces increases. However, the decoupling method stays effective for all the combination of external inputs tested in the experiments and the percentage error of the amplitude peak reduced considerably with the maximum error percentage coming down to 3%.

Table 8: Percentage error of peak amplitude for measured forces and decoupled applied forces

Applied Forces (N)			Percentage Error (%)					
Freq	Amp	Static	Measured Force Outputs			Decoupled Applied Forces		
Hz	F_x, F_y	F_z	F_1	F_2	F_3	$\tilde{F}_x$	$\tilde{F}_y$	$\tilde{F}_z$
100	6.5	7.8	4.57	-15.67	2.56	-1.92	2.74	-0.77
100	12	17.8	7.99	-19.39	2.99	0.56	-0.12	-0.26
100	17.5	27.8	10.03	-19.99	3.42	-2.44	-1.00	0.076
100	31.5	47.3	5.97	-20.59	3.12	-2.94	-3.13	-0.19

The forces measured for the combination of applied forces stated in the second row of the Table 8 were decoupled and the results are plotted in Figure 33. The plot confirms the effectiveness of the decoupling method to significantly reduce the force measurement errors occurring due to the mechanical coupling.

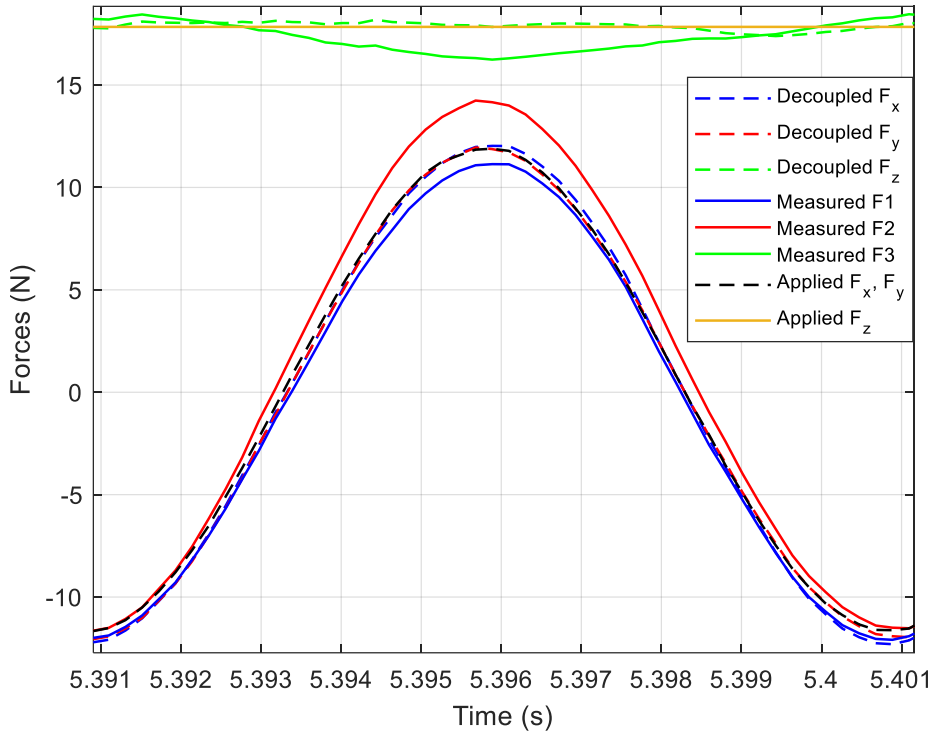

Figure 33: Decoupling method applied to the dynamic force measurements

4.9 Discussion of results

Results of the calibration procedure showed the expected linear behavior of the force sensors that measured the applied axial forces with reasonable accuracy but it also showed coupling error in the unloaded sensor branches due to the mechanical coupling. Apart from the transmission of mechanical coupling, the error can also be attributed to the slight inaccuracy in positioning of the sensors during the assembly. Other factors will also determine the accuracy of the contact forces that will be measured by the tri-directional contact force measurement system and the possible sources of error are:

- Measurement chain consisting of force sensors, measurement amplifiers and data acquisition systems with repeatability and linearity deviation error less than 0.2% for each force sensor as specified in the sensor datasheet
- Manufacturing and geometric tolerances of the mechanical parts
- Calibration errors that include dead weight error and uncertainties due to friction in the pulleys used for suspending dead weights.
- Alignment errors due to misalignment of wire – pulley setup.

Nevertheless, for necked collar links, the coupling error was observed to be slightly less as compared to the locknut collar links due to its geometry with slender section that allowed bending and acted as hinge. Repeatability test indicated that the disassembling and reassembling process affects the calibration matrix, which means that for accurate measurement, the calibration of the force measurement system will have to be performed before it is installed on the experimental test rig and will have to be repeated if the sensors are disassembled and reassembled.

Results of the simultaneous loading test yet again proved the existence of the coupling between the three branches. Coupling errors were found to be substantial after examining the force measured by each force sensor for each load case. However, it was observed once more that the coupling error for the necked collar link was less than that for the locknut collar. Alternatively, the decoupling matrix was used to compute the decoupled applied forces that considerably reduced the error percentage and were checked to be within 2% of the actual values. The decoupling method was marginally more effective for measurement system with necked collar links as compared with locknut collar links because of the relatively less coupling error in the first place.

The dynamic loading experiment demonstrated the ability of the measurement system to measure the dynamic forces. Generally, the three force sensors independently displayed good dynamic characteristics with fast response and with no delay. However, operating in the tripod configuration, dynamic errors were observed that can also be attributed to the mechanical coupling and to the slight misalignment during the assembly and during the loading of the third sensor. The decoupling method was effective in computing the decoupled forces from the measured dynamic forces irrespective of their amount. The percentage errors evaluated for the decoupled forces were fairly less as compared to the percentage errors calculated with the forces measured directly during the dynamic loading experiment. However, the performance of the tri-directional force measurement system was adversely affected when the excitation frequency was above the 1st natural frequency of the system. This factor limited the range of excitation frequency at which the force measurement system could be dynamically tested. Nevertheless, it should be noted that the frequency band determined in this experiment is only limited to the simplified calibration setup and does not define the general threshold frequency of the force measurement system or the frequency band of the final test rig. This is because the supporting structure where the force measurement system is mounted in the actual test rig is different from the simplified calibration setup. This study demonstrated that the proposed force measurement

system was able to measure dynamic forces with good accuracy for excitation frequency less than the 1st natural frequency of the system. Therefore, it is mandatory to pre-determine the natural frequencies of the system on which the measurement system is mounted to avoid that the inertial forces of the system affect the measurement so the frequency band of the actual test rig will be determined by experimental modal testing of the final assembly.

4.10 Conclusion

In this chapter, the proposed tri-directional contact force measurement system consisting of three uniaxial force sensors arranged in a tripod configuration was tested, calibrated and validated. The following conclusions can be drawn:

- The proposed solution is cost effective and adaptable without any complex assembly and with a straightforward calibration procedure.

- Although a complete mechanically decoupled measurement system could not be fully achieved, good results were obtained by using the decoupling matrix of the calibrated system to compute the decoupled applied forces for the static as well as for dynamic forces.

Therefore, the tri-directional contact force measurement system investigated in this study can be effectively used to measure the actual three directional contact forces at blade shrouds, representing an improvement with respect to the existing contact force measurement systems currently limited to the uni- and bi-directional force measurements. As a result, a better and detailed representation of the shroud contact parameters can be achieved, and a more reliable experimental validation of the contact models can be accomplished.

NOTE: Part of the work described in this chapter has been previously published in [52] Ahmed R, Firrone C.M., Zucca S., Design and Calibration of a Tri-Directional Contact Force Measurement System. Applied Sciences. 2021; 11(2):877. https://doi.org/10.3390/app11020877”

Chapter 5

Test Rig Commissioning

5.1 Introduction

The proposed experimental test rig involving the mockup shrouded blade as the test specimen and incorporating the tri-directional contact force measurement system and torque screw mechanism was designed to measure the nonlinear forced response of the shrouded blade and the three-dimensional shroud contact forces simultaneously during the forced vibration testing. This chapter describes the different aspects of the experimental campaign in detail. Firstly, the experimental modal testing of the test rig with shrouded blade is described that is carried out to determine the actual natural frequencies of the system. This is followed by details of the final calibration procedure of the installed contact force measurement systems. Subsequently, for the post-calibration final assembly of the test rig, the components and the equipment that make up the experimental setup are described. Finally, the testing and measurement processes are discussed.

5.2 Assembly Process

The test rig was used in two different configurations and the assembly process was determined accordingly. The two configurations were:

1. Blade with open shroud
2. Blade with closed shroud

In case of the first configuration, which is useful only in the preliminary modal analysis to estimate the modal parameters of the blade, the assembly process was very straightforward:

a) Placement and positioning of the blade housing block in the cavity with the help of two pins
b) Placement of the mockup shrouded blade by inserting the cylindrical base in the socket of the blade housing block.

c) Application of clamping force using the hydraulic clamp press to lock and fix the blade in the position.

In case of the second configuration, which allows simultaneous measurement of forced response and shroud contact forces, the assembly process includes the following steps:

a) Fastening the assembled supporting frame walls on the clamp rig test bench.
b) Attachment of the measurement box consisting of the calibrated 3D contact force measurement system on top of the supporting frame walls.
c) Assembly of the mockup shrouded blade assembly beforehand by inserting the cylindrical base of the shrouded blade in the socket of the blade housing block.
d) Positioning of the mockup shrouded blade assembly in the designated space of the clamp rig, while aligning the shrouds between the two contact force measurement systems and inserting the pins to hold the blade housing block.
e) Placement of the torque pin and preliminary check of the engagement of shroud contacts by blade twisting.
f) Application of the designated normal preload by the torque screw mechanism.
g) Application of clamping force using the hydraulic clamp press to lock and fix the blade in the position.

5.3 Preliminary Modal Analysis: Experimental testing

5.3.1 Impact hammer testing with uniaxial accelerometer

In order to determine the actual natural frequencies of the structure and to compare them with the design values, an experimental modal testing activity was carried out for the mockup shrouded blade and the test rig. Before the final assembly, impact hammer testing of the shrouded blade was performed with the blade shroud ends in free condition and the blade root clamped with 100 bar hydraulic pressure. The response was acquired using a uniaxial accelerometer fixed near the shrouded blade tip in three orthogonal directions X, Y and Z whereas the impacts were made near the root of the blade and at the center of the blade as shown in Figure 34.

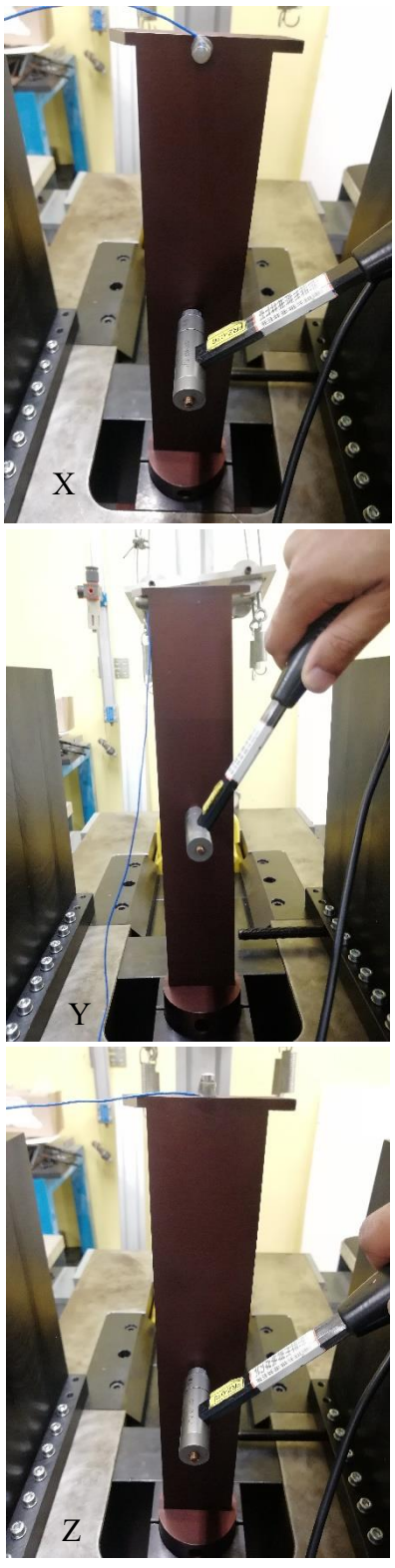

Figure 34: Impact hammer testing of mockup shrouded blade in free condition

The first natural frequency that indicates the first bending mode of the shrouded blade with free shroud condition was observed to be at 70Hz as seen in Figure 35. This is equal to the natural frequency of the shrouded blade in free condition that was established during the FE modal analysis.

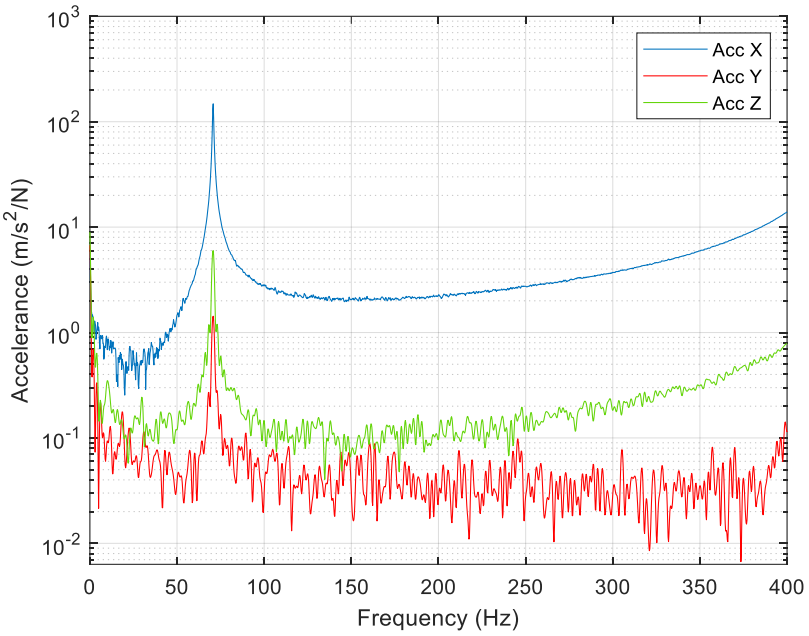

Figure 35: FRF plot of mockup shrouded blade in free condition

After the final assembly, the experimental modal testing of the whole test rig with engaged shrouded blades was performed. Impact hammer testing was repeated with the shrouds in contact with the contact pads by using the torque screws. A nominal normal preload of 50N was applied on both the shroud contacts with unbalanced actual normal preloads after the clamping process. The unbalanced normal preload distribution is discussed in detail in Section 5.7.1. For this activity, the accelerometer was fixed at midpoints along the length of the blade and the impacts were made near the blade root as well as at the center of the blade. In this case, the first bending mode of the blade with engaged shroud contacts was observed at 313 Hz as indicated in Figure 36. This value is close to the natural frequency of the engaged shrouded blade that was found during the FE modal analysis i.e. 323.6 Hz but not exactly equal. The difference can be linked with the uncertainty associated with the modeling of joints and modeling of constraints i.e., the boundary conditions as well as the uncertainty involved in simulating the contact condition in FE model as compared to the actual test rig. Nevertheless, the FRFs obtained from the experimental modal testing of the mockup-shrouded blade

in free and in engaged contact condition was useful to define the excitation frequency range to be implemented during the forced response testing.

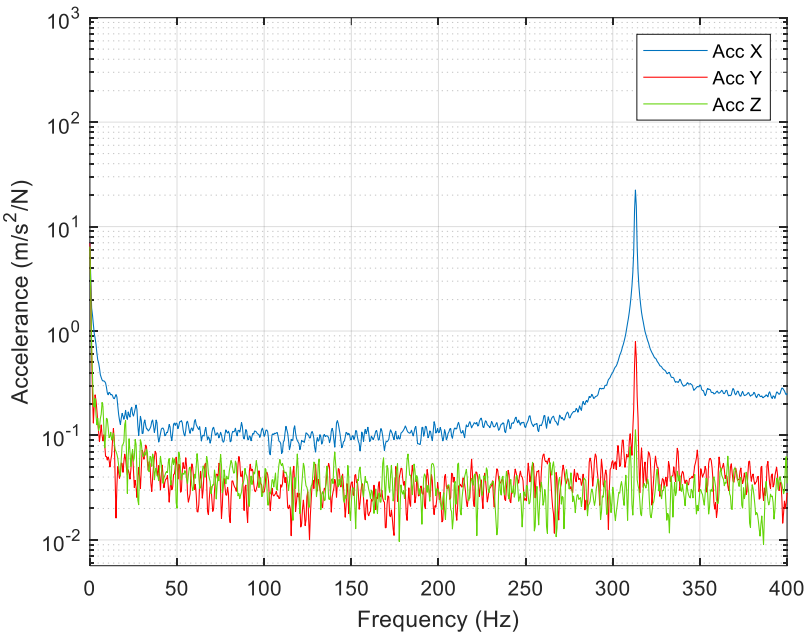

Figure 36: FRF plot of mockup shrouded blade in engaged condition

5.3.2 Modal Testing with Scanning Laser Doppler Vibrometer (SLDV)

To validate the results obtained by the impact hammer testing with uniaxial accelerometer, experimental modal testing was performed by using the Scanning Laser Doppler Vibrometer (SLDV) by Polytec. This type of SLDV offers laser-based technology for fast, accurate, and non-intrusive solution for non-contact vibration analysis. The instrumentation involves the measurement of instant velocity by sensing the Doppler effect on the laser beam reflected and propagated by the surface. SLDV comprises of an interferometer and a pair of mirrors moved by actuators to precisely point the laser beam in the required direction and scan the selected grid points. The major components of the SLDV system by Polytec include a PSV-400 Scanning Head mounted on a tripod, a PSV-A-420 Geometry Scan Unit to acquire the 3D geometry and a OFV 5000 Vibrometer Controller.

First, the scanning head was pointed towards one of the sidewalls of the test rig and the vibration analysis of the supporting frame was performed by exciting

the lower part with an impact hammer (Figure 37). This allowed determining the actual natural frequencies of the test rig structure and the first bending mode of the sidewall was observed around 100Hz (Figure 38).

Figure 37: Using SLDV to find the modes of the test rig structure

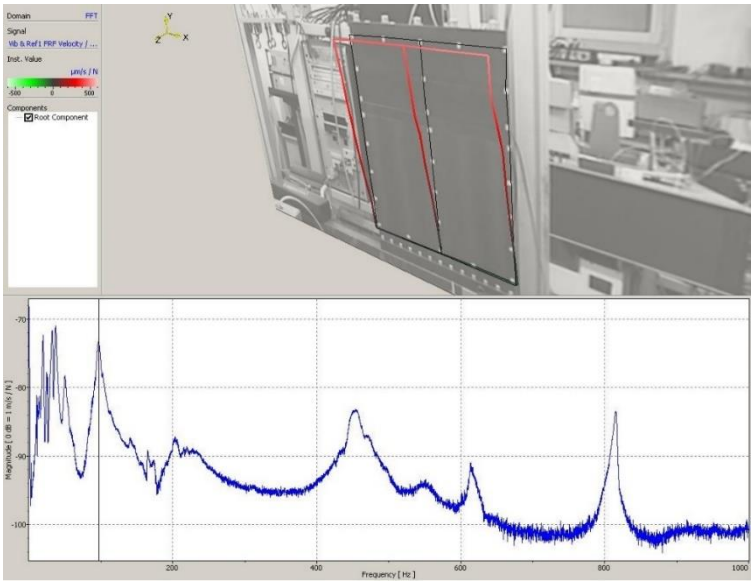

Figure 38: Animated mode shape observed in PSV software

In the next step, SLDV was placed in front of the shrouded blade and the laser beam was pointed to different points marked by reflective tape making up a predetermined grid on the blade. The vibration response of the free and engaged shrouded blade was measured by the SLDV as the blade was excited between the center and the blade root (Figure 39).

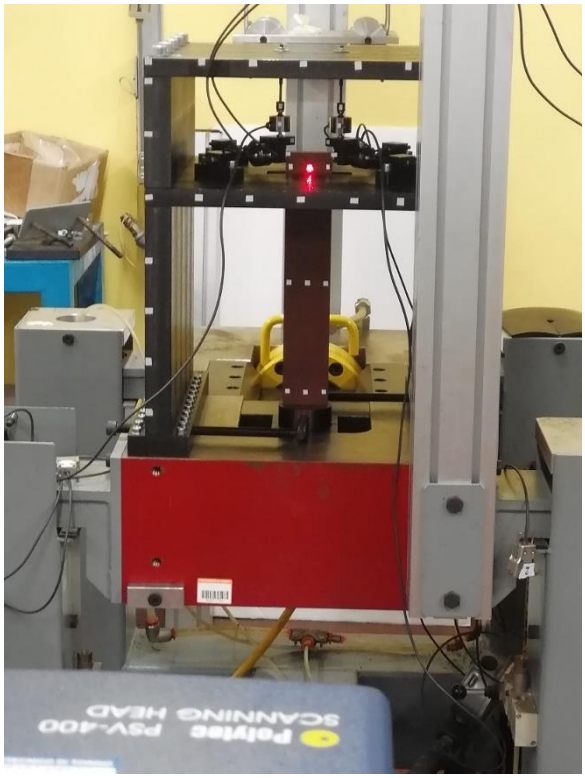

Figure 39: Modal testing of the shrouded blade using SLDV

FRF plot in Figure 40 display the natural frequency of the free and engaged shrouded blade as the velocity response was acquired by SLDV. The natural frequencies determined by acquiring the velocity response from SLDV matched the natural frequencies determined by acquiring the acceleration response from the accelerometers. In both the cases, the first bending mode of the free shrouded blade was 70Hz and the first bending mode of the engaged shrouded blade was 313Hz.

The validation process with SLDV improved the preliminary modal analysis and identification of the natural frequencies as well as the mode shapes of interest that play a significant role in determining the excitation frequency range during the forced response testing of the mockup shrouded blade. Table 9 summarizes the comparison of the numerical and experimental results of the modal testing that was

performed to investigate the dynamics of the mockup shrouded blade in the free condition and in the engaged condition.

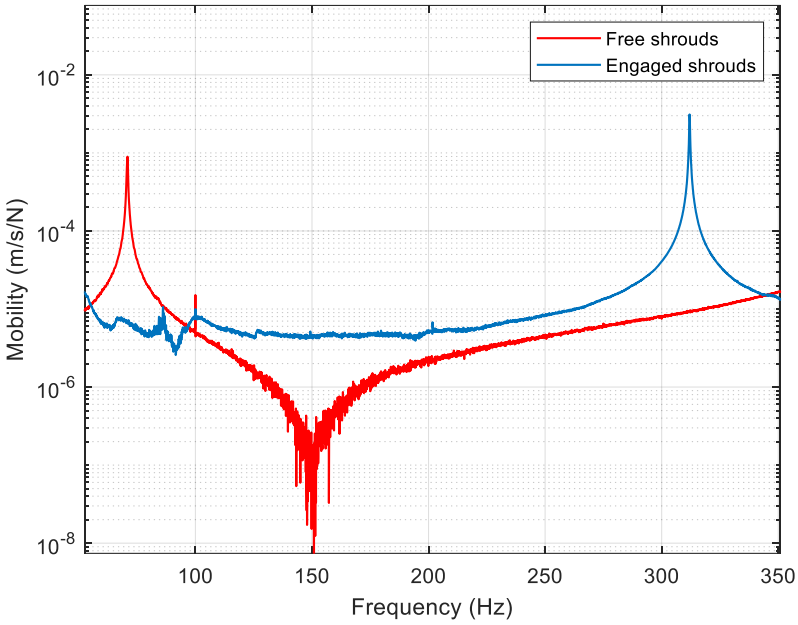

Figure 40: FRF plot of free and engaged shrouded blade using SLDV

Table 9: Natural frequencies of the 1st bending mode

Contact Condition	Numerical model	Experimental results
Open shrouds	69.6 Hz	70 Hz
Close shrouds	323.5 Hz	313 Hz

5.4 Final calibration of contact force measurement systems

As discussed in the previous chapter, in order to compensate the mechanical coupling that exists in the force measurement system due to the interconnected orthogonal branches, the tri-directional contact force measurement system should be calibrated. Standard calibration procedure involved sequential loading along the axial direction of each force sensor to assemble the calibration matrix. Later, when the force measurement system is subjected to a three-dimensional force during the experiment, the decoupling matrix derived from the calibration is used to compute the decoupled applied forces in each direction. Details regarding the testing and validation of the decoupling method was also explained in the previous chapter.

Before commencing the forced response testing of the mockup shrouded blade using the proposed test rig, the final calibration was performed after fixing the two contact force measurement systems inside the measurement box. The two tripod assemblies were adjusted while they were mounted to ensure properly aligned engagement of the shroud contacts with the contact pads and only then the collar links were tightly screwed. For their calibration, the measurement box comprising of the fixed contact force measurement systems, was disassembled and removed from the supporting frame and installed on a separate calibration bench.

The contact pads on each of the contact reference blocks were removed and replaced by calibration pads (Figure 41). The calibration pads were specially designed with threaded holes machined at the center of its three orthogonal faces. Hence this modification allowed for the attachment of hooks in three orthogonal directions for the application of axial loads as dead weights for each of the six force sensors.

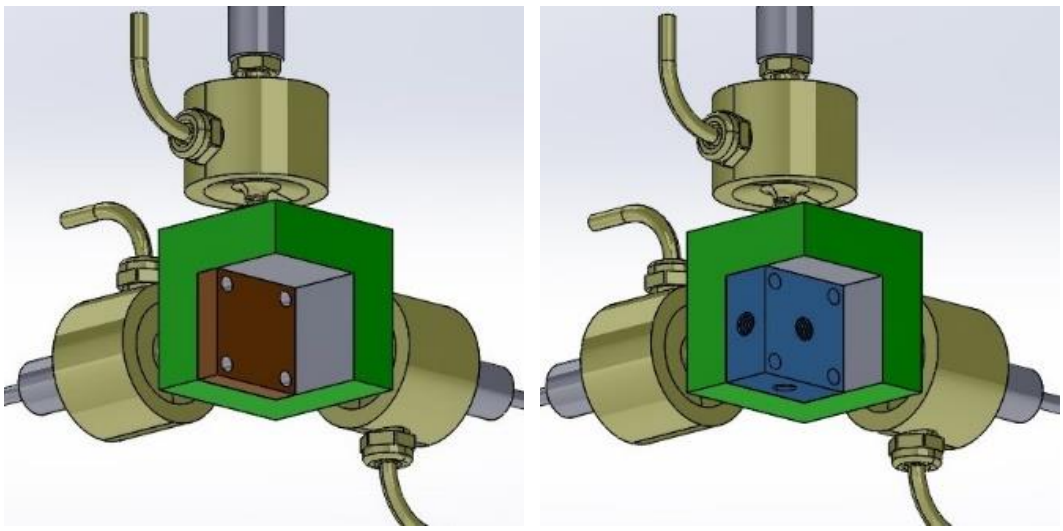

(a) (b)

Figure 41: Tripod assembly with (a) Contact pad (b) Calibration pad

First, the tri-directional contact force measurement systems were calibrated one at a time for Side A and Side B with the tensile forces by using a wire-pulley setup (Figure 42) allowing load application in the form of dead weights along the axial direction of each force sensor individually.

Additionally to improve the accuracy in case of final calibration, and assuming linear behavior of the force sensors in both tensile and compressive axial

directions, calibration procedure was also performed for the equivalent compressive forces by using rod-pusher system (Figure 43). In this case, the hooks were unscrewed and replaced by a flat head bolt. Subsequently, a rod attached to the rod pusher system was pressed with a controlled compressive force against the flat head bolt screwed to the calibration pad along the axial direction of each force sensor and corresponding forces measured by the other sensors were logged.

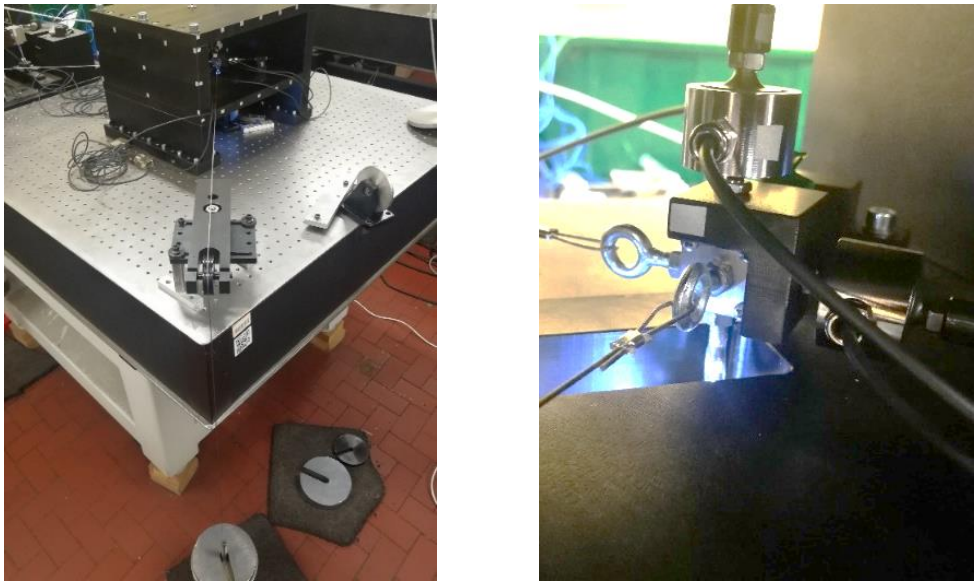

Figure 42: Wire-Pulley setup for tensile force calibration

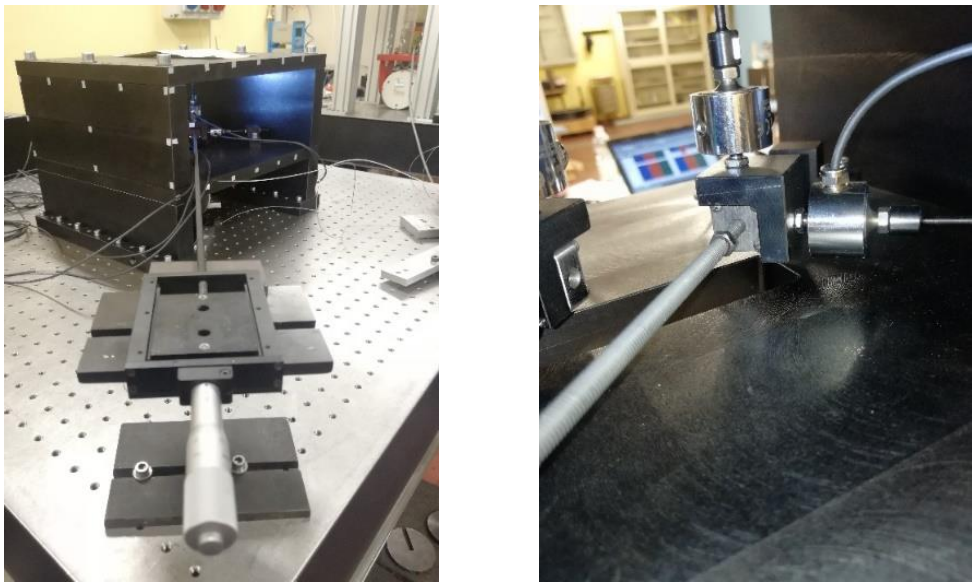

Figure 43: Rod pusher setup for compressive force calibration

The load cycles that ranged from 0 – 100N were applied during the calibration for both axial loads i.e., tensile, as well as compressive and the forces measured by the force sensors during each load cycle were recorded in a table. These measurements allowed to determine the decoupling matrix for each shroud side i.e. A and B, which will be later used to compute the decoupled contact forces when three-dimensional shroud contact forces act on the contact pads. During the calibration for both, tensile and compressive forces, the loading cycles were repeated three times for each force sensor and the repeatability of the measured forces in the calibration process was ensured.

Table 10: Calibration of Side A and Side B contact force measurement systems

SIDE A

Averaged Percentage - % (Standard Deviation) Tensile force calibration		**Applied loads**		
		F_x	F_y	F_z
Measured Force Outputs (%)	F_1	98.87 (0.11)	-0.79 (0.16)	-1.57 (0.22)
	F_2	-1.79 (0.23)	97.69 (0.07)	1.28 (0.15)
	F_3	1.86 (0.19)	-1.33 (0.11)	97.43 (0.55)
Averaged Percentage - % (Standard Deviation) Compressive force calibration		**Applied loads**		
		F_x	F_y	F_z
Measured Force Outputs (%)	F_1	98.87 (0.11)	-1.39 (0.28)	4.40 (0.14)
	F_2	2.17 (0.34)	97.69 (0.07)	-4.06 (1.52)
	F_3	-0.89 (0.16)	-1.49 (0.07)	97.43 (0.55)

SIDE B

Averaged Percentage - % (Standard Deviation) Tensile force calibration		**Applied loads**		
		F_x	F_y	F_z
Measured Force Outputs (%)	F_1	97.18 (0.49)	-0.66 (0.11)	1.72 (0.07)
	F_2	-0.70 (0.16)	97.85 (0.17)	1.90 (0.10)
	F_3	0.60 (0.24)	-0.83 (0.20)	97.79 (0.21)
Averaged Percentage - % (Standard Deviation) Compressive force calibration		**Applied loads**		
		F_x	F_y	F_z
Measured Force Outputs (%)	F_1	97.18 (0.49)	-0.96 (0.09)	1.01 (0.12)
	F_2	2.25 (1.40)	97.85 (0.17)	-1.49 (0.94)
	F_3	-1.62 (0.28)	-1.52 (0.09)	97.79 (0.21)

In Table 10, the average normalized calibration matrices are shown with standard deviation stated in parenthesis. The mechanical coupling for the measurement system in case of tensile force calibration for both sides is less as

compared to the compressive force calibration also seen in Figure 44. This difference depends on the mounting orientation of the force sensors and the strain gage arrangement inside the force sensors that is not available to the user. For tensile forces, mechanical coupling observed is not very high i.e., up to 2 % in the worst case whereas for compressive forces, especially for Side A, percentage error is up to 4%.

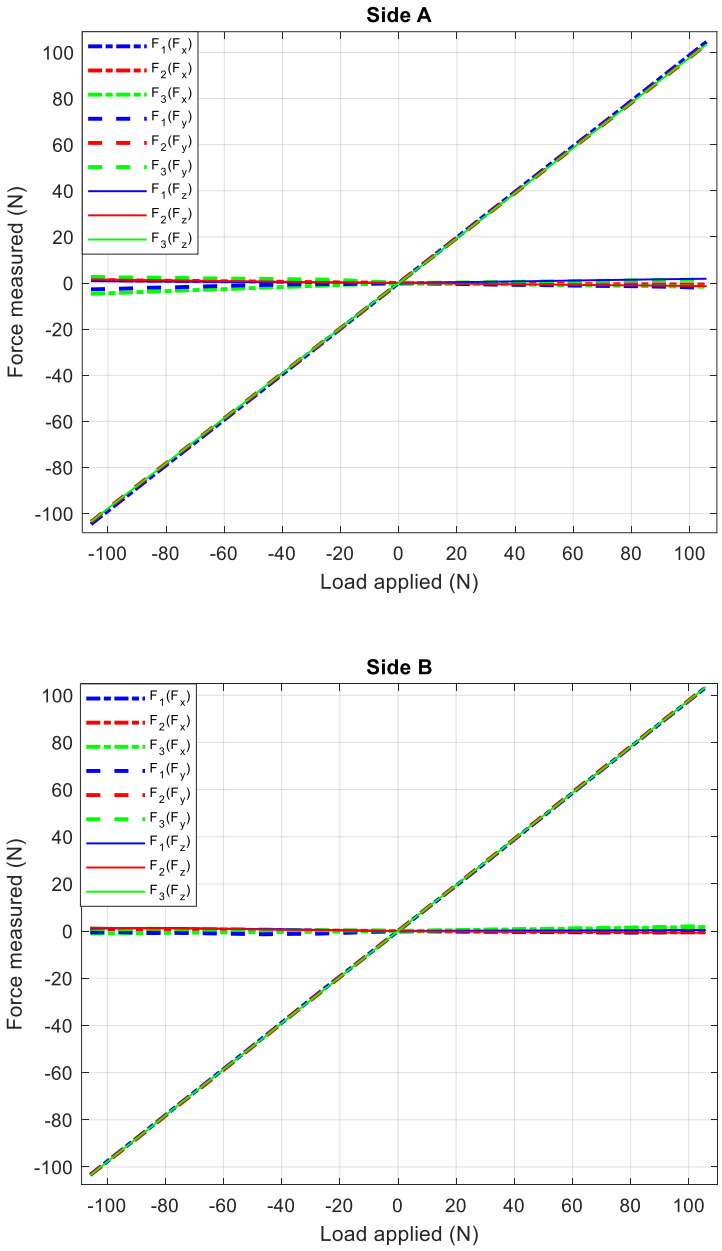

Figure 44: Calibration plot for Side A (above) and Side B (below)

After the completion of calibration procedure, the calibration pads were replaced with the contact pads and the measurement box was relocated to the top of the supporting frame. It is vital to signify that during the relocation of the measurement box before and after the calibration as well as during the calibration process of the measurement system, the position and final setting of the force sensors was not disturbed or modified. Hence, the calibration performed on the separate calibration bench was completely valid and usable in the main experimental rig with shrouded blade after the relocation of the measurement box.

5.5 Investigation of the actual shroud contact condition

During the mounting of the contact force measurement systems, the tripod assemblies were adjusted to achieve centrally aligned contact between the contact pads and shroud contacts. However, due to the manufacturing tolerances and the re-attachment of measurement box after the calibration, it was necessary to examine the final status of the actual contact condition before proceeding with the experiment. The assessment of the actual contact condition was also required for accurate prediction of the forced response of the shrouded blade and the shroud contact forces in the numerical simulations. Therefore, after the final assembly, to investigate the actual contact condition for both the shroud sides, PRESCALE pressure measurement film [53] was utilized.

The PRESCALE pressure measurement film allows to visually observe and measure the pressure distribution as the color density changes according to the amount of pressure applied. The two sheet type of measurement film consisting of color forming material and color developing material was used by first, putting the chemical coated sides over each other. It was then placed in between the contact surfaces and a nominal normal preload of 50N was applied using the torque screw mechanism. Pressure causes breakage of the microcapsules in color forming layer and this results in the absorption of colorless dye into color developing layer where a red color is produced due to a chemical reaction. After few minutes, when the measurement film was removed by disengaging the contact, a qualitative analysis of the pressure distribution was done that exhibited the contact force distribution at the interface area. Different contact area distributions were observed for both the shroud sides with Side A having more localized contact area as compared to Side B as seen in Figure 45. Moreover, the impression on the measurement film displayed a localized contact area distribution fairly similar to the localized contact state of real shrouded turbine blades as observed in [54] .

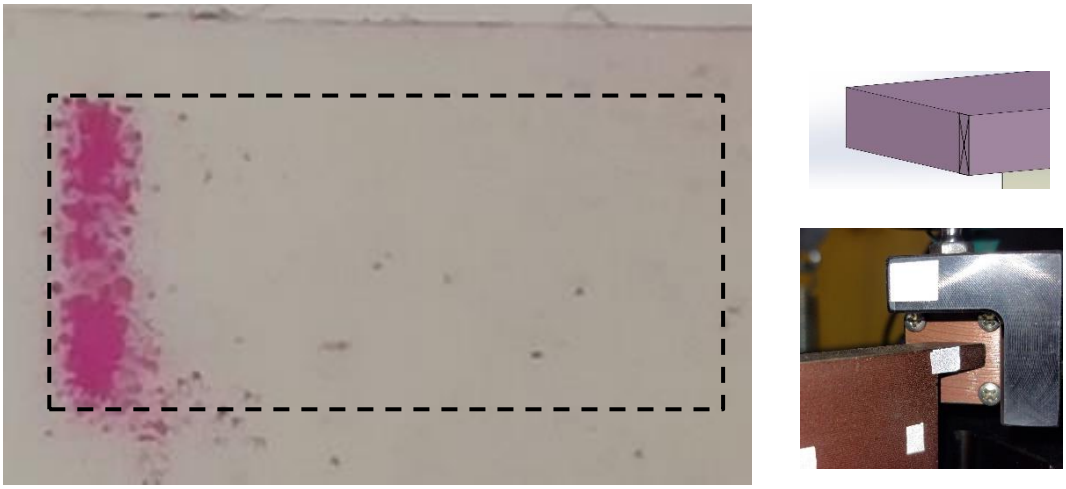

(a)

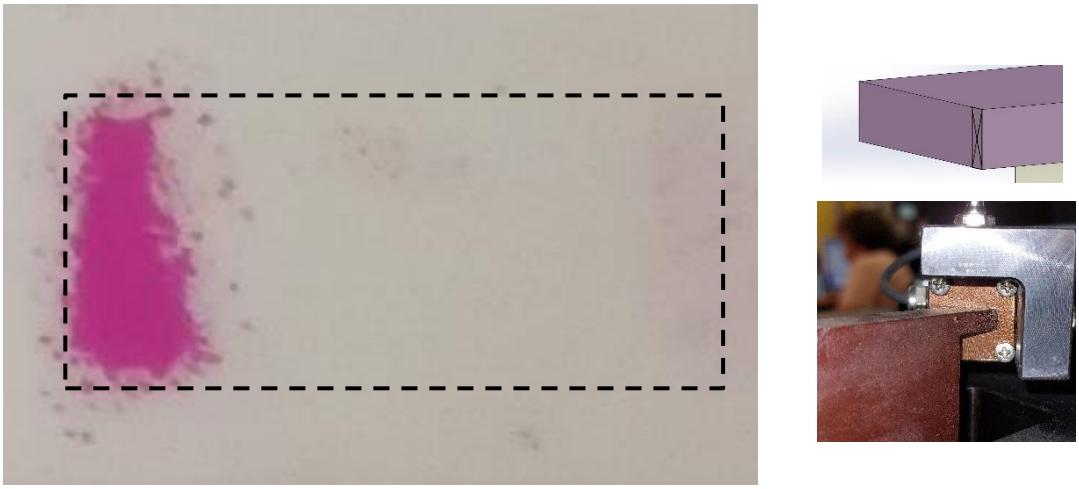

(b)

Figure 45: Pressure measurement film impression for (a) side A and (b) side B

5.6 Experimental setup

The final test rig assembly as seen in Figure 46 comprised of the two calibrated tri-directional contact force measurement systems engaging two shroud contacts of side A and B while the mockup shrouded blade was placed in the blade housing block which is initially held by two support pins and later clamped by a hydraulic press.

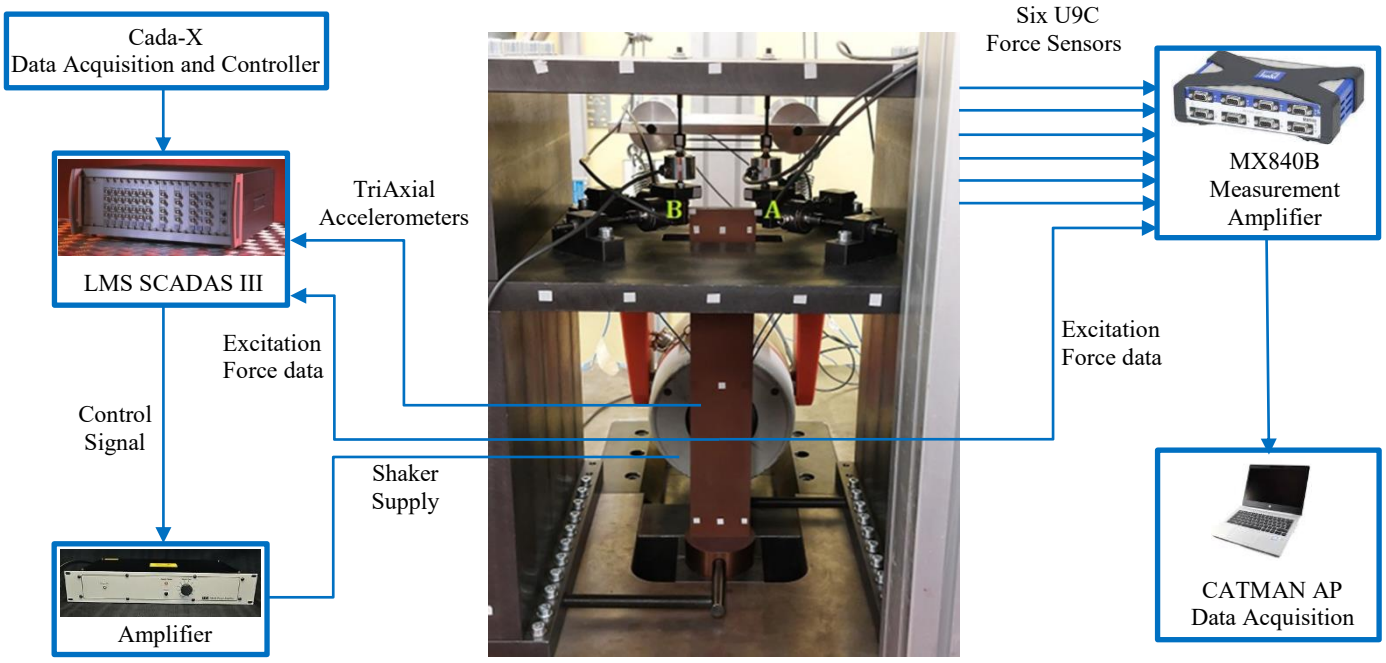

Figure 46: Layout of the experiment

For the forced response testing of the mockup-shrouded blade, in addition to the designed experimental test rig, the experimental setup comprised of instrumentation involving shaker as excitation device and sensors (force sensors and accelerometers) as well as the data acquisition systems used to acquire, monitor and control the installed instrumentation.

The shaker was connected to the mockup-shrouded blade by means of a stinger with a piezoelectric force sensor fitted between the stinger and the blade to measure and control the excitation force as seen in Figure 47. The flat part of force sensor is firmly attached to the blade using an adhesive glue. The other end of the stinger was attached to the moving mass of the shaker. The stinger acts like a pushrod and is usually designed keeping in view the amount of excitation force to be applied to produce a measured response in order to study the damping characteristics of the structure. However, it should be lightweight to prevent mass loading of the structure and flexible to compensate for the lateral component of the applied force. It is also necessary to ensure proper alignment of the stinger with respect to the blade while the shaker is being installed since stinger misalignment can affect the FRFs of the structure.

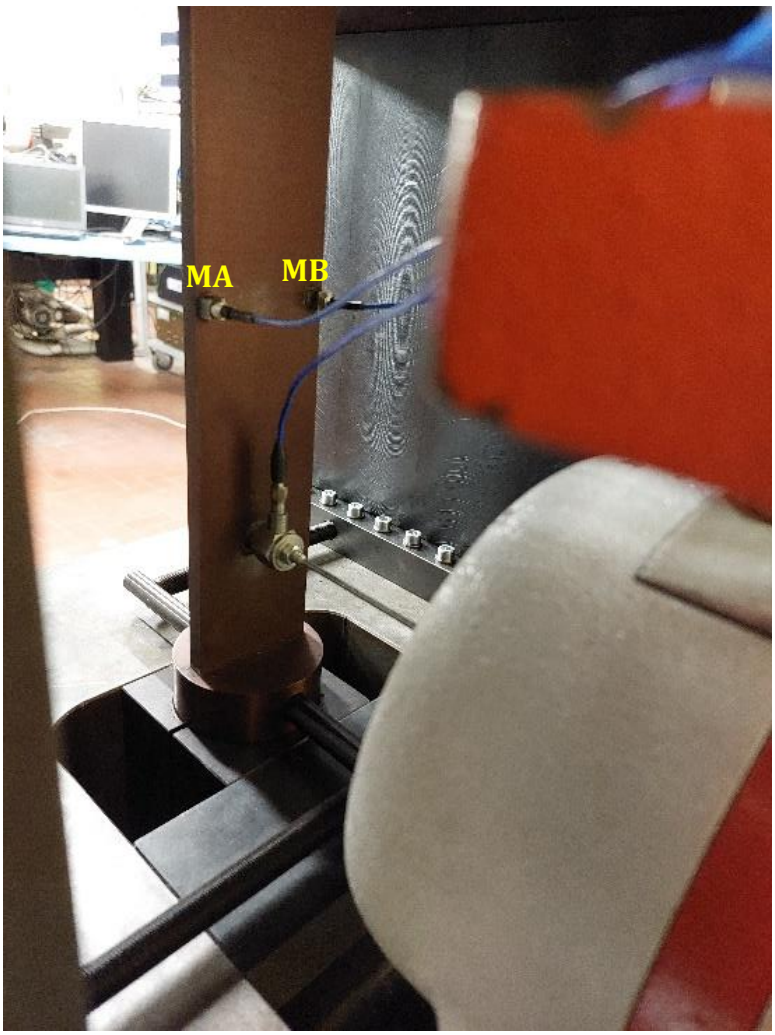

Figure 47: Shaker-stinger-force sensor and accelerometers attached at the rear face of the shrouded blade

To measure the response during force controlled sine sweep tests, two tri-axial accelerometers were fixed near the edges of the blade at midpoints along the length of the blade on measurement points MA and MB as seen in Figure 47. Being small and lightweight, the accelerometers were not expected to affect the dynamics of the shrouded blade.

LMS Scadas III (Figure 48) was used for the forced response testing of the shrouded blade. It can be integrated with both, LMS Cada-X or LMS Test.Lab testing and analysis software. For the proposed forced response testing, two modules, one for output (QDAC) and one for input (PQFA) were used.

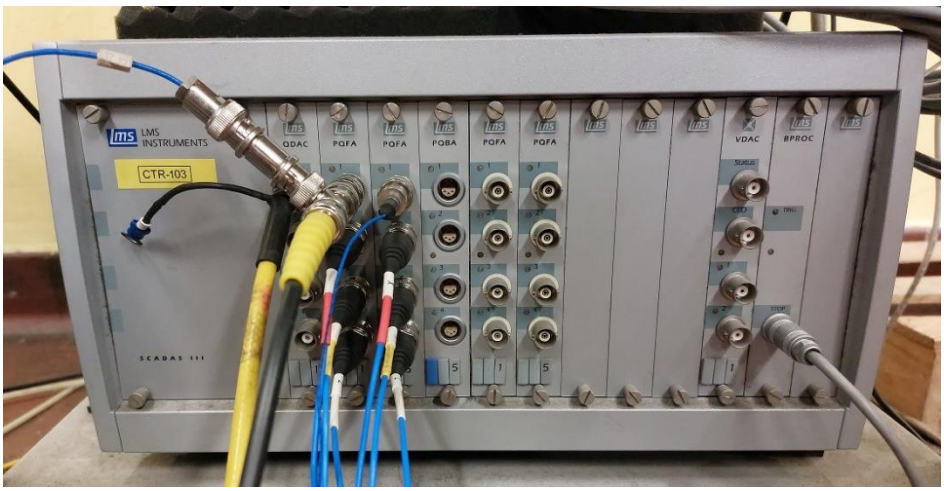

Figure 48: LMS Scadas III front end

During the forced response testing, QDAC was used in the control loop to send output signals to the LDS amplifier that drives the electrodynamic shaker. The piezoelectric force sensor and the accelerometers were connected to PQFA's grounded BNC connectors. As seen in Figure 48, there are three inputs (X, Y, Z) from each of the two tri-axial accelerometers (marked with red, yellow and white cable sleeves) connected to LMS Scadas III. The input from the piezoelectric force sensor that measures the excitation force applied by the shaker is also connected to this module and is used to compute the control signal to be sent to the LDS amplifier.

LMS Cada-X software was used to process the signals acquired by LMS Scadas III. The exclusive function of the Cada-X software involved the measurement and control of the excitation force applied by the shaker through implementation of a control strategy in a closed loop system with feedback. Secondly, the use of LMS Cada-X allowed the acquisition of the response at higher resolution to compute the FRFs during the forced response testing. In other words, the software enabled the use of more spectral lines distributed over the specified bandwidth resulting in finer resolution.

QuantumX measurement amplifier MX840B type as seen in Figure 49 was used in the experiment for the measurement of the shroud contact forces. In addition to the time data of the six HBM U9C force sensors, it was used to acquire the time data of the applied excitation force measured by the piezoelectric force sensor using a T-connector (Figure 48) and a QuantumX adapter (Figure 49). This adapter was

used to get the data coming from the piezoelectric force sensor with BNC connector into MX840B measurement amplifier.

Figure 49: MX 840B measurement amplifier

CATMAN AP was the software used with the MX840B to acquire, visualize, record and analyze the measurement data from the force sensors. The settings in the software involved the input of the sensor's sensitivity-scaling factor provided by the manufacturers. The software was used to zero the force sensors at the beginning of the experiment, to visualize the force data in real time during the experiment and to save the data after the experiment.

Further details regarding the components of the experimental setup can be referred in Appendix B.

5.7 Experimental procedure

5.7.1 Setting the initial conditions and normal preload

The first step of the experiment was to set the initial conditions for the experimental test. Initially, the position of the shrouded blade was fixed by applying a very small clamping force on the blade housing block using the hydraulic clamp press. The position of the shrouded blade was fixed such that there was no obstruction to the rotation of the cylindrical base placed in the housing block. Subsequently, the two torque screws were gently rotated simultaneously to horizontally push on the torque pin driven through the cylindrical base at the blade root. As expected, the blade

twisted and consequently the shroud contacts applied a normal force on the contact pads that was checked. Application of the normal preload on the two contact surfaces was controlled manually by regulating the turning of the torque screws. When the chosen nominal normal pre-load value was reached, the torque screws were not rotated any further and rotation was stopped while recording the static contact force values. Following that, the clamping pressure was increased to 100 bar in order to hold and lock the mockup shrouded blade strongly in that place. After applying the final clamping pressure, the torque screws were unscrewed back and the torque pin was removed from the cylindrical base. Likewise, as before, the static contact forces after the final clamping press were logged. As stated, during the clamping procedure, the measured static contact forces were noted before and after the application of the clamping force to observe any difference the clamp press would make. Table 11 indicates the static contact force values achieved by the torque screw mechanism and those measured after the clamp press was applied. A larger change in the static contact forces of Side A was observed as compared to Side B. For the applied clamping force, static contact forces in all the three directions at Side A were affected and at Side B, tangential contact force in Y direction showed more pronounced effect as compared to static contact forces in other directions. The observed asymmetrical distribution of the normal preload at Side A and Side B can be due to the following reasons:

1. The clamping force applied in one direction.
2. The occurrence of contact uncertainties as a result of contact settling with respect to the pre-calibration stage and post-calibration reattachment of measurement box on top of the supporting frame.
3. The cylindricity errors in the mockup blade base and the blade housing block resulting in misalignment of the shroud contact surfaces with contact pads when the clamping force is applied.

Table 11: Static contact forces before and after the clamping process

Stage	Static contact forces (N)	Side A	Side B
Torque Screw Setting	Tangential X	18.38	17.15
	Tangential Y	-2.73	-2.41
	Normal Z	33.36	31.77
Post - Clamping force	Tangential X	8.15	18.42
	Tangential Y	-27.26	-11.87
	Normal Z	57.47	30.00

5.7.2 Forced response testing

The mockup shrouded blade with the shroud contacts engaged with the contact pads for the designated normal preload was excited by a stepped sine signal across the frequency range of 305-320Hz with frequency step of 0.25 Hz and controlled excitation force. The force-controlled stepped sine tests were performed with LMS Scadas III using Cada-X software for different normal preloads and different excitation forces (F_E) during the experimental campaign.

The amplitude of the harmonic excitation force passed on as the controlled signal to the shaker through the amplifier was updated to achieve the required excitation force levels to within ±5% of the nominal excitation force level. Thus, the control strategy employed in the Cada-X software allowed to control the amplitude of the first harmonic component only and higher harmonic contents encountered by the shaker due to the interaction with test rig dynamics were neglected. The measured contact forces and excitation force values were acquired and recorded through QuantumX MX840B data acquisition measurement amplifier using CATMAN AP software at high sampling frequency of 19.2 kHz. To confirm repeatability of the test setup, numerous runs were executed for each test campaign that comprised of a particular set of normal preloads and excitation forces. Each time the normal preloads had to be newly set, the shroud contact conditions were reset by untwisting the shrouded blade and then reinitiated as explained in the previous section for test runs where the FRF and the corresponding shroud contact forces at Side A and B were measured simultaneously.

Table 12 summarizes the test runs performed during the experimental campaign. The detailed procedure of setting up Cada-X and QuantumX MX840B to perform the forced response testing can be found in Appendix C.

Table 12: Test matrix

	Normal Preloads (Side A – Side B)		
Test Cases	*CASE 1* *Nominal:30N – 30N* *Actual:57.5N – 30N*	*CASE 2* *Nominal:40N – 40N* *Actual:73.5N – 39N*	*CASE 3* *Nominal:50N – 50N* *Actual: 79N – 51N*
F_E = 1 N	5 runs (1-5)	5 runs (1-5)	5 runs (1-5)
F_E = 2 N	3 runs (6-8)	3 runs (6-8)	3 runs (6-8)
F_E = 3 N	3 runs (9-11)	3 runs (9-11)	3 runs (9-11)
F_E = 5 N	3 runs (12-14)	3 runs (12-14)	3 runs (12-14)
F_E = 7 N	3 runs (15-17)	3 runs (15-17)	3 runs (15-17)

NOTE: Part of the work described in this chapter has been previously published in:

Ahmed, R., Firrone, C. M., and Zucca, S., 2022, "Experimental investigation of three-dimensional shroud contact forces in forced vibration testing of a shrouded blade," Proc. ASME Turbo Expo 2022

Ahmed, R., Firrone, C. M., and Zucca, S., 2022, "A novel test rig to investigate shroud contact forces of turbine blades", Mechanical Systems and Signal Processing 2022 (Submitted)

Chapter 6

Experimental results and discussion

6.1 Introduction

The forced response testing plan as outlined in Table 12, was carried out for various excitation forces with different nominal normal preload values categorized as Case 1, Case 2 and Case 3. The test campaign enabled us to understand the effect of the excitation forces on the frequency response and the shroud contact forces that were simultaneously acquired.

6.2 Frequency Response Function (FRF)

The FRF obtained for all the cases i.e., Case 1, Case 2, and Case 3 are displayed in Figure 50 where an increase in the excitation force (F_E) results in more damped response. For low excitation force level, the dynamic response behavior is almost linear whereas for higher excitation force levels, nonlinear behavior having softening effect on the FRF is observed. On the other hand, Figure 50 also indicates how the FRF changes for each case i.e., with the variation of normal preloads. An increase in the normal preload as we proceed from Case 1 to Case 3, increases the contact area and thus makes the contact interface stiffer, moving the FRF peak up towards the linear full stick condition.

The partial and incomplete overlapping of the FRF in the linear regions of the curve for different cases can be attributed to the initial settings procedure. This means that before running the stepped sine test for new case with new normal preload values, the shrouded blade was unclamped and untwisted, and the torque screw rotation was repeated as initial static conditions were reset resulting in slightly different shroud engagement and new contact interface conditions for the new case. Another interpretation of FRF for the above mentioned cases can be seen in the proceeding figures, i.e., for this specific range of excitation frequencies, Figure 51 displays greater response amplitude with increasing normal preload to excitation force ratio and Figure 52 exhibits higher resonance frequencies for larger

normal preload to excitation force ratio that stiffened the shroud contact interface and vice versa.

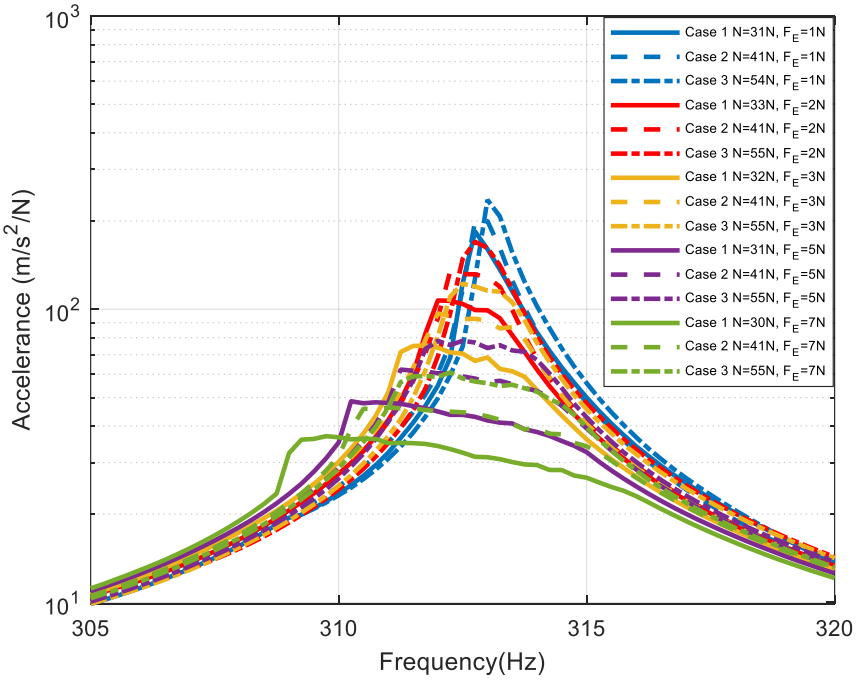

Figure 50: FRF of shrouded blade for different excitation forces and normal preloads as in Case 1, Case 2 and Case 3

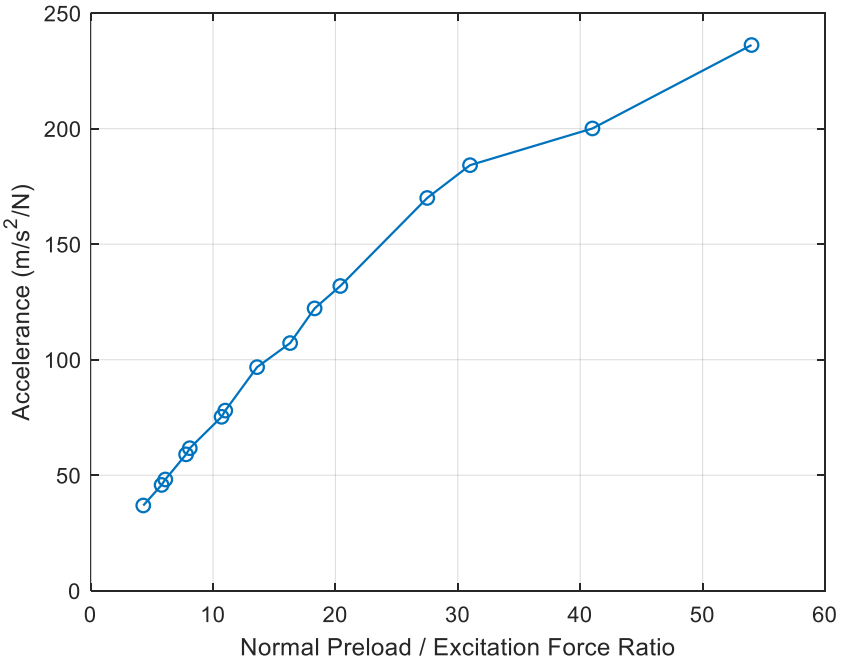

Figure 51: Response against normal preload to excitation force ratio

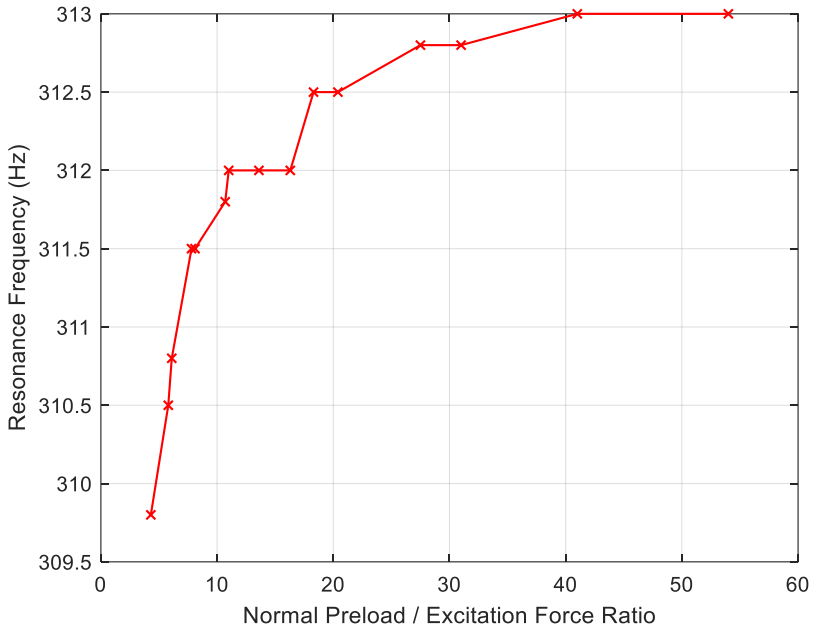

Figure 52: Resonance frequency against normal preload to excitation force ratio

The difference in contact condition between the two shroud contacts A and B due to contact uncertainty and geometric tolerances appeared during the measurement of static normal preload and investigation using pressure measurement film (Figure 45). Two possible scenarios of the engaged shrouded blade with respect to the distribution of the normal preloads on both shroud sides are:

1. Symmetrical and balanced normal preloads;

2. Asymmetrical and unbalanced normal preloads

In the first scenario for the specific range of excitation frequencies and normal preloads, there will exist a pure bending mode whereas in the second scenario there is a possibility of an additional torsional component effecting the bending mode. Considering that the shroud loading mechanism in this test rig results in the second scenario, it was necessary to confirm the influence of the torsion mode if any, to the first bending mode of the engaged shrouded blade. The FRFs computed using the response measured at the two edges MA and MB were compared and it was found that the torsion mode is least likely to effect the first bending mode of the engaged shrouded blade for this specific range of excitation frequencies and normal preloads. Figure 53 displays the FRF curves for the three cases specified in Table 12 when the excitation force was 5N. It was found that the

torsion is negligible in these conditions and the minor difference is consistent for all the cases. Furthermore, the plot reiterates the effect of the increasing normal preload in stiffening the system.

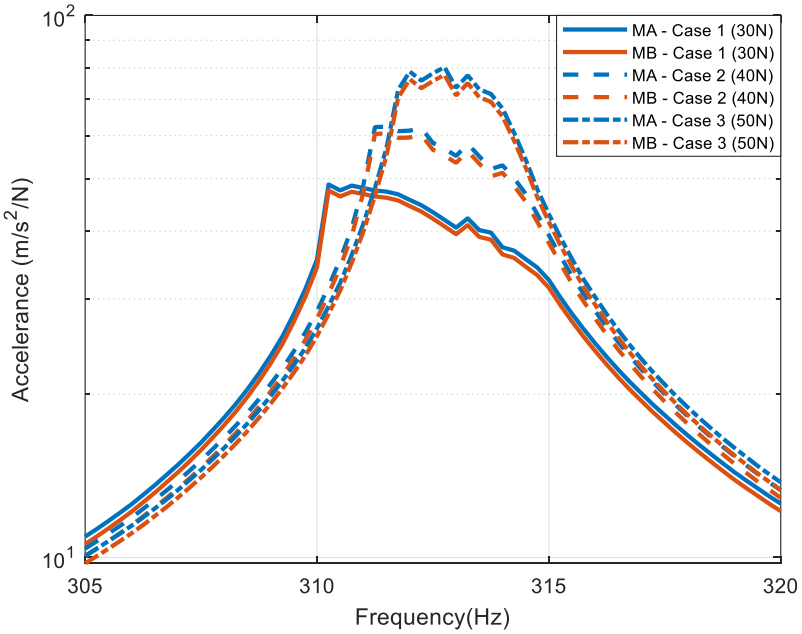

Figure 53: Forced Response at measuring points MA and MB of the shrouded blade (F_E = 5N)

6.3 Static contact forces

6.3.1 Variation of excitation forces in ascending order

For all the test cases, it was observed that the static contact force values recorded after the clamping, changed significantly after the first run of sine sweep test with the defined excitation force. Repetition of test run with the same excitation force resulted in these static contact force values stabilizing without varying significantly in the consequent runs. Hence the contact interface was stabilized by initially performing five consecutive test runs with the excitation force of 1N and at least three test runs for the ensuing higher excitation forces. Figure 54 shows the trend for all the cases, where the static contact forces vary initially during the first runs as the excitation force was increased but settled after successive runs with the same excitation force. The markers in the plots i.e., circles (Case 1), triangles (Case 2) and squares (Case 3) refer to the static contact force values measured at the end of each test run. These changes in the static contact force values during subsequent runs with increased excitation forces exhibit that actual normal preload for every

test run are different from the initial static contact forces measured after the clamping force was applied. The drifting behavior of the static contact forces is more prominent for Side A as compared to Side B.

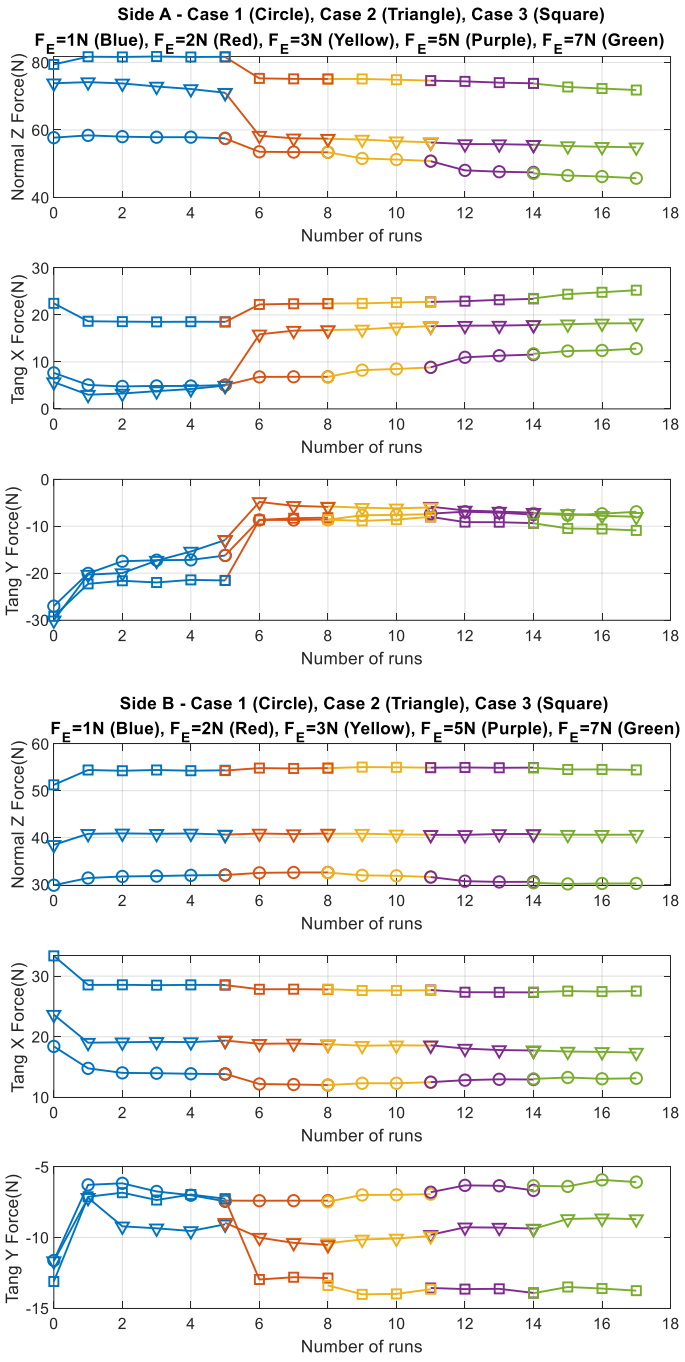

Figure 54: Variation of static contact forces for Case 1, Case 2 and Case 3 test runs with different excitation force levels for Side A (above) and Side B (below)

The tendency of the static contact force values to change during two of the test runs and their corresponding FRFs were analyzed i.e., at shroud side B for test run 1 of Case 1 and at shroud side A for test run 6 of Case 2.

Figure 55 shows the periodic contact forces measured on Side B during the entire run 1 of Case 1 where the excitation force was 1N. The plot indicates that the major change of the static component occurred as the excitation frequency goes through the resonance which is also evident when the FRF for this run and consecutive run are analyzed. The FRF of test runs 1-5 are displayed in Figure 56. The difference of the FRF plot for the first and the consecutive runs indicate that after the resonance, the contact interface stabilized for the first run and the plots overlap each other due to the stabilization of the static contact force values in the subsequent runs.

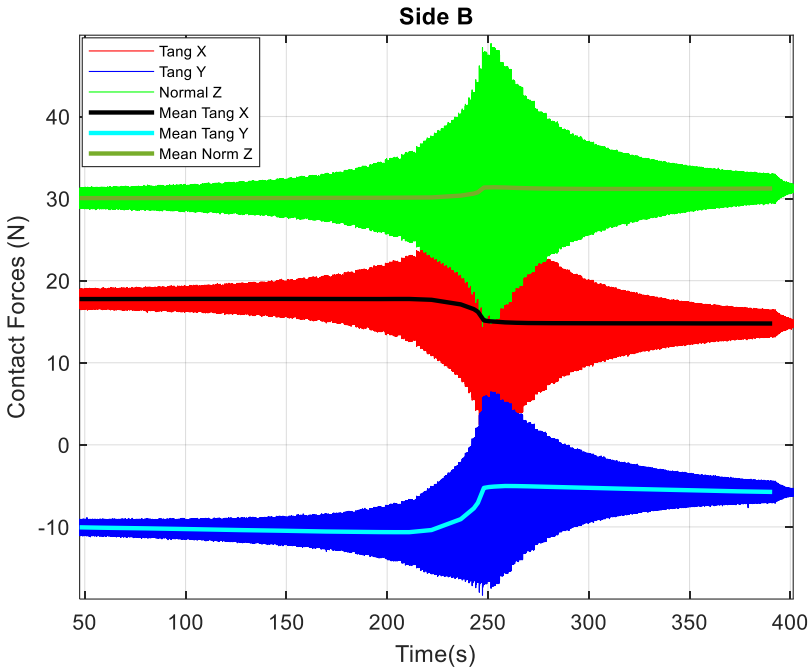

Figure 55: Variation in static contact forces at Side B during test run 1 for case 1 (F_E=1N)

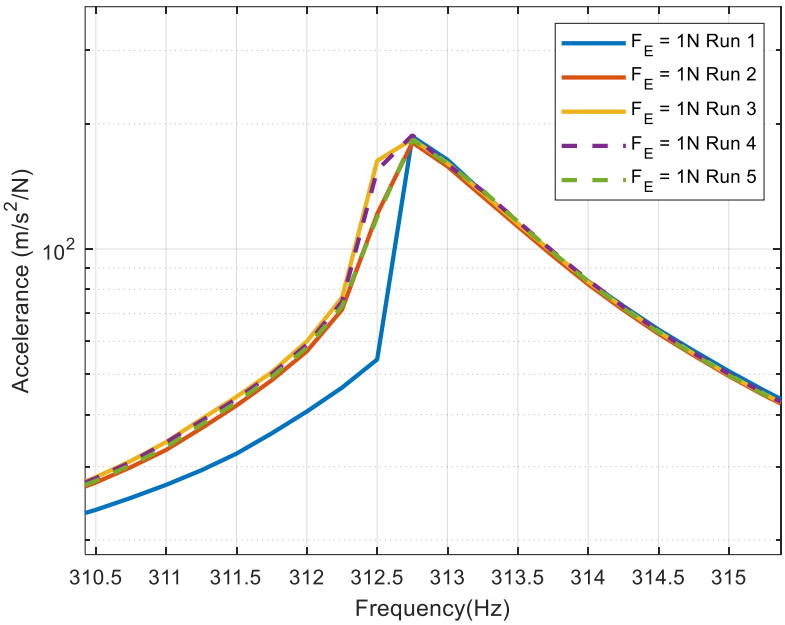

Figure 56: FRFs of the first five runs of Case 1 with F_E =1N

The same trend can be observed for shroud side A in test run 6 of Case 1 which is the first run with the excitation force of 2N. Figure 57 displays the variation in the static contact forces during the run 6. The plot shows the major change happening at resonance which is backed by the observations of the FRF for runs 6, 7, and 8. The FRF of test runs 6-8 are shown in Figure 58. The change in the FRF for the first and the consecutive runs imply the stabilization of shroud contacts and contact forces after the resonance as the plots overlap each other.

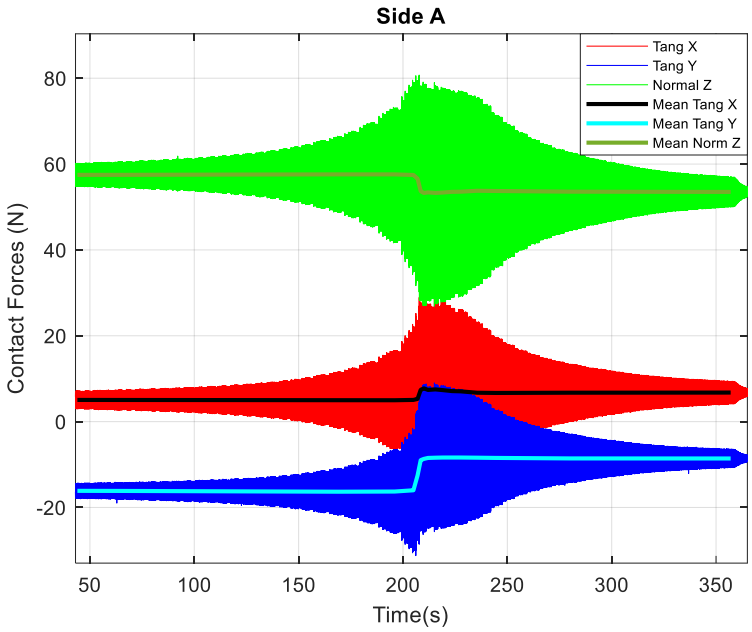

Figure 57: Variation in static contact forces at Side B during test run 6 for case 1 (F_E=2N)

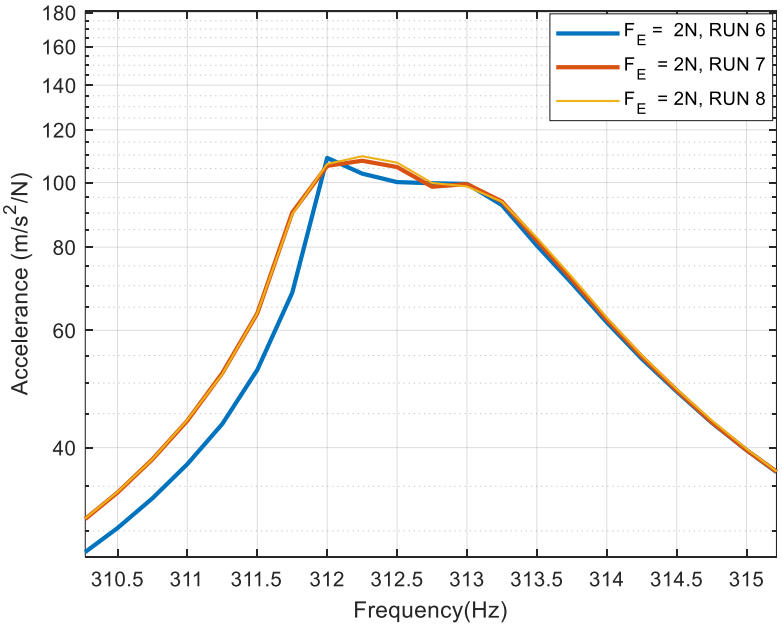

Figure 58: FRFs of test runs 6, 7, and 8 for Case 1 when F_E=2N

6.3.2 Variation of excitation forces in descending order

To observe the effect of the order (ascending/descending) in which excitation force was applied, a similar test campaign was done by implementing a descending order where the excitation force levels were decreased in the subsequent test runs. Figure 59 displays the variation of the static contact forces for this test campaign with descending excitation force levels. Overall, the results repeat the variation and stabilization trend observed previously in case of ascending excitation forces except that the maximum change in the static contact forces in this test campaign occurred for the first run with the maximum excitation force level of 7N.

6.3.3 Inference

It can be stated that due to the nonlinearity of the shroud contacts at the end of each run during which the nonlinear phenomena occurs, new and non-controllable static conditions are established and measured. The change in the static normal load on both the sides is because of the settling of the contact as the excitation force level is changed. For ascending or descending excitation force sequence, each level of excitation force displaces the contact from its initial position only in the first runs until a specific point as the contact is stabilized and static contact forces remain constant for the subsequent runs of the same excitation force. The following excitation force level is able to displace the contact interface further from that point to the next point where the contact stabilizes for that excitation force level. Considering that the test campaign resulted in around 2 million cycles, the level of wear that the contact surfaces went through is expected to be low as observed in a study investigating friction wear using a similar material [55]. The observation implies that in order to reliably compare the experimental and numerical results, the actual value of static contact forces for a given frequency range should be considered in the non-linear solvers and if possible, a wear model must also be introduced into the numerical methods for a full simulation of the contact behavior for a very high number of cycles.

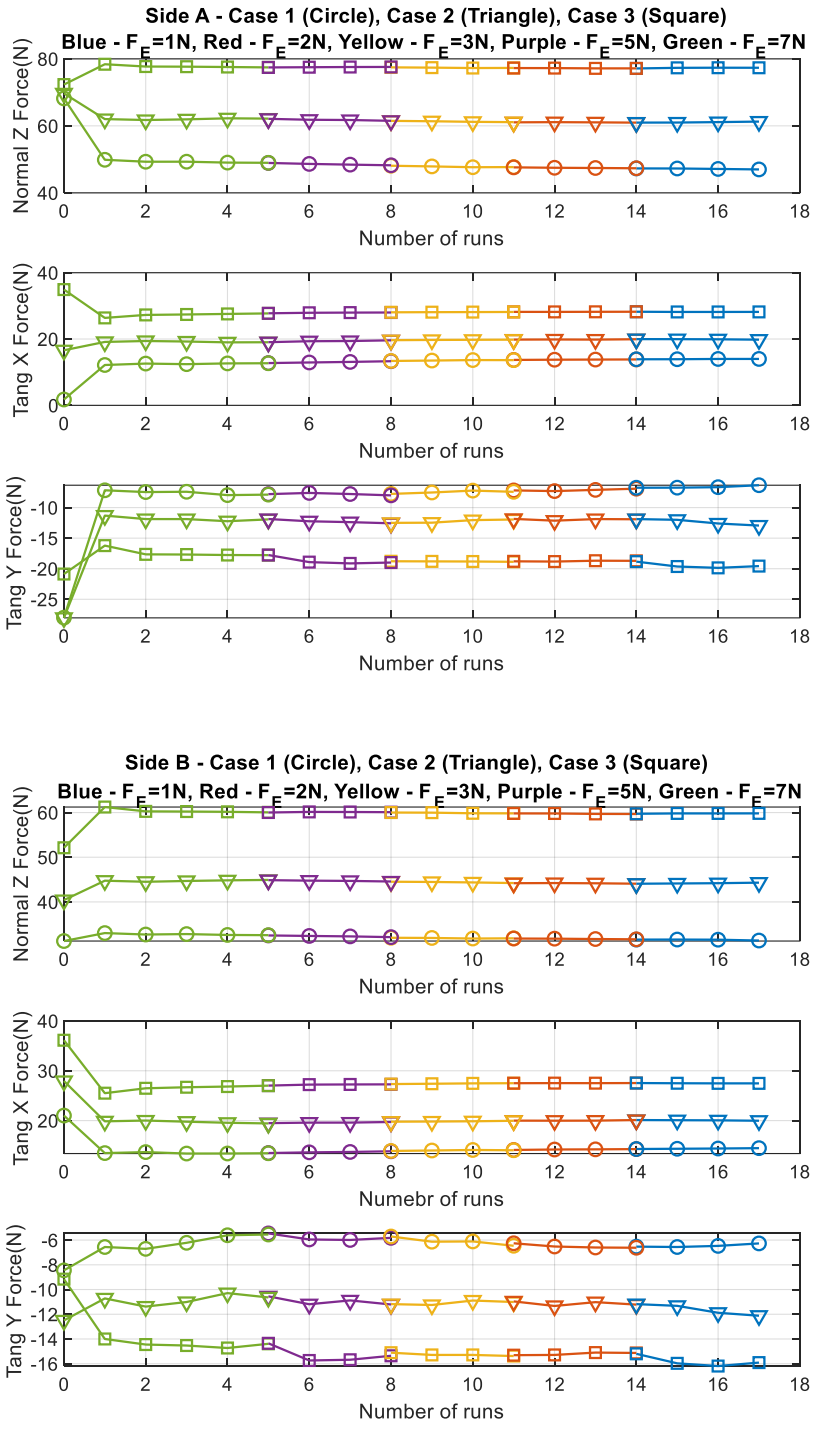

Figure 59: Variation of static contact forces for Case 1, Case 2 and Case 3 test runs with descending excitation force levels for Side A (above) and Side B (below)

6.4 Periodic contact forces

6.4.1 Effect of change in excitation forces

During the stepped sine testing of the shrouded blade, as the shroud contacts were engaged with the contact surfaces of the contact reference blocks, in addition to the forced response, 3D periodic contact forces were also measured. The measured periodic contact forces were decoupled using the decoupling matrix determined during the calibration. For Case 1 at the excitation frequency of 312 Hz, the 3D shroud contact forces are shown in Figure 60 (Side A) and Figure 61 (Side B) for different excitation force levels. The increase in the excitation force levels increase the tendency of the shroud contacts to go from stick to slip condition, which results in the increase of nonlinearity at contact surfaces depicted by the multi-harmonic behavior of the periodic contact forces at larger excitation force levels. The difference of the normal preload between the two shroud sides i.e., higher at Side A than at Side B is the reason for more nonlinear behavior observed at Side B as compared to Side A. Similar trend of nonlinear behavior can be observed in the bar chart (Figure 62) that displays the FFT of the time signals acquired at 312Hz for different excitation forces where multi-harmonic behavior is more pronounced for higher excitation forces.

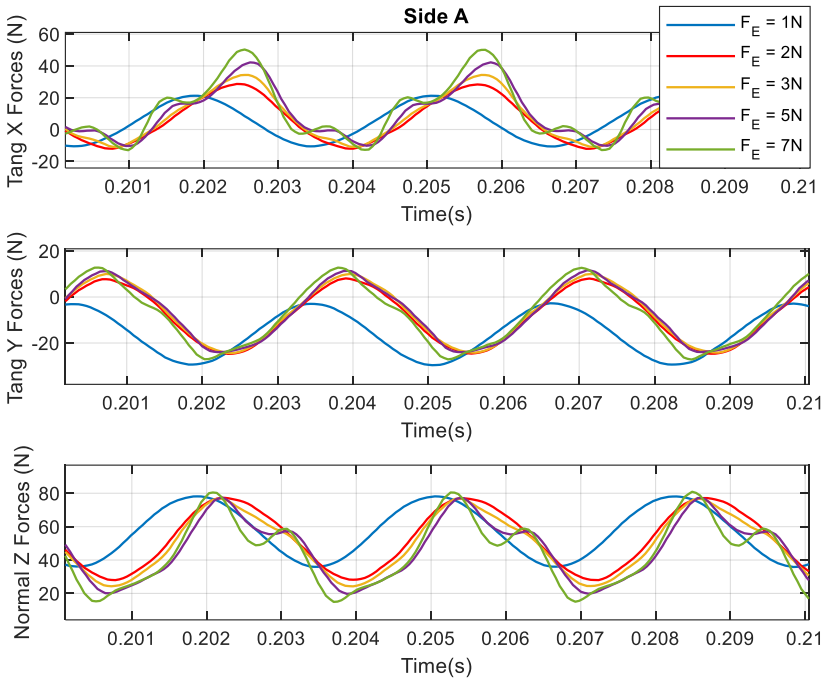

Figure 60: Periodic contact forces at shroud side A for Case 1 at 312 Hz

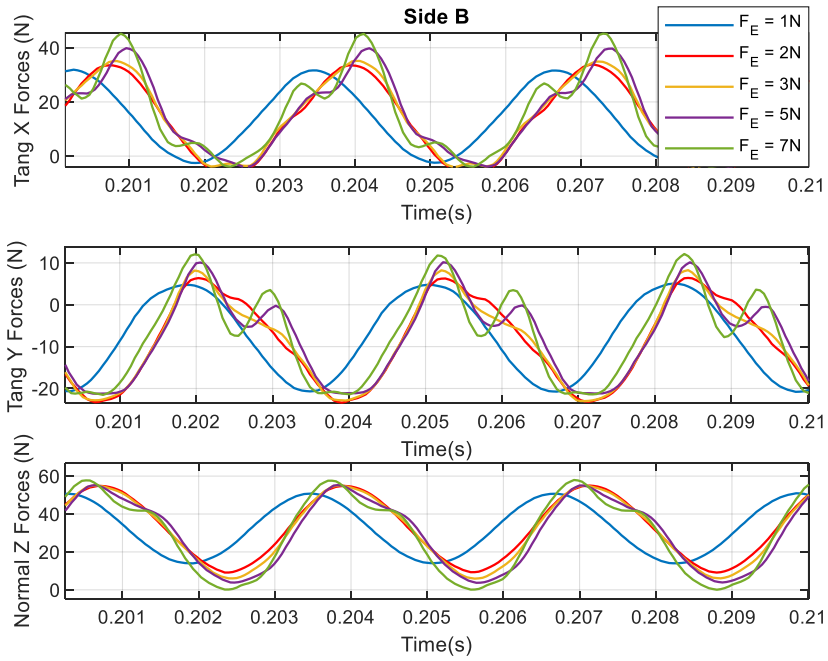

Figure 61: Periodic contact forces at shroud side B for Case 1 at 312 Hz

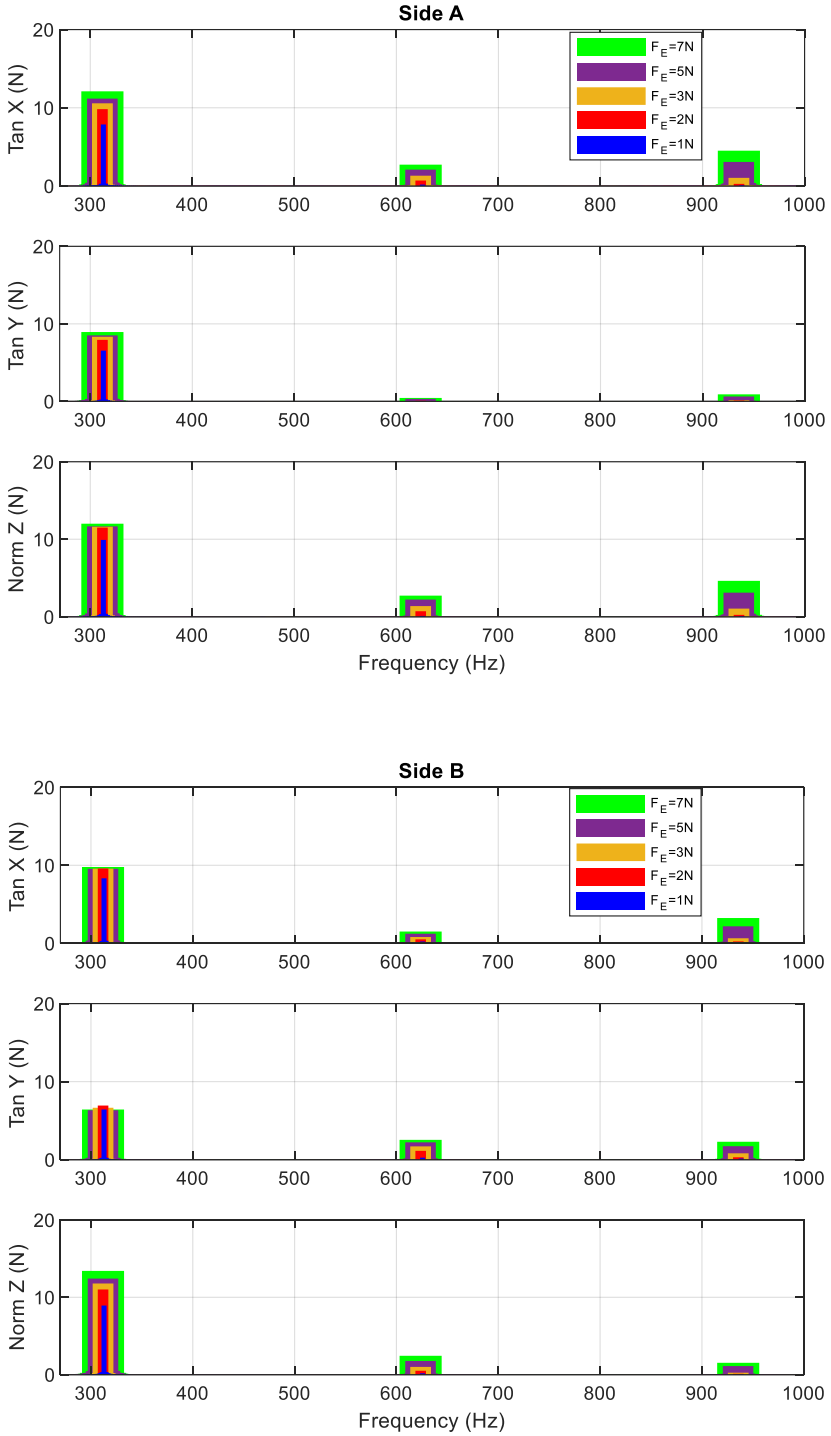

Figure 62: FFT of the measured contact forces at 312 Hz for different excitation forces

6.4.2 Effect of change in normal preload values

In order to observe the effect of normal preloads, the periodic contact forces of Case 1 were compared with those of Case 2 at resonance frequency of 312 Hz when excitation force was 5N. For increasing normal preload as we move from Case 1 (Figure 63) to Case 2 (Figure 64), there is a decrease in the nonlinearity observed in the behavior of the periodic contact forces during the stepped sine test run.

Lower normal preloads increase the likelihood of gross slip whereas higher normal preloads mean more resistance to slipping at contact interface and retaining linear stick condition. Moreover, plotting the modulus of tangential contact forces show us that for both the shroud sides, the actual magnitude of the tangential contact force depends on both the X and Y components of the tangential forces and neither of them can be ignored or be considered negligible.

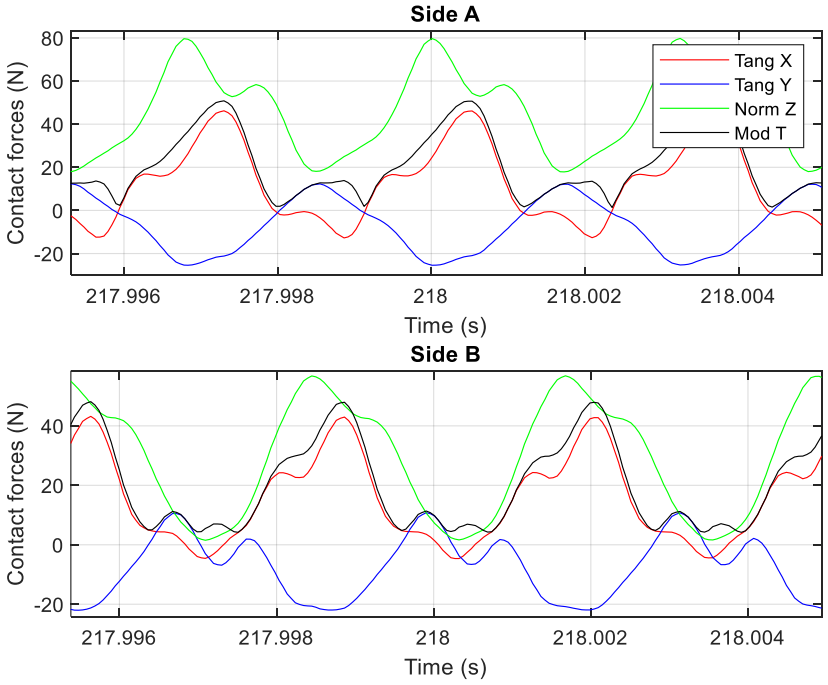

Figure 63: Periodic contact forces at shroud side A and B for Case 1 at 312 Hz (F_E = 5N)

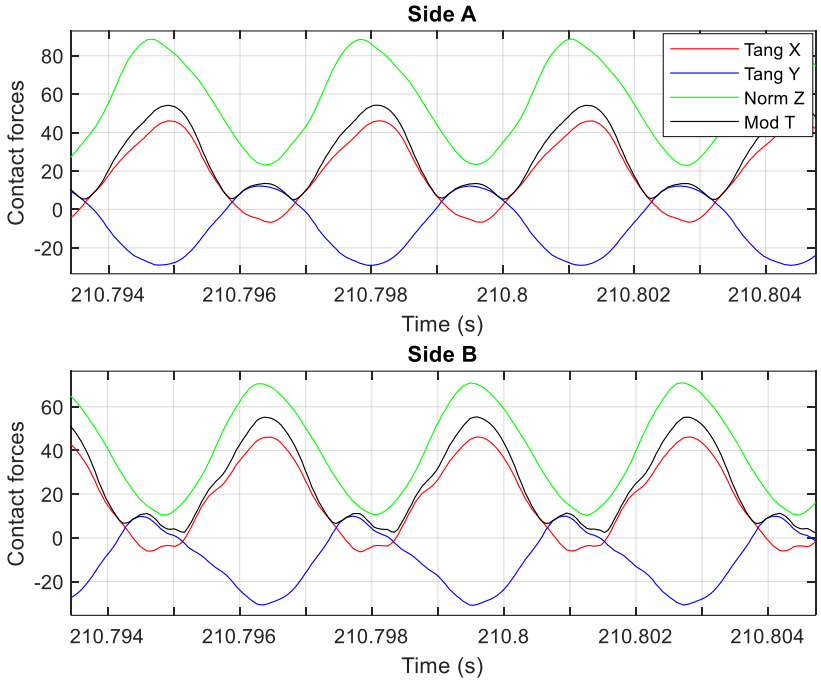

Figure 64: Periodic contact forces at shroud side A and B for Case 2 at 312 Hz (F_E = 5N)

6.4.3 Correlation of forced response and periodic contact forces

Correlation of the time domain data of periodic contact forces with the frequency domain data of the forced response acquired during each run was done using as reference, the time data of the excitation force that was acquired in both the data acquisition systems. Figure 65 displays run 14 of Case 1, the excitation force (F_E) being 5N where an increase in the dynamic component of the contact forces can be observed near the resonance frequency. A sudden increase or a jump in the response and amplitude of contact forces happen around 310 Hz, when the system moves into highly nonlinear regime.

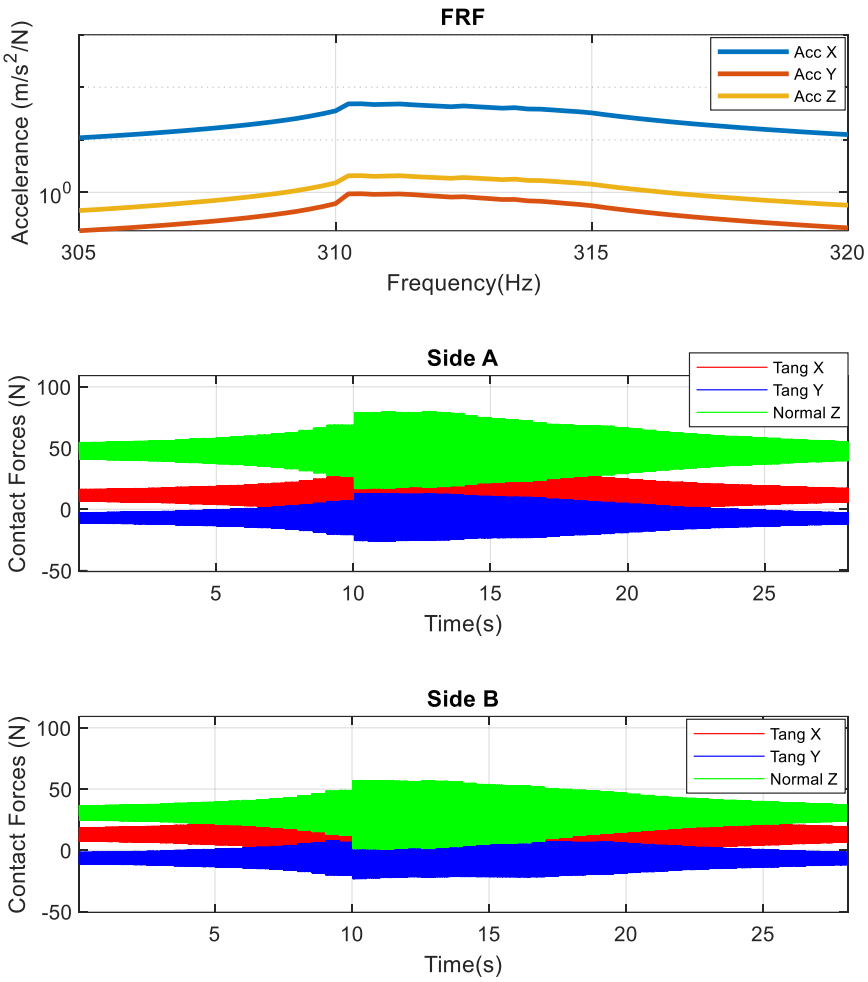

Figure 65: 3D periodic shroud contact forces acquired during stepped sine testing (Case 1, F_E = 5N)

Furthermore, investigation of the periodic contact forces at selected excitation frequencies shows linear and harmonic behavior of the contact forces at 308Hz before resonance and 316 Hz after the resonance, whereas at 311.5 Hz i.e. near the resonance frequency, non-linear and multi-harmonic behavior of the contact forces was observed (Figure 66).

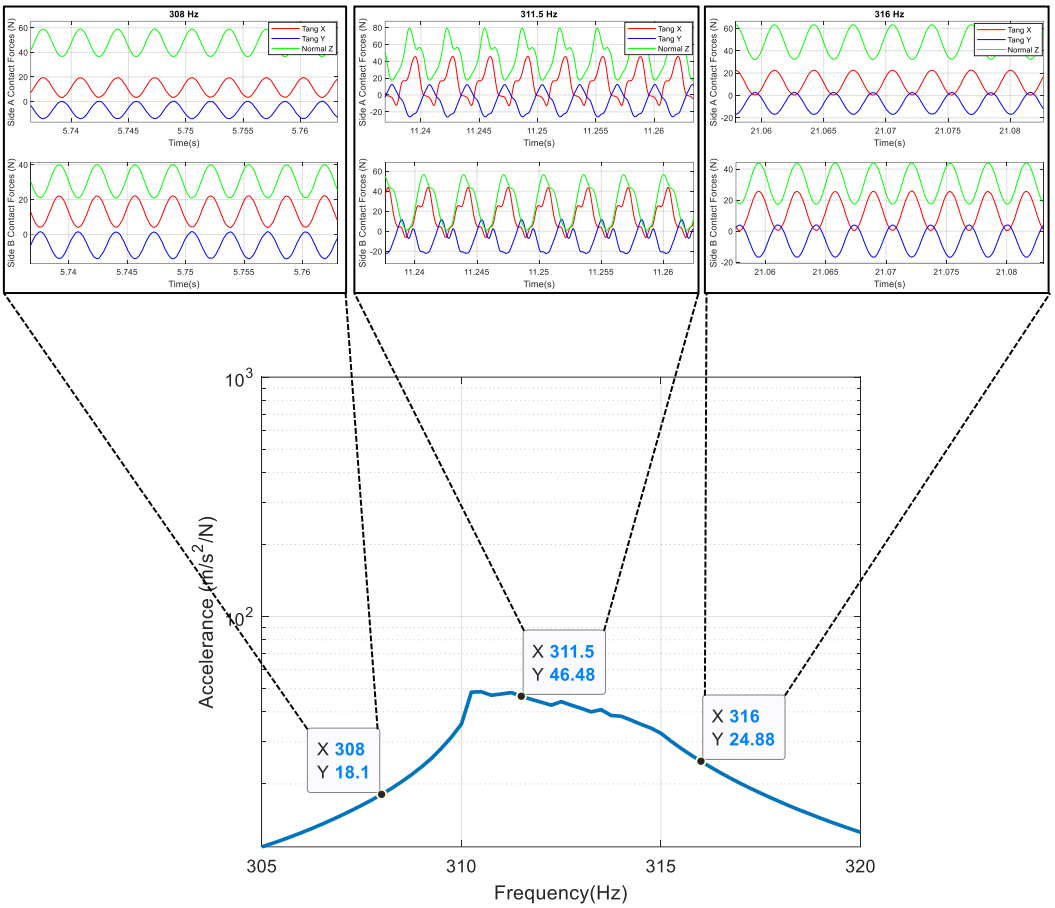

Figure 66: Periodic contact forces at different excitation frequencies during the sine sweep run for Case 1 (F_E=5N)

The observed nonlinear behavior of the periodic contact forces at resonance frequencies can be explained with respect to the first bending mode of the engaged shrouded blade being investigated. The increase in the vibration amplitude of shrouded blade at resonance tends to increase the relative displacement at the contact surfaces, which seem to undergo slip especially at lower normal preloads as in Case 1. As seen in Figure 63, the flat portions of the tangential contact forces in the X and Y directions indicate nearly constant friction force during the slip that takes place at different instants. Moreover, in Figure 66, at resonance frequency, for Side B, the minimum normal preload values that almost reach zero value coincide with the minimum value of the tangential contact forces indicating the possibility of partial separation or partial lift-off of the contact.

6.4.4 Upsweep vs downsweep

The results discussed above were obtained from experiments that involved upsweep sine runs with excitation frequencies increasing from 305-320 Hz to observe the behavior of the 3D shroud contact forces during the forced vibration testing. In order to understand the effects of frequency down sweep, test runs were also performed with decreasing excitation frequencies from 320-305 Hz. Normal preloads similar to Case 1 and Case 2 were set initially followed by the down sweep runs where forced response and contact forces were measured simultaneously. Finally, a comparative study was done to understand the difference in the behavior of shroud contact forces at different instances during the test runs. For excitation force of 5N, it was observed in the down sweep run for Case 1 (Figure 67) that the jump frequency was lower than the jump frequency of the upsweep test run. For Case 2 (Figure 68) i.e. with higher normal preload than Case 1, this difference was not significant.

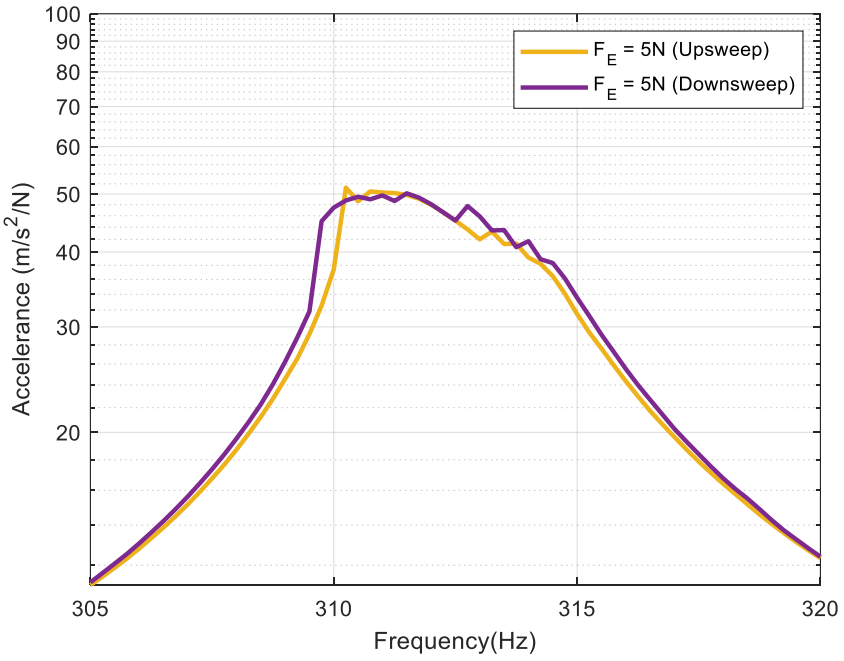

Figure 67: FRF (Upsweep vs Downsweep) for Case 1

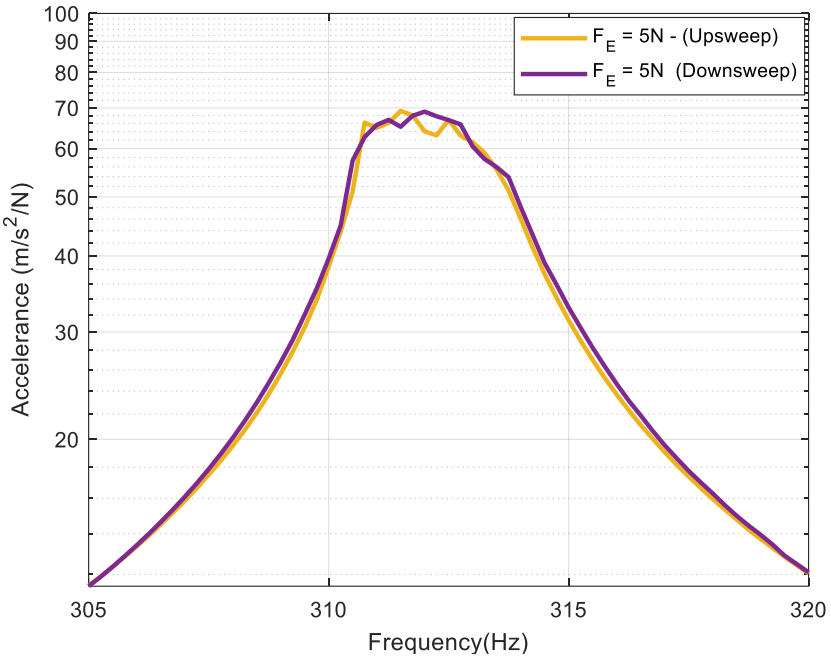

Figure 68: FRF (Upsweep vs Downsweep) for Case 2

The difference observed in Figure 67 for Case 1 at jump frequency was correlated with the periodic contact forces measured at 310 Hz. At 310Hz, the behavior of the periodic contact forces was linear for the upsweep test run and nonlinear for the down sweep test run (Figure 69).

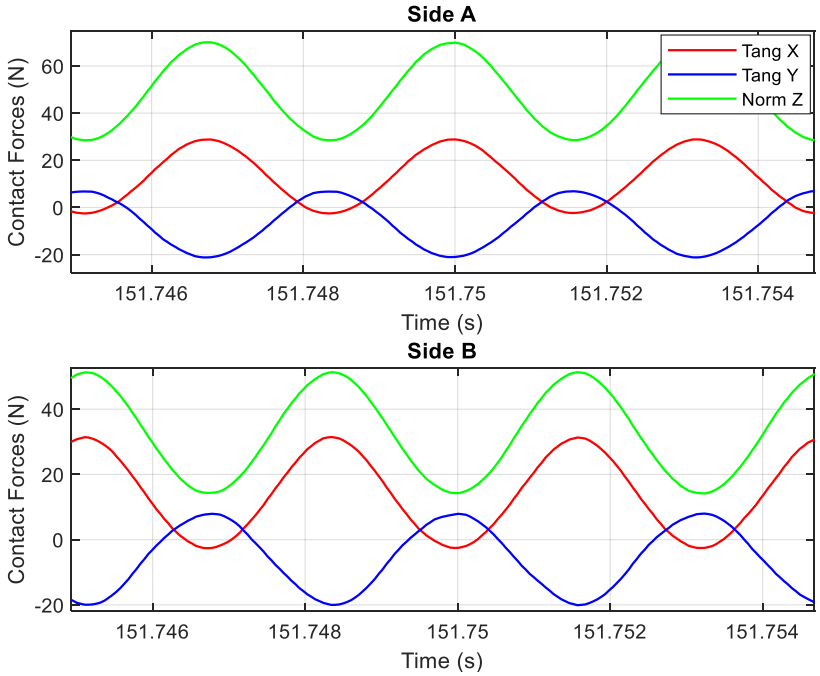

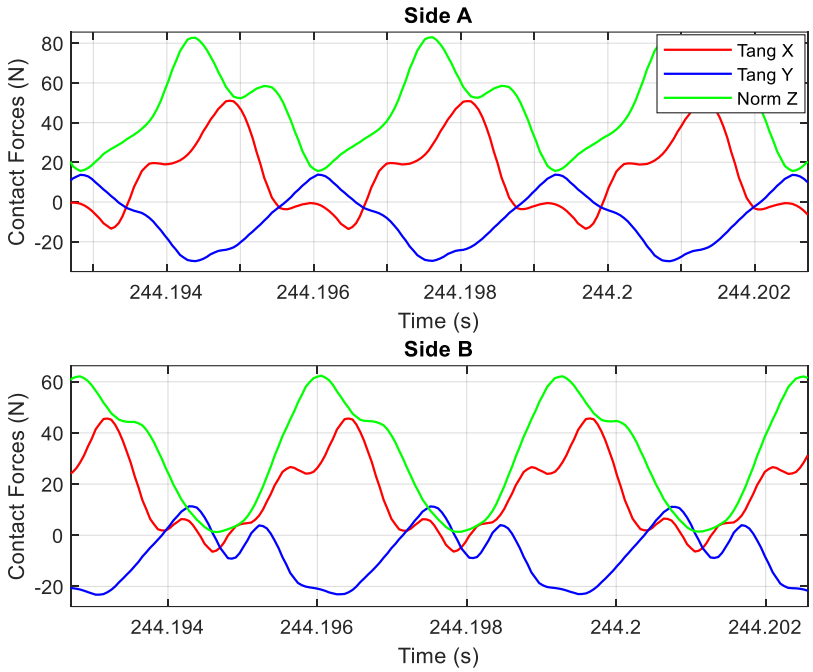

Figure 69: Periodic contact forces - Case 1 at 310 Hz for upsweep (above) and down sweep (below) for F_E = 5N

These observations were further investigated by analyzing the controlled excitation force during the upsweep and down sweep runs for both the cases. As stated in Section 5.7.2, the controller achieves the required excitation force levels to within ±5% of the nominal excitation force level. For both the cases i.e. Case 1 and Case 2, as shown in Figure 70, the difference in the excitation force level at resonance frequencies during upsweep and down sweep amounts to maximum of 6% which results in the small difference observed in the FRF curves in the nonlinear region. However, at 310 Hz, the difference of jump frequency between the upsweep and down sweep runs for Case 1 with lower normal preload can be associated to the stick-slip transition that is occurring at the contact interface. Therefore, the results indicate that for lower normal preloads, multiple solutions exist in certain frequency range. And as expected in case of softening nonlinearities friction contact, the jump frequency during the upsweep is higher than the jump frequency during the down sweep.

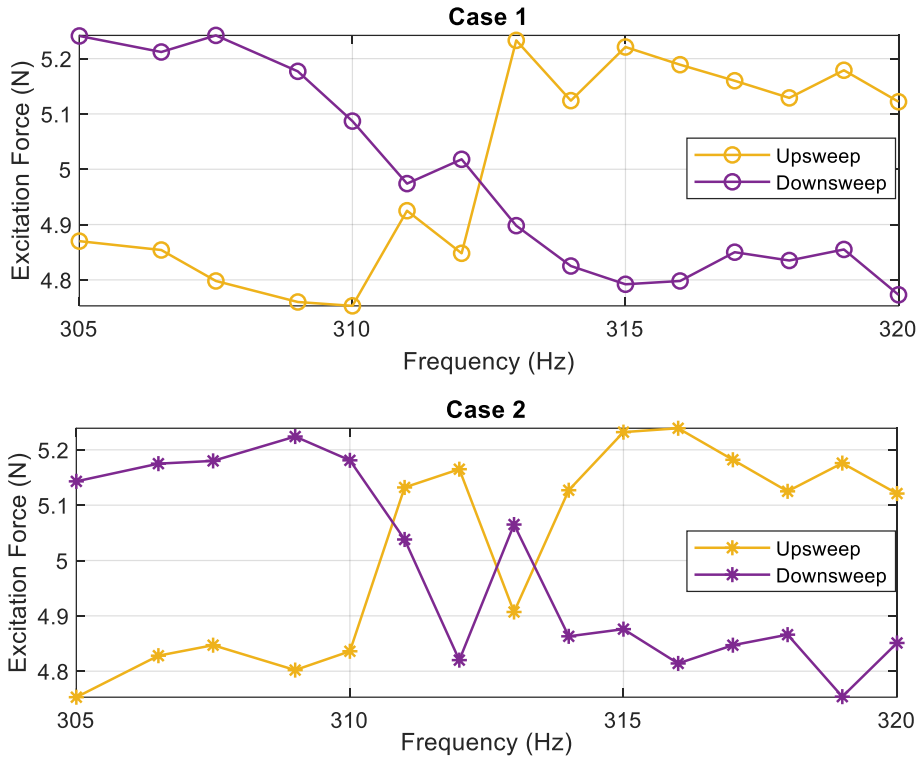

Figure 70: Excitation force level recorded during upsweep and downsweep runs for Case 1 and Case 2

NOTE: Part of the work described in this chapter has been previously published in:

Ahmed, R., Firrone, C. M., and Zucca, S., 2022, "Experimental investigation of three-dimensional shroud contact forces in forced vibration testing of a shrouded blade," Proc. ASME Turbo Expo 2022

Ahmed, R., Firrone, C. M., and Zucca, S., 2022, "A novel test rig to investigate shroud contact forces of turbine blades", Mechanical Systems and Signal Processing 2022 (Submitted)

Chapter 7

Numerical modeling of friction contacts in shrouded blade

7.1 Introduction

In the previous chapter, the experimental results obtained from the experimental campaign using the novel test rig were presented and the effect of the normal preloads and the excitation force levels on the dynamic response of the shrouded blade and the 3D shroud contact forces were discussed. The next step was to use the obtained experimental results to validate the contact model in nonlinear solver that is used to predict and compute the nonlinear forced response as well as the 3D shroud contact forces. For this purpose, the FE model of the test rig was used for the nonlinear solver with the objective to simulate the actual test conditions in order to predict the dynamic response of the engaged shrouded blade and shroud contact forces. A general overview of the contact models and their implementation was presented in Section 1.1.3. In this chapter, the Harmonic Balance Method is described as applied with the coupled static-dynamic approach to the shrouded blade dynamics involving 2D tangential relative displacement with variable normal load contact model. Subsequently, the input parameters for the nonlinear solver and the numerical prediction procedure are described followed by the comparison of the numerical and experimental results.

7.2 FE model for nonlinear forced response calculation

For the computation of nonlinear forced response of shrouded blade, an FE model shown in Figure 71, of the mockup shrouded blade installed in the test rig will be used by the nonlinear solver. In the FE model, the shroud contacts and the contact pads of both the shroud sides A and B were discretized with 15 contact nodes each (3 rows and 5 columns). For each node pair, the local coordinate system was rotated by 45 degrees since the shroud engages the contact pad at the shroud angle of 45 degrees with respect to the global coordinate system.

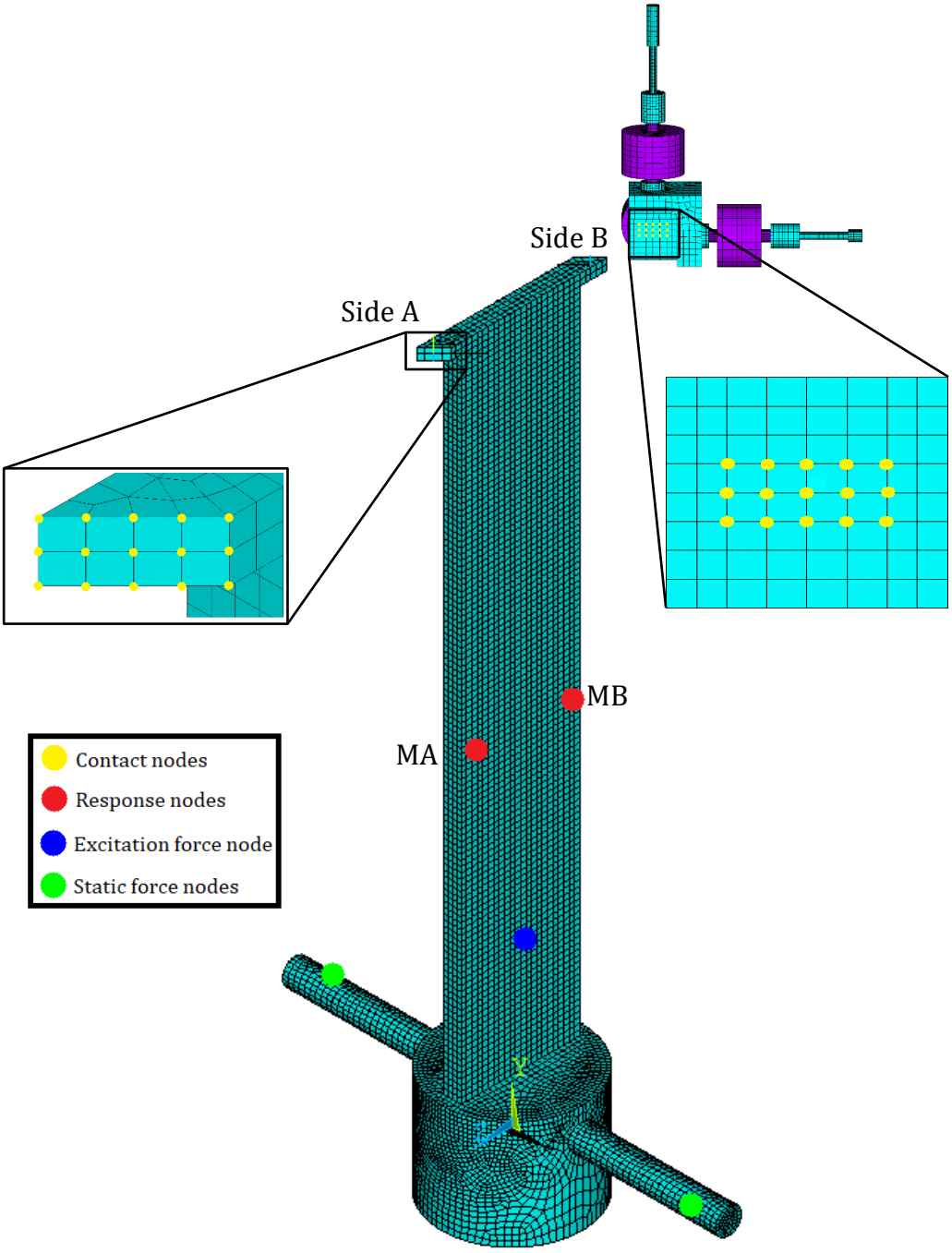

Figure 71: FE model for nonlinear forced response calculation

Figure 71 also shows the specified response output nodes and the input nodes i.e. the excitation force node and the static force node. The response nodes were specified at the blade edges halfway along the length of the blade where the

accelerometers were attached and the excitation node was specified at the point where the shaker was attached through the stinger.

7.3 Harmonic Balance Method

Harmonic Balance Method (HBM) is a numerical technique used in frequency domain to obtain solution of nonlinear ordinary differential equations by changing them into frequency domain nonlinear algebraic equations denoting the forces and displacements as truncated Fourier series. Classical HBM considers single harmonic whereas in case of friction contacts involving nonlinearities, additional harmonics are taken into account making it Multi Harmonic Balance Method (MHBM).

To compute the forced response of a mechanical system with friction contacts and to calculate the corresponding contact forces, the first step is to develop an FE model with the following governing equation of motion:

$$M\ddot{Q} + C\dot{Q} + KQ = F_E + F_{contact}(Q, \dot{Q}) \tag{7.1}$$

where M is the mass matrix, C is the damping matrix, K is the stiffness matrix, Q is the nodal displacement vector that includes the displacement of contact nodes, input and output nodes and $\dot{Q}$ being the derivative of Q, F_E is the periodic excitation force vector and $F_{contact}$ is the nonlinear contact force vector, produced at the contact interface due to the relative displacements of the contact nodes.

Prior to the computation of the nonlinear solution, the size of the nonlinear model is usually reduced. Considering the fine discretization of the FE models to achieve accuracy, reduced order modeling can be applied to reduce the size of the system dynamically. In this study, the classical Craig-Bampton Component Mode Synthesis [56] (CB-CMS) reduction method was utilized and the DOFs at the contact nodes, input/output nodes were retained as master nodes, and the number of fixed interface modes were specified.

In HBM, for periodic external excitation with excitation frequency ω, the periodic displacements and periodic nonlinear contact forces at steady state can be expressed as truncated series of harmonic terms as following:

$$Q = Q^{(0)} + \boldsymbol{Re}\left(\sum_{h=1}^{nH} Q^{(h)}.\, e^{i.h.\omega.t}\right) \tag{7.2}$$

$$F_E = F_E{}^{(0)} + \boldsymbol{Re}\left(\sum_{h=1}^{nH} F_E^{(h)}.e^{i.h.\omega.t}\right) \tag{7.3}$$

$$F_{contact} = F_{contact}^{(0)} + \boldsymbol{Re}\left(\sum_{h=1}^{nH} F_{contact}^{(h)}.e^{i.h.\omega.t}\right) \tag{7.4}$$

Where nH represents the number of harmonics and $\boldsymbol{Re}$ denotes the real part of the term. Substituting the terms into equation 7.1, algebraic complex equations are obtained as

$$D^{(h)}.Q^{(h)} = F_E^{(h)} + F_{contact}^{(h)} \;;\; h = 0..nH \tag{7.5}$$

Where $D^{(h)} = -(h\omega)^2 m + ih\omega c + k$ is the h^{th} dynamic stiffness matrix of the system and h = 0 corresponds to the zeroth order i.e. the static balance equation. The equation contains both the static and dynamic components of the system coupled with each other through coefficients of the nonlinear contact force. The specification of the number of harmonics nH is defined to achieve reasonable accuracy while approximating the dynamics of the system.

As the nonlinear contact forces $F_{contact}$ are dependent only on the relative displacement of contact nodes which are usually much less than the number of total nodes, the balance equations are rearranged to decouple the linear and nonlinear parts of the system for simplicity. For this purpose, the inverse of $D^{(h)}$ matrix i.e. the $R^{(h)}$ receptance matrix is computed to write the balance equations in the form of receptance.

$$Q^{(h)} = Q_E^{(h)} + R^{(h)}.F_{contact}^{(h)} \tag{7.6}$$

where $Q_E^{(h)} = R^{(h)}.F_E^{(h)}$ and indicates the linear response because of the excitation force whereas the other terms imply the role of the nonlinear contact forces. Subsequent splitting of $Q^{(h)}$ into the nonlinear $Q_{NL}^{(h)}$ and linear $Q_L^{(h)}$ dofs produce

$$\begin{Bmatrix} Q_{NL}^{(h)} \\ Q_L^{(h)} \end{Bmatrix} = \begin{Bmatrix} Q_{E,NL}^{(h)} \\ Q_{E,L}^{(h)} \end{Bmatrix} + \begin{bmatrix} R_{NL,NL}^{(h)} & R_{NL,L}^{(h)} \\ R_{L,NL}^{(h)} & R_{L,L}^{(h)} \end{bmatrix}.\begin{Bmatrix} F_{contact}^{(h)} \\ 0 \end{Bmatrix} \tag{7.7}$$

As observed, the nonlinear contact forces $F_{contact}^{(h)}$ are dependent only on the nonlinear dofs $Q_{NL}^{(h)}$, which allows to iteratively solve the nonlinear part of the

equation with a nonlinear solver and when the nonlinear contact forces $F_{contact}^{(h)}$ are known, the linear dofs $Q_L^{(h)}$ can be obtained respectively. However, for the solution of the nonlinear balance equation, a contact model is needed for the computation of the harmonic components of periodic nonlinear contact forces $F_{contact}^{(h)}$ from the given harmonic components of nonlinear nodal displacements $Q_{NL}^{(h)}$.

7.4 Contact Model

As discussed in Section 1.1.3, literature review has shown that several contact models have been implemented in numerical solvers for the computation of the forced response of systems with friction contacts and the respective periodic contact forces. In this study, contact model with 2D tangential displacement and variable normal load was implemented considering the scope of the developed experimental test rig. As shown in Figure 72, the contact element at each contact node pair is represented by three linear springs i.e. in the two orthogonal tangential directions in the (x-y) contact plane with two tangential contact stiffness (k_{tx} and k_{ty}) and in one normal direction out of the contact plane with normal contact stiffness (k_n).

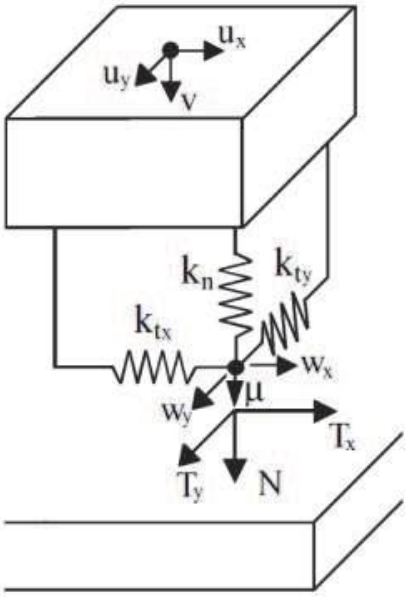

Figure 72: Contact element with 2D tangential displacement and variable normal load [20]

For every vibration cycle, the contact interface comprising of several contact node pairs can simulate three possibilities of contact condition i.e. stick, slip

and lift-off (separation). Friction coefficient μ between the contact surfaces is assumed and the varying static normal load holding the surfaces in contact with each other can be expressed as

$$N(t) = \max(N_0 + k_n.v(t),0) \tag{7.8}$$

For every contact element, the tangential $(T_x(t), T_y(t))$ and normal $N(t)$ contact forces rely on the relative tangential displacements $(u_x(t),u_y(t))$ and normal displacements $(v(t))$ of the respective node pair. Tangential slip $w(t)$ between the contact surfaces in the contact plane is defined as $(w_x(t);\ w_y(t))$ when the tangential contact forces exceed the Coulomb limit $\mu N(t)$.

In stick mode, the contact behaves elastically, slip does not occur and the tangential contact forces are equal to

$$\begin{Bmatrix} T_x \\ T_y \end{Bmatrix} = \begin{bmatrix} k_{tx} & 0 \\ 0 & k_{ty} \end{bmatrix} . \left(\begin{Bmatrix} u_x \\ u_y \end{Bmatrix} - \begin{Bmatrix} w_x \\ w_y \end{Bmatrix} \right) ;\ \begin{Bmatrix} w_x \\ w_y \end{Bmatrix} = \begin{Bmatrix} 0 \\ 0 \end{Bmatrix} \ and\ N \geq 0 \tag{7.9}$$

In slip mode, the modulus of the tangential contact forces equals the Coulomb limit whose direction is parallel to the velocity of tangential slip $\dot{w}$.

$$\begin{Bmatrix} T_x \\ T_y \end{Bmatrix} = \frac{\mu N}{\|\dot{w}\|} . \begin{Bmatrix} \dot{w}_x \\ \dot{w}_y \end{Bmatrix} ;\ \|\dot{w}\| = \sqrt{\dot{w}_x^2 + \dot{w}_y^2} \tag{7.10}$$

In case of lift off or separation of the contact, there are no normal and tangential contact forces acting so in this condition, both are equivalent to zero.

The evaluation of the tangential contact forces $(T_x(t), T_y(t))$ is based on predictor corrector procedure [12] that checks and satisfies the Coulomb's friction law at each time step t. Initially, a full stick condition is assumed with tangential contact forces being zero. If contact condition is separation i.e. the normal load is zero, the tangential contact forces remain zero, otherwise it must be checked whether the contact is in stick or slip state. The tangential contact forces are predicted and computed at t^{th} time step by

$$T_x^p(t) = k_{tx}\big(u_x(t) - w_x(t)\big) = k_{tx}\big(u_x(t) - w_x(t - \Delta t)\big) \tag{7.11}$$

$$T_y^p(t) = k_{ty}\left(u_y(t) - w_y(t)\right) = k_{ty}\left(u_y(t) - w_y(t - \Delta t)\right) \tag{7.12}$$

For a stick state assumption and based on this prediction, the correction procedure will compute the tangential contact force $T^p(t) = \sqrt{T_x^p(t)^2 + T_y^p(t)^2}$ at the t^{th} time step by

$$T(t) = \begin{cases} T^p(t) & stick\ state \\ \mu N(t) sign\left(T^p(t)\right) & slip\ state \\ 0 & separation \end{cases} \tag{7.13}$$

Computation of nonlinear contact forces in frequency domain can be difficult. Review of the literature indicates that more accurate computation of nonlinear forces can be achieved in time domain whereas in case of vibration, efficient solutions can be obtained in frequency domain. Therefore, the implementation of the contact models is accomplished using Alternating Frequency Time (AFT) method in following stages:

1. Computation of the relative displacements at the contact nodes from the contact kinematics for the given Fourier coefficients of the displacement of contact nodes.
2. Computation of periodic relative displacements in the time domain by application of Inverse Fast Fourier Transform (IFFT) to the relative displacements computed in stage 1.
3. Computation of periodic nonlinear contact forces in the time domain using the constitutive laws of the contact model.
4. Computation of harmonic components of periodic nonlinear contact forces by application of Fast Fourier Transform (FFT) to the periodic nonlinear contact forces computed in stage 3.

For the iterative procedure to obtain the solution for the unknown displacements the Newton-Raphson method was used with MATLAB's built-in fsolve function and the Jacobian was calculated numerically with the Forward Finite Difference Method.

7.5 Input parameters for the simulation

The nonlinear solver developed for the computation of the nonlinear forced response and three-dimensional shroud contact forces was provided the inputs with respect to the designed experimental test rig and the mockup shrouded blade. In this regard, the first input i.e., the stiffness and mass matrices of the reduced order model

were obtained from ANSYS using the classical CB-CMS reduction method while retaining the DOFs at the contact nodes and input/output nodes as master nodes.

For a reliable comparison between the experimental and numerical results, it was important to consider two significant factors:

1. To model the initial contact condition like the actual shroud contact condition observed during the experiment.
2. To simulate the normal preload distribution between the two shroud sides A and B equivalent to the actual unsymmetrical normal preload distribution observed during the experiment after the application of the clamping force.

Regarding the first aspect of actual shroud contact condition, the investigation performed with the pressure measurement film to identify the actual contact condition was revisited (Figure 45) and the localized contact that occurred at the edges of the shroud was modeled. In order to do so, only one column of three contact node pairs for each shroud contact and contact pad at the respective edges were considered as the contact dofs in the simulation, as shown in Figure 73.

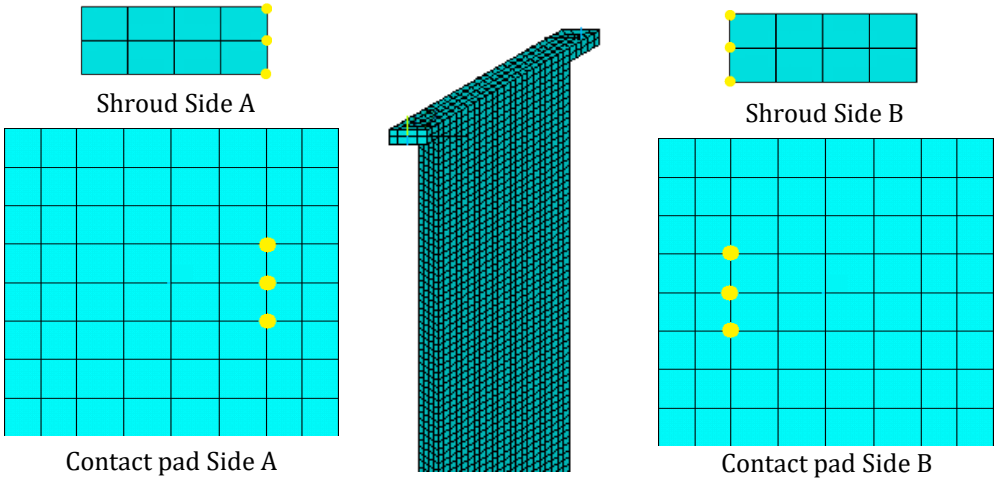

Figure 73: Contact dofs modeled in simulation

About the second factor that dealt with simulating the unsymmetrical normal preload distribution, a small gap of 0.25 - 0.3 mm was specified between the shroud contact and the contact pad at shroud side B. This resulted in the higher normal preload at Side A as compared to Side B, which is very similar to what was observed when clamping force was applied during the experiment. In this way, the nonlinear forced response and the nonlinear shroud contact forces will be computed using the same initial conditions that were observed during the experiment.

The damping ratio determined as 0.0014 by half-power bandwidth method was used for the simulation. Since the relative displacement between the shroud contacts was not measured during the experiments, the actual value of the contact stiffness and the friction coefficient cannot be determined. Therefore, the numerical simulation was performed with the estimated values of the contact stiffness and coefficient of friction. For the given contact conditions, the value of the contact stiffness was chosen in order to achieve the FRF of the linear full stick condition comparable to the actual FRF obtained during the experimental modal testing with engaged shrouded blade for the highest normal preload and lowest excitation force. Similarly, the value of friction coefficient was estimated as 0.8 by tuning the Coulomb limit for periodic tangential contact forces measured during the test campaign with the highest excitation force and lowest normal preload.

During the initial setting of the experiment, the static torque generated by the torque screw mechanism yields the static normal preload applied by the shroud contacts. Likewise, in the FE model, the two equal and opposite static forces applied on the ends of the torque pin that form the force couple system are also provided to the nonlinear solver as input.

7.6 Simulation results

Using the input parameters discussed in the previous section, numerical simulations were performed for different excitation force levels and different static force values. Figure 74 shows the nonlinear forced response computed by the nonlinear solver for different excitation force levels using single harmonic balance method for input static force of 12N. As expected, an increase in the amplitude of the excitation force results in a damped response due to an increase in the tendency of the contact interface to undergo gross slip.

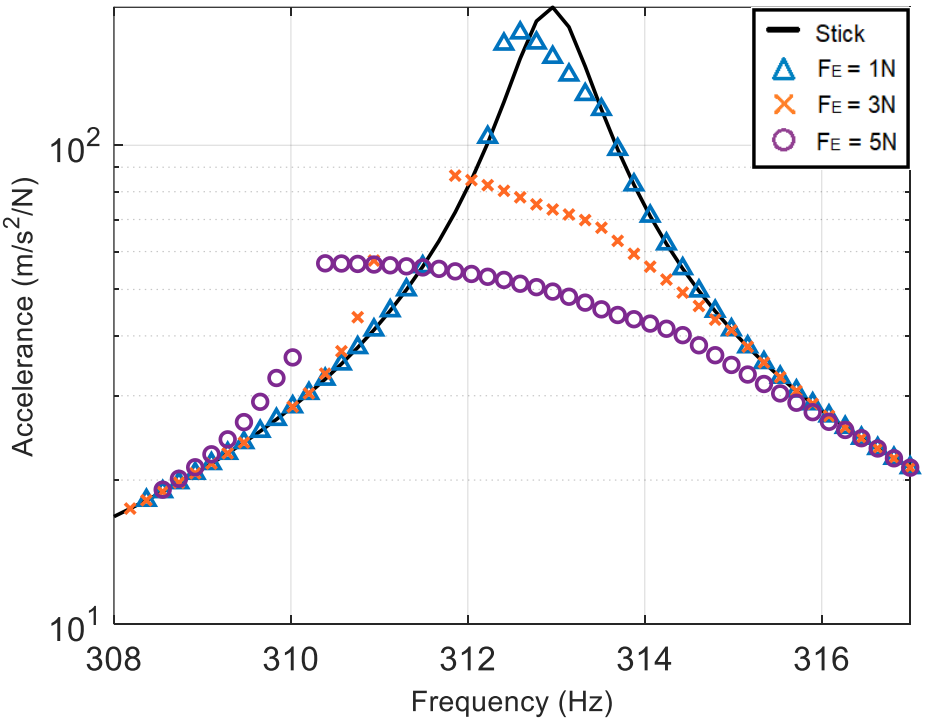

Figure 74: FRF computed for different excitation forces (St. F=12N)

Figure 75 displays the nonlinear forced response computed for different static forces applied to the torque pin and the excitation force equal to 5N. Increase in the static force values indicate an increase in the normal preload applied by the shroud contacts on the contact pads. Likewise, the increase in the normal preload had a stiffening effect on the contact interface resulting in higher response, which is also evident from the numerical results.

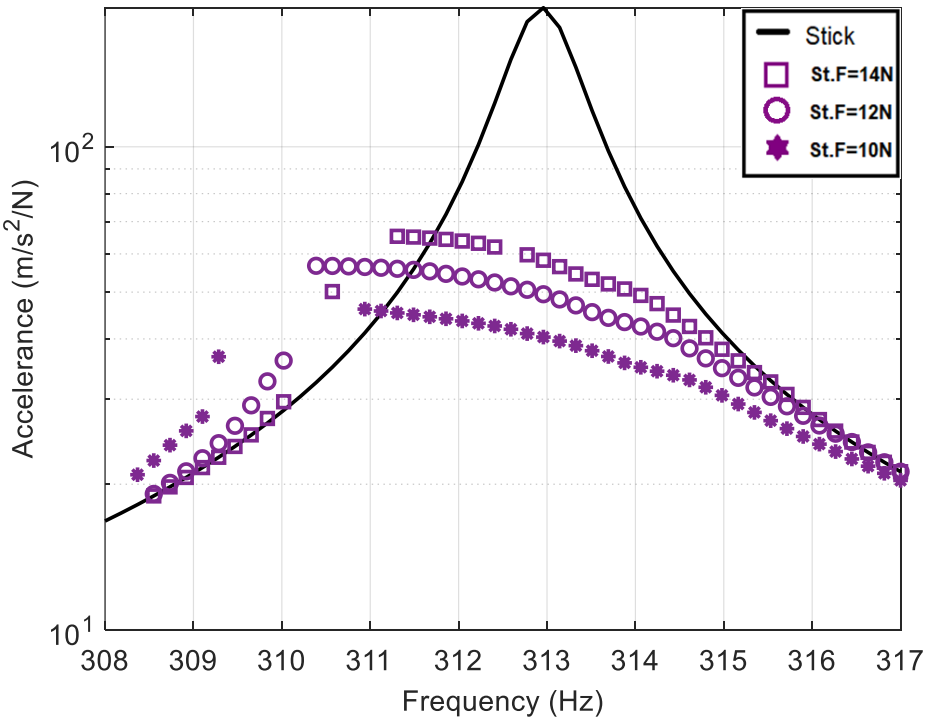

Figure 75: FRF computed for different static force values (FE=5N)

The variation of the static contact forces across the excitation frequency range was computed with the excitation force of 5N for three different static force levels implying three different normal preloads. It was observed, as seen in Figure 76, that for both the sides the maximum change occurred at the resonance as the contact is displaced when the system enters the nonlinear regime.

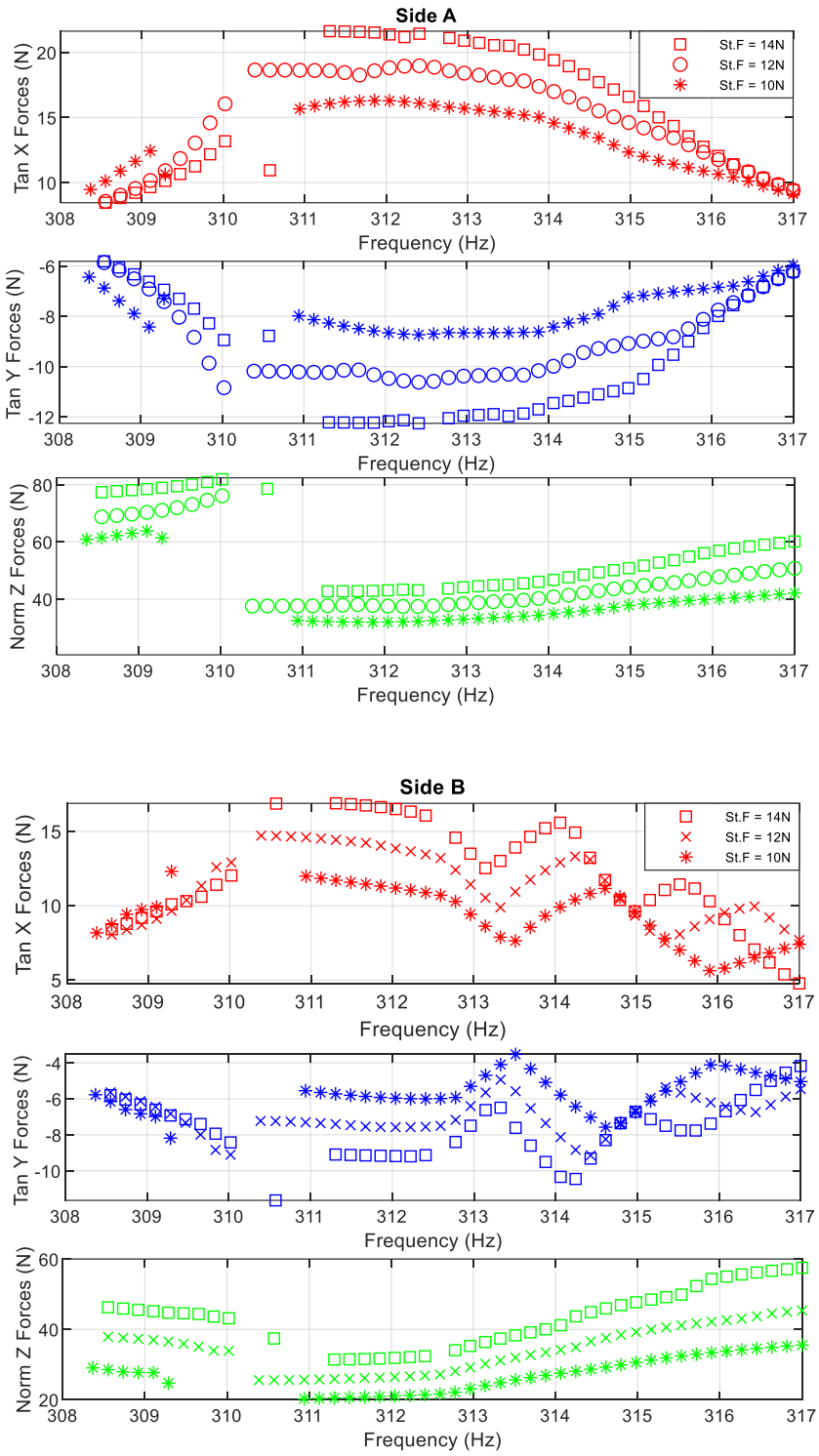

Figure 76: Variation of static contact forces for Side A (above) and Side B (below)

7.7 Comparison with experimental results

To predict and compute the nonlinear forced response and the shroud contact forces for the given initial conditions and input parameters, numerical simulations were performed for different excitation force values and static forces and the numerical results were compared with the experimental results. Figure 77 displays the nonlinear forced response computed by the nonlinear solver with excitation force of 3N and the static force of 12N for single harmonic (nH=1). The comparison with the experimental FRF of similar test conditions indicate a slight offset between the two curves.

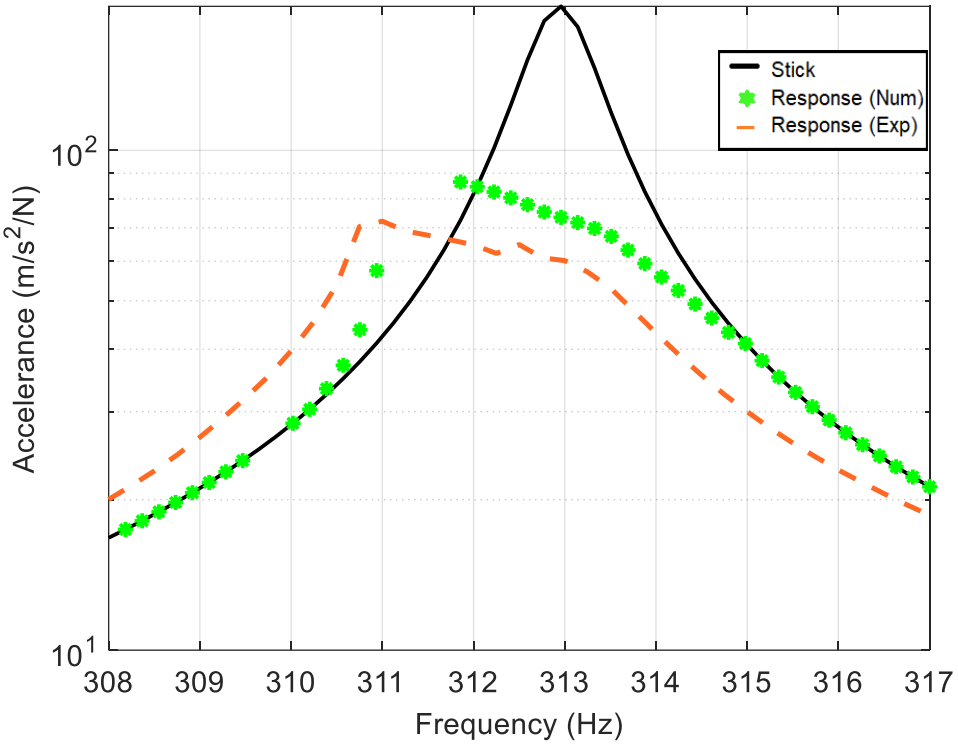

Figure 77: Comparison of numerical and experimental response (F_E=3N, nH=1)

On comparing the static contact forces at the converged points with those measured from the experiments in the resonance region (Figure 78), differences are minor except for the static normal contact force for Side B. This can be due to uncertainty in the gap introduced to achieve unsymmetrical normal preload distribution. Likewise, as displayed in Figure 79, the periodic contact forces obtained numerically were matched with the experimentally acquired periodic contact forces at 312 Hz and a good comparison was observed for both the sides A and B.

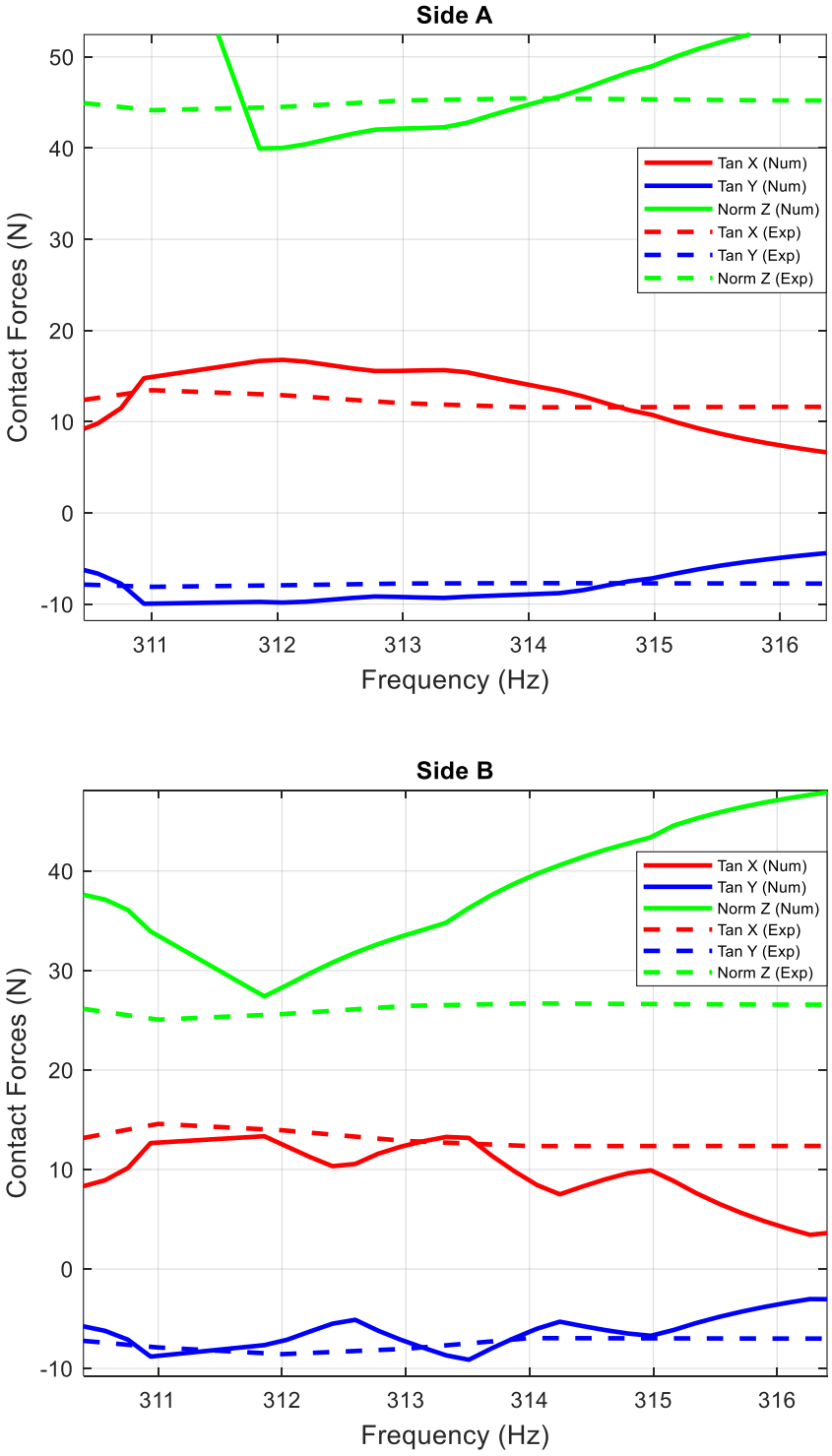

Figure 78: Comparison of static contact forces at Side A (above) and Side B (below) for numerical and experimental results (F_E=3N, nH=1)

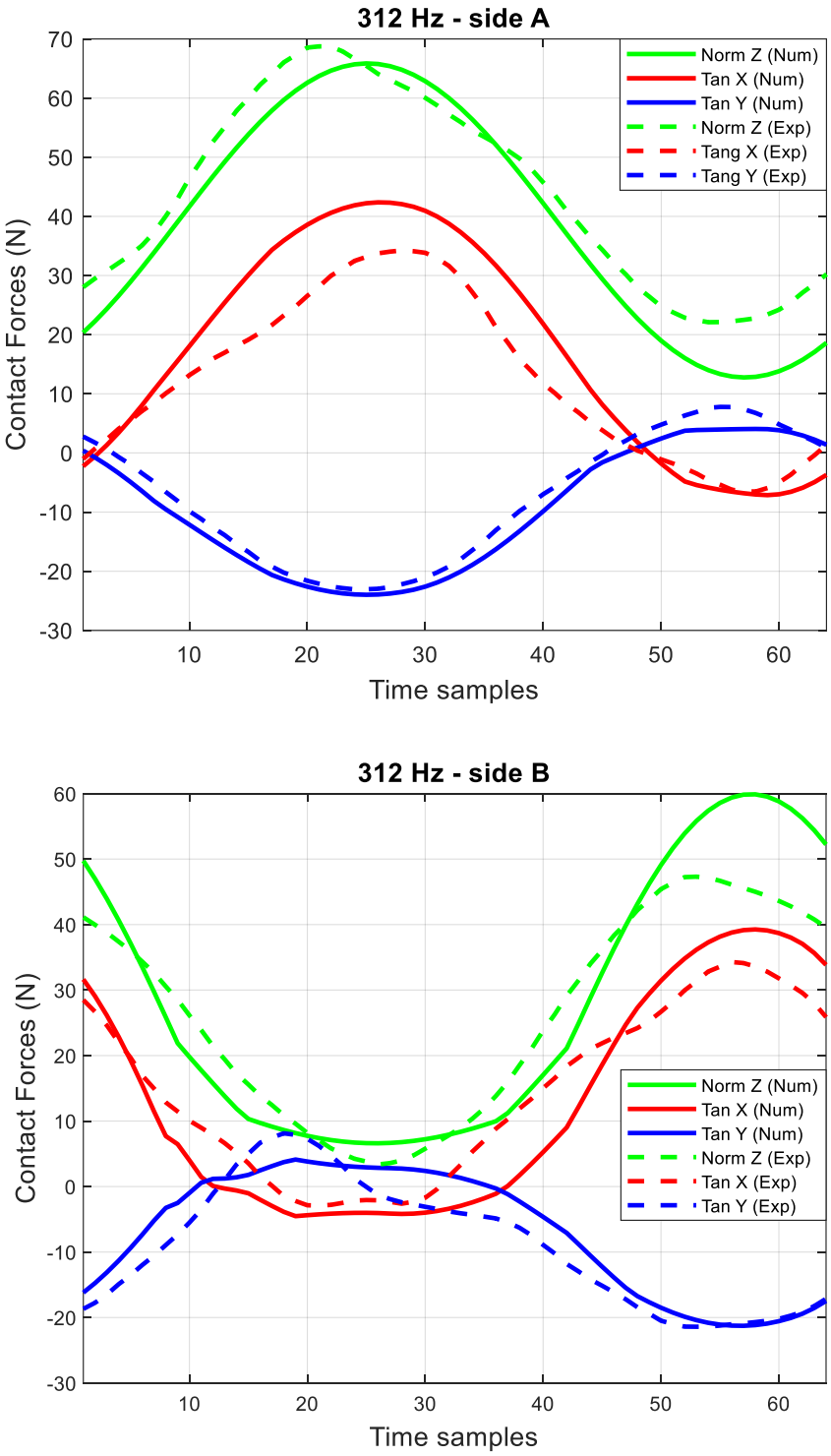

Figure 79: Comparison of periodic contact forces at Side A (above) and Side B (below) at 312 Hz (F_E=3N, nH=1)

For the same conditions i.e. the excitation force of 3N and the static force of 12N, the numerical simulation was also performed for three harmonics (nH=3). In this case, the FRF plot corresponding to the fundamental harmonic shown in Figure 80 displayed better matching with the experimental results.

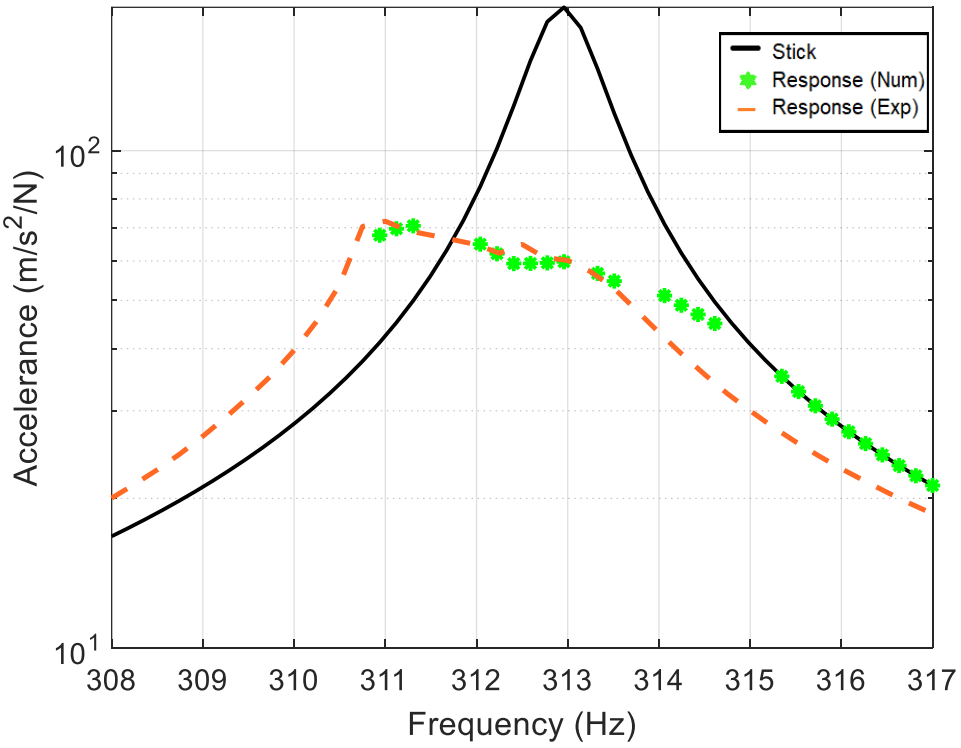

Figure 80: Comparison of numerical and experimental response (F_E=3N,nH=3)

As shown in Figure 81, comparison of the static contact forces at the converged points with the experimental static contact forces was reasonable except for normal static contact force for Side B where the same trend of difference was observed. Nevertheless, on comparing the numerically computed periodic contact forces for three harmonics with the experimentally measured periodic contact forces at 312 Hz, a better comparison with very good matching was observed for both the sides A and B as displayed in Figure 82. The results demonstrate that by increasing the number of harmonics, the accuracy of the numerical simulation improved for the computation of nonlinear response and nonlinear contact forces. As shown in Figure 62, the periodic contact forces measured during the experiments also indicated multi-harmonic components for higher excitation forces.

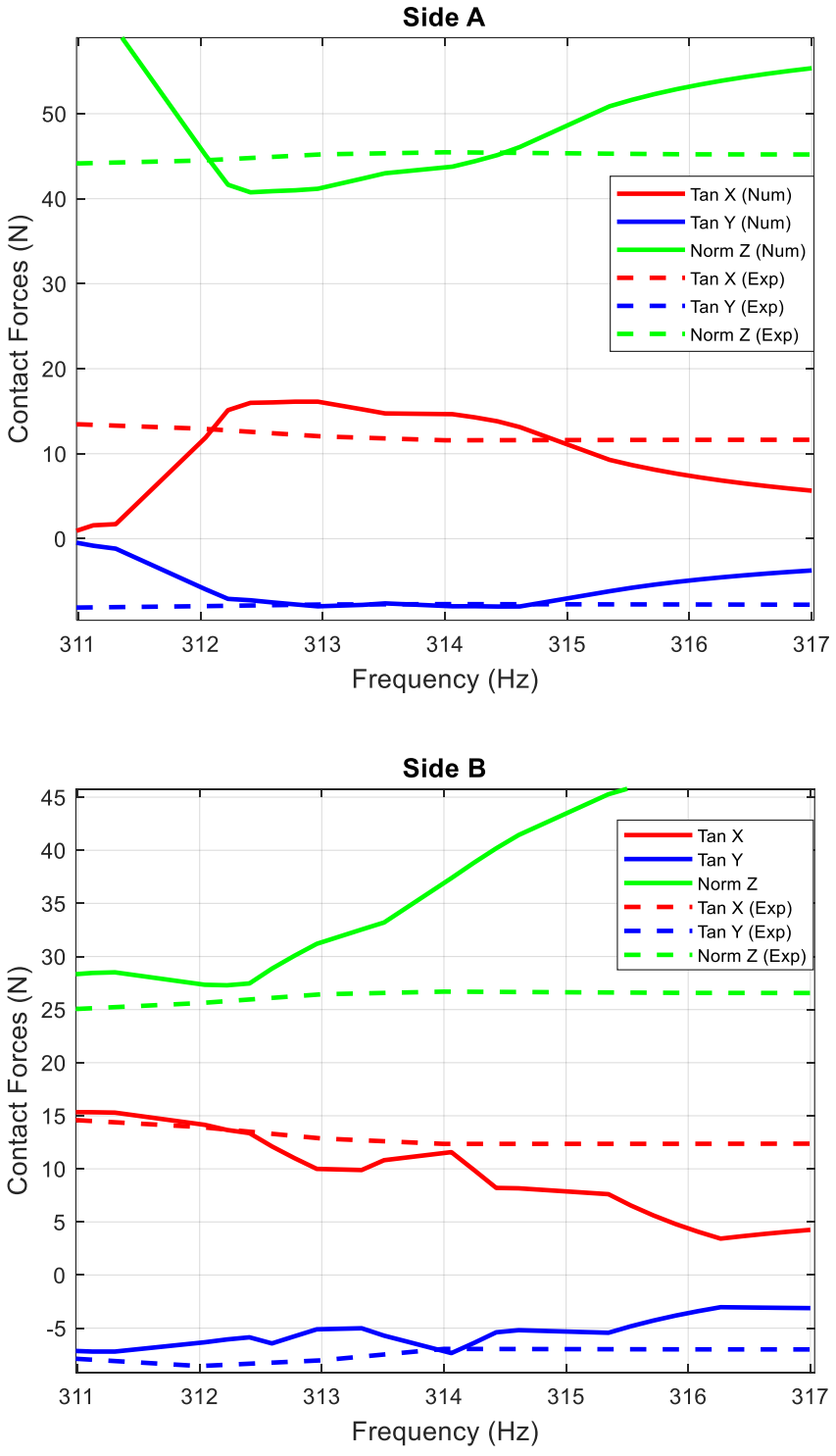

Figure 81: Comparison of static contact forces at Side A (above) and Side B (below) for numerical and experimental results (F_E=3N, nH=3)

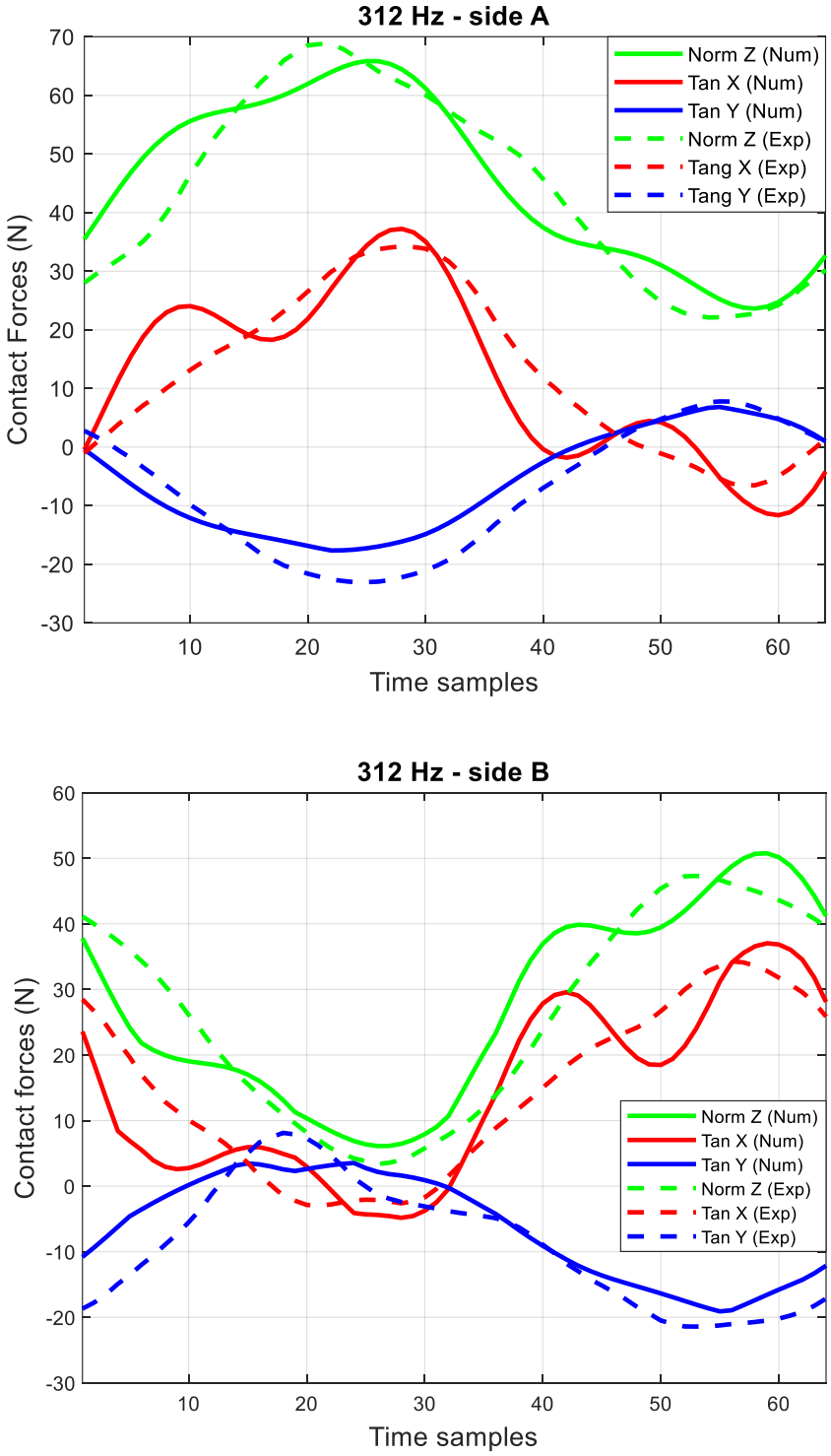

Figure 82: Comparison of periodic contact forces at Side A (above) and Side B (below) at 312 Hz (F_E=3N, nH=3)

In order to capture the nonlinear behavior more accurately, the numerical simulation with the higher excitation force of 5N and static force of 12N was also performed to solve for three harmonics and the numerical results were compared with the experimental results. Figure 83 shows the FRF computed by the solver for these conditions where the comparison with the experimental FRF with similar test conditions was good.

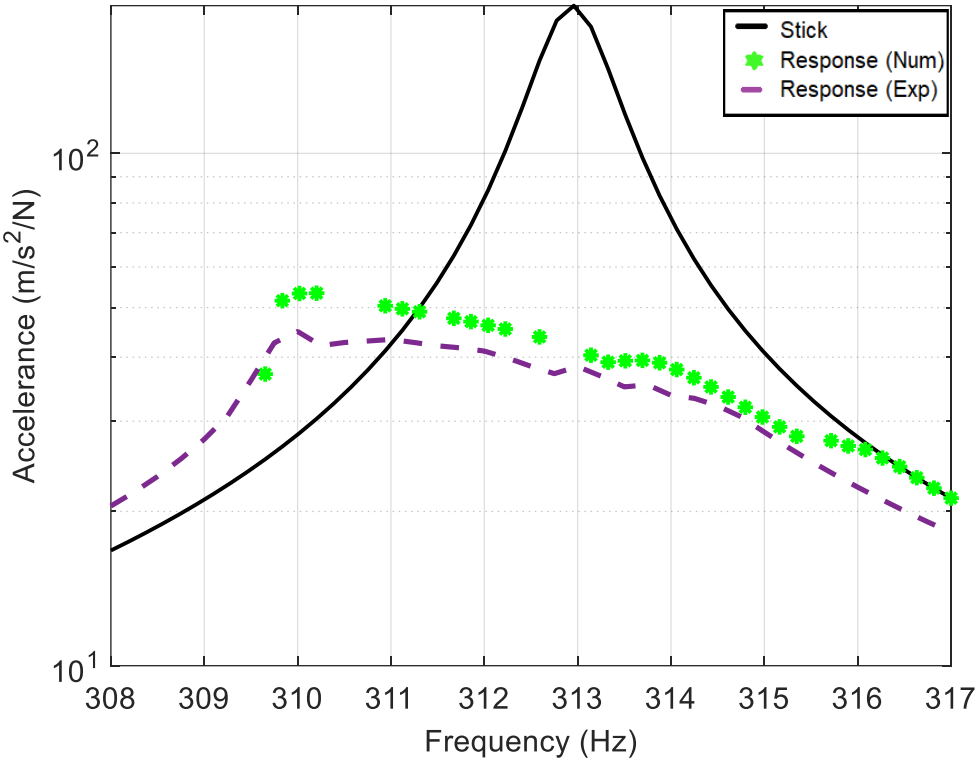

Figure 83: Comparison of numerical and experimental response (F_E=5N, nH=3)

For the converged solutions in the resonance region, the computed static contact forces for Side A and Side B were compared with those measured during the test run with similar conditions. As seen in Figure 84, a decent comparison between the experimental and numerical static contact forces was observed with more difference found for the static normal contact force of Side B towards the end of the resonance region. The difference can be attributed to the contact uncertainty due to the gap specified as input in the solver for Side B to simulate the unsymmetrical distribution of the normal preload. For the resonance frequency of 312 Hz, the periodic contact forces computed numerically were matched with the periodic contact forces measured during the experiment. Figure 85 indicates that, for the given test conditions, the nonlinear solver was able to predict the nonlinear multi harmonic periodic contact forces for both the shroud sides at 312 Hz with excellent accuracy.

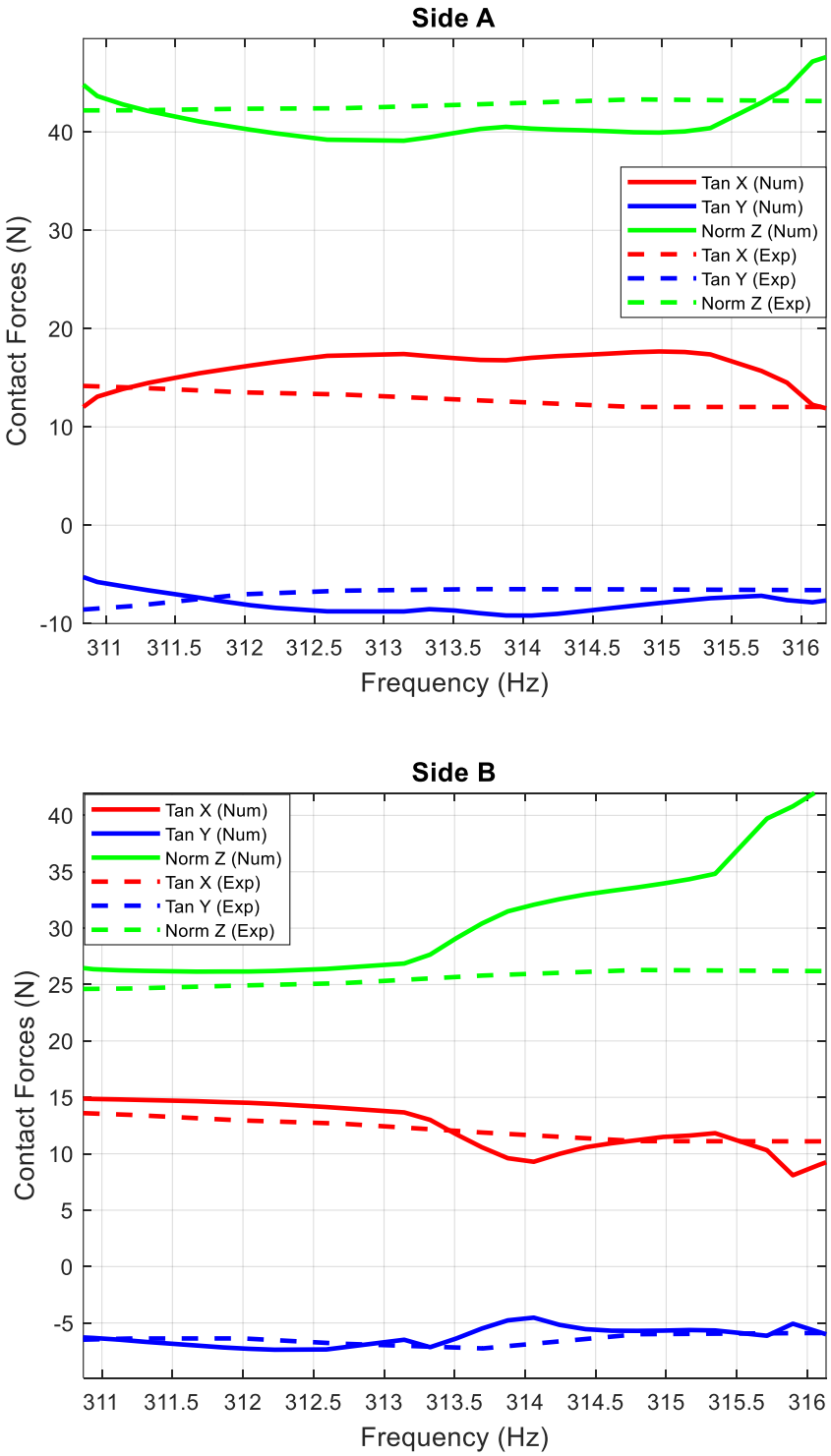

Figure 84: Comparison of static contact forces at Side A (above) and Side B (below) for numerical and experimental results (F_E=5N, nH=3)

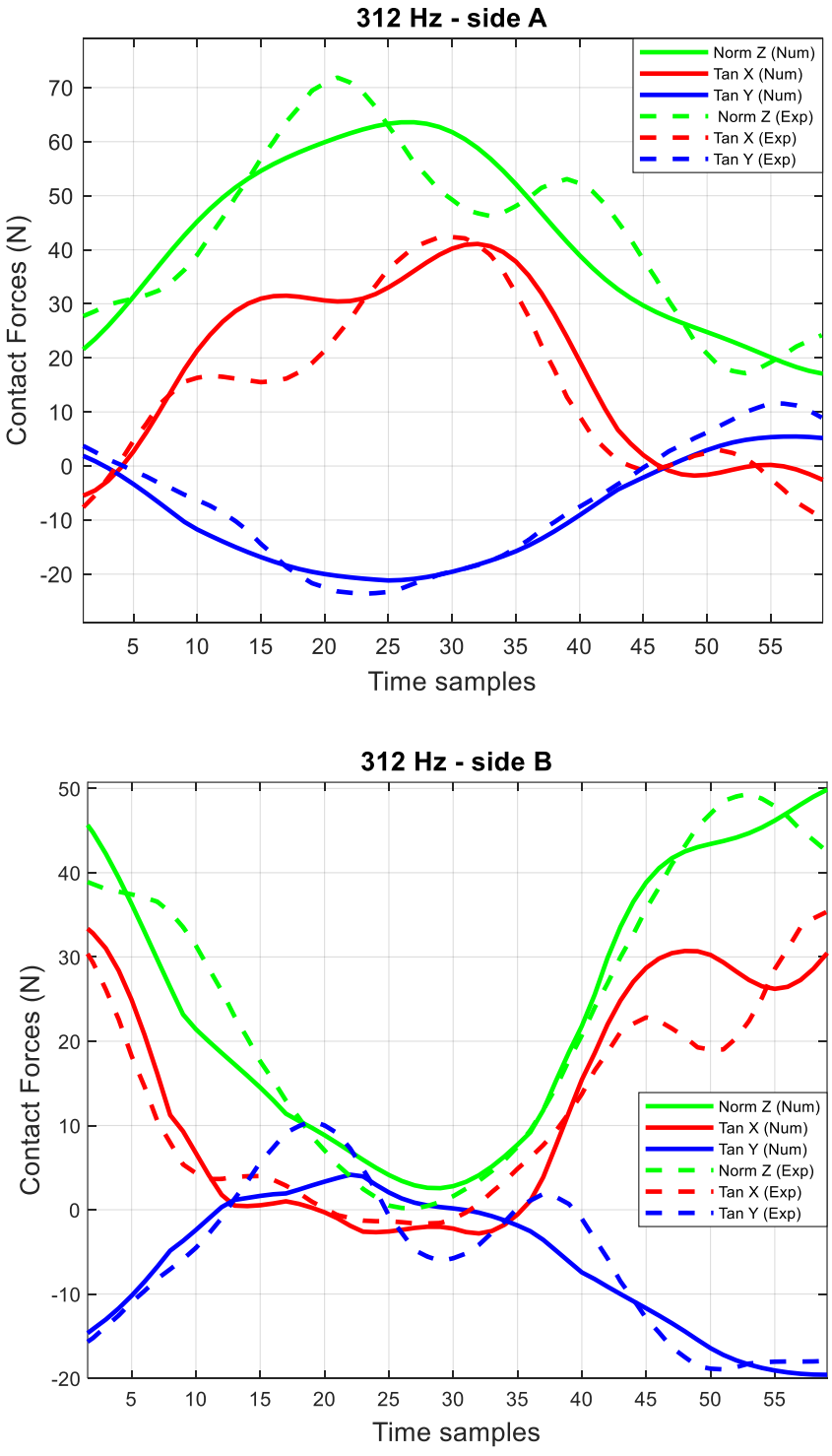

Figure 85: Comparison of periodic contact forces at Side A (above) and Side B (below) at 312 Hz (F_E=5N, nH=3)

Numerical simulation was also performed with a lower excitation force of 1N and static force of 12N for single harmonic (nH=1). FRF plot in Figure 86 displays the comparison of response computed numerically with the response measured experimentally for similar test conditions, where a slight difference in the nonlinear region and resonance frequency can be observed.

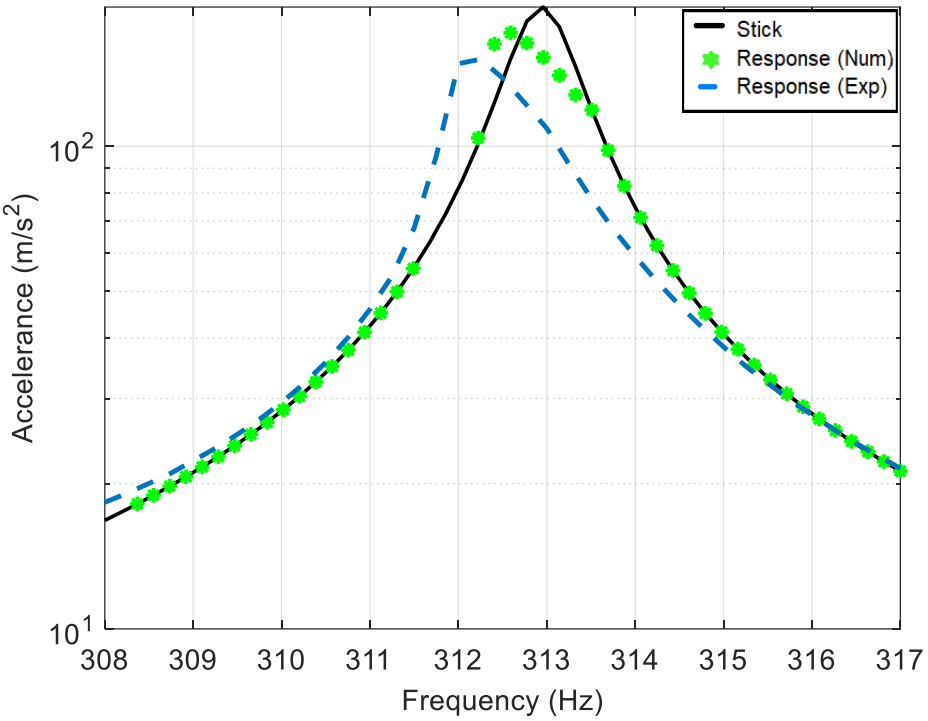

Figure 86: Comparison of numerical and experimental response (F_E=1N, nH=1)

Comparing the static contact forces in the frequency range of 311 Hz – 316 Hz (Figure 87), the results indicate considerable difference between the numerical and experimental results for both the sides A and B, particularly the normal static contact force and tangential static contact force in the Y direction. At 312.4 Hz, the computed periodic contact forces were compared with the measured periodic contact forces. As shown in Figure 88, it was observed that there was a definite offset between the numerical and experimental values and this difference was more for Side A as compared to Side B.

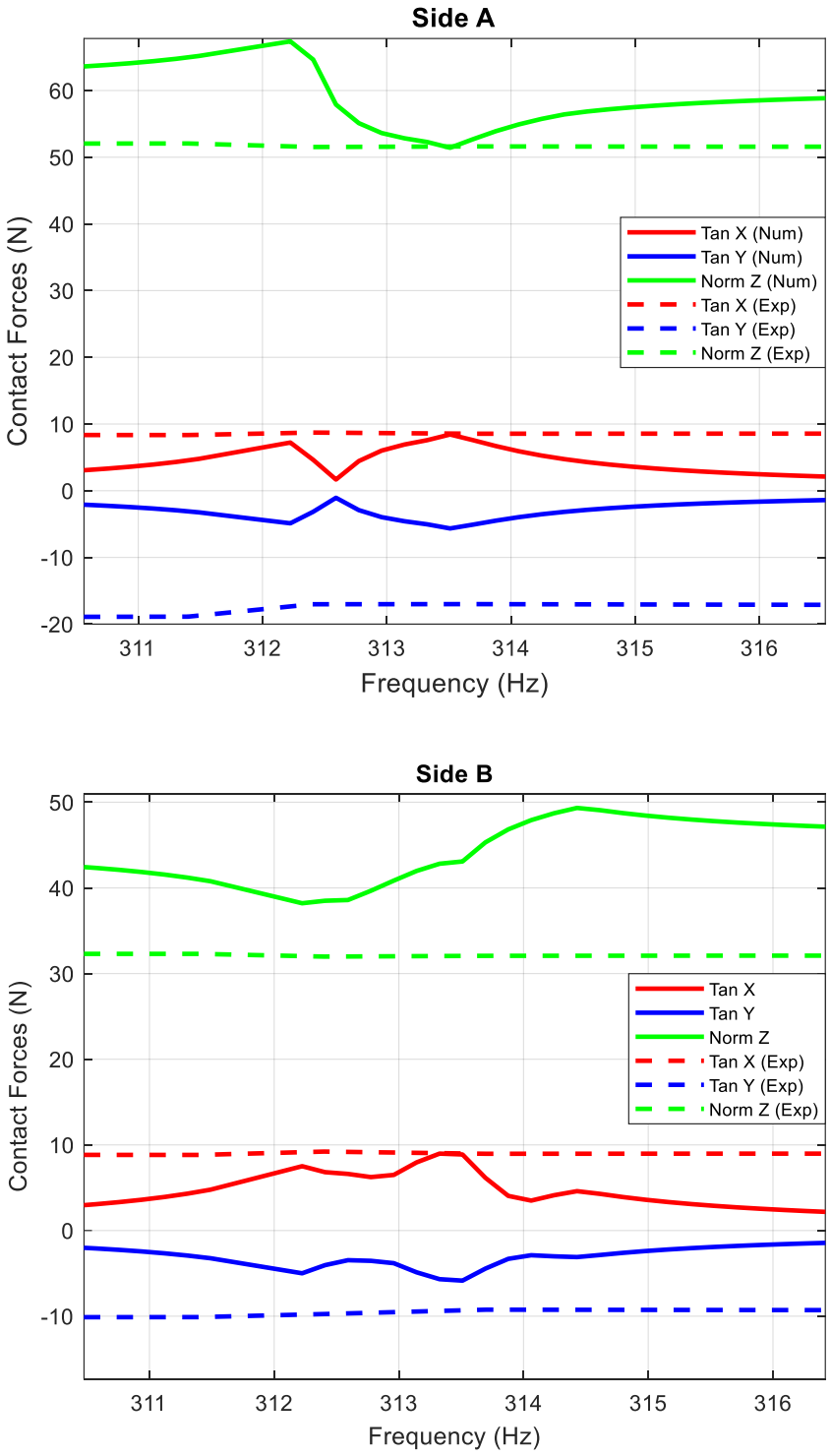

Figure 87: Comparison of static contact forces at Side A (above) and Side B (below) for numerical and experimental results (F_E=1N, nH=1)

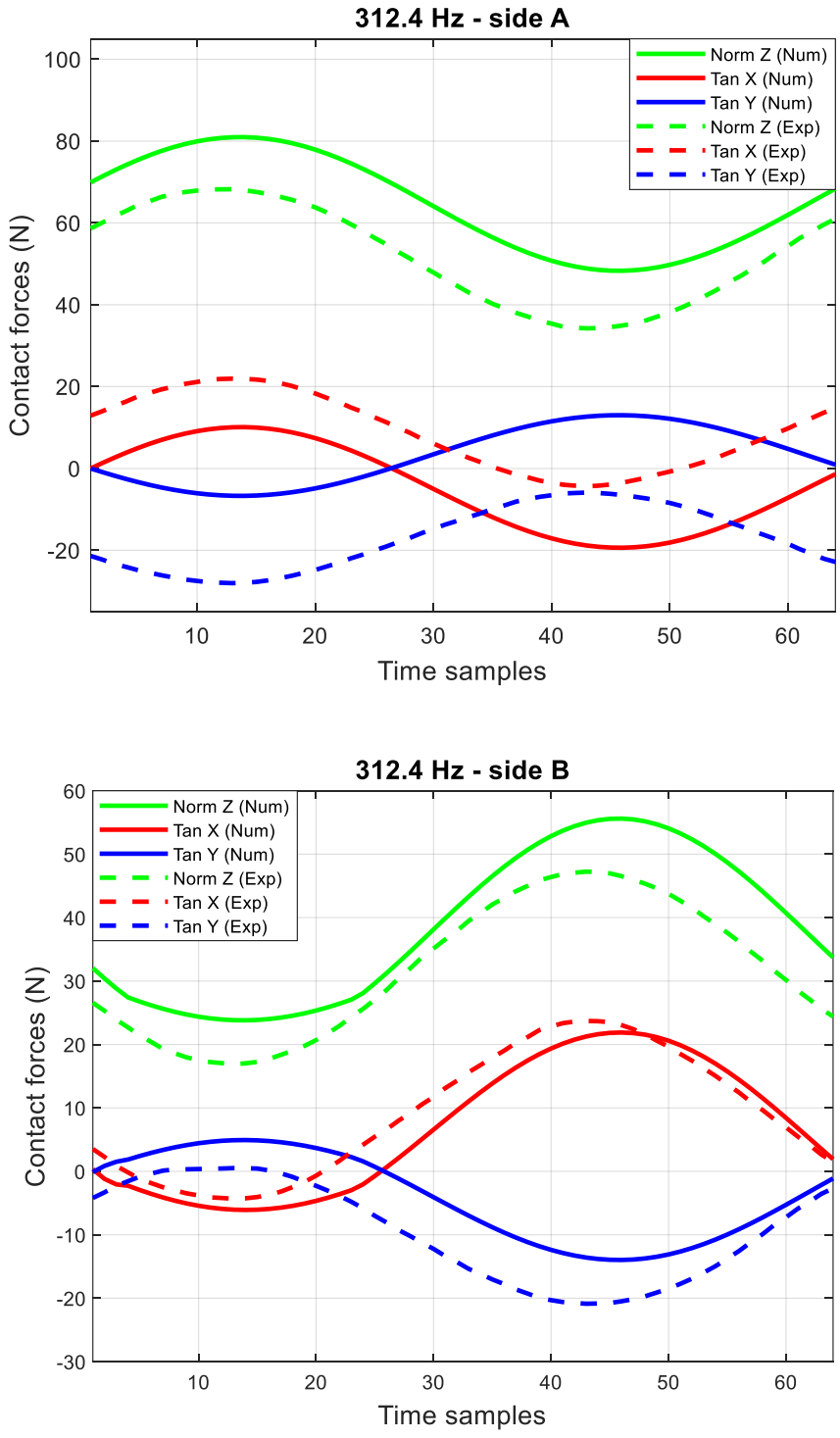

Figure 88: Comparison of periodic contact forces at Side A (above) and Side B (below) at 312.4 Hz (F_E=1N, nH=1)

The difference in the response and the contact forces noted with the lower excitation force of 1N can be associated with the response variability [57] that arises due to uncertainty of the contact forces [58]–[60]. For a full stick contact condition, the tangential contact forces should always remain within the boundaries of the range set by the Coulomb's friction law. This results in non-unique tangential contact forces within that specific range. Considering the shroud side A is in a fully stuck condition and the shroud side B is undergoing slip due to asymmetrical normal preloads, multiple steady state responses for completely similar system parameters is likely due to non-unique contact forces in normal and tangential directions and their interactions. Likewise, multiple steady state responses are also possible at lower excitation force of 1N when there is high probability of the system undergoing stick – micro slip transitions. Non unique steady state response due to the uncertainty of the contact forces for the same input parameters have been reported in the literature for the under-platform dampers [35], [61], [62] and experimental observations have indicated that the obtained variability is a real physical phenomenon rather than a modeling outcome. Consequently, recent studies [63], [64] have presented numerical approaches and optimization algorithms to compute the upper and lower boundaries for the non-unique vibration amplitudes and non-unique contact forces that cover all the possible solutions.

NOTE: Part of the work described in this chapter has been published in:

Ahmed, R., Ferhatoglu, E., Tamatam, L.R., Firrone, C. M., and Zucca, S., 2022, "An improved experimental validation of nonlinear forced response simulation of shrouded blades," Nonlinear Dynamics (Submitted)

Chapter 8

Conclusion

8.1 Summary / Overview

Low Pressure Turbine (LPT) blades subjected to highly stressed forced vibrations risk failure due to the high cycle fatigue (HCF). Such fatigue failures can be catastrophic and must be dealt with during the design phase. Friction damping devices like under-platform dampers and shrouds are employed to reduce these vibration amplitudes. For vibrating shrouded blades that are coupled to each other at blade tips, the vibration levels are significantly influenced by three-dimensional periodic contact forces acting at the shroud contacts that lead to stick/slip transitions and consequently energy dissipation. LPT blade forced response and shroud contact forces are also computed numerically utilizing the contact models in nonlinear solvers. For this purpose, experimental validation is obligatory to guarantee the accuracy and correctness of the simulation tools for the computation of LPT blade response and contact forces. For comprehensive numerical models, wide-ranging experimental validation is needed that includes the measurement of additional important parameters which has not been addressed by the existing test rigs. In case of shrouded blades, there is a need to measure the three-dimensional shroud contact forces to achieve an improved experimental validation. This study described an experimental test rig for simultaneous measurement of the forced response of the shrouded blade and the three-dimensional contact forces acting on the shroud contacts. The proposed tri-directional contact force measurement system installed in the test rig was able to measure two orthogonal tangential contact force components in addition to the normal preload that was applied using a torque screw mechanism.

Experiments were performed on a mockup shrouded blade with different normal preloads and excitation force levels as the forced response and the periodic 3D shroud contact forces were simultaneously measured. During the experimental campaign, variation of the static contact force values in the initial runs and the subsequent stabilization in successive test runs was observed. The significant shift

in these static contact force values was found to occur around the resonance. This trend was investigated for ascending as well as descending sequence of excitation force levels in consecutive test runs. The findings confirmed that for reliable validation process, actual static contact force values should be used for the simulations instead of the nominal values logged after the static loading process.

Additionally, the test rig allowed to observe the non-linear behavior of 3D periodic contact forces at resonance. This nonlinearity was found to increase for larger excitation force levels and decrease for larger normal preloads as each of these parameters influence the contact interface with respect to the stick and slip condition. A difference of jump frequency for the upsweep and down sweep with lower normal preload was also detected due to multiple solutions possible at stick-slip transition.

The advantage of using the 3D contact force measurement system was noticeable as the experiments performed around the first bending mode of the engaged mockup shrouded blade revealed complete three-dimensional profile of the periodic contact forces. It was observed that both orthogonal components of the contact force in the contact plane are significant during vibration. Moreover, by varying the amplitude of excitation force and the amount of static torque, the experiments covered a wide range of contact kinematics, from micro-slip to gross slip. Therefore, the measurements attested the necessity of 3D contact elements and exposed the insufficient 2D contact elements in models used to compute the nonlinear forced response of the shrouded blades.

A nonlinear solver equipped with 3D contact model was used to simulate the forced response testing of the mockup shrouded blade in the novel test rig. With the application of Harmonic Balance Method (HBM) using AFT approach, the nonlinear solver predicted the nonlinear forced response and the three-dimensional shroud contact forces. Numerical simulations performed for the given test conditions computed numerical results that were validated by the experimental results obtained during the experimental campaign with the proposed test rig.

Even though the experiments in this test campaign were performed on a single shrouded blade, the dynamics of the blade in the rig does not differ significantly from the dynamics of the blade-dominated modes in bladed disks, characterized by high number of nodal diameters, the shrouds are designed for.

8.2 Future work

Considering that a basic platform has already been designed, developed and provided with the proposed test rig, the experimental campaign can be further extended to investigate and test shrouded blades of different blade lengths and different shroud angles. With removable measurement box and modular supporting frame walls, the test rig can be easily modified to perform such a comparative study.

Although a mockup shrouded blade was used for this experimental campaign, the test rig is adaptable and can be customized for the investigation of real shrouded blades. In particular, the cylindrical base can be tailored to accommodate the real blade root attachment. Moreover, the contact reference blocks, and contact pads can be modified to engage real shrouds.

Additionally, the test rig can also be used to measure the relative displacement of the shroud contact surfaces with the help of differential laser during the forced response testing of the blade. These measurements will enable us to obtain the hysteresis cycle and consequently allow us to determine the contact stiffness and friction coefficient which can be used as an input to the nonlinear solver.

References

[1] M. P. Boyce, *Gas Turbine Engineering Handbook*, Fourth Edi. Butterworth-Heinemann, 2011.

[2] A. V. Srinivasan, "Flutter and Resonant Vibration Characteristics of Engine Blades," *J. Eng. Gas Turbines Power*, vol. 119, no. 4, pp. 742–775, Oct. 1997, doi: 10.1115/1.2817053.

[3] D. J. Ewins, "Control of vibration and resonance in aero engines and rotating machinery - An overview," *Int. J. Press. Vessel. Pip.*, vol. 87, no. 9, pp. 504–510, 2010, doi: 10.1016/j.ijpvp.2010.07.001.

[4] R. K. Mishra, J. Thomas, K. Srinivasan, V. Nandi, and R. Raghavendra Bhatt, "Investigation of HP turbine blade failure in a military turbofan engine," *Int. J. Turbo Jet Engines*, vol. 2015, no. 1, pp. 23–31, 2015, doi: 10.1515/tjj-2015-0049.

[5] J. H. Griffin, "Friction Damping of Resonant Stresses in Gas Turbine Engine Airfoils," *J. Eng. Power*, vol. 102, no. 2, pp. 329–333, Apr. 1980, doi: 10.1115/1.3230256.

[6] J. H. Griffin, "A Review of Friction Damping of Turbine Blade Vibration," *Int. J. Turbo Jet Engines*, vol. 7, no. 3–4, pp. 297–308, 1990, doi: 10.1515/TJJ.1990.7.3-4.297.

[7] G. Sheng Chen, *Handbook of friction – vibration interactions*. 2014.

[8] G. Csaba, "Forced response analysis in time and frequency domains of a tuned bladed disk with friction dampers," *J. Sound Vib.*, vol. 214, no. 3, pp. 395–412, 1998, doi: 10.1006/jsvi.1997.1513.

[9] A. A. Ferri and E. H. Dowell, "Frequency domain solutions to multi-degree-of-freedom, dry friction damped systems," *J. Sound Vib.*, vol. 124, no. 2, pp. 207–224, 1988, doi: 10.1016/S0022-460X(88)80183-4.

[10] E. P. Petrov and D. J. Ewins, "Analytical formulation of friction interface elements for analysis of nonlinear multi-harmonic vibrations of bladed disks," *J. Turbomach.*, vol. 125, no. 2, pp. 364–371, 2003, doi:

10.1115/1.1539868.

[11] E. P. Petrov, “A method for use of cyclic symmetry properties in analysis of nonlinear multiharmonic vibrations of bladed disks,” *J. Turbomach.*, vol. 126, no. 1, pp. 175–183, 2004, doi: 10.1115/1.1644558.

[12] C. Siewert, L. Panning, J. Wallaschek, and C. Richter, “Multiharmonic forced response analysis of a turbine blading coupled by nonlinear contact forces,” *J. Eng. Gas Turbines Power*, vol. 132, no. 8, pp. 1–9, 2010, doi: 10.1115/1.4000266.

[13] B.-D. Yang and C.-H. Menq, “Modeling of Friction Contact and Its Application to the Design of Shroud Contact,” *J. Eng. Gas Turbines Power*, vol. 119, no. 4, pp. 958–963, Oct. 1997, doi: 10.1115/1.2817082.

[14] E. Cigeroglu, W. Lu, and C. H. Menq, “One-dimensional dynamic microslip friction model,” *J. Sound Vib.*, vol. 292, no. 3–5, pp. 881–898, 2006, doi: 10.1016/j.jsv.2005.09.019.

[15] E. Cigeroglu, N. An, and C. H. Menq, “A microslip friction model with normal load variation induced by normal motion,” *Nonlinear Dyn.*, vol. 50, no. 3, pp. 609–626, 2007, doi: 10.1007/s11071-006-9171-4.

[16] B. D. Yang, M. L. Chu, and C. H. Menq, “Stick-slip-separation analysis and non-linear stiffness and damping characterization of friction contacts having variable normal load,” *J. Sound Vib.*, vol. 210, no. 4, pp. 461–481, 1998, doi: 10.1006/jsvi.1997.1305.

[17] K. Y. Sanliturk and D. J. Ewins, “Modelling two-dimensional friction contact and its application using Harmonic balance method,” *J. Sound Vib.*, vol. 193, no. 2, pp. 511–523, 1996, doi: 10.1006/jsvi.1996.0299.

[18] B. D. Yang and C. H. Menq, “Characterization of 3D contact kinematics and prediction of resonant response of structures having 3D frictional constraint,” *J. Sound Vib.*, vol. 217, no. 5, pp. 909–925, 1998, doi: 10.1006/jsvi.1998.1802.

[19] S. Zucca and C. M. Firrone, “Nonlinear dynamics of mechanical systems with friction contacts: Coupled static and dynamic Multi-Harmonic Balance Method and multiple solutions,” *J. Sound Vib.*, vol. 333, no. 3, pp. 916–926, 2014, doi: 10.1016/j.jsv.2013.09.032.

[20] C. Maria and S. Zucca, “Modelling Friction Contacts in Structural Dynamics and its Application to Turbine Bladed Disks,” *Numer. Anal. - Theory Appl.*, 2011, doi: 10.5772/25128.

[21] W. Sextro, “The calculation of the forced response of shrouded blades with friction contacts and its experimental verification,” *Proc. ASME Turbo Expo*, vol. 4, no. C, pp. 1–8, 2000, doi: 10.1115/2000-GT-0540.

[22] F. D’Ambrosio, E. Chatelet, J. Ravoux, and G. Jacquet-Richardet, “Forced response of shrouded bladed disc assemblies: A jointed experimental numerical approach,” *Proc. ASME Turbo Expo 2004*, vol. 6, pp. 337–347, 2004, doi: 10.1115/gt2004-53705.

[23] H. Jie, Z. Dayi, S. Yajie, and Z. Zigen, “Experimental study of damping characteristic of shrouded blade,” *Proc. ASME Turbo Expo*, vol. 5, no. January 2007, pp. 485–491, 2007, doi: 10.1115/GT2007-27610.

[24] M. Albanesi, “Experimental Investigation of the Non-Linear Dynamics of Shrouded Turbine Blades,” Politecnico di Torino, 2012.

[25] L. Pešek, M. Hajžman, L. Půst, V. Zeman, M. Byrtus, and J. Brůha, “Experimental and numerical investigation of friction element dissipative effects in blade shrouding,” *Nonlinear Dyn.*, vol. 79, no. 3, pp. 1711–1726, 2014, doi: 10.1007/s11071-014-1769-3.

[26] F. Kaptan, L. Panning-von Scheidt, and J. Wallaschek, “Numerical and Experimental Study of Shrouded Blade Dynamics Considering Variable Operating Points,” in *Volume 7C: Structures and Dynamics*, Jun. 2018, pp. 1–12, doi: 10.1115/GT2018-76692.

[27] K. Savchenko, A. Zinkovskii, and I. Tokar, “Determination of contact interaction influence on forced vibrations of shrouded blades,” *25th Int. Congr. Sound Vib. 2018, ICSV 2018 Hiroshima Call.*, vol. 5, no. July, pp. 2635–2640, 2018.

[28] C. Cui, H. Ma, Y. Jin, F. Xie, T. Yang, and S. Liu, “Numerical and experimental investigation on the vibro-impact responses analysis of shrouded blade,” *J. Low Freq. Noise Vib. Act. Control*, vol. 38, no. 3–4, pp. 1188–1201, 2019, doi: 10.1177/1461348418811456.

[29] S. Filippi, A. Akay, and M. M. Gola, “Measurement of tangential contact hysteresis during microslip,” *J. Tribol.*, vol. 126, no. 3, pp. 482–489, 2004, doi: 10.1115/1.1692030.

[30] C. W. Schwingshackl, E. P. Petrov, and D. J. Ewins, “Validation of Test Rig Measurements and Prediction Tools for Friction Interface Modelling,” in *Volume 6: Structures and Dynamics, Parts A and B*, Jun. 2010, pp. 1015–1024, doi: 10.1115/GT2010-23274.

[31] M. Lavella, D. Botto, and M. M. Gola, “Design of a high-precision, flat-on-flat fretting test apparatus with high temperature capability,” *Wear*, vol. 302, no. 1–2, pp. 1073–1081, 2013, doi: 10.1016/j.wear.2013.01.066.

[32] K. Asai and M. M. Gola, “Experimental Verification of Friction Behaviors Under Periodically-Varied Normal Force by Developing a Two-Directional Friction Test System,” Jun. 2015, doi: 10.1115/GT2015-42318.

[33] A. Fantetti and C. Schwingshackl, “Effect of friction on the structural dynamics of built-up structures: An experimental study,” *Proc. ASME Turbo Expo*, vol. 11, pp. 21–23, 2020, doi: 10.1115/GT2020-14945.

[34] R. Tamai *et al.*, “Vibration analysis of shrouded turbine blades for a 30 MW gas turbine,” *ASME 2013 Turbine Bl. Tip Symp. TBTS 2013*, 2013, doi: 10.1115/TBTS2013-2014.

[35] D. Botto and M. Umer, “A novel test rig to investigate under-platform damper dynamics,” *Mech. Syst. Signal Process.*, vol. 100, pp. 344–359, 2018, doi: 10.1016/j.ymssp.2017.07.046.

[36] J. O. Templeman, B. B. Sheil, and T. Sun, “Multi-axis force sensors: A state-of-the-art review,” *Sensors Actuators A Phys.*, vol. 304, p. 111772, Apr. 2020, doi: 10.1016/j.sna.2019.111772.

[37] N. Krouglicof, L. M. Alonso, and W. D. Keat, “Development of a mechanically coupled, six degree-of-freedom load platform for biomechanics and sports medicine,” *Conf. Proc. - IEEE Int. Conf. Syst. Man Cybern.*, vol. 5, pp. 4426–4431, 2004, doi: 10.1109/ICSMC.2004.1401228.

[38] L. Beccai *et al.*, “Design and fabrication of a hybrid silicon three-axial force sensor for biomechanical applications,” *Sensors Actuators, A Phys.*, vol. 120, no. 2, pp. 370–382, 2005, doi: 10.1016/j.sna.2005.01.007.

[39] É. Vázsonyi, M. Ádám, C. Dücs, Z. Vízváry, A. L. Tóth, and I. Bársony, “Three-dimensional force sensor by novel alkaline etching technique,” *Sensors Actuators, A Phys.*, vol. 123–124, pp. 620–626, 2005, doi: 10.1016/j.sna.2005.04.035.

[40] C. M. Oddo, P. Valdastri, L. Beccai, S. Roccella, M. C. Carrozza, and P. Dario, “Investigation on calibration methods for multi-axis, linear and redundant force sensors,” *Meas. Sci. Technol.*, vol. 18, no. 3, pp. 623–631, 2007, doi: 10.1088/0957-0233/18/3/011.

[41] A. Song, J. Wu, G. Qin, and W. Huang, “A novel self-decoupled four degree-of-freedom wrist force/torque sensor,” *Meas. J. Int. Meas. Confed.*, vol. 40,

no. 9–10, pp. 883–891, 2007, doi: 10.1016/j.measurement.2006.11.018.

[42] M. Fontana, S. Marcheschi, F. Salsedo, and M. Bergamasco, “A three-axis force sensor for dual finger haptic interfaces,” *Sensors (Switzerland)*, vol. 12, no. 10, pp. 13598–13616, 2012, doi: 10.3390/s121013598.

[43] Y. Zhao, L. Jiao, D. Weng, D. Zhang, and R. Zheng, “Decoupling principle analysis and development of a parallel three-dimensional force sensor,” *Sensors (Switzerland)*, vol. 16, no. 9, 2016, doi: 10.3390/s16091506.

[44] M. Mencattelli, E. Donati, M. Cultrone, and C. Stefanini, “Novel universal system for 3-dimensional orthodontic force-moment measurements and its clinical use,” *Am. J. Orthod. Dentofac. Orthop.*, vol. 148, no. 1, pp. 174–183, 2015, doi: 10.1016/j.ajodo.2015.01.028.

[45] H. K. Lee, J. Chung, S. Il Chang, and E. Yoon, “Real-time measurement of the three-axis contact force distribution using a flexible capacitive polymer tactile sensor,” *J. Micromechanics Microengineering*, vol. 21, no. 3, 2011, doi: 10.1088/0960-1317/21/3/035010.

[46] P. Yu, W. Liu, C. Gu, X. Cheng, and X. Fu, “Flexible piezoelectric tactile sensor array for dynamic three-axis force measurement,” *Sensors (Switzerland)*, vol. 16, no. 6, 2016, doi: 10.3390/s16060819.

[47] G. G. J. M. Van Zoest, H. T. C. M. Van den Berg, and F. C. Holtkamp, “Three-dimensionality of contact forces during clinical manual examination and treatment: A new measuring system,” *Clin. Biomech.*, vol. 17, no. 9–10, pp. 719–722, 2002, doi: 10.1016/S0268-0033(02)00132-8.

[48] S. Shimachi, F. Kameyama, Y. Hakozaki, and Y. Fujiwara, “Contact force measurement of instruments for force-feedback on a surgical robot: Acceleration force cancellations based on acceleration sensor readings,” *Lect. Notes Comput. Sci. (including Subser. Lect. Notes Artif. Intell. Lect. Notes Bioinformatics)*, vol. 3750 LNCS, pp. 97–104, 2005, doi: 10.1007/11566489_13.

[49] K. Moriyasu, T. Nishiwaki, T. Yamaguchi, and K. Hokkirigawa, “New technique of three directional ground reaction force distributions,” *Footwear Sci.*, vol. 2, no. 2, pp. 57–64, 2010, doi: 10.1080/19424281003685710.

[50] T. Liu, Y. Inoue, K. Shibata, Y. Hirota, and K. Shiojima, “A mobile force plate system and its application to quantitative evaluation of normal and pathological gait,” *IEEE/ASME Int. Conf. Adv. Intell. Mechatronics, AIM*, pp. 272–277, 2010, doi: 10.1109/AIM.2010.5695811.

[51] Thomas Kleckers; HBM, “Spoilt for choice : piezoelectric or strain gauge based force transducers?,” pp. 1–5, [Online]. Available: http://www.hbm.com/es/.

[52] R. Ahmed, C. M. Firrone, and S. Zucca, “Design and calibration of a tri-directional contact force measurement system,” *Appl. Sci.*, vol. 11, no. 2, pp. 1–16, 2021, doi: 10.3390/app11020877.

[53] Fujifilm, “Pressure measurement film -Prescale.” https://www.fujifilm.com/it/en/business/inspection/measurement-film/prescale.

[54] S. Zucca, M. M. Gola, and F. Piraccini, “Non-Linear Dynamics of Steam Turbine Blades With Shroud: Numerical Analysis and Experiments,” in *Volume 6: Oil and Gas Applications; Concentrating Solar Power Plants; Steam Turbines; Wind Energy*, Jun. 2012, pp. 665–674, doi: 10.1115/GT2012-69692.

[55] L. R. Tamatam, D. Botto, and S. Zucca, “A novel test rig to study the effect of fretting wear on the forced response dynamics with a friction contact,” *Nonlinear Dyn.*, vol. 105, no. 2, pp. 1405–1426, 2021, doi: 10.1007/s11071-021-06658-y.

[56] R. Craig and M. Bampton, “Coupling of Substructures for Dynamic Analyses To cite this version : HAL Id : hal-01537654 Coupling of Substructures for Dynamic Analyses,” *AIAA J.*, vol. 6, no. 7, pp. 1313–1319, 1968.

[57] M. R. W. Brake, C. W. Schwingshackl, and P. Reuß, “Observations of variability and repeatability in jointed structures,” *Mech. Syst. Signal Process.*, vol. 129, pp. 282–307, 2019, doi: 10.1016/j.ymssp.2019.04.020.

[58] B. D. Yang and C. H. Menq, “Characterization of Contact Kinematics and Application to the Design of Wedge Dampers in Turbomachinery Blading: Part 1—Stick-Slip Contact Kinematics,” *J. Eng. Gas Turbines Power*, vol. 120, no. 2, pp. 410–417, Apr. 1998, doi: 10.1115/1.2818138.

[59] B. D. Yang and C. H. Menq, “Characterization of Contact Kinematics and Application to the Design of Wedge Dampers in Turbomachinery Blading: Part 2—Prediction of Forced Response and Experimental Verification,” *J. Eng. Gas Turbines Power*, vol. 120, no. 2, pp. 418–423, Apr. 1998, doi: 10.1115/1.2818139.

[60] S. Zucca, D. Botto, and M. M. Gola, “Range of Variability in the Dynamics of Semi-Cylindrical Friction Dampers for Turbine Blades,” in *Volume 5:*

Structures and Dynamics, Parts A and B, Jan. 2008, pp. 519–529, doi: 10.1115/GT2008-51058.

[61] D. Botto, C. Gastadi, M. M. Gola, and M. Umer, "An Experimental Investigation of the Dynamics of a Blade with Two Under-Platform Dampers," *J. Eng. Gas Turbines Power*, vol. 140, no. 3, 2018, doi: 10.1115/1.4037865.

[62] C. Gastaldi, J. Gross, M. Scheel, T. M. Berruti, and M. Krack, "Modeling complex contact conditions and their effect on blade dynamics," *J. Eng. Gas Turbines Power*, vol. 143, no. 1, pp. 1–8, 2021, doi: 10.1115/1.4049186.

[63] E. Ferhatoglu and S. Zucca, "On the non-uniqueness of friction forces and the systematic computation of dynamic response boundaries for turbine bladed disks with contacts," *Mech. Syst. Signal Process.*, vol. 160, p. 107917, 2021, doi: 10.1016/j.ymssp.2021.107917.

[64] E. Ferhatoglu, C. Gastaldi, D. Botto, and S. Zucca, "An experimental and computational comparison of the dynamic response variability in a turbine blade with under-platform dampers," *Mech. Syst. Signal Process.*, vol. 172, no. March, p. 108987, 2022, doi: 10.1016/j.ymssp.2022.108987.

[65] LDS, "V400 Series Vibrators: Installation and Operating Manual."

Appendix A

Test Rig Drawings

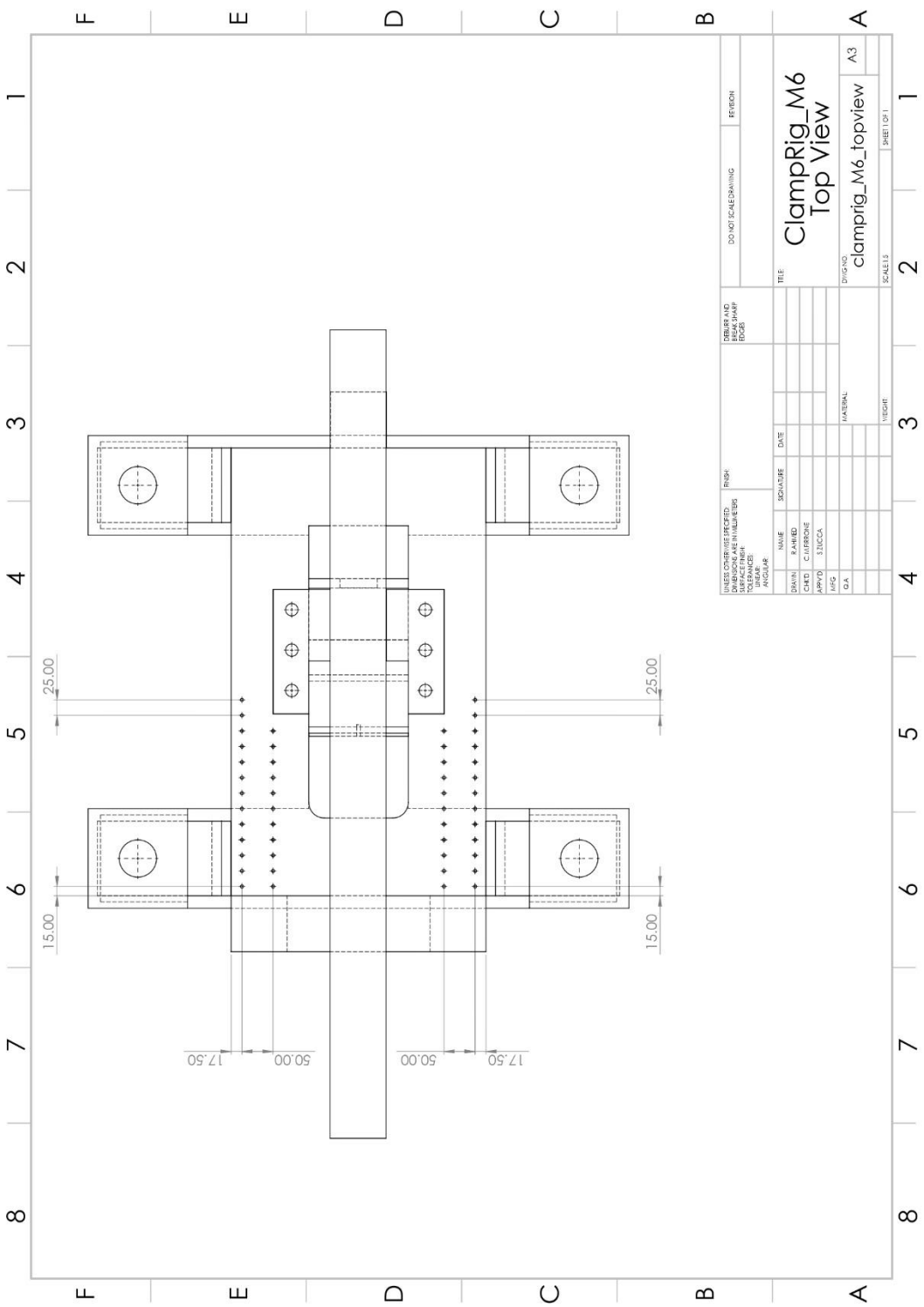
ClampRig_M6
Top View
clamprig_M6_topview
A3
DO NOT SCALE DRAWING
REVISION
TITLE
DWG NO
SCALE 1:1
SHEET 1 OF 1
MATERIAL
WEIGHT
NAME
SIGNATURE
DATE
DRAWN
R.AHMED
CHKD
C.LEFEBVRE
APPVD
S.IUCCA
MFG
Q.A
25.00
25.00
15.00
15.00
17.50
50.00
50.00
17.50

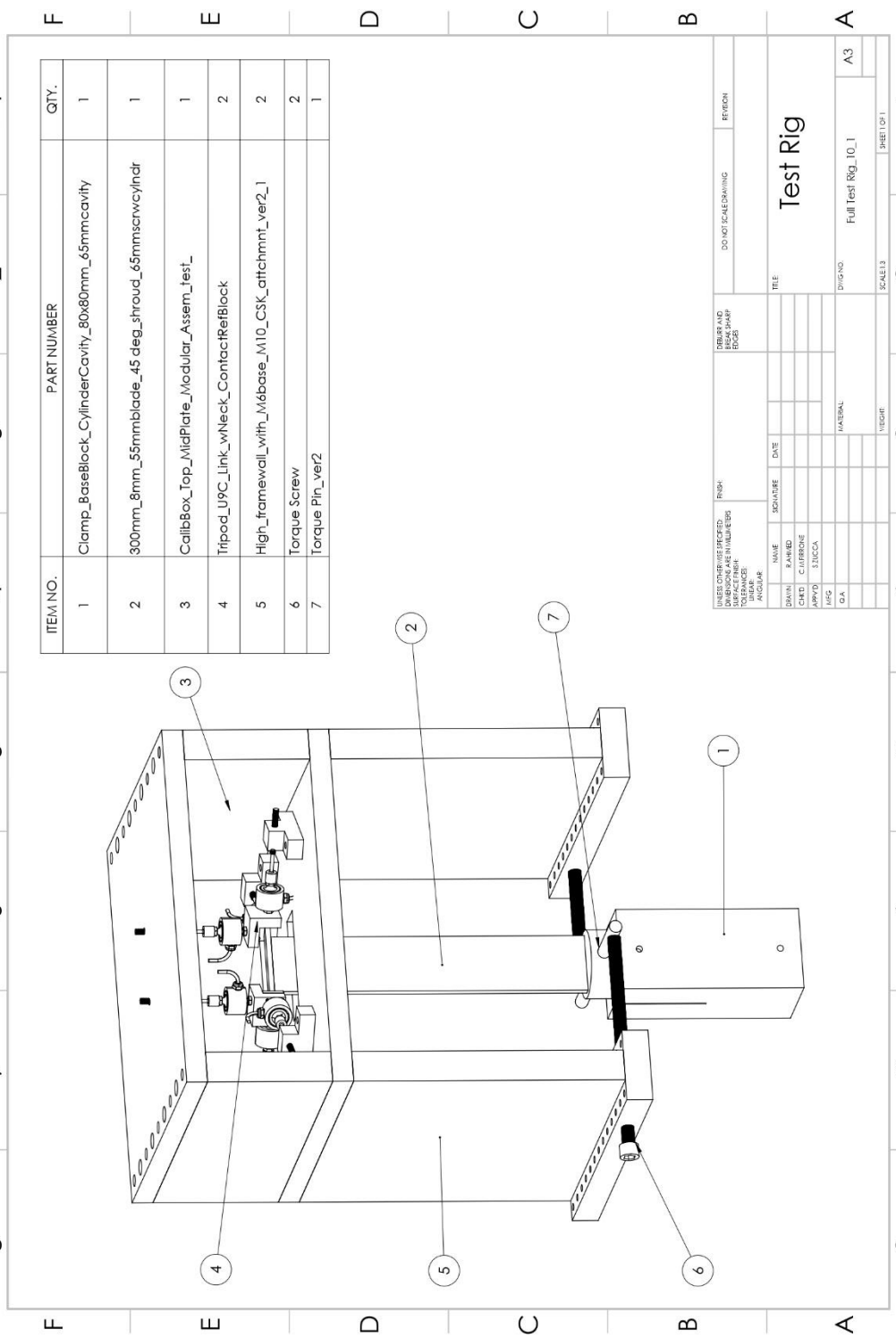
ITEM NO.
PART NUMBER
QTY.
1
Clamp_BaseBlock_CylinderCavity_80x80mm_65mmcavity
1
2
300mm_8mm_55mmblade_45 deg_shroud_65mmscrwcylndr
1
3
CalibBox_Top_MidPlate_Modular_Assem_1est_
1
4
Tripod_U9C_Link_wNeck_ContactRefBlock
2
5
High_framewall_with_Mébase_M10_CSK_attchmnt_ver2_1
2
6
Torque Screw
2
7
Torque Pin_ver2
1
Test Rig
Full Test Rig_10_1
A3
DO NOT SCALE DRAWING
SHEET 1 OF 1

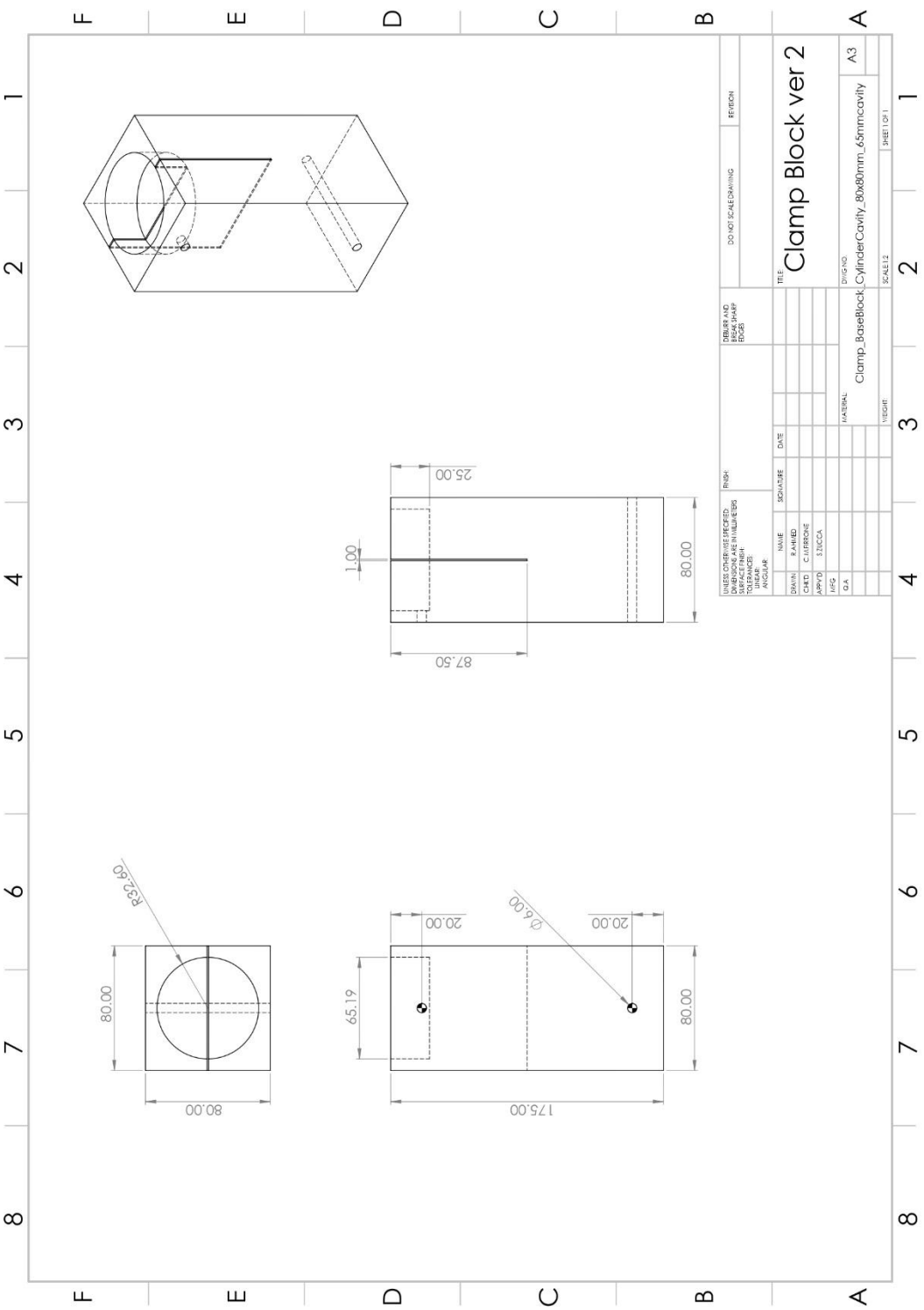
Clamp Block ver 2
Clamp_BaseBlock_CylinderCavity_80x80mm_65mmcavity
A3
SCALE 1:2
SHEET 1 OF 1
DO NOT SCALE DRAWING
REVISION
TITLE
DWG NO
MATERIAL
WEIGHT
DEBURR AND BREAK SHARP EDGES
FINISH
UNLESS OTHERWISE SPECIFIED: DIMENSIONS ARE IN MILLIMETERS SURFACE FINISH TOLERANCES LINEAR ANGULAR
NAME
SIGNATURE
DATE
DRAWN R.AHMED
CHKD C.LEFEBVRE
APPVD S.IUCCA
MFG
Q.A
25.00
1.00
80.00
87.50
R32.60
80.00
80.00
20.00
Ø6.00
20.00
65.19
80.00
175.00

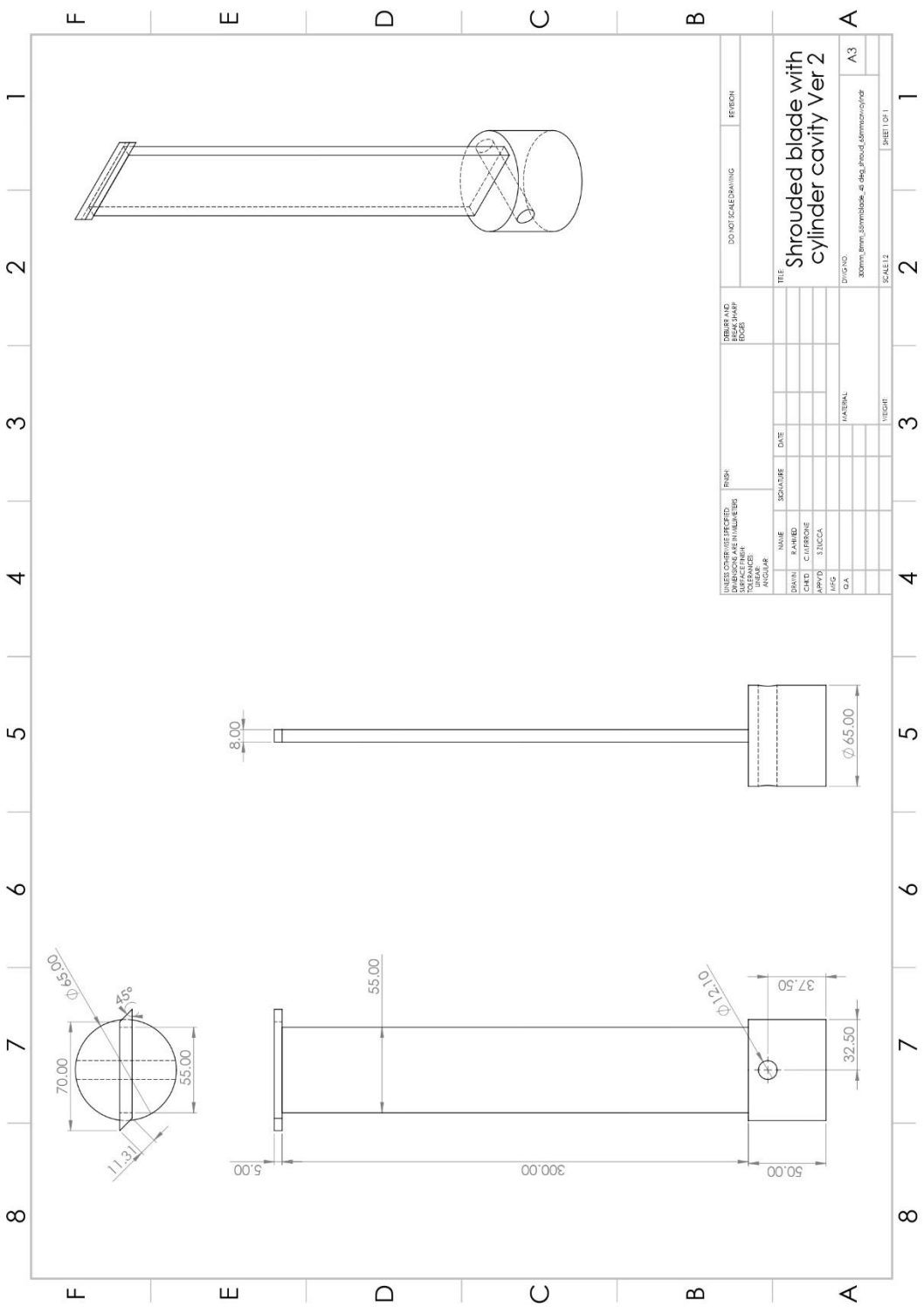
Shrouded blade with cylinder cavity Ver 2
A3
DO NOT SCALE DRAWING
REVISION
TITLE
DWG NO
300mm_6mm_shrouldblade_45 deg_shroud_45mmcylinder
SCALE 1:2
SHEET 1 OF 1
MATERIAL
WEIGHT
DRAWN
R AHMED
CHK'D
C LEFRANCHE
APP'D
S LUCCA
MFG
Q.A
DATE
SIGNATURE
NAME
FINISH
DEBURR AND BREAK SHARP EDGES
UNLESS OTHERWISE SPECIFIED: DIMENSIONS ARE IN MILLIMETERS SURFACE FINISH TOLERANCES: LINEAR ANGULAR
8.00
Ø 65.00
55.00
Ø 65.00
45°
70.00
55.00
11.31
Ø 12.10
37.50
32.50
5.00
300.00
50.00

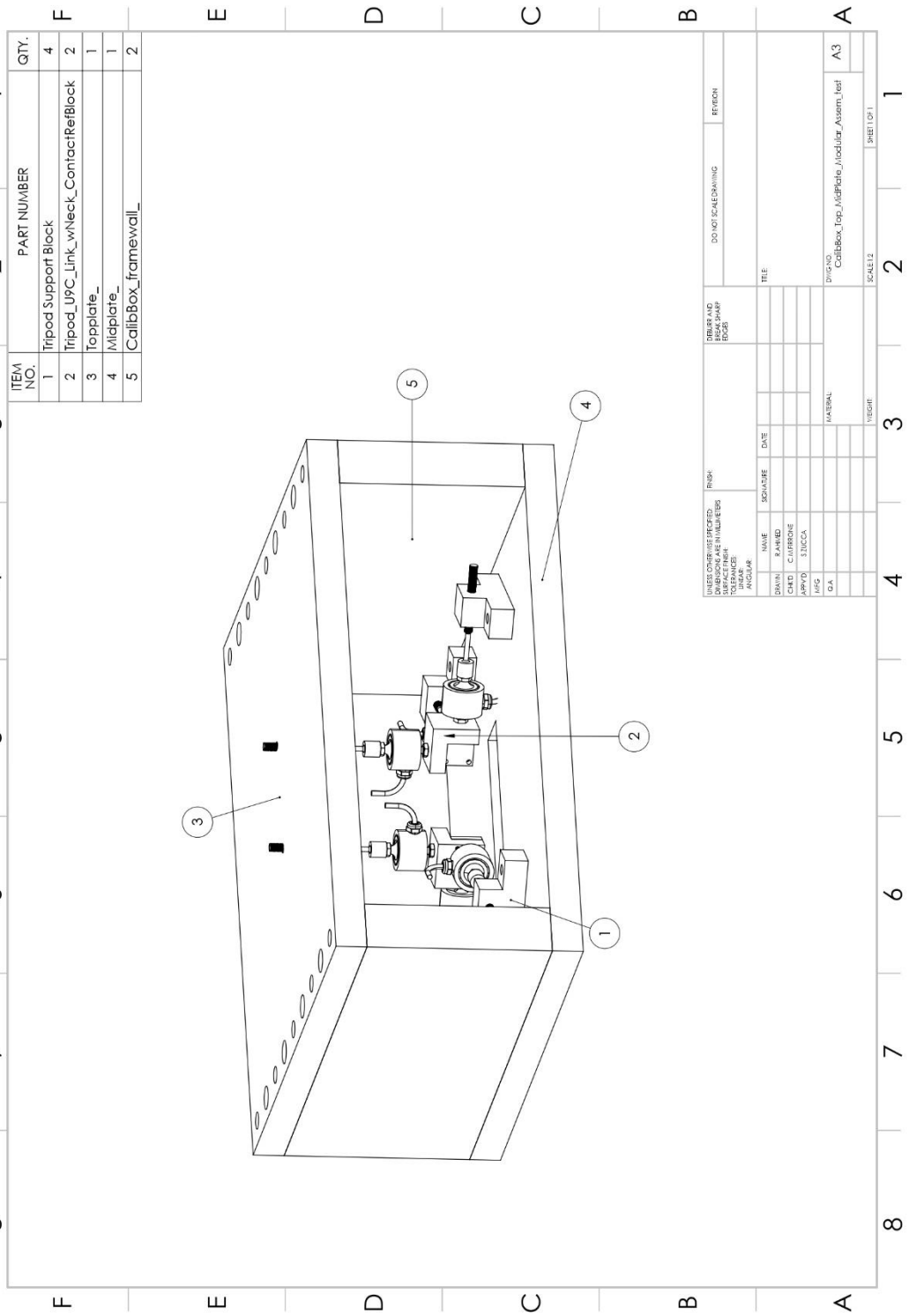
ITEM NO.
PART NUMBER
QTY.
1
Tripod Support Block
4
2
Tripod_U9C_Link_wNeck_ContactRefBlock
2
3
Topplate_
1
4
Midplate_
1
5
CalibBox_framewall_
2
DO NOT SCALE DRAWING
REVISION
DEBURR AND BREAK SHARP EDGES
FINISH
UNLESS OTHERWISE SPECIFIED:
DIMENSIONS ARE IN MILLIMETERS
SURFACE FINISH:
TOLERANCES:
LINEAR
ANGULAR
NAME
SIGNATURE
DATE
DRAWN
R AHMED
CHKD
C.FERRONE
APPVD
S.SICCA
MFG
Q.A
MATERIAL
WEIGHT
TITLE:
DWG NO.
CalibBox_Top_MidPlate_Modular_Assem_test
A3
SCALE 1:2
SHEET 1 OF 1

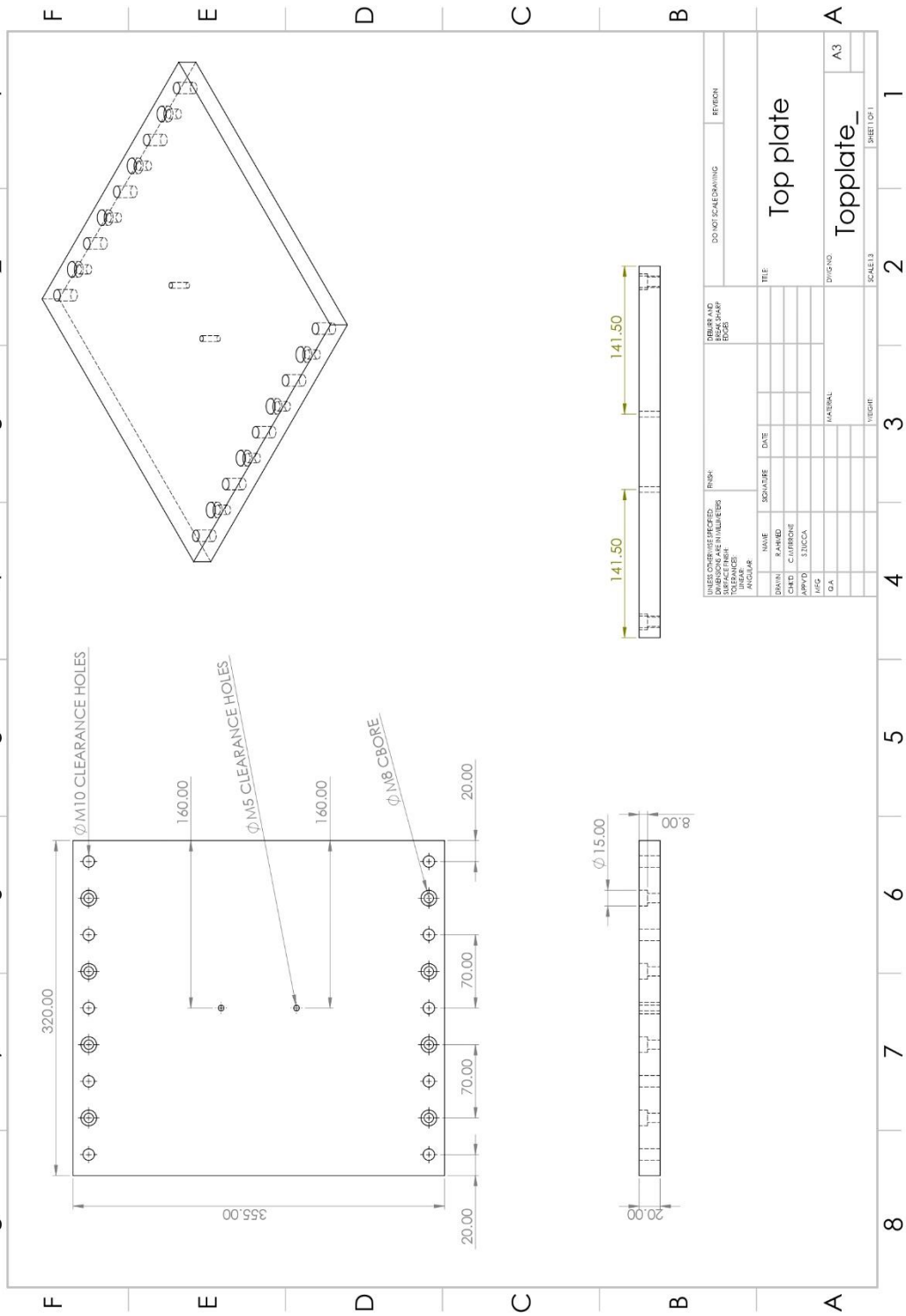
Top plate
Topplate_
A3
SCALE:1:3
SHEET 1 OF 1
DO NOT SCALE DRAWING
REVISION
DEBURR AND BREAK SHARP EDGES
FINISH
MATERIAL
WEIGHT
DWG NO.
TITLE
UNLESS OTHERWISE SPECIFIED:
DIMENSIONS ARE IN MILLIMETERS
SURFACE FINISH:
TOLERANCES:
LINEAR
ANGULAR
NAME
SIGNATURE
DATE
DRAWN
R.AHMED
CHKD
C.FERRONE
APPV'D
S.SICCA
MFG
Q.A
ØM10 CLEARANCE HOLES
ØM5 CLEARANCE HOLES
ØM8 CBORE
160.00
160.00
20.00
70.00
70.00
320.00
355.00
20.00
Ø15.00
8.00
20.00
141.50
141.50

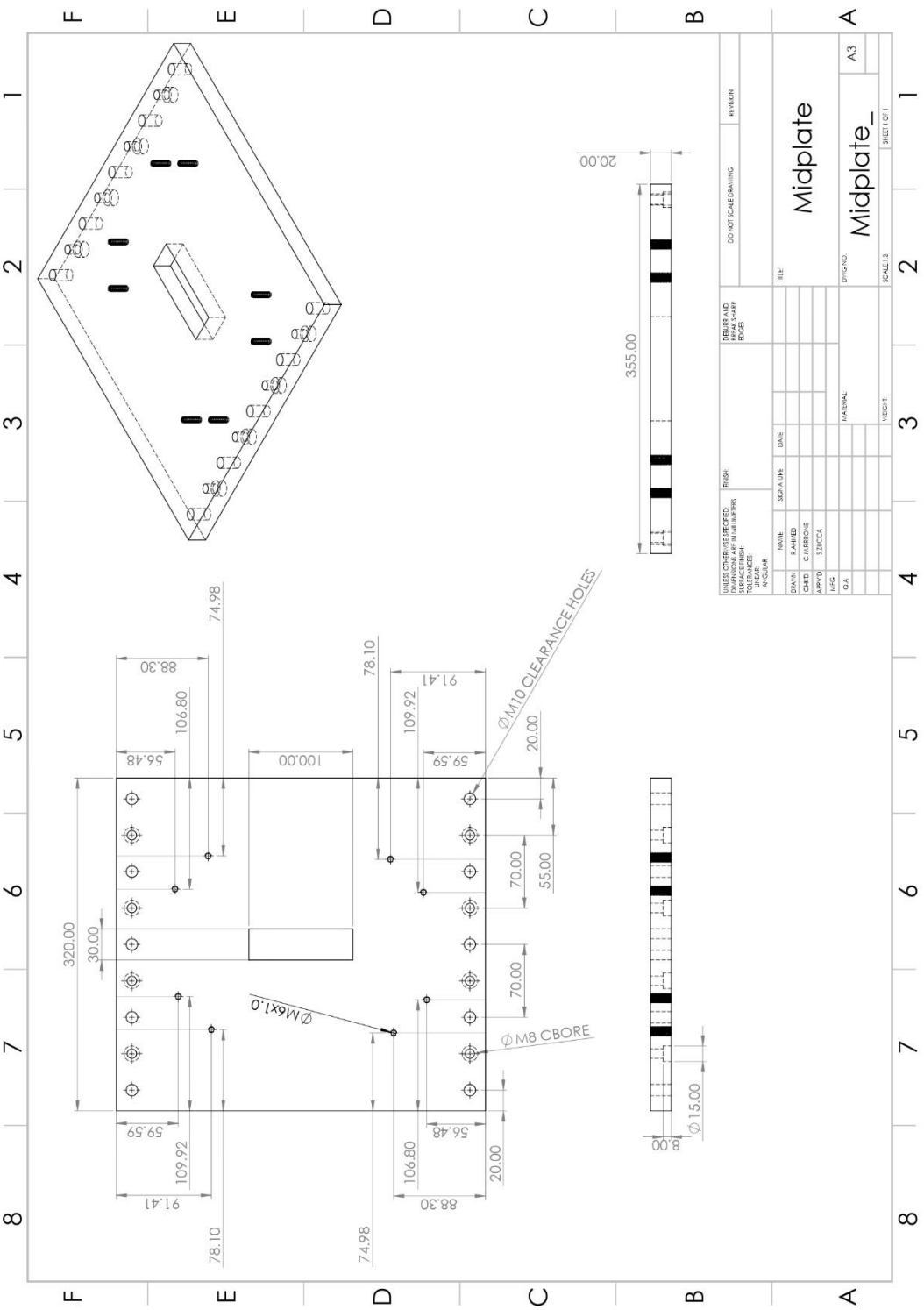
Midplate
Midplate_
A3
SCALE:1:3
SHEET 1 OF 1
DO NOT SCALE DRAWING
REVISION
DRAWN
R.AHMED
CHKD
C.LEFBVRE
APPVD
S.MCCOY
MFG
Q.A
MATERIAL
WEIGHT
DWG NO
TITLE
FINISH
DEBURR AND BREAK SHARP EDGES
UNLESS OTHERWISE SPECIFIED:
DIMENSIONS ARE IN MILLIMETERS
SURFACE FINISH:
TOLERANCES:
LINEAR
ANGULAR
NAME
SIGNATURE
DATE
355.00
20.00
8.00
Ø15.00
Ø M10 CLEARANCE HOLES
Ø M8 CBORE
ØM6X1.0
320.00
30.00
100.00
106.80
109.92
91.41
88.30
59.59
56.48
78.10
74.98
70.00
55.00
20.00

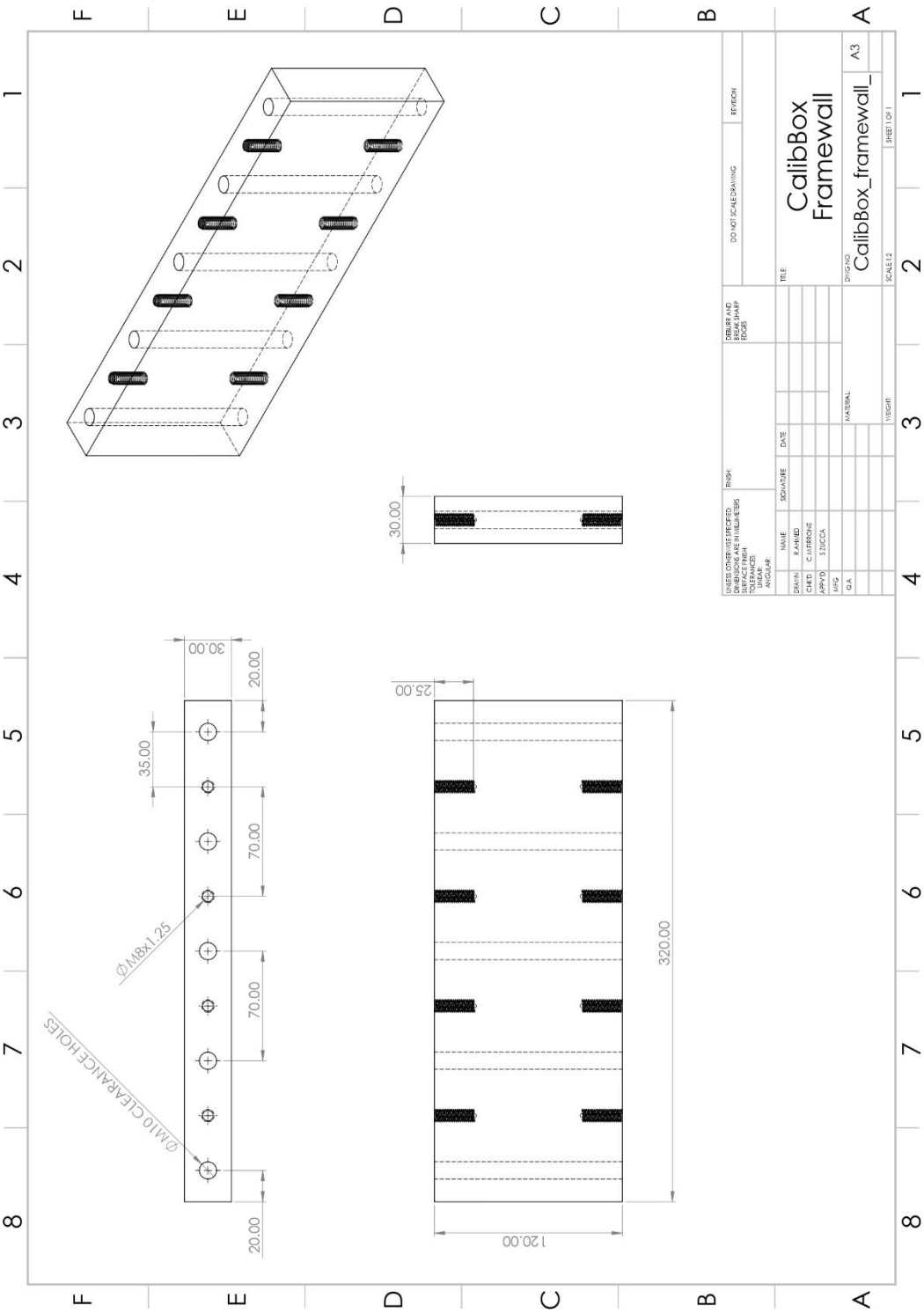
CalibBox
Framewall
CalibBox_framewall_
A3
SCALE 1:2
SHEET 1 OF 1
DO NOT SCALE DRAWING
REVISION
DRAWN
CHKD
APP'D
MFG
Q.A
NAME
SIGNATURE
DATE
MATERIAL
WEIGHT
DEBURR AND BREAK SHARP EDGES
FINISH
UNLESS OTHERWISE SPECIFIED:
DIMENSIONS ARE IN MILLIMETERS
SURFACE FINISH:
TOLERANCES:
LINEAR
ANGULAR
30.00
20.00
35.00
70.00
70.00
20.00
Ø M8x1.25
Ø M10 CLEARANCE HOLES
30.00
25.00
320.00
120.00

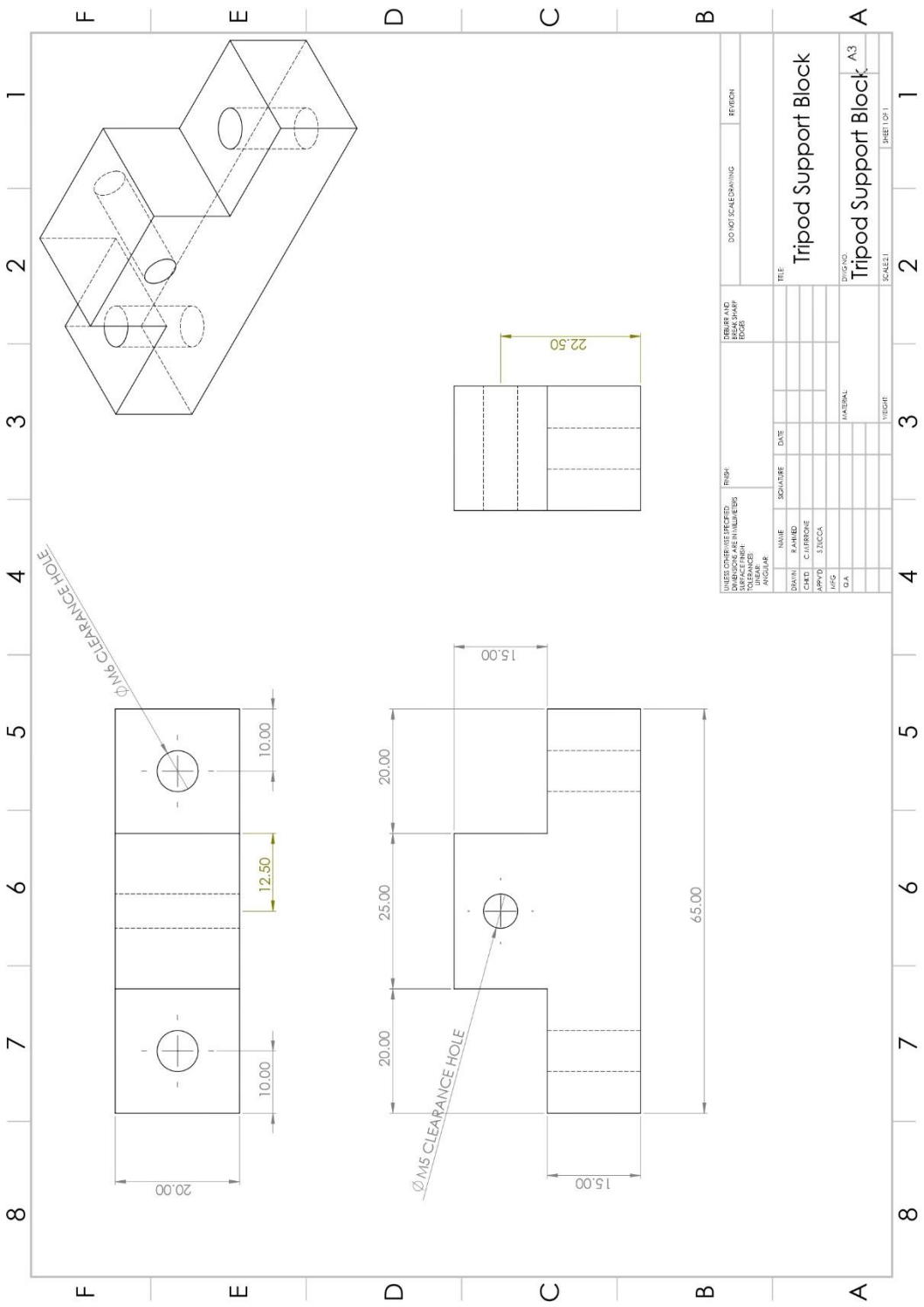
Tripod Support Block
Tripod Support Block
A3
22.50
15.00
20.00
25.00
20.00
65.00
15.00
10.00
12.50
10.00
20.00
Ø M5 CLEARANCE HOLE
Ø M6 CLEARANCE HOLE
DO NOT SCALE DRAWING
REVISION
TITLE:
DWG NO
SCALE:2:1
SHEET 1 OF 1
MATERIAL
WEIGHT
DRAWN
CHKD
APP'D
MFG
Q.A
NAME
SIGNATURE
DATE
FINISH
DEBURR AND BREAK SHARP EDGES

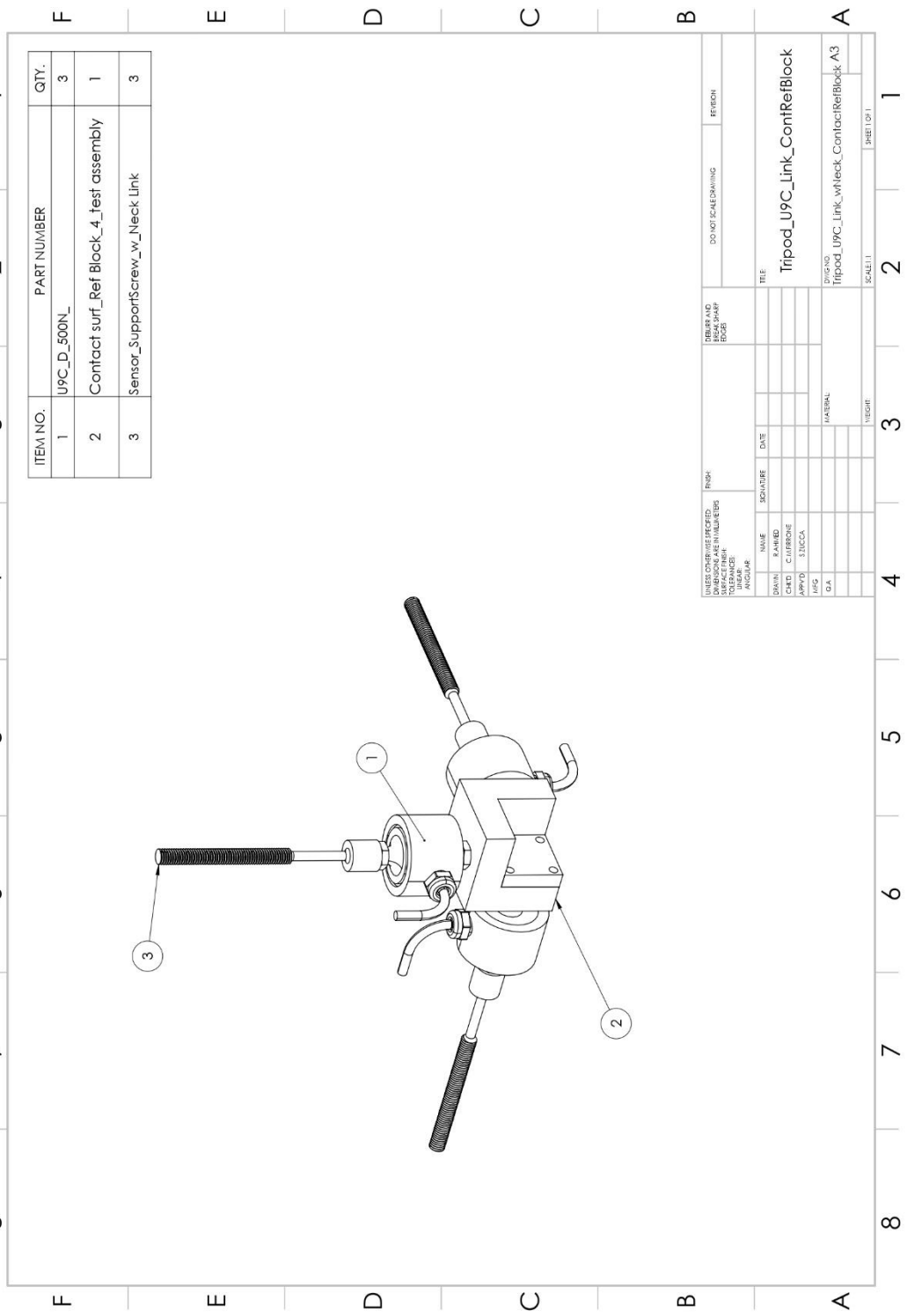
ITEM NO.
PART NUMBER
QTY.
1
U9C_D_500N_
3
2
Contact surf_Ref Block_4_test assembly
1
3
Sensor_SupportScrew_w_Neck Link
3
1
2
3
TITLE:
Tripod_U9C_Link_ConfRefBlock
DWG NO.
Tripod_U9C_Link_wNeck_ContactRefBlock A3
SCALE: 1:1
SHEET 1 OF 1
DO NOT SCALE DRAWING
REVISION
DRAWN
CHKD
APP'D
MFG
Q.A
MATERIAL
WEIGHT

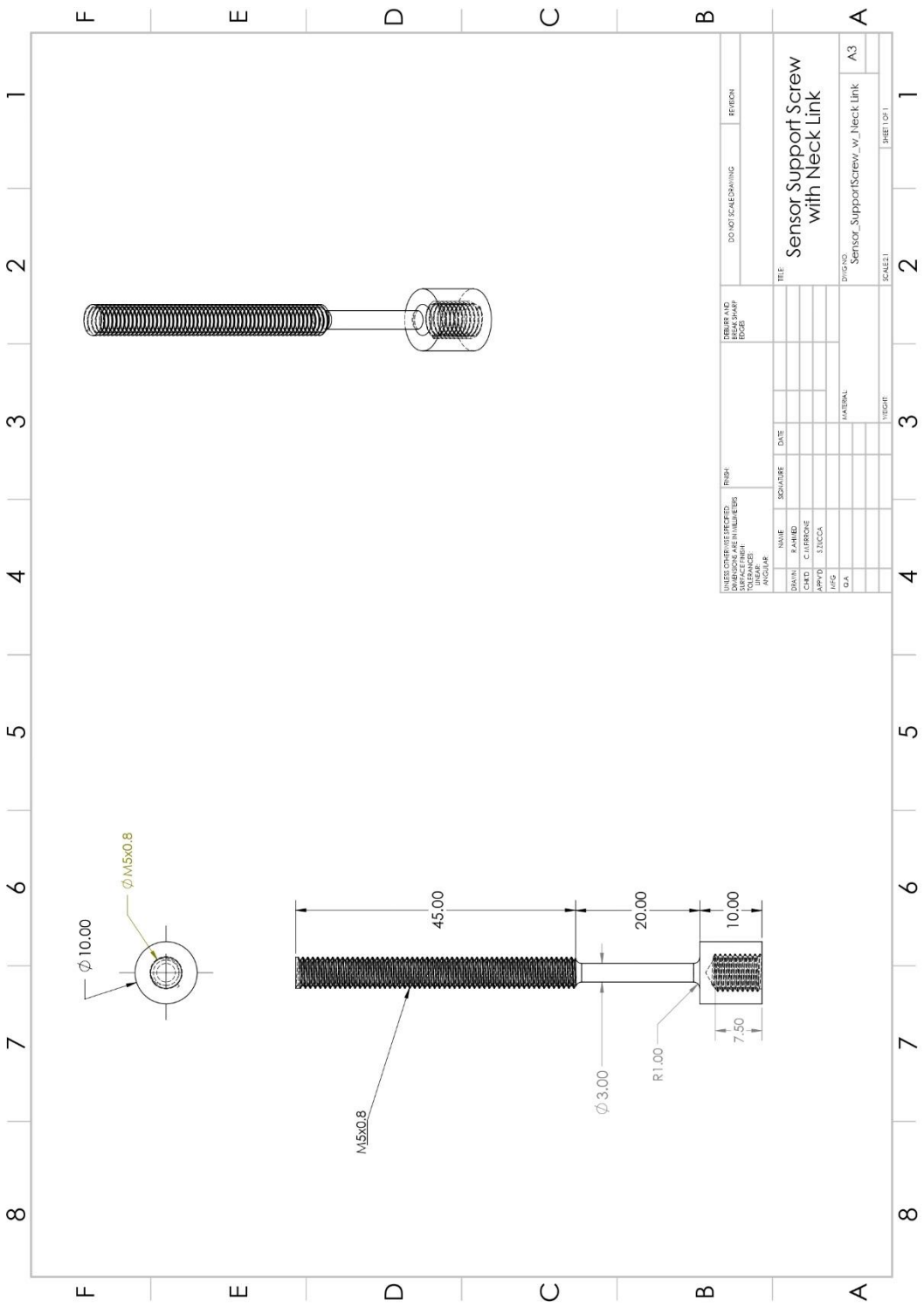
Sensor Support Screw with Neck Link
Sensor_SupportScrew_w_Neck Link
A3
SCALE:2:1
SHEET 1 OF 1
DO NOT SCALE DRAWING
REVISION
DRAWN
R AHMED
CHKD
C LEFBVRE
APPVD
S MCCA
MFG
Q A
MATERIAL
WEIGHT
DATE
SIGNATURE
NAME
FINISH
DEBURR AND BREAK SHARP EDGES
UNLESS OTHERWISE SPECIFIED:
DIMENSIONS ARE IN MILLIMETERS
SURFACE FINISH:
TOLERANCES:
LINEAR
ANGULAR
Ø10.00
Ø M5x0.8
45.00
20.00
10.00
7.50
R1.00
Ø3.00
M5x0.8

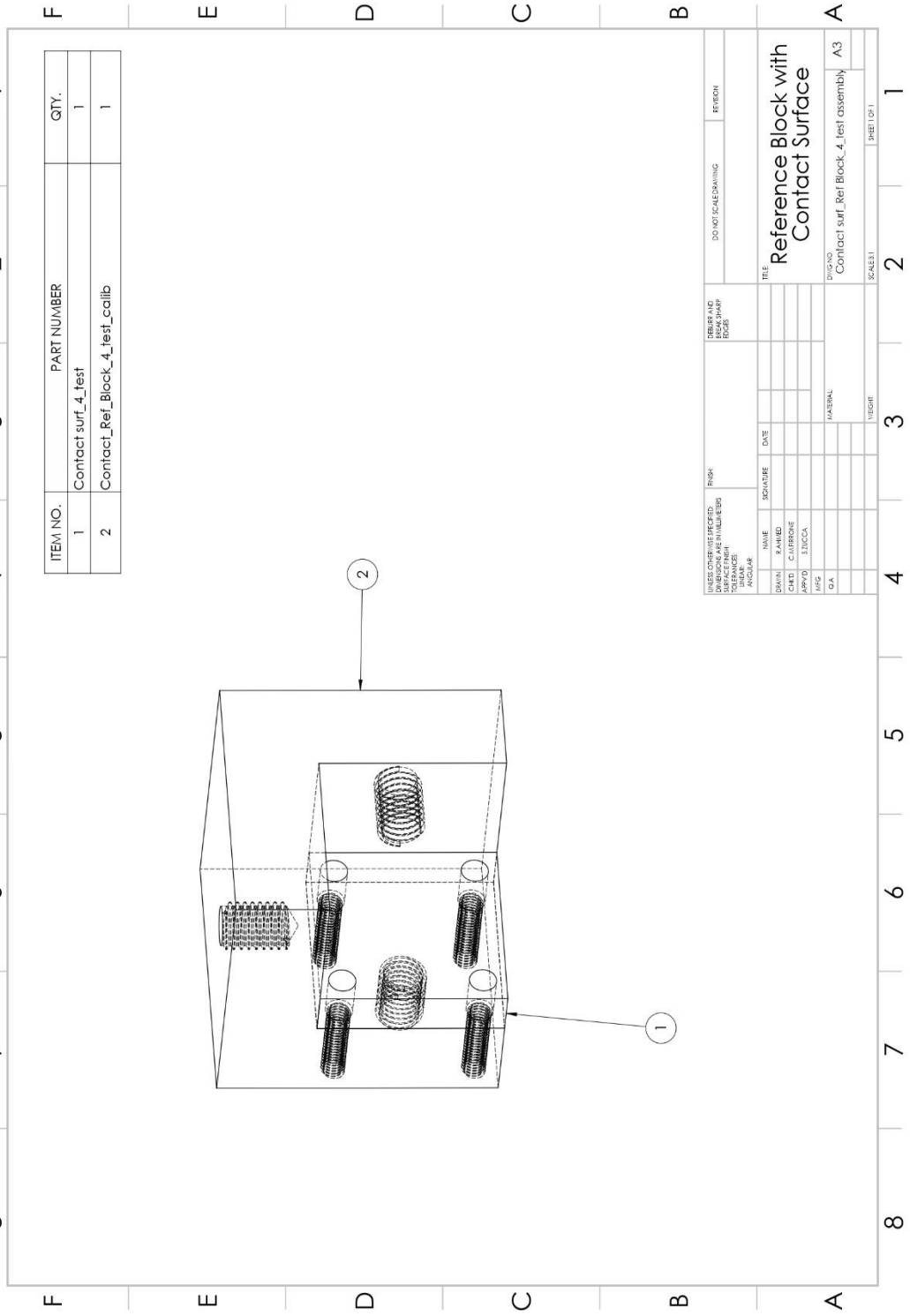
ITEM NO.
PART NUMBER
QTY.
1
Contact surf_4_test
1
2
Contact_Ref_Block_4_test_calib
1
Reference Block with Contact Surface
Contact surf_Ref Block_4_test assembly
A3
DO NOT SCALE DRAWING
REVISION
SCALE:2:1
SHEET 1 OF 1
1
2

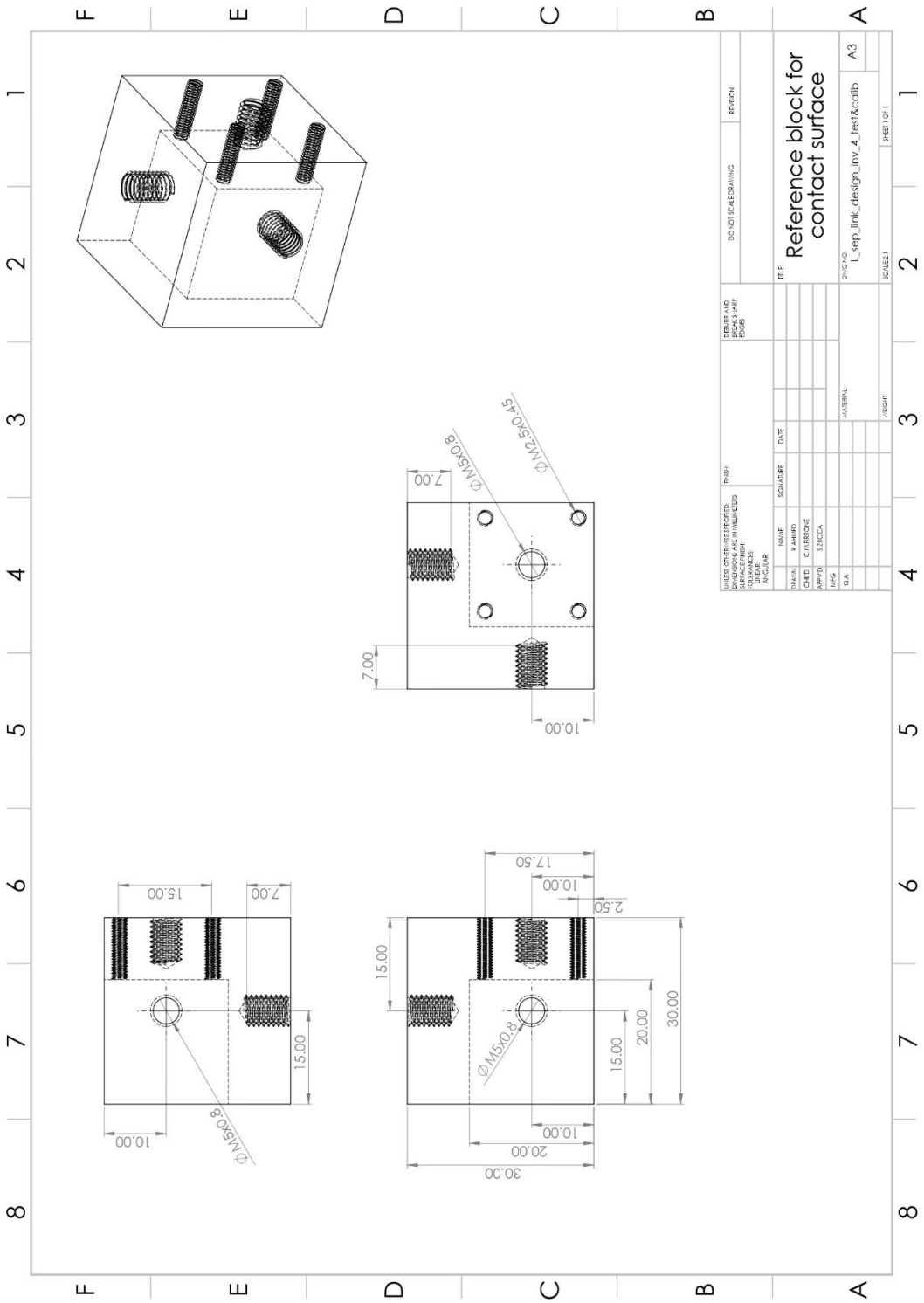
Reference block for contact surface
L_sep_link_design_inv_4_test&calib
A3
DO NOT SCALE DRAWING
DEBURR AND BREAK SHARP EDGES
UNLESS OTHERWISE SPECIFIED: DIMENSIONS ARE IN MILLIMETERS SURFACE FINISH: TOLERANCES: LINEAR: ANGULAR:
NAME
SIGNATURE
DATE
DRAWN
R.AHMED
CHKD
C.LEFEBVRE
APPVD
S.SICCA
MFG
Q.A
MATERIAL
WEIGHT:
SCALE:2:1
SHEET 1 OF 1
ϕM5x0.8
ϕM2.5x0.45
7.00
10.00
15.00
17.50
2.50
20.00
30.00

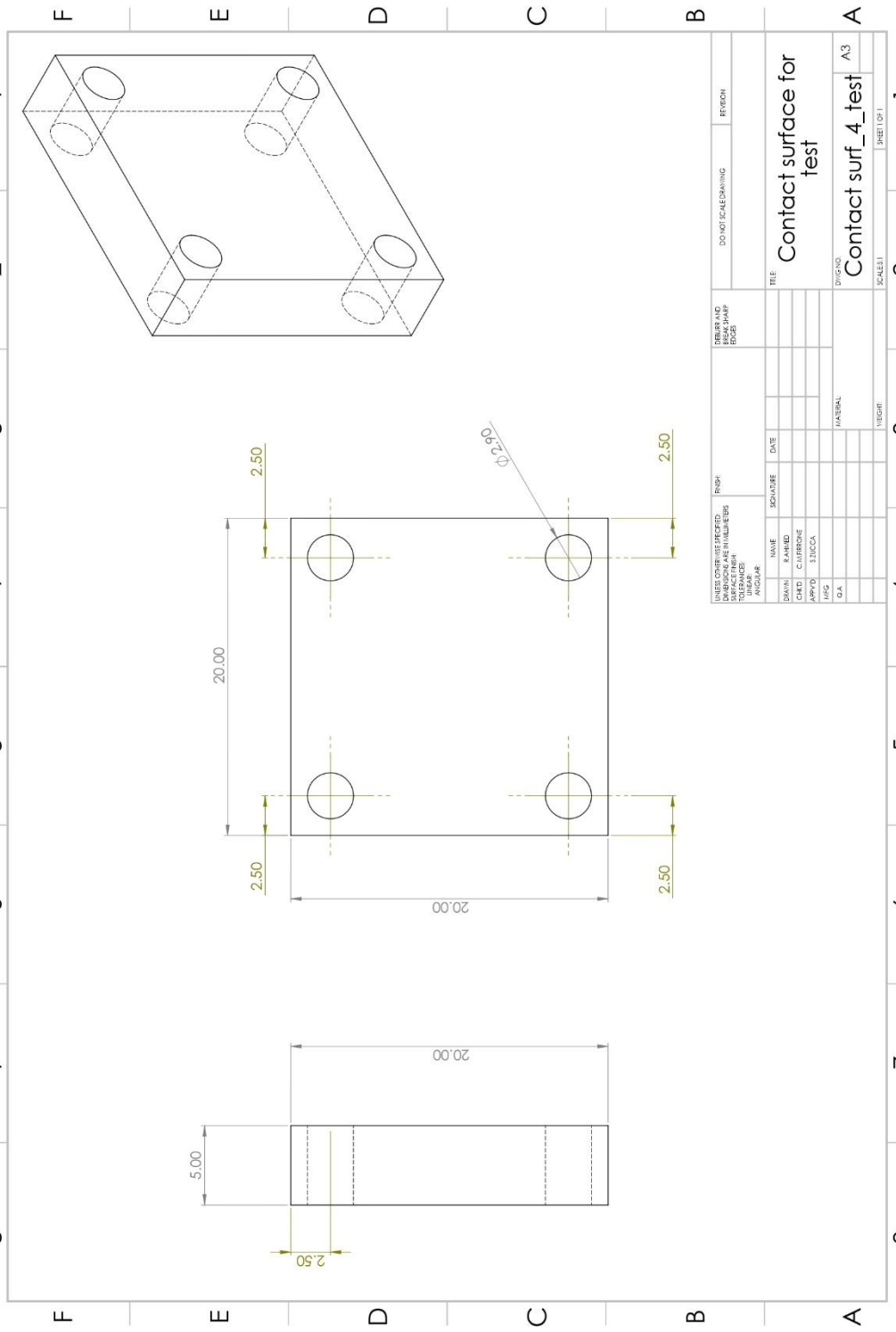
Contact surface for test
Contact surf_4_test
A3
SCALE:1
SHEET 1 OF 1
DO NOT SCALE DRAWING
REVISION
DRAWN
R.AHMED
CHKD
C.LEFEBVRE
APPVD
S.SICCA
MFG
Q.A
MATERIAL
WEIGHT
FINISH
DATE
SIGNATURE
NAME
DEBURR AND BREAK SHARP EDGES
TITLE
DWG NO
UNLESS OTHERWISE SPECIFIED:
DIMENSIONS ARE IN MILLIMETERS
SURFACE FINISH:
TOLERANCES:
LINEAR
ANGULAR
2.50
2.50
2.50
2.50
20.00
20.00
20.00
5.00
2.50
Ø2.90

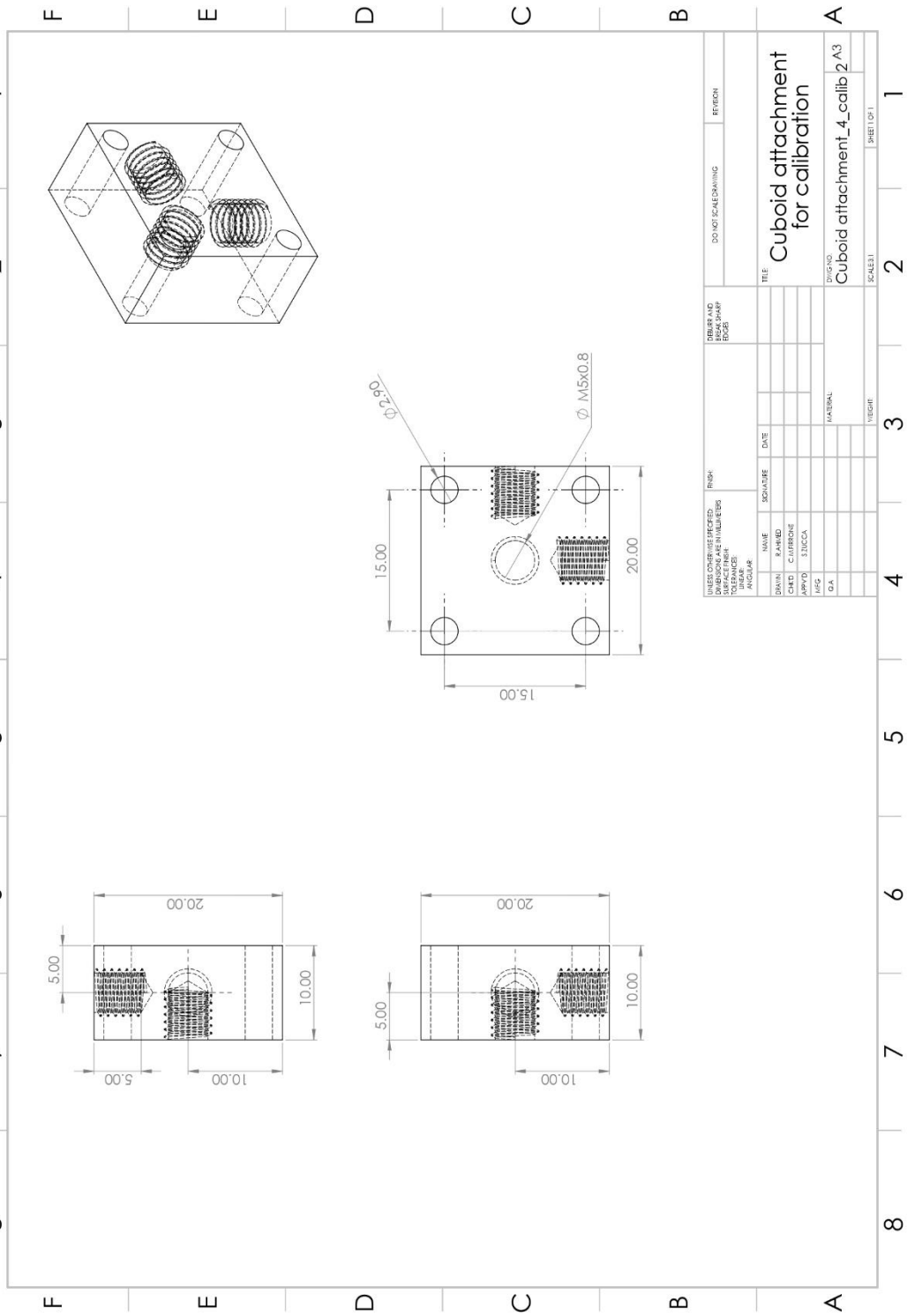
Cuboid attachment for calibration
Cuboid attachment_4_calib 2
A3
SCALE:2:1
SHEET 1 OF 1
DO NOT SCALE DRAWING
REVISION
DRAWN
CHKD
APP'D
MFG
Q.A
NAME
SIGNATURE
DATE
MATERIAL
WEIGHT
DEBUR AND BREAK SHARP EDGES
FINISH
UNLESS OTHERWISE SPECIFIED:
DIMENSIONS ARE IN MILLIMETERS
SURFACE FINISH:
TOLERANCES:
LINEAR
ANGULAR
Ø 2.90
Ø M5x0.8
15.00
20.00
15.00
20.00
5.00
10.00
5.00
10.00
20.00
5.00
10.00
10.00

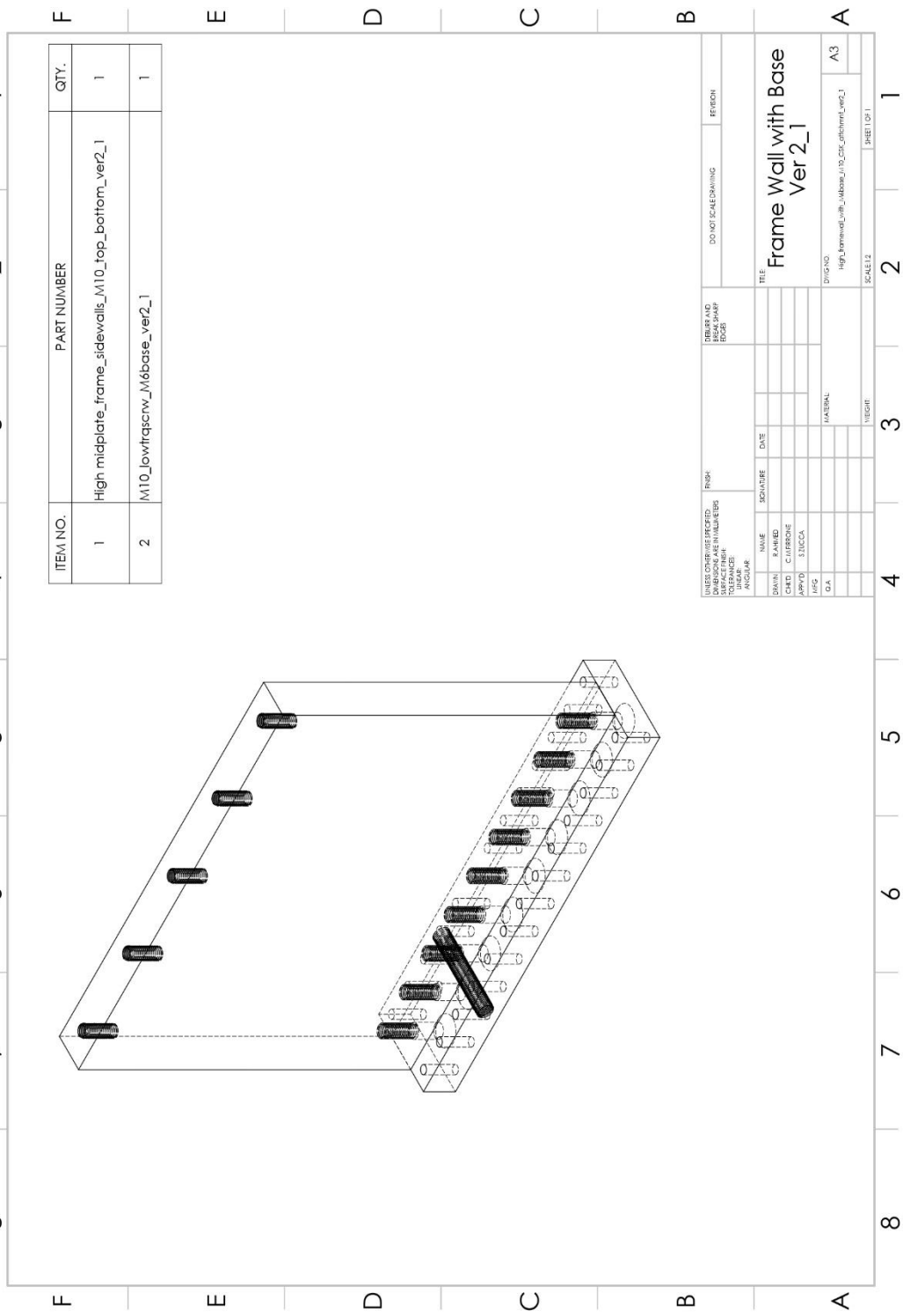
ITEM NO.
PART NUMBER
QTY.
1
High midplate_frame_sidewalls_M10_top_bottom_ver2_1
1
2
M10_lowtrqscrw_M6base_ver2_1
1
Frame Wall with Base
Ver 2_1
A3
SCALE:1:2
SHEET 1 OF 1

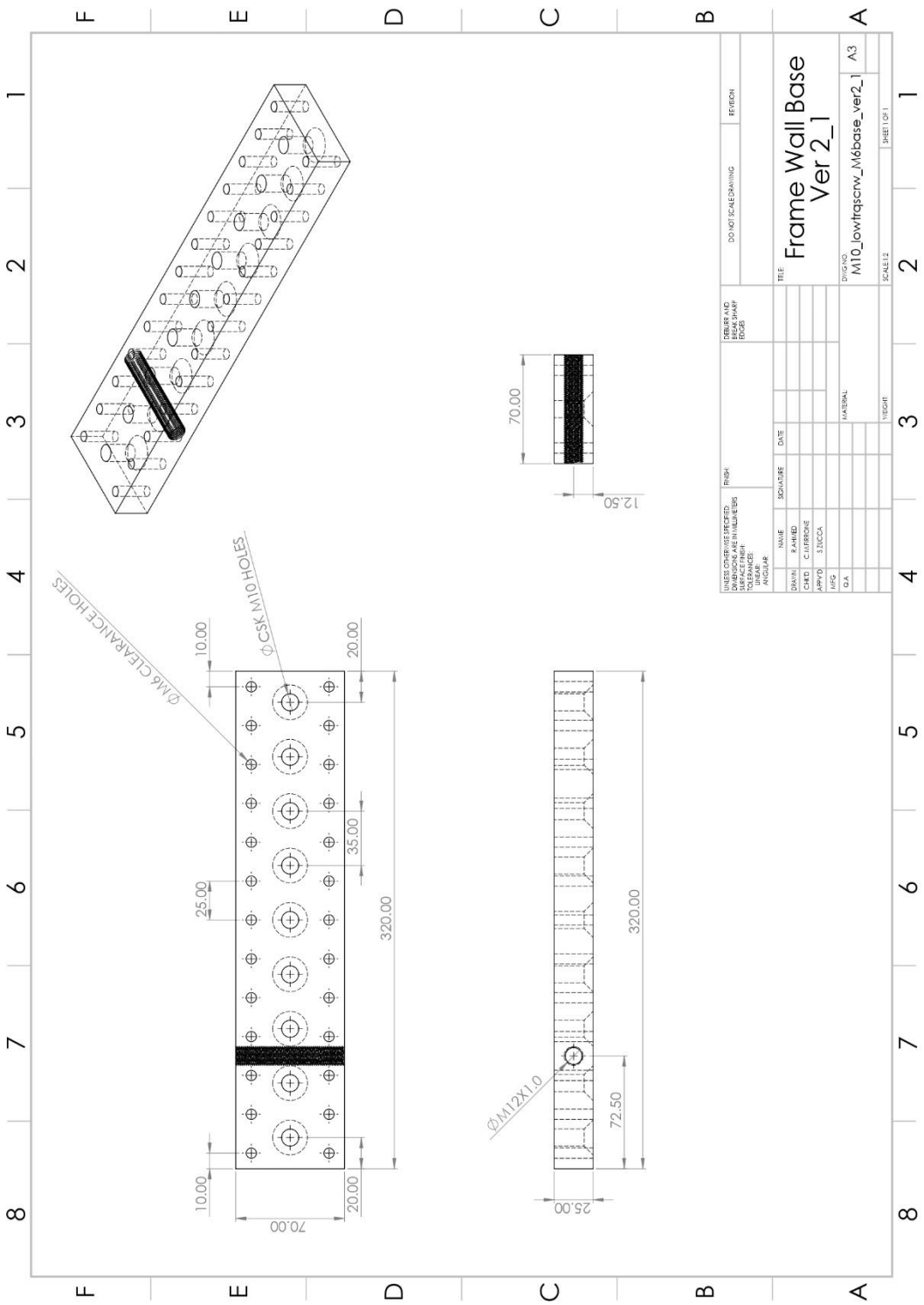
Frame Wall Base
Ver 2_1
M10_lowfrqscrw_M6base_ver2_1
A3
SCALE:1:2
SHEET 1 OF 1
DO NOT SCALE DRAWING
REVISION
TITLE:
DRAWING NO.
MATERIAL
WEIGHT:
DRAWN
CHKD
APPV'D
MFG
Q.A
NAME
SIGNATURE
DATE
R.AHMED
C.FERRONE
S.MCCOY
FINISH:
DEBURR AND BREAK SHARP EDGES
UNLESS OTHERWISE SPECIFIED:
DIMENSIONS ARE IN MILLIMETERS
SURFACE FINISH:
TOLERANCES:
LINEAR
ANGULAR
A
B
C
D
E
F
1
2
3
4
5
6
7
8
70.00
12.50
Ø6.6 CLEARANCE HOLES
Ø CSK M10 HOLES
10.00
20.00
35.00
25.00
320.00
10.00
20.00
70.00
320.00
72.50
ØM12X1.0
25.00

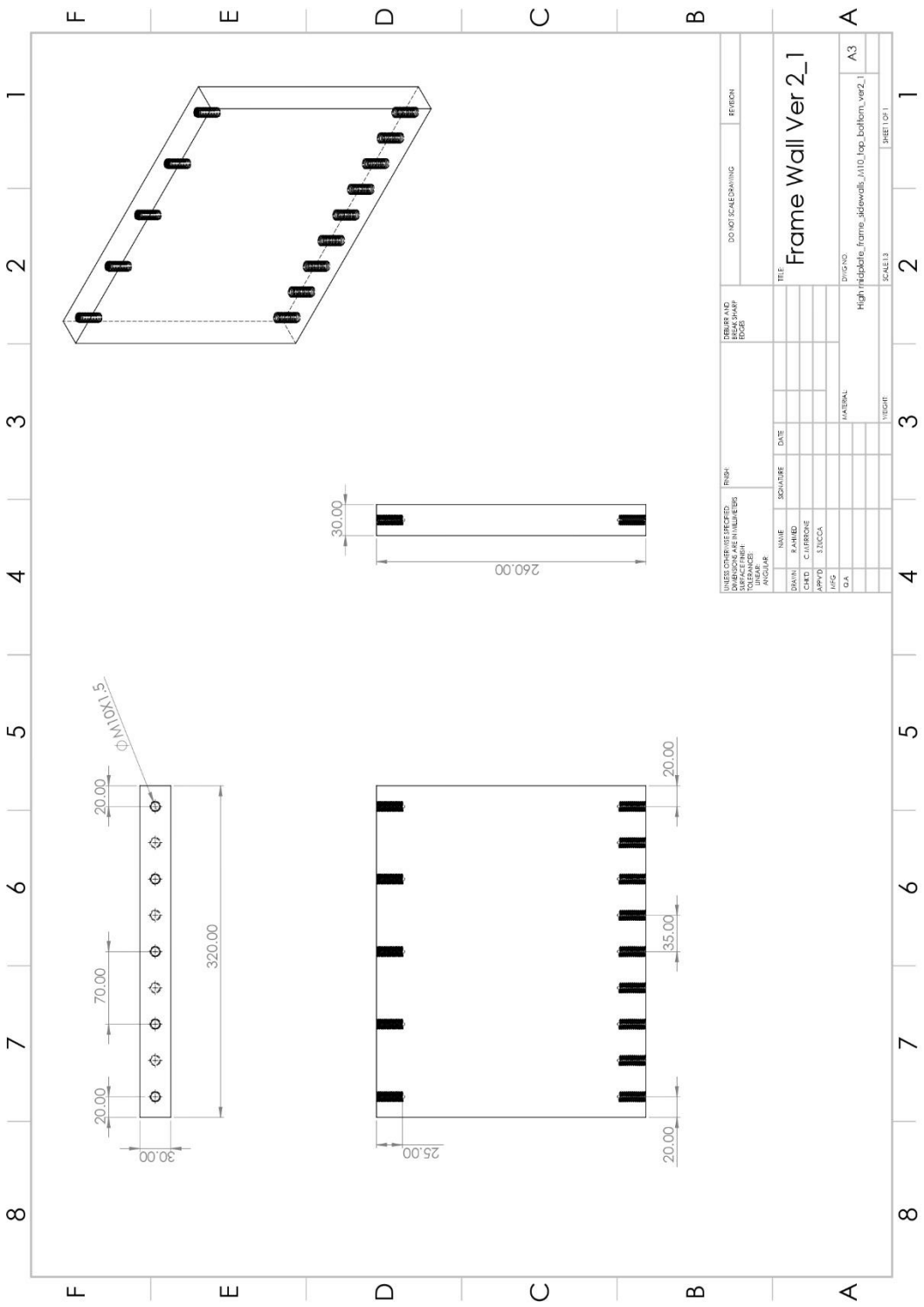
Frame Wall Ver 2_1
A3
DO NOT SCALE DRAWING
REVISION
DEBURR AND BREAK SHARP EDGES
FINISH
UNLESS OTHERWISE SPECIFIED:
DIMENSIONS ARE IN MILLIMETERS
SURFACE FINISH:
TOLERANCES:
LINEAR
ANGULAR
NAME
SIGNATURE
DATE
DRAWN
R.AHMED
CHKD
C.LEFEBVRE
APPVD
S.MCCOY
MFG
Q.A
MATERIAL
WEIGHT
DWG NO
High ridgplate_frame_sidewalls_JA110_top_bottom_ver2_1
SCALE:1:3
SHEET 1 OF 1
ΦM10X1.5
20.00
70.00
320.00
30.00
25.00
35.00
260.00

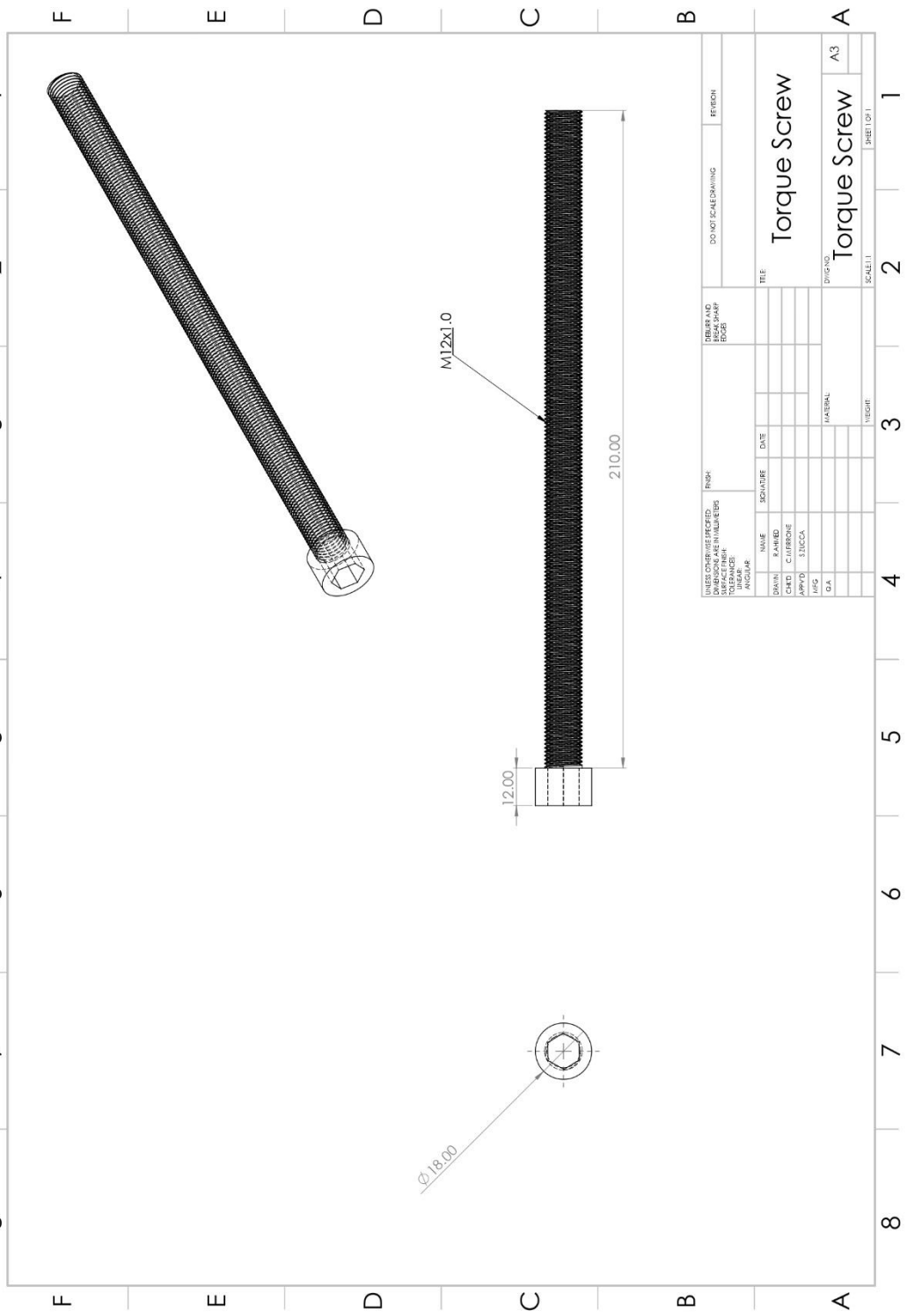
M12x1.0
210.00
12.00
Ø18.00
Torque Screw
Torque Screw
A3
DO NOT SCALE DRAWING
REVISION
DEBURR AND BREAK SHARP EDGES
UNLESS OTHERWISE SPECIFIED:
DIMENSIONS ARE IN MILLIMETERS
SURFACE FINISH:
TOLERANCES:
LINEAR
ANGULAR
FINISH
NAME
SIGNATURE
DATE
DRAWN
R AHMED
CHKD
C LEFBVRE
APP'D
S SICCA
MFG
Q A
MATERIAL
WEIGHT:
SCALE: 1:1
SHEET 1 OF 1

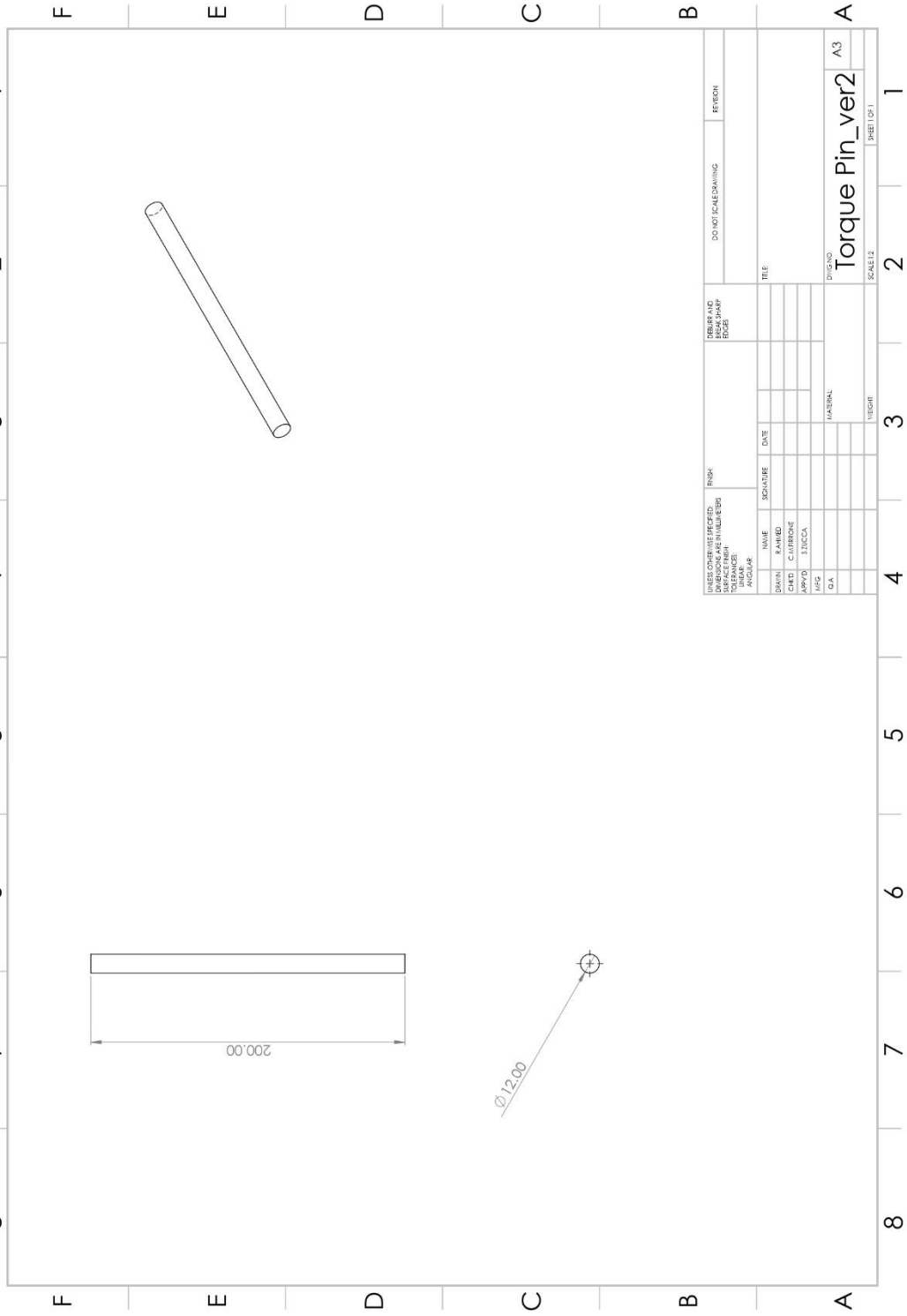
Torque Pin_ver2
A3
200.00
Ø12.00

Appendix B

Details of the components in experimental setup

ELECTRODYNAMIC SHAKER

The electrodynamic shaker used as the excitation device in the experiment was a V400 series vibrator from Ling Dynamic Systems (LDS). This type of shaker is usually driven by LDS PA500L amplifier. In this setup, the shaker was suspended in the test bench using cables and positioned horizontally to excite the mockup-shrouded blade. With natural cooling, this shaker could produce a sine vector force of up to 98N with the maximum acceleration sine peak of 490 m/s^2. The achievable excitation frequency range with this shaker is 5-9000 Hz.

The electrodynamic shaker comprises of a magnet housing that has a permanent magnet. In the annular gap, surrounding the armature drive coil, a magnetic field is produced. On applying current to the armature coil conductors, which are perpendicular to the magnetic flux in the air gap, a force is generated that is mutually perpendicular to the air gap flux and direction of the armature current. Hence, an alternating current generates an alternating force [65]. Since an amplifier drives the shaker, it is possible to produce an accurate force which is also controllable.

PIEZOELECTRIC FORCE SENSORS

The piezoelectric force sensors consists of two crystal disks and electrode foil between them. Force applied on the crystal disk results in the flow of an electric charge that is measured by a charge amplifier. The installed piezoelectric force sensor PCB 208C02 by PCB PIEZOTRONICS had a measurement range of around 0.4kN (100lb) and upper frequency limit of 36 kHz.

TRI-AXIAL ACCELEROMETERS

The tri-axial accelerometer 356A03 also by PCB PIEZOTRONICS used in the experiment, is a lightweight miniature accelerometer that measured acceleration in the three directions (X, Y, Z). Moreover it possessed good sensitivity (1.02 mV/(m/s²)) and measurement range (±4905 m/s² pk).

LMS Scadas III (DAQ)

LMS Scadas III is a multi-channel high performance dynamic data acquisition system that was used for the forced response testing of the shrouded blade. The LMS Scadas III has a flexible architecture and allows configuring from a choice of different modules designed for different functions. It can be integrated with both, LMS Cada-X or LMS Test.Lab testing and analysis software. For the proposed forced response testing, two modules, one for output (QDAC) and one for input (PQFA) were used.

QDAC, which stands for Quad Digital to Analog Converter, provides output signals with very low noise and distortion using a 24-bit digital to analog converters and advanced digital filtering techniques. The module allows generating sine, random burst, chirp and arbitrary signals.

PQFA, which stands for Programmable Quad Floating Amplifier, is the input signal-conditioning module where input range of every channel can be set from ±62.5 mV to ±10V with AC/DC/ICP coupling.

Another input module that could be useful is PQBA that stands for Programmable Quad Bridge Amplifier. This module comprises of four channels for strain gauges or strain gauge based transducers. It can be used for full, half and quarter bridge configurations. With the help of this module, in the proposed experimental setup, the possibility of acquiring the data from the six strain gauge based force sensors measuring the 3D shroud contact forces was explored. The data from the force sensors during the test run was successfully stored and represented in the frequency domain. However, due to the limitation of the LMS Test.lab software to be unable to record the initial static contact force values during the stepped sine test run and the inability to save the force data in time domain at high resolution for longer period, this data acquisition option was not utilized in the forced response experiments. Details of the procedure carried out to acquire the data of the strain gauge-based force sensors in frequency domain using LMS Test.Lab can be found in Appendix D.

QUANTUMX MEASUREMENT AMPLIFIER MX-840B

QuantumX measurement amplifiers are universal measuring amplifiers that reduce the setup time and offer plug & measure capability for the HBM U9C force sensors. The MX840B type was used in the experiment and consisted of 8-channels with 24 bit analog to digital converter per channel. With accuracy class of 0.05 and high sample rates of up to 40kS/s, MX840B provided precise and reliable data acquisition that was required for the measurement of the shroud contact forces.

Appendix C

User manual of test rig operation

This user manual is intended to present step by step instructions to acquire 3D shroud contact force measurements during forced response testing of shrouded turbine blade using the novel experimental test rig.

Software and Data acquisition settings

1. Ensure proper connection of the force sensors with QuantumX MX840B and accelerometers and piezoelectric force sensor with LMS Scadas III.
The details and figures are given as following :

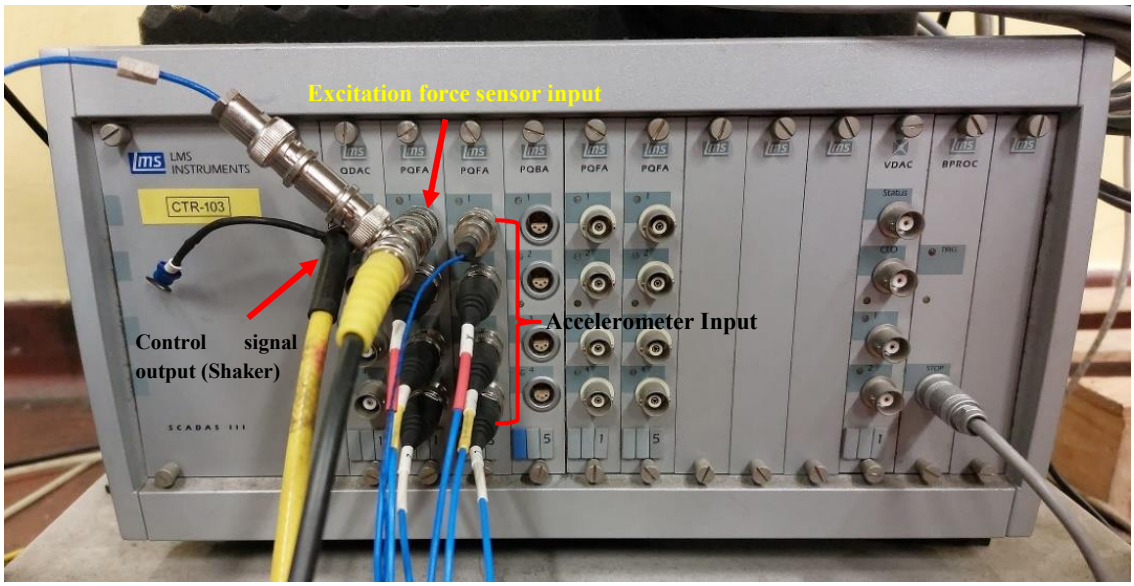

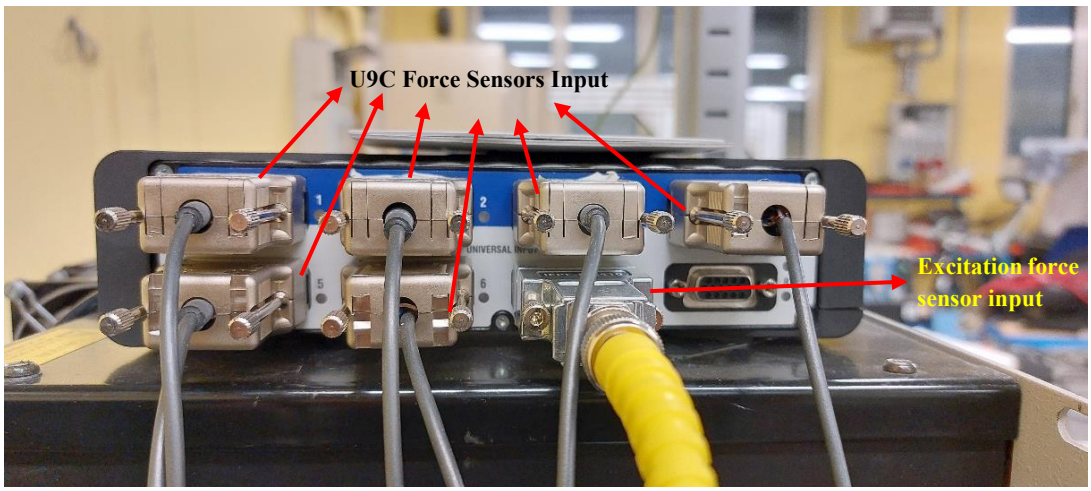

2. Switch on QuantumX MX840B, LMS Testlab, Cada-X PC.

3. Connect TCP/IP ethernet cable to your laptop having CATMAN/AP

4. Run CATMAN /AP

5. Click on ‘Resume last settings’ and check the status of the connected force sensors.

6. Check the sensitivity of the force sensors and verify. Specify the sampling frequency and the alias filter.

7. After ensuring that the shrouds are not in contact with the contact pads, select all the sensors and ‘Execute’ zero balance to zero the force sensors.

8. Wait for 30-45 mins and check if there is any drift. Execute zero balance again and proceed with measurement only if there is no more drift and the force sensors stay at zero value.

9. On Cada-X PC, run Cada-X 3.5E. In open project window, click ‘create new’ and write new project name in the Project field. Then click ‘open’

10. Next click ‘ Test’ on the menu and go to Fourier monitor

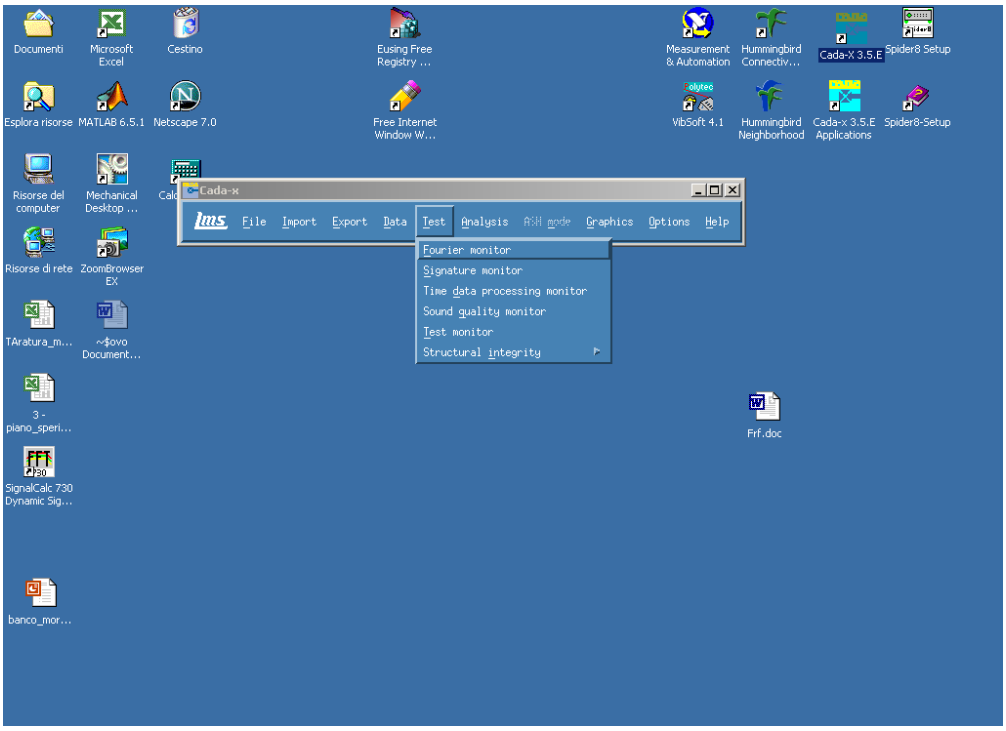

11. In Fourier monitor menu, click ASM mode and go to stepped sine monitor

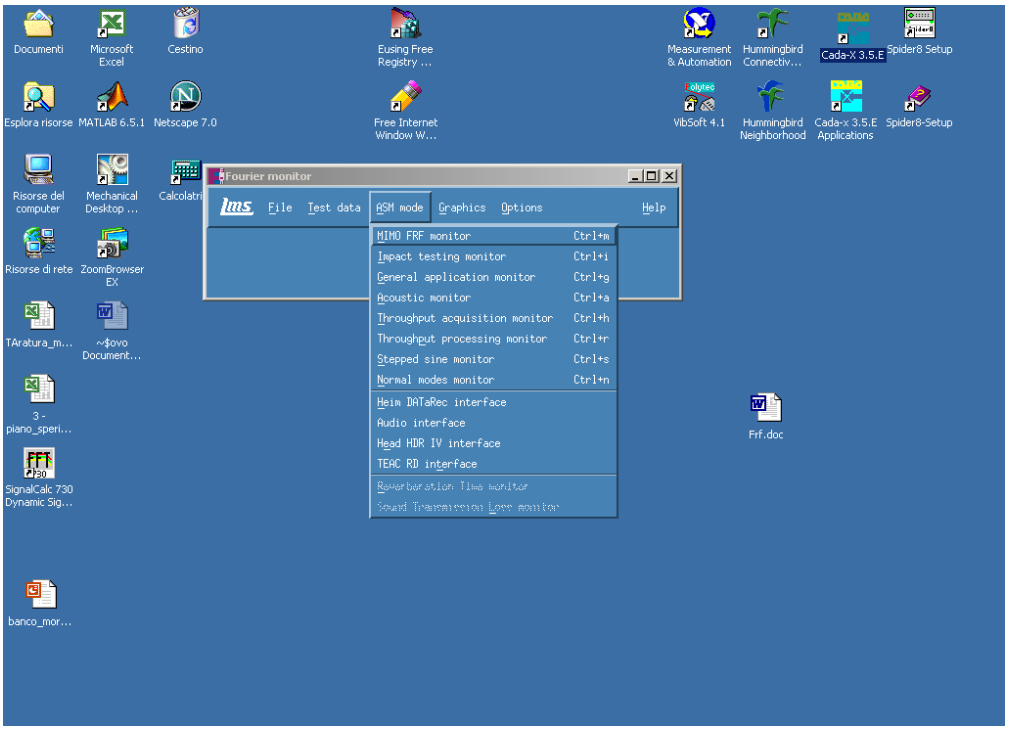

14. Create new test file by writing its name on top right, click Yes when asked for confirmation

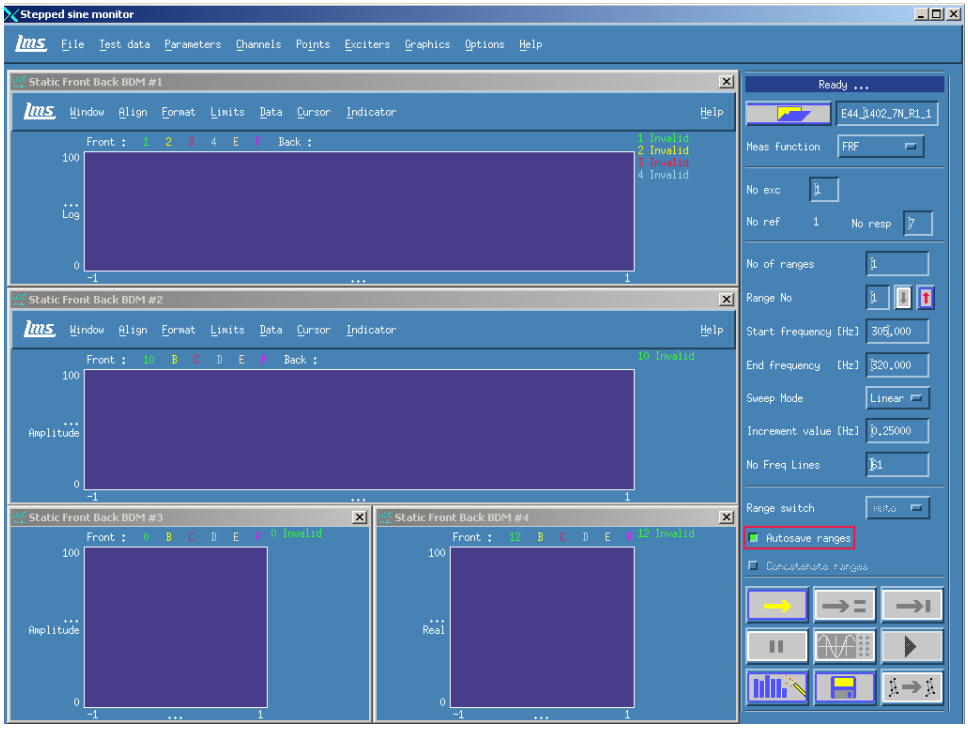

15. On the right menu, keep the settings as shown in the figure above

16. Go to ‘Parameters’, set ‘acquisition’ settings and advanced as shown

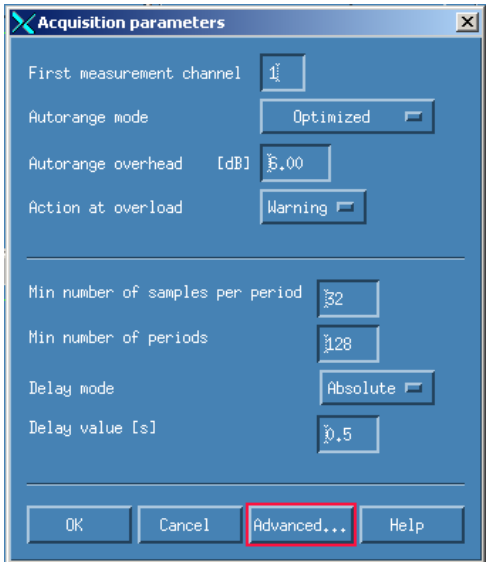

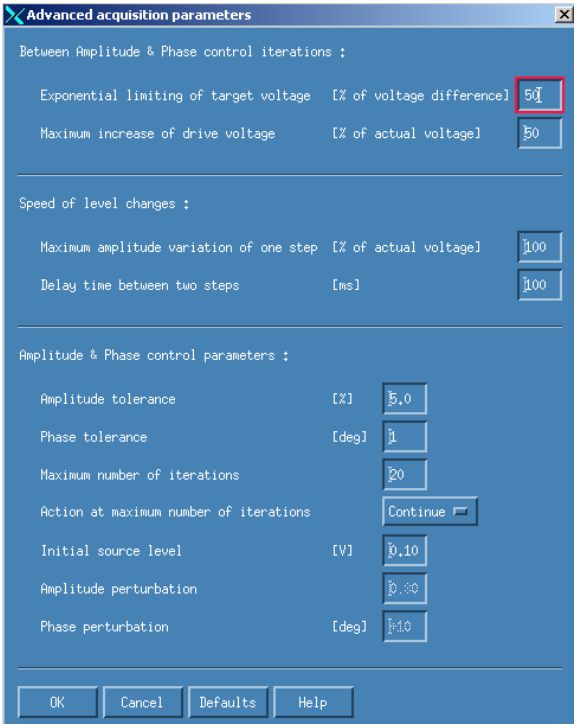

17. Go to ‘Parameters’ and check ‘signal processing’ parameters, activate measurement logging for acquiring excitation force sensor data in time domain

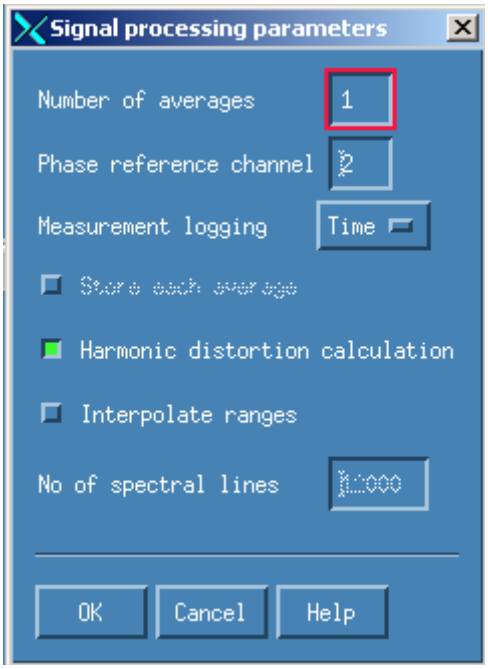

18. Go to ‘channels’ and channel id. Specify the channels according as shown below

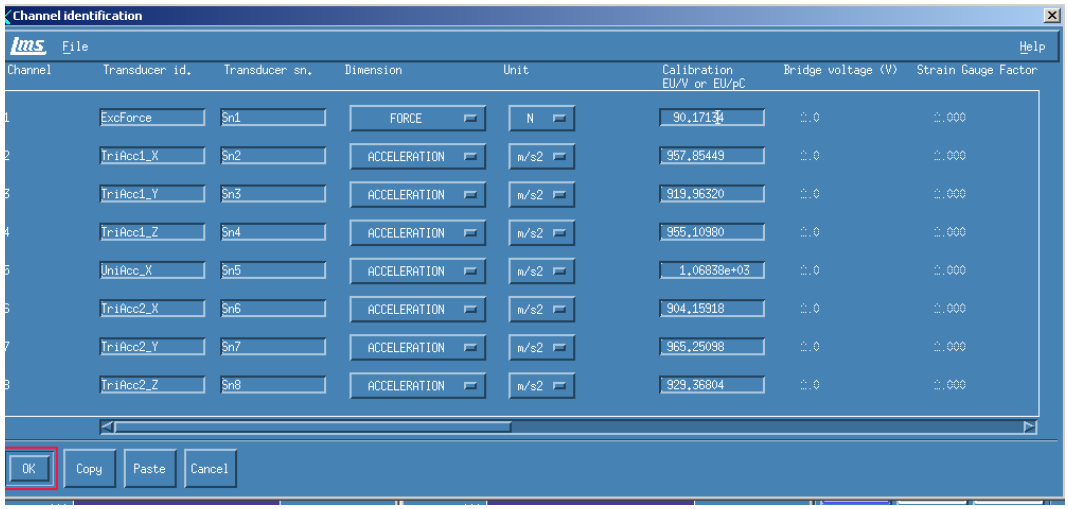

19. Go to ‘exciters’ and control mode, check amplitude

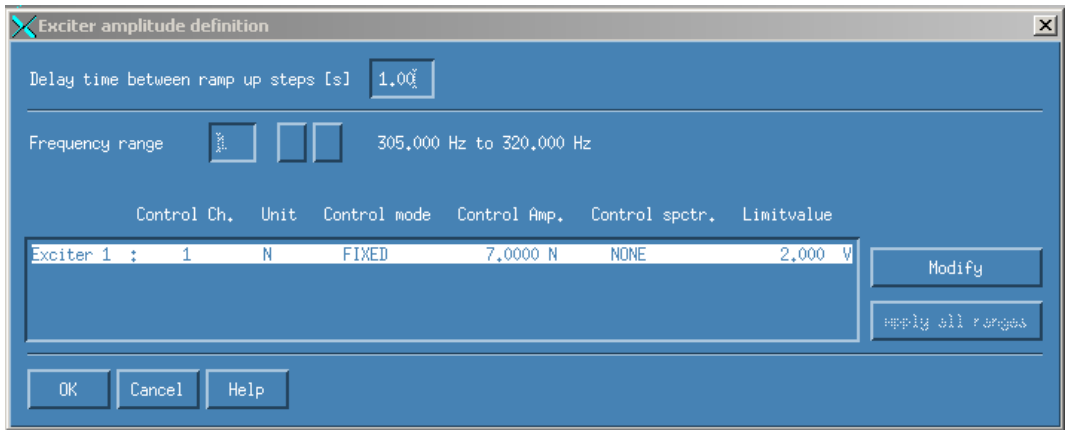

20. Go to ‘exciters’ and then ‘amplitude’ to specify the excitation force level

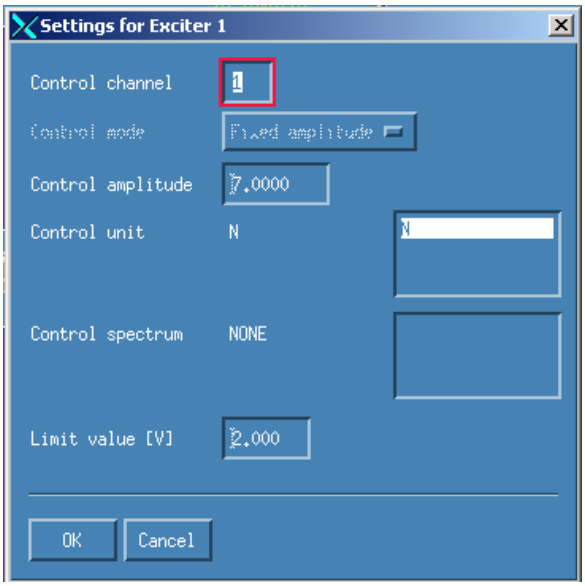

21. Press arm (yellow arrow) and for the plot in the second row, set the data for the excitation force to monitor in real time. Click ‘data’ and then list, double click time_exc1

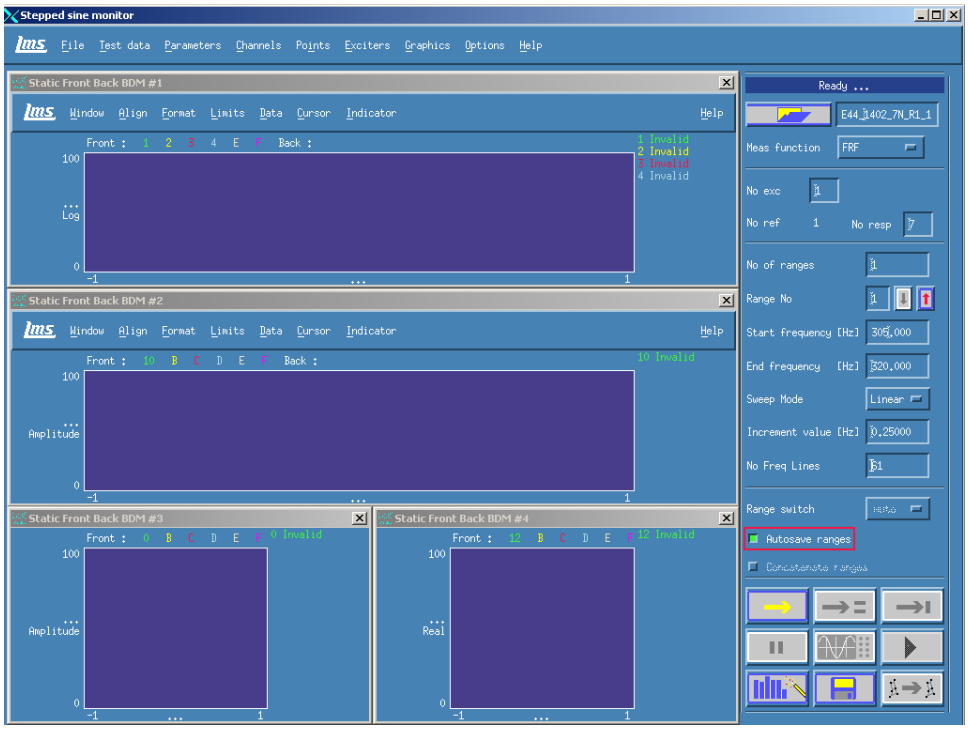

22. DO NOT PRESS START BEFORE APPLYING THE NORMAL PRELOAD AND CLAMPING PRESSURE

23. Switch on the amplifier, press ‘reset’ and rotate the master gain knob to 2 for the first test run. For higher excitation forces, the gain on the amplifier has to be increased.

<u>Shrouded blade – application of normal preload and clamping procedure</u>

1. Using the torque pin, slightly twist the blade such that the shrouds are just touching the contact pads without applying any significant force i.e less than 1N

2. Move the lever of hydraulic press a few times just to apply a small clamping force such that the piston is just touching the block to lock the blade. Record the initial contact forces measured

3. Now rotate torque screws engaged with the torque pin to apply the nominal normal preload on the shroud contacts and monitor the applied normal preload on CATMAN /AP software.

4. Keep rotating the torque screws until the designated normal preload value is reached. Record the measured contact force values.

5. Increase the clamping force and move the lever several times until the clamping pressure reaches 100 bar. Now record the measured force values after the clamping process.

6. Now press ‘Start’ in the Cada-X software to begin the stepped sine test. When the stepped sine test is running, in Cada-X, FRF plot in the first row and the excitation force data in the second row can be monitored. In CATMAN/AP, the data of the force sensors can be monitored.

Saving the data in CATMAN AP and Cada-X

1. Once the test run has finished, press Stop in CATMAN/AP and save the file in *.mat format in the specified directory

2. In Cada-X, press the floppy disk icon to save the file, select 'FRF measurements' from the top and name the file to be saved.

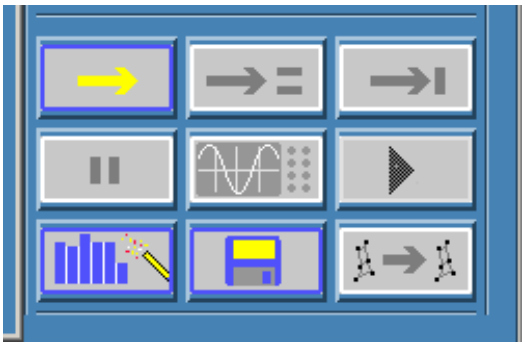

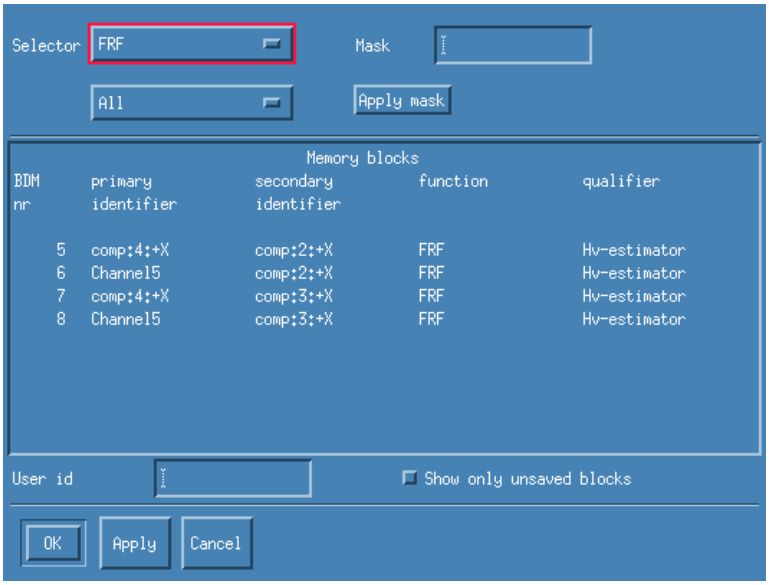

3. For the next test run with the same excitation force, create a new test file with the same settings in Cada-X, arm the system and then press Start in CATMAN to start data acquisition followed by pressing Start in Cada-X software to initiate the sine sweep test run. To change the excitation force, repeat step 17 and step 18 of the previous section 'Software and Data acquisition settings' and then arm the system.

4. After all the test runs have been performed, exit the ‘Stepped sine monitor’ and ‘Fourier monitor’ and in the main menu, click ‘Export’ and save the file with the data of all the test runs as the universal file.

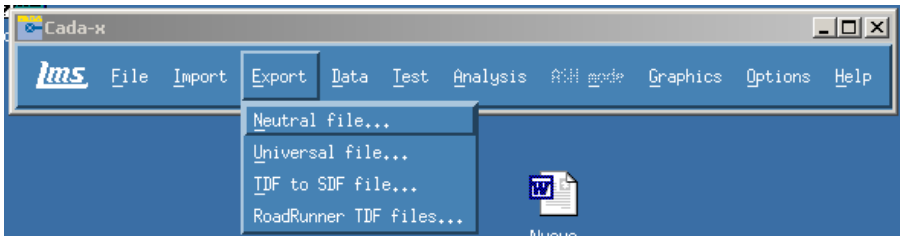

The ‘acceleration’ and ‘include measurements’ have to be checked and then clicking ‘OK’ will save the file which can be opened in any text editor.

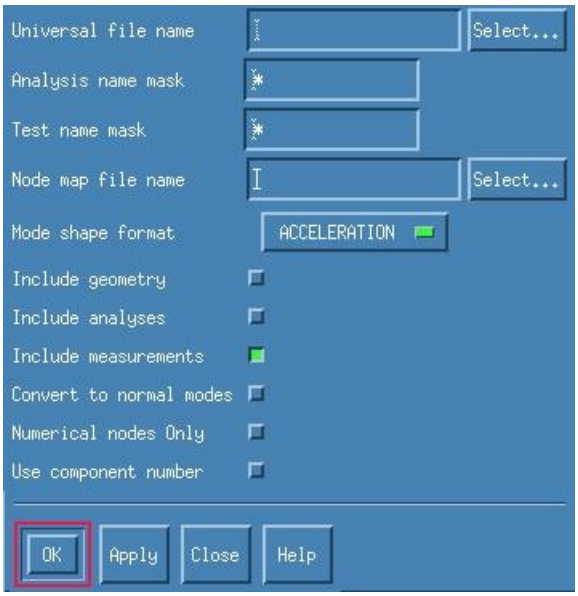

Appendix D

Data acquisition of strain-gauge based force sensors in LMS TestLab using LMS Scadas III

The activity was performed using the MIMO sine testing software of LMS Testlab Ver 8A. Data from the strain gauge based force sensors was acquired using the input module PQBA provided by the LMS Scadas III hardware. Programmable Quad Bridge Amplifier (PQBA) is a 4 channel bridge amplifier for full bridge, half bridge and quarter bridge configurations, available with bridge completion resistors and can be fully controlled by the software. For each channel, the bridge supply voltages can be set separately. It also provides the capability of automatic bridge nulling by using current injection techniques that allows compensation of unbalanced bridge without adjusting the bridge sensitivity. The current injection technique provides complete dynamic gain calibration resulting in better performance and stability as compared to the conventional calibration resistors. Analog overloads and digital overloads are indicated by the overload LED. The figure below shows the connector configuration of the PQBA module.

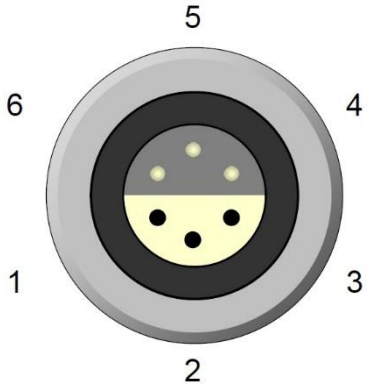

In this study, the data from the strain gauge based force sensors HBM U9C was acquired by using HBM Quantum MX410 measurement amplifier whose pin configuration is shown below:

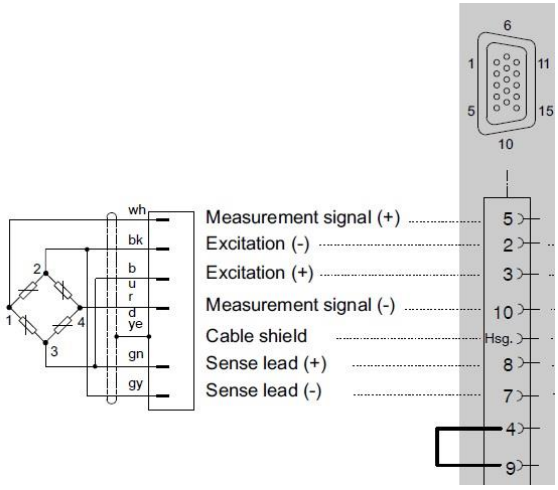

To connect the HBM U9C force sensors to the PQBA, an adapter was made to convert the signals from SubHD 15 pin connector to the 6 pin LEMO connector for PQBA with a 15 pin female connector on one end and LEMO socket mating connector FFA.1S.306.CLAC42 on the other end. The specifications of the adapter cable are as follows:

SubHD 15 pin Female Connector		FFA.1S.306.CLAC42
2	Excitation Voltage(-)	6
3	Excitation Voltage(+)	1
5	Measurement Signal (+)	3
10	Measurement Signal (-)	4
7	Sense lead (-)	2

After connecting the force sensors to the PQBA card through the adapter cable, the first step is to setup the channels that are used for PQBA card. In the channel setup tab, Channel 5,6,7,8 can be configured to be used for PQBA card. To configure, the option for Input Mode column must be changed to 1/1 Bridge, 1/2 Bridge, 1/4

Bridge, 1/1 Bridge AC , 1/2 Bridge AC, 1/4 Bridge AC depending upon the type of strain gauge-based transducers that are being used. In case of HBM U9C 0.5kN force sensors, 1/1 Bridge was selected. The measured quantity in this case would be 'Force'. The actual sensitivity must be specified in mV/N.

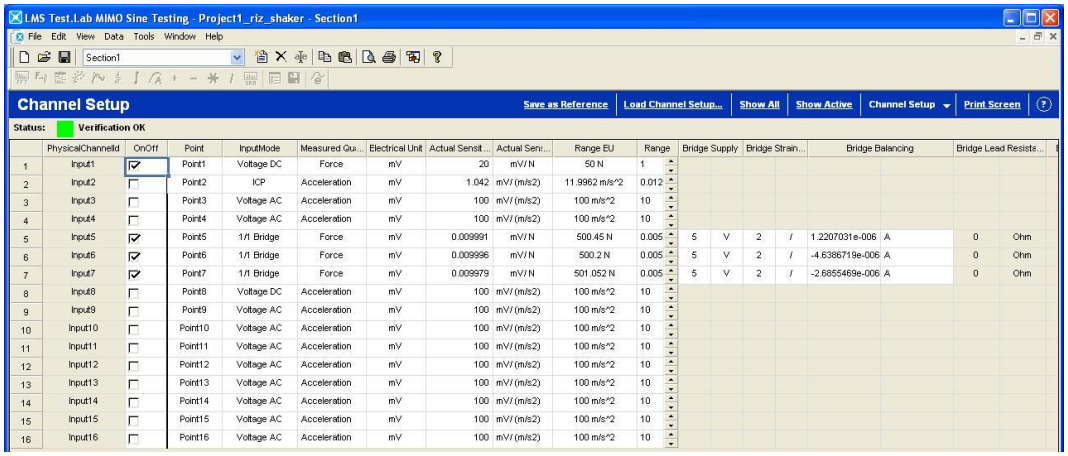

	PhysicalChannelId	OnOff	Point	InputMode	Measured Qu...	Electrical Unit	Actual Sensit...	Actual Sens...	Range EU	Range	Bridge Supply		Bridge Strain...		Bridge Balancing		Bridge Lead Resiste...	
1	Input1	☑	Point1	Voltage DC	Force	mV	20	mV/N	50 N	1								
2	Input2	☐	Point2	ICP	Acceleration	mV	1.042	mV/(m/s2)	11.9962 m/s^2	0.012								
3	Input3	☐	Point3	Voltage AC	Acceleration	mV	100	mV/(m/s2)	100 m/s^2	10								
4	Input4	☐	Point4	Voltage AC	Acceleration	mV	100	mV/(m/s2)	100 m/s^2	10								
5	Input5	☑	Point5	1/1 Bridge	Force	mV	0.009991	mV/N	500.45 N	0.005	5	V	2	/	1.2207031e-006	A	0	Ohm
6	Input6	☑	Point6	1/1 Bridge	Force	mV	0.009996	mV/N	500.2 N	0.005	5	V	2	/	-4.6386719e-006	A	0	Ohm
7	Input7	☑	Point7	1/1 Bridge	Force	mV	0.009979	mV/N	501.052 N	0.005	5	V	2	/	-2.6855469e-006	A	0	Ohm
8	Input8	☐	Point8	Voltage DC	Acceleration	mV	100	mV/(m/s2)	100 m/s^2	10								
9	Input9	☐	Point9	Voltage AC	Acceleration	mV	100	mV/(m/s2)	100 m/s^2	10								
10	Input10	☐	Point10	Voltage AC	Acceleration	mV	100	mV/(m/s2)	100 m/s^2	10								
11	Input11	☐	Point11	Voltage AC	Acceleration	mV	100	mV/(m/s2)	100 m/s^2	10								
12	Input12	☐	Point12	Voltage AC	Acceleration	mV	100	mV/(m/s2)	100 m/s^2	10								
13	Input13	☐	Point13	Voltage AC	Acceleration	mV	100	mV/(m/s2)	100 m/s^2	10								
14	Input14	☐	Point14	Voltage AC	Acceleration	mV	100	mV/(m/s2)	100 m/s^2	10								
15	Input15	☐	Point15	Voltage AC	Acceleration	mV	100	mV/(m/s2)	100 m/s^2	10								
16	Input16	☐	Point16	Voltage AC	Acceleration	mV	100	mV/(m/s2)	100 m/s^2	10								

"For strain gauge based force transducers, the sensor's exact nominal (rated) sensitivity can be found in the test/calibration certificate. In most cases, this sensitivity is given in mV/V, with the nominal (rated) force being applied. The amplifier systems feed the measuring bridge with a bridge excitation voltage. This bridge excitation voltage often is 5 V. If force transducer's nominal (rated) sensitivity is 2 mV/V, 10 mV are available at the amplifier's input stage when the force transducer is loaded with nominal (rated) force. For example, when you use a 100 N force sensor (100 N nominal (rated) force, 2 mV/V sensitivity at nominal (rated) force) and load it with 100 N you obtain 10 mV. In general, the measured value is not always 100 N; in fact, it should also be possible to detect smaller values. If we want to have a measurement signal resolution of 0.1 N, 10 µV are available at the input stage. If the amplifier has a resolution of 100,000 divisions, which is still less than a high-precision instrument such as HBM's DMP41 offers, this corresponds to the relationship between the height of the Eiffel tower (321 m) and the thickness of a CD case. Requirements are significantly higher with increasingly complex measurement tasks. The better the connection corresponds to the measurement task the more reliable are our measurement results." (https://www.hbm.com/en/4248/electrical-connection-of-force-transducers/)

In our case, the nominal rated (500N) sensors sensitivity of six force sensors in mV/V as specified in the calibration certificate are Sensor 328 : -0.9984 mV/V;

Sensor 329 : -0.9979 mV/V; Sensor 330 : -0.9985 mV/V; Sensor 331 : -0.9982 mV/V; Sensor 723 : -0.9991 mV/V; Sensor 724 : -0.9996 mV/V

The reference excitation voltage specified in the calibration certificate is 5V. So for example, if the Sensor 723 is connected to Input5 and from the calibration certificate we can check the sensitivity is -0.9991mV/V when it is loaded with nominal load of 500N. In this case, 4.9955 mV (0.9991mV/V x 5V) are available at amplifier's input stage. For PQBA bridge settings, where the actual sensitivity must be specified in mV/N, we have the measurement resolution of 1N, which in case of Sensor 723 would be 0.009991 mV/N (4.9955mV/500N). The corresponding actual sensitivity values for the other sensors are calculated likewise and entered in the channel setup window.

The next tab is the 'Calibration' tab where 'Bridge Settings' is selected from the top right options. After reviewing the channel properties and settings, we must perform bridge nulling.

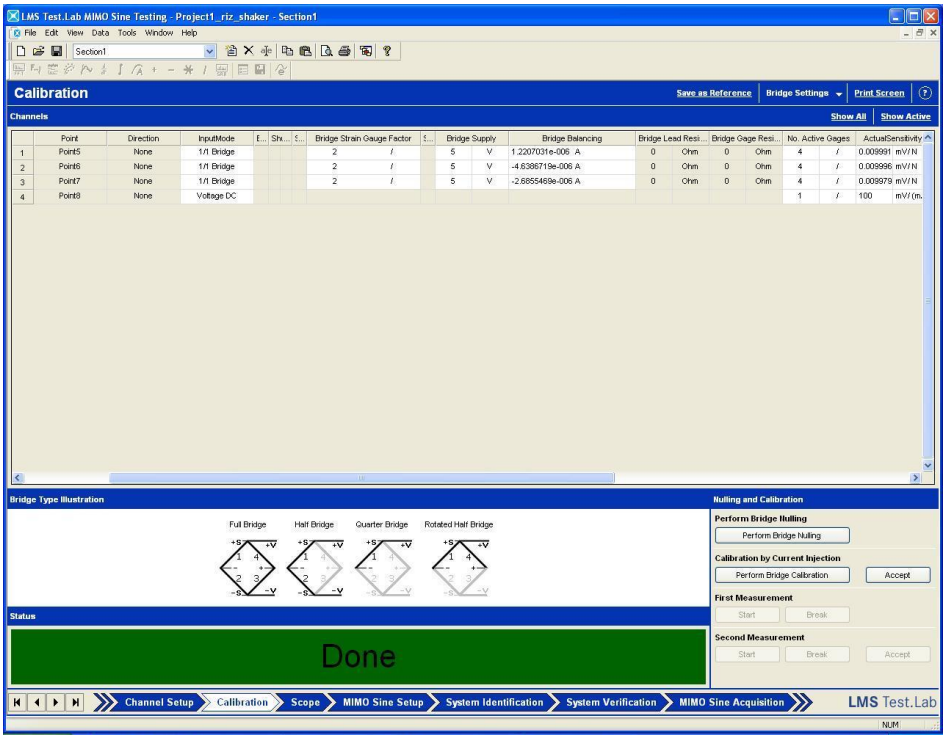

To correct for the DC offset, bridge nulling (or bridge balancing) is performed. This involves 4 steps:

− Measure the offset error on the bridge channel.

− Inject a known current into the bridge.

− Measure the effect on the bridge output voltage.

− Calculate the current needed to zero the bridge output voltage. This current is the balancing current.

These steps are done internally in PQBA when we start the nulling procedure. This balancing current that is injected into the bridge does not influence the bridge sensitivity. After the nulling procedure we can observe the change of the bridge balancing current. More details regarding this procedure can be obtained from the 'help' section of the software.

After bridge nulling, we must calibrate the force sensors. There are 3 ways for calibrating a bridge sensor:

1. Direct calibration

In this case, a well-known mechanical load is applied to the bridge sensor.

2. Indirect calibration: shunt calibration.

With this method, a mechanical load is simulated by connecting a known shunt resistor parallel to one of the bridge branches.

3. Calibration by current injection

For this type of calibration, the calculation of the sensitivity is based on a well-known current that is injected into the bridge. This type of calibration is only possible for the PQBA. After the calibration, we must 'Accept' to implement the new changes.

In the 'Scope' tab, we can now check the force values that is measured by the force sensors. The force levels can be observed as a plot or as numerical values by pressing 'More' button that opens the Range Checking window. In the same

window, we can select the format in which we want to view the measured force values. E.g. the ‘Absolute’ option shows the force measured in terms of N.

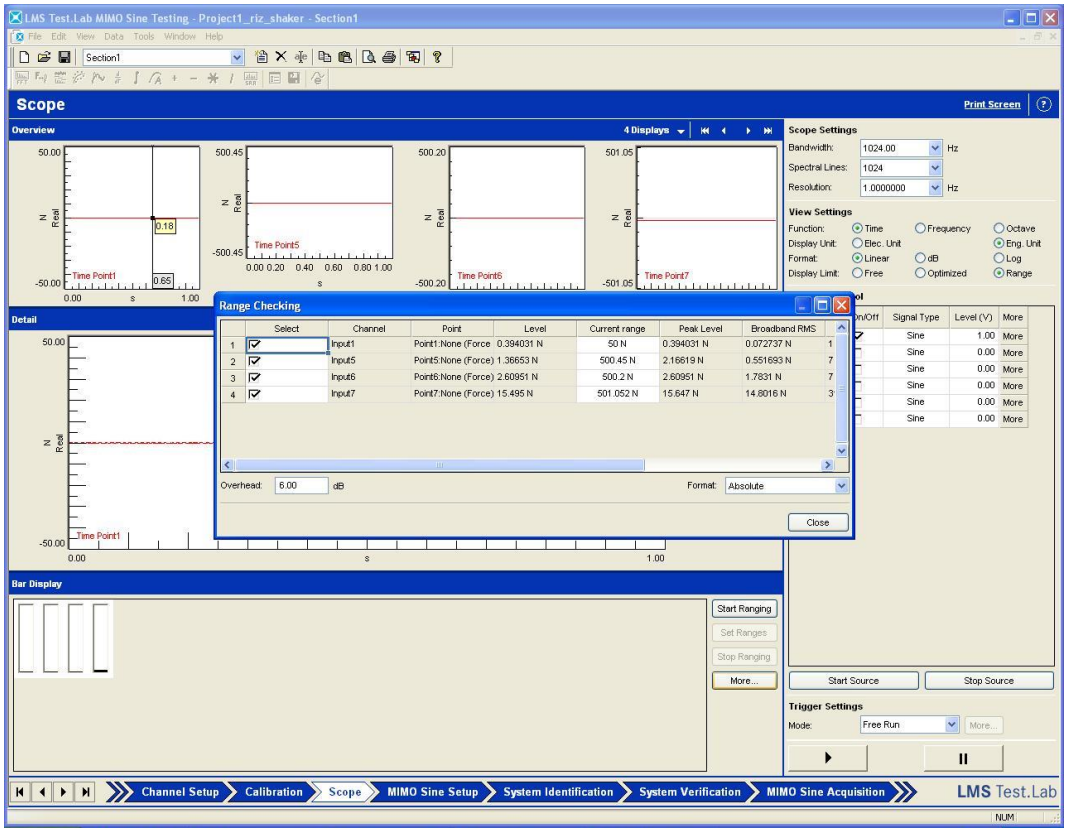

However, the initial force value shown for each sensor cannot be zeroed for zero load and it changes gradually with the passage of time. Nevertheless, when the sensor is loaded with the known load, the force measured can be observed.

After the configuration of the force sensors with PQBA module, the rest of the procedure is the same which is followed for the stepped sine testing using the LMS TestLab. This involves specifying the reference profile in the Mimo Sine Setup tab, after which the software undertakes various check of the settings in the System Identification and System Verification. Subsequently, during the test run, data was acquired from strain gauge-based force sensors that was recorded in the frequency domain. Currently, LMS TestLab does not allow the recording of the data in the time-domain. The time data obtained from the scope is limited to very few samples and low resolution.